厚生労働科学研究費補助金

労災疾病臨床研究事業

悪性胸膜中皮腫に対するヒト化抗 CD26 抗体と免疫チェックポイント阻害薬との革新的併用療法の開発

令和３年度　総括・分担研究報告書

研究代表者　森本　幾夫

令和４(2022)年３月

目　次

Ⅰ．総括研究報告

労災疾病臨床研究事業費補助金

総括研究報告書

悪性胸膜中皮腫に対するヒト化抗 CD26 抗体と免疫チェックポイント阻害薬との革新的併用療法の開発

研究代表者　森本　幾夫　順天堂大学大学院医学研究科
免疫病・がん先端治療学講座 特任教授

研究要旨

悪性胸膜中皮腫はアスベストばく露によって起こる難治性悪性腫瘍だが、満足できる治療法はなく、新たな治療法の確立が望まれる。われわれは、新規治療標的分子として悪性胸膜中皮腫に発現する CD26 に着目し、ヒト化 CD26 抗体 YS110 を開発した。フランスにて悪性中皮腫を中心とした第 I 相臨床試験を実施し、国内でも悪性中皮腫に対する第 I/II 相臨床試験を実施した。2019 年中に第 II 相臨床試験の最終患者への投与が終了し、結果の集計が完了したところだが、安全性が確認され、フランスでの第 I 相臨床試験と同等の有効性を示唆する結果が得られている。治療抵抗性の悪性中皮腫患者に対して、CD26 抗体単剤でも高い割合で Stable Disease・Partial Response となり抗腫瘍効果は認められたが、より長期間抗腫瘍効果を発揮し、無増悪生存期間を与えられる本抗体を用いた新たな併用療法の開発も重要な課題である。そこで、ヒト免疫化マウスを用いたヒト悪性中皮腫細胞株担がんモデルを確立し、YS110 と PD-1 抗体との併用効果を検討した結果、それぞれの単剤よりも強い相乗効果が認められるデータを得た。また、YS110 投与によって血清中の Th1 遊走ケモカイン濃度が顕著に増加する一方で、Th2 遊走ケモカイン濃度は減少することを見出し、腫瘍に浸潤する免疫細胞を変化させている可能性が考えられる。

今年度は国内の第 I/II 相臨床試験患者の腫瘍病理組織から腫瘍部分を切り出し、RNA 抽出と DNA マイクロアレイ解析を行った。Progressive Disease 症例群と比較して Stable Disease 症例群で共通して発現が高い遺伝子、発現が低い遺伝子の絞り込みを行い、CD26 抗体の有効性予測バイオマーカー候補を見出した。今後、悪性中皮腫の病理組織の免疫染色を検討し、CD26 抗体投与を開始する前に抗体療法が有効な患者を判別できるバイオマーカーとなり得るかを明らかにする。

研究分担者
岸本　卓巳：独立行政法人労働者健康安全機構 アスベスト疾患研究・研修センター 所長
山田　健人：埼玉医科大学医学部 病理学 教授
波多野　良：順天堂大学大学院医学研究科 免疫病・がん先端治療学講座 特任助教
研究協力者
藤本　伸一：岡山労災病院 腫瘍内科部長
青江　啓介：山口宇部医療センター 腫瘍内科 内科系診療部長
伊藤　匠：順天堂大学大学院医学研究科 免疫病・がん先端治療学講座 博士研究員
大沼　圭：順天堂大学大学院医学研究科 免疫病・がん先端治療学講座 准教授
金子　有太郎：ワイズ・エー・シー株式会社 代表取締役 CEO
近畿大学 客員教授(元)

A. 研究目的

悪性中皮腫はアスベスト暴露により発症する難治性がんであり、予後は極めて不良で労災疾病行政上も大きな問題となっている。

研究代表者はCD26の抗体開発、cDNAの単離を世界に先駆けて行い(Immunol Rev 1998)、30年に渡りCD26研究を続け、特にCD26のヒト免疫及びがんにおける機能、臨床応用の研究で世界をリードしている。抗腫瘍効果の強いヒト化CD26抗体を開発し、悪性中皮腫におけるCD26の発現、抗体の抗腫瘍作用機構を明らかにしてきた(Clin Cancer Res 2007, PLoS One 2013, Nat Immunol 2015)。フランスにて治療抵抗性の悪性中皮腫を中心とした計33例にFirst-in-Human第I相臨床試験を実施し、**安全性が確認され、有効性を示唆するデータも得られた**(Br J Cancer 2017)。本邦でも治療抵抗性の悪性中皮腫に対する第I相臨床試験を開始し(第1〜3コホート)、2018年に全9例への投与が終了した(Lung Cancer 2019)。本結果から抗体推奨用量を6mg/kgとし、第II相臨床試験も2019年中に全31例への投与が終了した。国内臨床試験でもフランスでの臨床試験と同等の有効性を示す結果が得られている(論文投稿中)。重要なことに、CD26抗体ではフランスでの臨床試験33例、国内での臨床試験40例中、**免疫チェックポイント阻害薬(ICI)で報告されているような自己免疫疾患様の有害事象はなく、安全性が証明**されている。特記すべきは、国内臨床試験40例中、PD-1抗体(Nivolumab (Nivo))無効例が13例含まれており、うち評価可能11例中Partial Response (PR)が1例・Stable Disease (SD)が7例・Progressive Disease (PD)が3例で、72.7% (8/11)がPR・SDであり、CD26抗体が**ICI抵抗性患者にも有効である可能性が示唆**された。近年、CTLA-4抗体, PD-1抗体などのICIの登場は、特に悪性黒色腫や肺癌などの領域で治療に変革をもたらした。本邦でも治療抵抗性の悪性中皮腫31例に対するNivoの第II相臨床試験で無増悪生存期間(PFS) 6.1ヶ月と突出して良好な結果が得られているが、欧米での治療抵抗性悪性中皮腫に対する臨床試験では、PD-1抗体はNivo, Pembrolizumabともに単剤ではPFS 2.6-4.5ヶ月ほどで、NivoとCTLA-4抗体の併用でも悪性中皮腫38例でPFS 6.2ヶ月である(Front Oncol 2020)。このように一般的に併用療法では単剤よりもPFSは向上するものの副作用出現率も上昇するため、更なる治療手段の改善が必要である。ヒト化CD26抗体の国内臨床試験でも全40例中Nivo抵抗性再発例が13例被験者となっており、ICIの治療抵抗性患者の治療をいかに向上させるかも今後、克服すべき課題といえる。

以上から、ヒト化CD26抗体単剤でも有効性を示す結果は得られているが、**多くの悪性中皮腫患者に、より長期間抗腫瘍効果を**

発揮できる、有効かつ安全な新規治療法の確立を最終的な目標とし、CD26 抗体と ICI との併用療法の開発を行う。初年度は、(1)ヒト免疫化マウスを用いた悪性中皮腫株の皮下移植モデル・胸腔内移植モデルを構築し、CD26 抗体と PD-1 抗体それぞれの単剤よりも併用投与では抗腫瘍効果がより強く認められるデータを得て特許出願を行った(特願 2021-091761)。さらに CD26 抗体の新たな抗腫瘍作用メカニズムとして、Th1 遊走ケモカイン MIG, IP-10 の発現を上昇させる一方で、Th2 遊走ケモカイン TARC, MDC の発現を低下させることを見出し、腫瘍内に浸潤する T 細胞のフェノタイプを変化させる可能性が考えられる。また、(2)CD26 抗体療法が有効な患者を選択できる新たなバイオマーカーを同定するために、CD26 抗体の国内臨床試験で SD が長期間持続した症例と PD 症例の病理組織から腫瘍部位を切り出し、DNA マイクロアレイによる遺伝子発現の網羅的解析を行い、バイオマーカー候補の絞り込みを行っている。

B. 研究方法

各分担研究報告書に著述

（倫理面への配慮）

ヒト臍帯血 CD34 陽性造血幹細胞および成人健常者の末梢血を用いた研究については、森本が講座責任者である順天堂大学大学院医学研究科で本研究を行うための研究計画書等を倫理審査委員会へ提出し、承認を得ている(順大医倫第 2020280 号, 2020291 号)。また、ヒト化 CD26 抗体の国内第 I/II 相臨床試験の患者検体を用いたバイオマーカー探索研究については、臨床試験審査委員会、各治験実施施設内の治験審査委員会にて、試験の実施と合わせてバイオマーカー探索用採血・腫瘍組織検体の提供について協議され、実施承認を取得済みである。末梢血の提供を受ける際には、研究対象者に対する人的擁護上の配慮及び研究により研究対象者が受ける不利益、利益等の説明を行い、書面でのインフォームド・コンセントを得ている。動物実験の実施はいわゆる 3R に基づいて行い、順天堂大学医学部実験動物委員会に実験計画書を提出し審議の上、承認されている(承認番号: 2021056)。

ヒト化 CD26 抗体の国内第 I/II 相臨床試験の患者検体を用いたバイオマーカー探索研究については、臨床試験審査委員会、各治験実施施設内の治験審査委員会にて、試験の実施と合わせてバイオマーカー探索用採血・腫瘍組織検体の提供について協議され、実施承認を取得済みである。検体の提供を受ける際には、研究対象者に対する人的擁護上の配慮及び研究により研究対象者が受ける不利益、利益等の説明を行い、書面でのインフォームド・コンセントを得ている。

C. 研究結果

1) ヒト免疫化マウスの作製

ヒト化 CD26 抗体はマウス CD26 には結合しないため、ヒトの悪性中皮腫を用いる必要があり、PD-1 抗体との併用効果を検討するためには、ヒト免疫細胞が生着したヒト免疫化マウスを作製する必要がある。そのためには、重度の免疫不全マウスである NOG マウスに低線量の放射線を照射し、ヒトの造血幹細胞を移植する必要がある。ヒト臍帯血造血幹細胞分画の解凍と洗浄条件を検討し、高い確率でヒト T 細胞が発生する方法を確立した。ヒト造血幹細胞を移植して 10 週間経過するまではマウスの血中のヒト免疫細胞の約 90%が B 細胞(CD19 陽性)で、10 週以降はヒト CD4 T 細胞(CD3 陽性 CD4 陽性)・CD8 T 細胞(CD3 陽性 CD8 陽性)の割合が

徐々に増えていき13週目ではヒトの血球細胞の約 10-15%が T 細胞、17 週目では約25-35%がT細胞であることを確認した。

悪性中皮腫細胞株 JMN(肉腫型)およびH226(上皮型)は、in vivo での増殖が非常に遅く、腫瘤を形成するまでに5-6週間かかるため、マウス体内でヒト T 細胞の細胞数が増えてくる造血幹細胞移植13週目に悪性中皮腫細胞株を皮下移入した。

2) ヒト化 CD26 抗体と PD-1 抗体との併用効果の検討

JMN および H226 をヒト免疫化マウスの側腹部に皮下移入して 5 週間経過し、小さな腫瘤形成を確認した時点から、control human IgG_1, ヒト化 CD26 抗体単独, mouse anti-human PD-1 mAb (以下、PD-1抗体)単独, ヒト化 CD26 抗体と PD-1 抗体の併用をそれぞれ 200μg/dose で週3回投与を続けた。腫瘍サイズを週に 2 回採寸した結果、control 抗体投与群と比較して、CD26抗体単独(YS alone)、PD-1 抗体単独(PD1 alone)それぞれで腫瘍増殖の抑制が見られたが、両抗体投与群(YS+PD1)ではさらに腫瘍サイズが小さいことが示された。H226においても同様の結果が得られている。

現時点でまだ各群の n 数が少ないが、解剖する 9 週時点での腫瘍体積および回収した腫瘍重量の両方で、control 群と YS alone群、または control 群と PD1 alone 群で有意差は認められない一方、control 群とYS+PD1 群で $p<0.05$ の有意差が認められ(Fisher の多重比較検定)、両抗体の併用効果が期待される。

3) ヒト化 CD26 抗体の新たな抗腫瘍作用メカニズムの可能性

CD26 抗体には多様な抗腫瘍作用メカニズムが考えられ、これまでに CD26 を発現するがん細胞の細胞膜上の CD26 に抗体が結合することで、直接的に増殖抑制に作用することを明らかにしてきた。さらに DPP4酵素活性を阻害することが腫瘍周囲への免疫細胞浸潤を増加させることが報告されている。

これまでに CD26 抗体の国内第 I/II 相臨床試験患者の血清や末梢血リンパ球を用いて、CD26 抗体の予後・治療効果を予測し得るバイオマーカーの探索を試みてきたが、血清中のサイトカイン・ケモカインの中でCD26 抗体投与によって絶対量が増加するもの、減少するものがあることが示された。中でも、代表的な Th1 細胞遊走ケモカインである MIG/CXCL9 と IP-10/CXCL10 はCD26 抗体投与によって血清中濃度が顕著に増加したのに対し、代表的な Th2 細胞遊走ケモカインである TARC/CCL17 と MDC/CCL22 の血中濃度は減少することを見出し、上皮型・二相型・肉腫型の組織型に分けて解析した場合でも、いずれの組織型でもほとんどの患者で共通して変化していることが示された。

これらの結果から、CD26 抗体は DPP4酵素活性を低下させることで、酵素によるケモカインの切断とそれにともなう活性低下を妨げるだけでなく、ケモカイン産生量自体にも影響を与えることで、腫瘍周囲に浸潤する免疫細胞を変化させることが予想された。

4) 国内第 I/II 相臨床試験患者の腫瘍病理組織の遺伝子発現解析

CD26 抗体の国内臨床試験で腫瘍病理組

織のバイオマーカー解析に同意が得られたのは、第Ⅰ相が全9例中2例、第Ⅱ相が全31例中21例の計23例(23/40)で、内訳はPR 0例・SD 16例・PD 6例・評価不能 1例であった。DNAマイクロアレイ解析でSD症例とPD症例の遺伝子発現比較を行う際に、考慮すべき事項として性別・組織型・抗PD-1抗体 Nivolumab 投与の有無が挙げられる。腫瘍病理組織のバイオマーカー探索同意が得られた23例中、抗腫瘍効果の判定ができた22例を性別・組織型・Nivolumab投与の有無の項目で整理した結果、性別・組織型・Nivolumab投与の有無が同じ条件で、SD症例とPD症例を3例以上取れるのは、「男性・上皮型・Nivolumab投与無し」(SD 6例/PD 4例)のみであったため、SD 6症例中無増悪生存期間PFSが長い3例とPD 4例から腫瘍部位を切り出し、DNAマイクロアレイ解析を行った。

SD群 3例とPD群 4例との間で遺伝子発現の群比較を行い、PD群と比較してSD群で高発現している遺伝子群とSD群と比較してPD群で高発現している遺伝子群をヒートマップにまとめ検討した。

CD26抗体の有効性予測バイオマーカーとして特許出願の可能性があるため、具体的な遺伝子名は公開しないが、SD症例3例に共通して高発現しておりPD症例4例ではほとんど発現していない遺伝子Xを見出した。また、SD症例3例に共通してほとんど発現しておらずPD症例では発現が見られる遺伝子YとZの絞り込みを行った。今後、X, Y, Zに関して腫瘍病理組織の免疫染色を行い、PFSの期間が長くCD26抗体療法が特に有効な症例と有効ではないPD症例との判別に有用かどうか検討する。

D. 考察

ヒト化CD26抗体の副作用が少ない利点を活かした新たな併用療法を開発するために、ヒト免疫化マウスを用いたヒト悪性中皮腫株担がんモデルにて、ヒト化CD26抗体とPD1抗体との併用効果を検討した。

CD26はヒトT細胞に活性化シグナルを伝達するT細胞共刺激分子でもあり、ヒト化CD26抗体はCD26のリガンドであるcaveolin-1とCD26との結合、つまりはT細胞へのCD26共刺激シグナルの伝達をブロックする。一方で、マウスT細胞のCD26は共刺激分子として機能しない。また、CD26の発現に関しても、ヒトT細胞ではCD26は強陽性・弱陽性・陰性の三相性パターンを示すのに対し、マウスT細胞は一律に弱陽性である。T細胞以外の免疫細胞におけるCD26の発現に関しても、ヒトではT細胞以外はNKT細胞でCD26発現が見られるが、B細胞やNK細胞ではCD26はほとんど発現していないのに対し、マウスではB細胞でもT細胞と同等の弱陽性を示す。このように、T細胞における機能や免疫細胞における発現パターンなどがヒトとマウスとでは大きな違いがあるため、免疫系におけるCD26の機能解析ではヒト免疫系での解析が不可欠である。ICIが抗腫瘍効果を発揮するためには、T細胞を中心とした免疫系の存在が不可欠であることから、ヒト化CD26抗体とICIとの併用効果を検討する実験にはヒト免疫化マウスを用いる必要がある。

また、CD26抗体が抗腫瘍効果を発揮すること、抗体が結合することで細胞膜上のCD26と抗体が細胞質に移行することは、抗体がCD26分子上のどの部位に結合するか(エピトープ)が重要であり、ヒト化CD26抗

体の抗腫瘍効果のデータを取得するには抗マウス CD26 抗体ではなく、抗ヒト CD26 抗体を用いることが不可欠である。

以上の理由から、CD26 抗体と PD-1 抗体との併用効果のデータを取得するには、ヒト免疫系での実験が必要だが、ヒト免疫化マウスを用いた担がんモデルでは、問題点も存在する。一つは、免疫細胞がヒト臍帯血造血幹細胞由来の HLA を発現しているのに対し、ヒト腫瘍細胞株は通常そのHLAとは異なる HLA を発現しているため、同種異系(allogeneic)の T 細胞応答を見ることになり、本来のがん抗原特異的な応答とは異なることが考えられる。

我々の解析でヒト化 CD26 抗体を投与することで血清中のサイトカイン・ケモカインが増加するもの、減少するものがあることが明らかとなった。この現象が CD26 を発現するがん細胞に CD26 抗体が結合することによるのか、もしくは T 細胞や線維芽細胞などのがん以外の CD26 陽性細胞に抗体が結合することによるのか、メカニズムの詳細を明らかにする必要がある。悪性中皮腫患者の MIG/CXCL9 や IP-10/CXCL10 の血清中濃度は決して低くないのに対し、JMN や H226 のそれらのケモカインの発現量は非常に低く、ヒト免疫化マウスに皮下移入した後のマウス血清中のヒト MIG /CXCL9, IP-10/CXCL10 濃度も同様に低く、これらの細胞株をマウスに移入しただけでは、悪性中皮腫患者のような長期間の慢性炎症病態を模倣できていない可能性が高い。

マウス担がんモデルにおいて、DPP4 inhibitor (Sitagliptin)をエサと一緒にマウスに食べさせることで、CXCR3 陽性の CD4 T 細胞、CD8 T 細胞、NK 細胞や CCR3 陽性の好酸球ががん細胞周囲により集積し、腫瘍を攻撃しやすくなることが報告された(Nat Immunol. 2015, 2019)。フランス及び国内のヒト化 CD26 抗体の臨床試験の結果から、CD26 抗体を投与すると血清中の可溶性 CD26 量が低下し、それに伴い DPP4 酵素活性も低下する(Br J Cancer. 2017, 論文投稿中)。このことから、CD26 抗体を投与した場合においても、がん細胞周囲に集積する免疫細胞数の増加が起こる可能性が考えられる。しかしながら、ヒト化 CD26 抗体はマウス CD26 には結合しないため、今回のヒト免疫化マウスを用いた担がんモデルにおいて、CD26 抗体はヒト T 細胞上の CD26 とヒト腫瘍細胞株上の CD26 には結合するが、マウスの血管内皮細胞や線維芽細胞などにも発現する CD26 には反応できず、それらのマウス CD26 にもヒト CD26 と同様に DPP4 酵素活性があるため、本来のがん患者に CD26 抗体を投与した時のような DPP4 酵素活性低下作用は期待できないと予想される。この点に関しても今後さらなる実験モデルの改善が必要と考えられる。

ヒト化 CD26 抗体の予後・治療効果予測バイオマーカーを探索するために、CD26 抗体の国内第 I/II 相臨床試験患者の腫瘍病理組織を用いて、SD 症例 3 例と PD 症例 4 例の DNA マイクロアレイ解析を行った。

CD26 抗体の有効性予測バイオマーカーとして特許出願の可能性があるため、具体的な遺伝子名は公開しないが、SD 群で発現が高かった遺伝子は抗線維化、炎症亢進、増殖・代謝亢進に関わるものが多く見られた。一方で、PD 群で発現が高かった遺伝子は筋細胞、中でも横紋筋に関係する遺伝子群が多数見られ、横紋筋分化が亢進している可能性

が考えられた。

また、それらの遺伝子を高発現する症例で何故 CD26 抗体が有効なのか無効なのかを解明することで、より CD26 抗体による治療効果が得られる併用療法の開発にも繋がることが期待される。

E. 結論

ヒト T 細胞と B 細胞が生着した免疫化マウスの作製に成功し、ヒト悪性中皮腫細胞株 JMN と H226 を皮下移入する担がんモデルにおいて、ヒト化 CD26 抗体と PD-1 抗体との併用効果を検討し、それぞれの単剤よりも強い腫瘍増殖抑制効果が見られることが示された。また、CD26 抗体の新たな作用として、Th1 細胞遊走ケモカインの産生を顕著に増加させることを見出した。

ヒト化 CD26 抗体の国内第 I/II 相臨床試験患者の悪性中皮腫組織から腫瘍部位をマイクロダイセクションで切り出し、得られた微量の Total RNA を用いて SD 症例 3 例と PD 症例 4 例の DNA マイクロアレイ解析を行った。その結果、SD 症例で共通して発現が高い遺伝子 X と共通して発現が低い遺伝子 Y, Z を見出した。

F. 健康危険情報

現時点では特記すべき健康危険情報はない。

G. 今後の展望

CD26 抗体と PD1 抗体との抗腫瘍作用メカニズムの違いについてより詳細に解析し、併用効果の有効性を実証する。また、悪性中皮腫細胞株を皮下移入するモデルの他に、より患者のがん細胞の特性を維持していると考えられる悪性中皮腫の患者腫瘍移植 (PDX; Patient-derived xenograft)モデルにおいても併用効果の有効性を検討する。

国内第 I/II 相臨床試験患者の腫瘍病理組織を用いて、今回の DNA マイクロアレイ解析により得られた候補分子の免疫染色を行い、これらの分子がヒト化 CD26 抗体の有効性を予測できるバイオマーカーになり得るかを明らかにする。

H. 研究発表

1. 論文発表

1) Ohmachi-Ono A, Yamada S, Uno S, Tamai M, Soga K, Nakamura S, Udagawa N, Nakamichi Y, Koide M, Morita Y, Takano T, Itoh T, Kakuta S, Morimoto C, Matsuoka S, Iwakura Y, Tomura M, Kiyono H, Hachimura S, Nakajima-Adachi H. Effector memory CD4 + T cells in mesenteric lymph nodes mediate bone loss in food-allergic enteropathy model mice, creating IL-4 dominance. Mucosal Immunol. 2021;14(6):1335-1346

2) Itoh T, Hatano R, Horimoto Y, Yamada T, Song D, Otsuka H, Shirakawa Y, Matsuoka S, Iwao N, Aune TM, Dang NH, Kaneko Y, Okumura K, Morimoto C, Ohnuma K. IL-26 mediates epidermal growth factor receptor-tyrosine kinase inhibitor resistance through endoplasmic reticulum stress signaling pathway in triple-negative breast cancer cells. Cell Death Dis. 2021;12(6):520

3) Kaneko Y, Hatano R, Hirota N, Isambert N, Trillet-Lenoir V, You B, Alexandre J, Zalcman G, Valleix F, Podoll T, Umezawa Y, Takao S, Iwata S, Hosono O, Taguchi T, Yamada T, Dang NH, Ohnuma K, Angevin E, Morimoto C. Serum soluble

CD26/DPP4 titer variation is a potential prognostic biomarker in cancer therapy with a humanized anti-CD26 antibody. Biomark Res. 2021;9(1):21

4) Komiya E, Tominaga M, Hatano R, kamikubo Y, Toyama S, Sakairi H, Honda K, Itoh T, Kamata Y, Tsurumachi M, Kishi R, Ohnuma K, Sakurai T, Morimoto C, Takamori K. Peripheral endomorphins drive mechanical alloknesis under the enzymatic control of CD26/DPPIV. J Allergy Clin Immunol. 2021Aug 16: S0091-6749(21)01211-2. Online ahead of print.
5) Pan K, Ohnuma K, Morimoto C, Dang NH. CD26/Dipeptidyl Peptidase IV and Its Multiple Biological Functions. Cureus. 2021; 13(2): e13495
6) Sasaki H, Saisho Y, Inaishi J, Watanabe Y, Tsuchiya T, Makio M, Sato M, Nishikawa M, Kitago M, Yamada T, Itoh H. Reduced beta cell number rather than size is a major contributor to beta cell loss in type 2 diabetes. Diabetologia.2021;64(8):1816-1821
7) Kishimoto T, Kojima Y, Fujimoto N. Significance of secretory leukocyte peptidase inhibitor in pleural fluid for the diagnosis of benign asbestos pleural effusion. Sci Rep. 2021;11(1):12965
8) Hayashi H, Ashizawa K, M, Kato K, Arakawa H, Kishimoto T, Otsuka Y, Noma S, Honda S. The diagnosis of early pneumoconiosis in dust-exposed workers: comparison of chest radiography and computed tomography. Acta Radiol. 2021; 7: 2841851211022501
9) Mizuhashi K, Okamoto K, Kishimoto T. A patient with epithelioid pleural mesothelioma (Myxoid variant) who survived for a long period without treatment.Respir Med Case Rep. 2021;33:101381

2. 著書

なし

3. 学会発表

1) Komiya E, Tominaga M, Hatano R, Itoh T, Honda K, Toyama S, Kamata Y, Otsuka H, Ohnuma K, Morimoto C, Takamori K. CD26/DPPIV regulates mechanical alloknesis at the periphery, 11th World Congress on Itch (WCI), Online congress, October 2021
2) 相羽 弘貴, 山田 健人. サルコイドーシスにおける CD26 陽性 T 細胞サブセットの解析. 第 110 回日本病理学会総会 2021 年 4 月 22 日
3) 古宮栄利子, 小島豪, 冨永光俊, 森本幾夫, 髙森建二. 加齢皮膚におけるアロネーシスの発症機構の解明, 第 17 回加齢皮膚医学研究会(オンライン) , 2021 年 8 月
4) 古宮栄利子, 冨永光俊, 波多野良, 外山扇雅, 伊藤匠, 鎌田弥生, 本田耕太郎, 大沼圭, 森本幾夫, 髙森建二. CD26/ dipeptidyl-peptidase IV は機械的かゆみの調節因子である, 第 26 回日本病態プロテアーゼ学会(オンライン), 2021 年 8 月
5) Hatano R, Otsuka H, Itoh T, Saeki H, Yamamoto A, Shirakawa Y, Iyama S, Iwao N, Sato T, Yamada T, Morimoto C, Ohnuma K. Anti-interleukin-26 therapy for the control of chronic inflammation in

GVHD. 第83回日本血液学会 2021年9月25日

6) 塚本翔, 倉谷麻衣, 鈴木 治, 片桐岳信, 山田健人, 濱井瞭, 土屋香織.マウス骨格筋における異所性石灰化モデルの確立と解析 Establishment and analysis of ectopic calcification in mouse skeletal muscle. 第39回日本骨代謝学会 2021年10月

7) Sho Tsukamoto, Mai Kuratani, Ryo Hamai, Kaori Tsuchiya, Osamu Suzuki, Taketo Yamada, Takenobu Katagiri. Establishment of an in vivo model of ectopic calcification in mouse skeletal muscle. ASBMR 2021 Annual Meeting 2021年10月1日

8) Komiya E, Tominaga M, Hatano R, Itoh T, Honda K, Toyama S, Kamata Y, Otsuka H, Ohnuma K, Morimoto C, Takamori K. Mu-opioid ligand endomorphin induces alloknesis at the periphery, 日本研究皮膚科学会, 第46回年次学術大会・総会 (オンライン), 2021年12月

3. その他
なし

I. 知的財産権の出願・登録状況（予定を含む）

1. 特許取得

1) 発明者: 森本幾夫、波多野良、大沼圭、金子有太郎. 発明の名称: 抗CD26抗体と免疫チェックポイント阻害剤との併用療法. 出願日: 2021年5月31日, 出願番号: 特願 2021-091761, 出願人: ワイズ・エー・シー株式会社、学校法人順天堂

2. 実用新案登録
なし

Ⅱ. 分担研究報告

労災疾病臨床研究事業費補助金
分担研究報告書

ヒト免疫化マウスを用いたヒト化 CD26 抗体と抗 PD-1 抗体との併用効果の検討

研究代表者　森本　幾夫　順天堂大学大学院医学研究科
免疫病・がん先端治療学講座 特任教授
研究分担者　波多野　良　順天堂大学大学院医学研究科
免疫病・がん先端治療学講座 特任助教
研究分担者　岸本　卓巳　独立行政法人労働者健康安全機構
アスベスト疾患研究・研修センター 所長
研究分担者　山田　健人　埼玉医科大学医学部 病理学 教授
研究協力者　大沼　圭　順天堂大学大学院医学研究科
免疫病・がん先端治療学講座 准教授
研究協力者　金子有太郎　ワイズ・エー・シー株式会社 代表取締役 CEO
近畿大学 客員教授(元)

研究要旨

悪性胸膜中皮腫はアスベストばく露によって起こる難治性悪性腫瘍だが、満足できる治療法はなく、新たな治療法の確立が望まれる。われわれは、新規治療標的分子として悪性胸膜中皮腫に発現する CD26 に着目し、ヒト化 CD26 抗体 YS110 を開発した。フランスにて悪性中皮腫を中心とした第 I 相臨床試験を実施し、国内でも悪性中皮腫に対する第 I/II 相臨床試験を実施した。2019 年中に第 II 相臨床試験の最終患者への投与が終了し、結果の集計が完了したところだが、安全性が確認され、フランスでの第 I 相臨床試験と同等の有効性を示唆する結果が得られている。治療抵抗性の悪性中皮腫患者に対して、CD26 抗体単剤でも高い割合で Stable Disease・Partial Response となり抗腫瘍効果は認められたが、より長期間抗腫瘍効果を発揮し、無増悪生存期間を与えられる本抗体を用いた新たな併用療法の開発も重要な課題である。そこで、ヒト免疫化マウスを用いたヒト悪性中皮腫細胞株担がんモデルを確立し、YS110 と PD-1 抗体との併用効果を検討した結果、それぞれの単剤よりも強い相乗効果が認められるデータを得た。また、YS110 投与によって血清中の Th1 遊走ケモカイン濃度が顕著に増加する一方で、Th2 遊走ケモカイン濃度は減少することを見出し、腫瘍に浸潤する免疫細胞を変化させている可能性が考えられる。

A. 研究目的

悪性胸膜中皮腫はアスベストばく露によって起こる胸膜中皮由来の難治性悪性腫瘍である。アスベストばく露から発症までの潜伏期間は約 30-50 年とされ、日本を含め中国やインドなどアジア・中東では患者数が今

後ますます増加すると考えられている。予後は極めて悪く、現時点で満足できる治療成績ではなく、新たな治療法の確立が望まれる。われわれは、新規治療標的分子として悪性中皮腫細胞に発現する CD26 に着目し、ヒト化 CD26 抗体を開発してフランスにて悪性中皮腫を中心に First-in-Human 第 I 相臨床試験を行った。Infusion reaction (急性輸注反応)を除いて特記すべき副作用もなく、安全性が確認されるとともに、抗がん剤抵抗性の悪性中皮腫患者 19 例中 10 例が modified RESIST 評価で Stable Disease (SD)となり、そのうち 5 例は 6 ヶ月以上、最長で 399 日 SD が持続し、有効性を示唆する結果も得られた(Br J Cancer. 2017)。

本邦でも抗がん剤抵抗性の悪性中皮腫に対する第 I/II 相臨床試験を実施し、第 I 相は 1～3 コホート各 3 例ずつの計 9 例、第 II 相は 31 例に投与を行い、2019 年中に第 II 相の最終患者への投与が終了した。第 I/II 相で計 40 例に投与を行い、うち抗腫瘍効果を評価可能だったのが 35 例で、内訳は Partial Response (PR) 2 例・SD 21 例・Progressive Disease (PD) 12 例で、PR・SD 率は 65.7% (23/35)で抗がん剤抵抗性の悪性中皮腫患者に対して高い割合で抗腫瘍効果が認められるも、完全奏功(Complete Response: CR))はなく、より長期間抗腫瘍効果を発揮し、無増悪生存期間を与えられる本抗体を用いた新たな併用療法の開発も重要な課題である。

我々はこれまでにヒト化 CD26 抗体の抗腫瘍作用メカニズムとして、抗体医薬特有の抗体依存性細胞傷害(ADCC)活性に加え、がん細胞の細胞膜上の CD26 に抗体が結合することによる直接的な増殖抑制作用を明らかにしてきた(Clin Cancer Res. 2001, Immunology. 2002, Clin Cancer Res. 2007, PLoS One. 2013)。また、CD26 抗体は、CD26 分子が有する DPP4 酵素活性には直接影響しないが、細胞膜上の CD26 分子の数や体液中に膜から切断された形で存在する soluble CD26 の数を減少させるため、CD26 抗体を投与すると DPP4 酵素活性も結果的に低下する。近年の知見から、DPP4 酵素活性を阻害すると DPP4 によるケモカインの切断と活性低下が妨げられ、腫瘍周囲に浸潤する免疫細胞が増加する、すなわち腫瘍免疫亢進に働くことが強く示唆され(Nat Immunol. 2015, Nat Immunol. 2019)、ヒト化 CD26 抗体は多様なメカニズムを介して抗腫瘍効果を発揮していると考えられる。特記すべきは、国内第 I/II 相臨床試験 40 例の中には PD-1 抗体 Nivolumab 無効例が 13 例含まれており、そのうち 11 例が抗腫瘍効果を評価可能で、PR 1 例・SD 7 例・PD 3 例で 72.7% (8/11)が PR・SD であり、このことから CD26 抗体は免疫チェックポイント阻害薬(ICI)抵抗性の患者にも有効であること、ICI とは異なるメカニズムで抗腫瘍効果を発揮することが強く示唆された。

そこで、副作用が非常に少ない CD26 抗体の利点を活かした他の分子標的薬、特に ICI との併用療法を開発すべく、ヒト化 CD26 抗体と PD-1 抗体との併用効果を検討した。ICI が抗腫瘍効果を発揮するためには T 細胞を中心とした免疫細胞が不可欠であり、マウスに同系のマウス腫瘍株を移入する担癌モデルがよく用いられる。一方で、CD26 抗体が抗腫瘍効果を発揮するためにはヒト CD26 分子上の結合部位も重要であり(Clin Cancer Res. 2007)、ヒトとマウスとでは免疫系における CD26 の機能も大きく

異なることから(Immunol Rev. 1998)、ヒト化 CD26 抗体のデータ取得にはヒト腫瘍株並びにヒト免疫系での解析が必須である。以上の理由から、ヒト免疫化マウスを作製し、このマウスを用いた悪性中皮腫株担がんモデルにおいてヒト化CD26抗体とPD-1抗体との併用効果を検討した。

B. 研究方法

1) 細胞

ヒト悪性中皮腫細胞株 JMN(肉腫型)とH226(上皮型)は、10% FBS を添加したRPMI1640培地中で37°C, 5% CO_2環境下で培養した。ヒト臍帯血 CD34 陽性造血幹細胞は RIKEN BioResource Center から購入した。

2) マウス

NOD/Shi-scid, IL-2RγKO Jic (NOD.Cg-Prkdc^{scid} Il2rg^{tm1Sug}/ShiJic)マウス(以下、NOG マウス)は In-Vivo Science Inc.から購入した。マウスは順天堂大学の specific pathogen free (SPF)施設で飼育した。

3) 抗体と試薬

Flow cytometry には下記のヒト抗原特異抗体を用いた。BUV395-labeled anti-CD3 mAb (clone SK7), PE-labeled anti-CD26 mAb (clone M-A261) 及び APC-R700 -labeled anti-CD4 (clone RPA-T4)は BD Biosciences から購入した。Brilliant Violet 421-labeled anti-CD45 mAb (clone HI30), Brilliant Violet 510-labeled anti-CD14 mAb (clone M5E2), Brilliant Violet 605-labeled anti-CD11c mAb (clone 3.9), FITC-labeled anti-CD11b mAb (clone ICRF44), PerCP/Cy5.5-labeled anti-CD8 mAb (clone RPA-T8), PE/Cy7-labeled anti-CD56 mAb (clone 5.1H11), APC -labeled anti-CD19 mAb (clone 4G7)及び APC/Fire 750-labeled anti-mouse CD45 mAb (clone 30-F11)及び抗体の非特異的な結合をブロックするための Human TruStain FcX, TruStain FcX (anti-mouse CD16/32)はBioLegendから購入した。また、Brilliant Violet 同士の非特異的な結合を抑えるための Brilliant Stain Buffer plus は BD Biosciences から購入した。

4) ヒト免疫化マウスを用いた担癌モデル

NOG マウスに低線量(100cGy)で放射線照射し、翌日ヒト臍帯血 CD34 陽性造血幹細胞 1x10^5 cells を尾静脈内から移入した。ヒト造血幹細胞を移入して 5 週, 9 週, 13 週, 17 週後にマウス尾静脈から経時的に採血を行い、ヒト免疫細胞の生着を確認した。ヒト造血幹細胞を移植して 13 週後のヒトT細胞が生着したマウスに、JMN または H226 の細胞懸濁液と Matrigel を 1:1 混合して 1 匹あたり 1x10^6 cells ずつ側腹部に皮下移入した。JMN または H226 を皮下移入して 5 週間経過し、小さな腫瘤形成を確認した時点から、control human IgG1 (Bio X Cell), ヒト化 CD26 抗体(Y's AC Co., Ltd)単独, mouse anti-human PD-1 mAb (Bio X Cell; clone J116)単独, ヒト化 CD26 抗体と PD-1 抗体の併用をそれぞれ 200 μg/dose で週 3 回投与を続けた。腫瘍サイズは週に 2 回採寸し、JMN または H226 移入 9 週間後にマウスを解剖し、皮下の腫瘤を回収して重量を測定した。腫瘍の一部は病理解析のために 10%ホルマリンで固定し、残りは Liberase TL

Research Grade (Roche) 0.25mg/ml で酵素処理を行い、DNase I (Roche)存在下で組織を破砕して腫瘍組織中の細胞を得た。腫瘍内浸潤リンパ球の解析では、MagniSort Human CD3 Positive Selection Kit (invitrogen) 及び EasySep Magnet (STEMCELL)を用いてリンパ球精製を行った。また、腫瘍内浸潤リンパ球との性質比較のために、脾臓のリンパ球解析も行った。

5) フローサイトメトリー

マウス体内のヒト免疫細胞の生着を確認するために、マウスの尾静脈から採血して得た末梢血を、Human と Mouse に対する TruStain FcX を両方添加し、蛍光色素標識抗体で染色した後、BD FACS Lysing Solution (BD Biosciences)にて溶血と固定処理を行い、洗浄した後、BD LSRFortessa (BD Biosciences)で測定を行い、得られたデータを FlowJo (BD Biosciences)で解析した。

6) 国内第 I/II 相臨床試験プロトコル

第 I 相臨床試験はヒト化 CD26 抗体を 2mg/kg, 4mg/kg, 6mg/kg でそれぞれ 3 例ずつ、初回投与日を day1 として day1, day8, day15, day22, day29 まで週 1 回の間隔で 5 回静脈内投与を行い、投与を開始してから 6 週間後(day42)の時点で医師による抗腫瘍効果の判定が行われ、PR または SD と判定された患者は、上記の抗体 5 回投与、6 週間後に抗腫瘍効果判定を 1 サイクルとして PD になるまでサイクルを継続した。

第 II 相臨床試験は全 31 例に CD26 抗体を 6mg/kg で週 1 回の間隔で 5 回静脈内投与を行い、上記と同様に抗体 5 回投与、6 週間後に抗腫瘍効果判定を 1 サイクルとして PD になるまでサイクルを継続した。

7) Bio-Plex マルチプレックスアッセイ

成人健常者および国内第 I/II 相臨床試験患者の CD26 抗体初回投与前(day1pre)・3 回目投与前(day15pre)・5 回目投与前(day29 pre)の血清の提供を受け、血清中サイトカイン・ケモカイン濃度を Bio-Plex マルチプレックスシステムにより測定した。Bio-Plex Pro Human Chemokine 40-Plex panel (Bio-Rad)を用いて、付属のプロトコルに従い Bio-Plex system (Bio-Rad)で測定を行い、得られたデータを Bio-Plex Manager (Bio-Rad)で解析した。

(倫理面への配慮)

ヒト臍帯血 CD34 陽性造血幹細胞および成人健常者の末梢血を用いた研究については、森本が講座責任者である順天堂大学大学院医学研究科で本研究を行うための研究計画書等を倫理審査委員会へ提出し、承認を得ている(順大医倫第 2020280 号, 2020291 号)。また、ヒト化 CD26 抗体の国内第 I/II 相臨床試験の患者検体を用いたバイオマーカー探索研究については、臨床試験審査委員会、各治験実施施設内の治験審査委員会にて、試験の実施と合わせてバイオマーカー探索用採血・腫瘍組織検体の提供について協議され、実施承認を取得済みである。末梢血の提供を受ける際には、研究対象者に対する人的擁護上の配慮及び研究により研究対象者が受ける不利益、利益等の説明を行い、書面でのインフォームド・コンセントを得ている。動物実験の実施はいわゆる 3R に基づいて行い、順天堂大学医学部実験動物委員会に実験計画書を提出し審議の上、承認されている(承

認番号: 2021056)。

C. 研究結果

1) ヒト免疫化マウスの作製

ヒト化 CD26 抗体はマウス CD26 には結合しないため、ヒトの悪性中皮腫を用いる必要があり、PD-1 抗体との併用効果を検討するためには、ヒト免疫細胞が生着したヒト免疫化マウスを作製する必要がある。そのためには、重度の免疫不全マウスである NOG マウスに低線量の放射線を照射し、ヒトの造血幹細胞を移植する必要があるが、臨床現場で造血幹細胞移植を行う際にも解凍から移植までの時間は非常に重要と考えられている。ヒト臍帯血造血幹細胞分画の解凍と洗浄条件を検討し、高い確率でヒト T 細胞が発生する方法を確立した。ヒト造血幹細胞を移植して 10 週間経過するまではマウスの血中のヒト免疫細胞の約 90%が B 細胞(CD19 陽性)で、10 週以降はヒト CD4 T 細胞(CD3 陽性 CD4 陽性)・CD8 T 細胞(CD3 陽性 CD8 陽性)の割合が徐々に増えていき 13 週目ではヒトの血球細胞の約 10-15%が T 細胞、17 週目では約 25-35%が T 細胞であることが確認された(図 1)。このモデルではヒト NK 細胞(CD56 陽性)は 1-2%程度、ヒト単球細胞(CD14 陽性)は約 1-2%程度、ヒト樹状細胞(CD11c 陽性)は 1%未満であった(図 1)。

悪性中皮腫細胞株 JMN(肉腫型)および H226(上皮型)は、in vivo での増殖が非常に遅く、マウスの皮下に移入してから腫瘤を形成するまでに 5-6 週間かかるため、マウス体内でヒト T 細胞の細胞数が増えてくる造血幹細胞移植 13 週目に悪性中皮腫細胞株を皮下移入することとした。

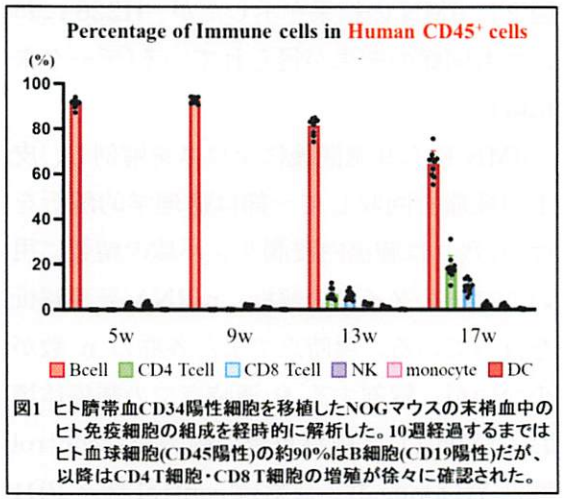

図1 ヒト臍帯血CD34陽性細胞を移植したNOGマウスの末梢血中のヒト免疫細胞の組成を経時的に解析した。10週経過するまではヒト血球細胞(CD45陽性)の約90%はB細胞(CD19陽性)だが、以降はCD4 T細胞・CD8 T細胞の増殖が徐々に確認された。

2) ヒト化 CD26 抗体と PD-1 抗体との併用効果の検討

JMN および H226 をヒト免疫化マウスの側腹部に皮下移入して 5 週間経過し、小さな腫瘤形成を確認した時点から、control human IgG_1, ヒト化 CD26 抗体単独, mouse anti-human PD-1 mAb (以下、PD-1 抗体)単独, ヒト化 CD26 抗体と PD-1 抗体の併用をそれぞれ 200μg/dose で週 3 回投与を続けた。腫瘍サイズを週に 2 回採寸した結果、control 抗体投与群と比較して、CD26 抗体単独(YS alone)、PD-1 抗体単独(PD1 alone)それぞれで腫瘍増殖の抑制が見られたが、両抗体投与群(YS+PD1)ではさらに腫瘍サイズが小さいことが示された(図 2)。

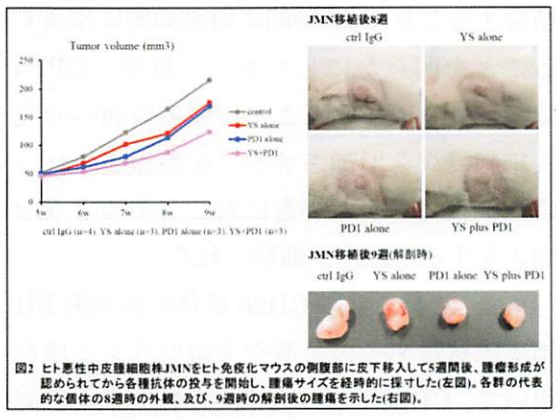

図2 ヒト悪性中皮腫細胞株JMNをヒト免疫化マウスの側腹部に皮下移入して5週間後、腫瘤形成が認められてから各種抗体の投与を開始し、腫瘍サイズを経時的に採寸した(左図)。各群の代表的な個体の8週時の外観、及び、9週時の解剖後の腫瘍を示した(右図)。

図 2 に JMN の結果を示したが、H226 においても同様の結果が得られている(データ未掲載)。

JMN 移入 9 週間後にマウスを解剖し、皮下の腫瘤を回収して一部は病理学的解析を行い、残りは腫瘍内浸潤リンパ球の精製に用いてフェノタイプの解析、mRNA 発現解析を行っている。現時点でまだ各群の n 数が少ないが、解剖する 9 週時点での腫瘍体積および回収した腫瘍重量の両方で、control 群と YS alone 群、または control 群と PD1 alone 群で有意差は認められない一方、control 群と YS+PD1 群で $p<0.05$ の有意差が認められ(Fisher の多重比較検定)、両抗体の併用効果が期待される。

今後、各群の n 数をさらに増やすとともに、腫瘍内浸潤リンパ球のフェノタイプ解析、腫瘍の病理学的解析を行い、CD26 抗体と PD1 抗体との抗腫瘍作用メカニズムの違いについてより詳細に解析し、併用効果の有効性を実証する。

3) ヒト化 CD26 抗体の新たな抗腫瘍作用メカニズムの可能性

CD26 抗体には多様な抗腫瘍作用メカニズムが考えられ、これまでに CD26 を発現するがん細胞の細胞膜上の CD26 に抗体が結合することで、直接的に増殖抑制に作用することを明らかにしてきた。近年、DPP4 酵素活性を阻害することが腫瘍周囲への免疫細胞浸潤を増加させることが報告され、CD26 抗体もがん患者に対してそのような働きをする可能性が期待される。

また、これまでに CD26 抗体の国内第 I/II 相臨床試験患者の血清や末梢血リンパ球を用いて、CD26 抗体の予後・治療効果を予測し得るバイオマーカーの探索を試みてきたが、血清中のサイトカイン・ケモカインの中で CD26 抗体投与によって絶対量が増加するもの、減少するものがあることが示された。中でも、代表的な Th1 細胞遊走ケモカインである MIG/CXCL9 と IP-10/CXCL10 は CD26 抗体投与によって血清中濃度が顕著に増加したのに対し、代表的な Th2 細胞遊走ケモカインである TARC/CCL17 と MDC /CCL22 の血中濃度は減少することを見出し、上皮型・二相型・肉腫型の組織型に分けて解析した場合でも、いずれの組織型でもほとんどの患者で共通して変化していることが示された(図 3)。

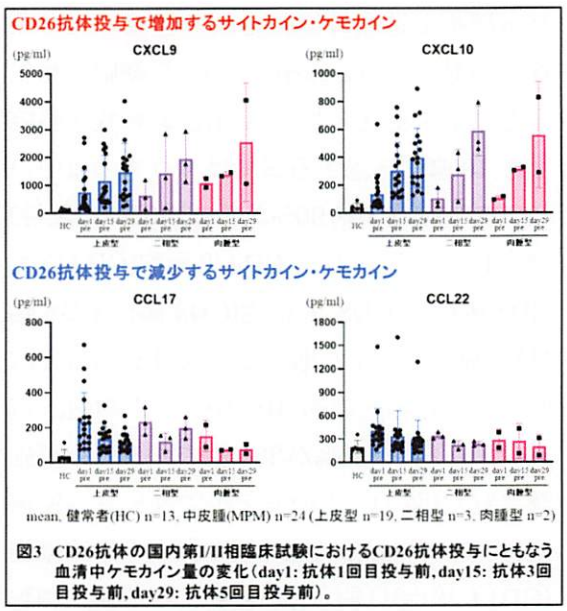

図3 CD26抗体の国内第I/II相臨床試験におけるCD26抗体投与にともなう血清中ケモカイン量の変化(day1: 抗体1回目投与前, day15: 抗体3回目投与前, day29: 抗体5回目投与前)。

これらの結果から、CD26 抗体は DPP4 酵素活性を低下させることで、酵素によるケモカインの切断とそれにともなう活性低下を妨げるだけでなく、ケモカイン産生量自体にも影響を与えることで、腫瘍周囲に浸潤する免疫細胞を変化させることが予想される。

D. 考察

ヒト化 CD26 抗体の副作用が少ない利点

を活かした新たな併用療法を開発するために、ヒト免疫化マウスを用いたヒト悪性中皮腫株担癌モデルにて、ヒト化 CD26 抗体と PD1 抗体との併用効果を検討した。

マウスを用いた担がんモデルでは、マウスと MHC のハプロタイプを揃えた腫瘍細胞株を用いることで、がんと免疫系が同種同系となり、がん患者と同様にがん抗原に特異的な免疫応答を解析することができる。また、腫瘍細胞株を用いずにマウスにアスベストをばく露させることで腫瘍を作らせるモデルなども用いられている。そのモデルでは悪性中皮腫患者のように長期間の慢性炎症を経てがん化が起こるため、細胞株を移入するモデルよりもより悪性中皮腫の病態を模倣していると考えられる。より疾患の病態を模倣したモデルの方が望ましいことは言うまでもないが、CD26 分子の研究ではマウスの免疫系を用いることができない理由が複数存在する。

CD26 はヒト T 細胞に活性化シグナルを伝達する T 細胞共刺激分子でもあり、ヒト化 CD26 抗体は CD26 のリガンドである caveolin-1 と CD26 との結合、つまりは T 細胞への CD26 共刺激シグナルの伝達をブロックする。一方で、マウス T 細胞の CD26 は共刺激分子として機能しない。また、CD26 の発現に関しても、ヒト T 細胞では CD26 は強陽性・弱陽性・陰性の三相性パターンを示すのに対し、マウス T 細胞は一律に弱陽性である。T 細胞以外の免疫細胞における CD26 の発現に関しても、ヒトでは T 細胞以外は NKT 細胞で CD26 発現が見られるが、B 細胞や NK 細胞では CD26 はほとんど発現していないのに対し、マウスでは B 細胞でも T 細胞と同等の弱陽性を示す。このように、T 細胞における機能や免疫細胞における発現パターンなどがヒトとマウスとでは大きな違いがあるため、免疫系における CD26 の機能解析ではヒト免疫系での解析が不可欠である。ICI が抗腫瘍効果を発揮するためには、T 細胞を中心とした免疫系の存在が不可欠であることから、ヒト化 CD26 抗体と ICI との併用効果を検討する実験にはヒト免疫化マウスを用いる必要がある。

また、CD26 抗体が抗腫瘍効果を発揮すること、抗体が結合することで細胞膜上の CD26 と抗体が細胞質に移行することは、抗体が CD26 分子上のどの部位に結合するか(エピトープ)が重要であり、ヒト化 CD26 抗体の抗腫瘍効果のデータを取得するには抗マウス CD26 抗体ではなく、抗ヒト CD26 抗体を用いることが不可欠である。ヒト化 CD26 抗体はマウス CD26 には交差性を示さず全く結合しないことからも、ヒトの悪性中皮腫を用いた実験系が不可欠になる。

以上の理由から、CD26 抗体と PD-1 抗体との併用効果のデータを取得するには、ヒト免疫系での実験が必要だが、ヒト免疫化マウスを用いた担がんモデルでは、問題点も存在する。一つは、免疫細胞がヒト臍帯血造血幹細胞由来の HLA を発現しているのに対し、ヒト腫瘍細胞株は通常その HLA とは異なる HLA を発現しているため、同種異系(allogeneic)の T 細胞応答を見ることになり、本来のがん抗原特異的な応答とは異なることが考えられる。また、ヒト免疫細胞の組成に関しても、今回のモデルではヒト T 細胞と B 細胞に関してはマウス体内で十分な生着が認められるが、一方でヒト NK 細胞や抗原提示細胞の生着率は非常に低い。この問題を解決するために、ヒト IL-2, IL-15, IL-3,

GM-CSF などの遺伝子を強制発現させたNOGマウスが樹立・市販されている。マウス 1 匹の価格がさらに高額になるが、ヒトNK 細胞や骨髄系細胞の役割を解析するには、それらのマウスでの検討も必要になると考えられる。

図 3 に示したようにヒト化 CD26 抗体を投与することで血清中のサイトカイン・ケモカインが増加するもの、減少するものがあることが明らかとなった。この現象が CD26 を発現するがん細胞に CD26 抗体が結合することによるのか、もしくは T 細胞や線維芽細胞などのがん以外の CD26 陽性細胞に抗体が結合することによるのか、メカニズムの詳細を明らかにする必要がある。悪性中皮腫患者の MIG/CXCL9 や IP-10/CXCL10 の血清中濃度は決して低くないのに対し(図 3)、JMN や H226 のそれらのケモカインの発現量は非常に低く、ヒト免疫化マウスに皮下移入した後のマウス血清中のヒト MIG/CXCL9, IP-10/CXCL10 濃度も同様に低く(データ未掲載)、これらの細胞株をマウスに移入しただけでは、悪性中皮腫患者のような長期間の慢性炎症病態を模倣できていない可能性が高い。CD26 抗体ががん細胞のケモカイン産生に影響を与えるかどうかに関しても、がん細胞自身を炎症性サイトカインで刺激するなど悪性中皮腫患者の病態を模倣する工夫が必要になると考えている。

近年、マウス担癌モデルにおいて、DPP4 inhibitor (Sitagliptin)をエサと一緒にマウスに食べさせることで、CXCR3 陽性の CD4 T 細胞、CD8 T 細胞、NK 細胞や CCR3 陽性の好酸球ががん細胞周囲により集積し、腫瘍を攻撃しやすくなることが報告された(Nat Immunol. 2015, 2019)。フランス及び国内のヒト化 CD26 抗体の臨床試験の結果から、CD26 抗体を投与すると血清中の可溶性 CD26 量が低下し、それに伴い DPP4 酵素活性も低下する(Br J Cancer. 2017, 論文投稿中)。このことから、CD26 抗体を投与した場合においても、がん細胞周囲に集積する免疫細胞数の増加が起こる可能性が考えられる。しかしながら、ヒト化 CD26 抗体はマウス CD26 には結合しない。そのため、今回のヒト免疫化マウスを用いた担癌モデルにおいて、CD26 抗体はヒト T 細胞上の CD26 とヒト腫瘍細胞株上の CD26 には結合するが、マウスの血管内皮細胞や線維芽細胞などにも発現する CD26 には反応できず、それらのマウス CD26 にもヒト CD26 と同様に DPP4 酵素活性があるため、本来のがん患者に CD26 抗体を投与した時のようなDPP4 酵素活性低下作用は期待できないと予想される。この点に関しても今後さらなる実験モデルの改善が必要と考えられる。

E. 結論

ヒト T 細胞と B 細胞が十分に生着した免疫化マウスの作製に成功し、ヒト悪性中皮腫細胞株 JMN と H226 を皮下移入する担がんモデルにおいて、ヒト化 CD26 抗体と PD-1 抗体との併用効果を検討した結果、それぞれの単剤よりも強い腫瘍増殖抑制効果が見られることが示された。また、CD26 抗体の新たな作用として、Th1 細胞遊走ケモカインの産生を顕著に増加させることを見出した。

F. 今後の展望

今後、各群の n 数をさらに増やすとともに、腫瘍内浸潤リンパ球のフェノタイプ解析、mRNA 発現解析、腫瘍の病理学的解析を行

い、CD26 抗体と PD1 抗体との抗腫瘍作用メカニズムの違いについてより詳細に解析し、併用効果の有効性を実証する。また、悪性中皮腫細胞株を皮下移入するモデルの他に、より患者のがん細胞の特性を維持していると考えられる悪性中皮腫の患者腫瘍移植(PDX; Patient-derived xenograft)モデルにおいても併用効果の有効性を検討する。

G. 研究発表

1. 論文発表

1) Ohmachi-Ono A, Yamada S, Uno S, Tamai M, Soga K, Nakamura S, Udagawa N, Nakamichi Y, Koide M, Morita Y, Takano T, Itoh T, Kakuta S, Morimoto C, Matsuoka S, Iwakura Y, Tomura M, Kiyono H, Hachimura S, Nakajima-Adachi H. Effector memory CD4+ T cells in mesenteric lymph nodes mediate bone loss in food-allergic enteropathy model mice, creating IL-4 dominance. Mucosal Immunol. 2021;14(6):1335-1346

2) Itoh T, Hatano R, Horimoto Y, Yamada T, Song D, Otsuka H, Shirakawa Y, Matsuoka S, Iwao N, Aune TM, Dang NH, Kaneko Y, Okumura K, Morimoto C, Ohnuma K. IL-26 mediates epidermal growth factor receptor-tyrosine kinase inhibitor resistance through endoplasmic reticulum stress signaling pathway in triple-negative breast cancer cells. Cell Death Dis. 2021;12(6): 520

3) Kaneko Y, Hatano R, Hirota N, Isambert N, Trillet-Lenoir V, You B, Alexandre J, Zalcman G, Valleix F, Podoll T, Umezawa Y, Takao S, Iwata S, Hosono O, Taguchi T, Yamada T, Dang NH, Ohnuma K, Angevin E, Morimoto C. Serum soluble CD26 /DPP4 titer variation is a potential prognostic biomarker in cancer therapy with a humanized anti-CD26 antibody. Biomark Res. 2021;9(1):21

4) Komiya E, Tominaga M, Hatano R, kamikubo Y, Toyama S, Sakairi H, Honda K, Itoh T, Kamata Y, Tsurumachi M, Kishi R, Ohnuma K, Sakurai T, Morimoto C, Takamori K. Peripheral endomorphins drive mechanical alloknesis under the enzymatic control of CD26/DPPIV. J Allergy Clin Immunol. in press

5) Pan K, Ohnuma K, Morimoto C, Dang NH. CD26/Dipeptidyl Peptidase IV and Its Multiple Biological Functions. Cureus. 2021; 13(2): e13495

2. 著書

なし

3. 学会発表

1) Komiya E, Tominaga M, Hatano R, Itoh T, Honda K, Toyama S, Kamata Y, Otsuka H, Ohnuma K, Morimoto C, Takamori K. Mu-opioid ligand endomorphin induces alloknesis at the periphery, 日本研究皮膚科学会, 第 46 回年次学術大会・総会 (オンライン), 2021 年 12 月

2) Komiya E, Tominaga M, Hatano R, Itoh T, Honda K, Toyama S, Kamata Y, Otsuka H, Ohnuma K, Morimoto C, Takamori K. CD26/DPPIV regulates mechanical alloknesis at the periphery, 11th World Congress on Itch (WCI), Online congress, October 2021

3) Hatano R, Otsuka H, Itoh T, Saeki H, Yamamoto A, Shirakawa Y, Iyama S, Iwao N, Sato T, Yamada T, Morimoto C,

Ohnuma K. Anti-interleukin-26 therapy for the control of chronic inflammation in GVHD. 第 83 回日本血液学会 2021 年 9 月

4) 古宮栄利子, 小島豪, 冨永光俊, 森本幾夫, 髙森建二. 加齢皮膚におけるアロネーシスの発症機構の解明, 第 17 回加齢皮膚医学研究会(オンライン) , 2021 年 8 月

5) 古宮栄利子, 冨永光俊, 波多野良, 外山扇雅, 伊藤匠, 鎌田弥生, 本田耕太郎, 大沼圭, 森本幾夫, 髙森建二. CD26/dipeptidyl-peptidase IV は機械的かゆみの調節因子である, 第 26 回日本病態プロテアーゼ学会(オンライン), 2021 年 8 月

H. 知的財産権の出願・登録状況（予定を含む）

1. 特許取得

1) 発明者: 森本幾夫、波多野良、大沼圭、金子有太郎. 発明の名称: 抗 CD26 抗体と免疫チェックポイント阻害剤との併用療法. 出願日: 2021 年 5 月 31 日, 出願番号: 特願 2021-091761, 出願人: ワイズ・エー・シー株式会社、学校法人順天堂

2. 実用新案登録

なし

3. その他

なし

労災疾病臨床研究事業費補助金

分担研究報告書

ヒト化 CD26 抗体の有効性予測バイオマーカーの探索：国内第 I/II 相臨床試験の腫瘍病理組織の遺伝子発現解析

研究代表者　森本　幾夫　順天堂大学大学院医学研究科
免疫病・がん先端治療学講座 特任教授

研究分担者　波多野　良　順天堂大学大学院医学研究科
免疫病・がん先端治療学講座 特任助教

研究分担者　山田　健人　埼玉医科大学医学部 病理学 教授

研究分担者　岸本　卓巳　独立行政法人労働者健康安全機構
アスベスト疾患研究・研修センター 所長

研究協力者　伊藤　匠　順天堂大学大学院医学研究科
免疫病・がん先端治療学講座 博士研究員

研究協力者　藤本　伸一　岡山労災病院 腫瘍内科部長

研究協力者　青江　啓介　山口宇部医療センター 腫瘍内科 内科系診療部長

研究要旨

悪性胸膜中皮腫はアスベストばく露によって起こる難治性悪性腫瘍であり、現時点で満足できる治療法はなく、新たな治療法の確立が望まれる。われわれは、新規治療標的分子として悪性胸膜中皮腫に発現する CD26 に着目し、ヒト化 CD26 抗体を開発しフランスにて第 I 相臨床試験を、2017 年から国内で悪性中皮腫に対する第 I/II 相臨床試験を開始した。安全性が確認され治療薬としての有効性を示唆する結果も得られ、2019 年中に第 I 相 9 例・第 II 相 31 例(計 40 例)への投与が終了し、結果の集計が完了した。これまでに国内第 I/II 相臨床試験の患者から提供を受けた血清及び末梢血リンパ球を用いて、CD26 抗体の有効性予測バイオマーカーの探索を行ってきたが、今年度は腫瘍病理組織から腫瘍部分を切り出し、RNA 抽出と DNA マイクロアレイ解析を行った。Progressive Disease 症例群と比較して Stable Disease 症例群で共通して発現が高い遺伝子、発現が低い遺伝子の絞り込みを行い、CD26 抗体の有効性予測バイオマーカー候補を見出した。今後、悪性中皮腫の病理組織の免疫染色を検討し、CD26 抗体投与を開始する前に抗体療法が有効な患者を判別できるバイオマーカーとなり得るかを明らかにする。

A. 研究目的

悪性胸膜中皮腫はアスベストばく露によって起こる胸膜中皮由来の難治性悪性腫瘍である。予後は極めて悪く、手術療法、化学療法、放射線療法などが行われるが、いずれも満足できる治療成績ではなく、新たな治療法の確立が望まれる。われわれは、新規治療標的分子として悪性中皮腫細胞に発現する

CD26 に着目し、ヒト化 CD26 抗体を開発してフランスにて悪性中皮腫を中心に First-in-Human 第 I 相臨床試験を行った。

このフランスでの結果を受け、どの患者に CD26 抗体療法が有効なのか、治療効果や予後を予測できるバイオマーカーの探索が課題として挙げられた。このことは、本抗体療法がより安全かつ効果的に行われるうえで極めて重要であり、かつ、抗体療法適用患者を適切に選択できれば期待していた治療効果が得られない患者にまで高額な医療費負担を強いることがなくなり、労災補償行政にも貢献できる。

そこで、本抗体の予後・治療効果予測バイオマーカーを同定するために、2017 年から本邦で開始した治療抵抗性(標準治療で Progressive Disease (PD))の悪性胸膜中皮腫に対するヒト化 CD26 抗体の第 I/II 相臨床試験患者の(1)中皮腫病理組織、(2)血清、(3)末梢血リンパ球を用いた解析に取り組んできた。

(2)血清に関しては、CD26/DPP4 と関連するサイトカイン・ケモカインの多項目解析を行い、CD26 抗体投与による血清中濃度の変動を解析し、CD26 抗体の有効性との相関関係を解析した。(3)末梢血リンパ球に関しては、末梢血中の CD4 T 細胞・CD8 T 細胞・CD25 強陽性の制御性 CD4 T 細胞、細胞傷害活性を有するエフェクターT 細胞の細胞数・割合、代表的な免疫チェックポイント分子の発現と、CD26 抗体の有効性との相関関係を解析した(2021 年度 労災疾病臨床研究事業費補助金 研究報告書に記載)。

本パートでは、(1)中皮腫病理組織を用いて、腫瘍部位の切り出し、RNA 抽出、DNA マイクロアレイ解析を行い、Stable Disease (SD)症例と PD 症例との遺伝子発現の比較から CD26 抗体の有効性予測バイオマーカーの絞り込みを行った。

B. 研究方法

1) 国内第 I/II 相臨床試験プロトコル

第 I 相臨床試験はヒト化 CD26 抗体を 2mg/kg, 4mg/kg, 6mg/kg でそれぞれ 3 例ずつ、初回投与日を day1 として day1, day8, day15, day22, day29 まで週 1 回の間隔で 5 回静脈内投与を行い、投与を開始してから 6 週間後(day42)の時点で医師による抗腫瘍効果の判定が行われ、Partial Response (PR) または SD と判定された患者は、上記の抗体 5 回投与、6 週間後に抗腫瘍効果判定を 1 サイクルとして PD になるまでサイクルを継続した。

第 II 相臨床試験は全 31 例に CD26 抗体を 6mg/kg で週 1 回の間隔で 5 回静脈内投与を行い、上記と同様に抗体 5 回投与、6 週間後に抗腫瘍効果判定を 1 サイクルとして PD になるまでサイクルを継続した。

2) 腫瘍病理組織

ヒト化 CD26 抗体の悪性胸膜中皮腫に対する国内第 I/II 相臨床試験は第 I 相が全 9 例、第 II 相が全 31 例で行われたが、その中で腫瘍病理組織のバイオマーカー探索に同意が得られたのは、第 I 相が 2 例、第 II 相が 21 例の計 23 例であった。抗がん剤治療や抗 PD-1 抗体 Nivolumab 治療を開始する前に採取された悪性中皮腫組織をホルマリン固定して作製されたパラフィンブロックの組織切片の提供を受け、マイクロダイセクションにより腫瘍部分の切り出しを行った。

3) DNA マイクロアレイ解析

ホルマリン固定・パラフィン包埋された悪性中皮腫組織からマイクロダイセクションで切り出した腫瘍部位を溶解し、miRNeasy FFPE Kit (QIAGEN)を用いて Total RNA 抽出を行った。全 7 サンプルの中で最も得られたRNA量が少なかったサンプルに合わせて RNA 44ng から TransPlex Whole Transcriptome Amplification Kit (Sigma-Aldrich) と Titanium Taq DNA Polymerase (Clontech)を用いて cDNA の合成と増幅を行った。SureTag DNA Labeling Kit (Agilent Technologies)を用いて cDNA の断片化、DNA の Cy3 標識、精製を行った後、SurePrint G3 Human GE マイクロアレイ 8 x 60K Ver 3.0 (Design ID:072363) (Agilent Technologies)を用いて DNA マイクロアレイ解析を行った。

(倫理面への配慮)

ヒト化 CD26 抗体の国内第 I/II 相臨床試験の患者検体を用いたバイオマーカー探索研究については、臨床試験審査委員会、各治験実施施設内の治験審査委員会にて、試験の実施と合わせてバイオマーカー探索用採血・腫瘍組織検体の提供について協議され、実施承認を取得済みである。検体の提供を受ける際には、研究対象者に対する人的擁護上の配慮及び研究により研究対象者が受ける不利益、利益等の説明を行い、書面でのインフォームド・コンセントを得ている。

C. 研究結果

1) 国内第 I/II 相臨床試験患者の腫瘍病理組織の遺伝子発現解析

本パートの目的は、ヒト化 CD26 抗体療法が有効な患者を選択できるバイオマーカーを探索することである。CD26 抗体の国内臨床試験で腫瘍病理組織のバイオマーカー解析に同意が得られたのは、第 I 相が全 9 例中 2 例、第 II 相が全 31 例中 21 例の計 23 例(23/40)で、内訳は PR 0 例・SD 16 例・PD 6 例・評価不能 1 例であった。DNA マイクロアレイ解析でSD症例とPD症例の遺伝子発現比較を行う際に、考慮すべき事項として性別・組織型・抗 PD-1 抗体 Nivolumab 投与の有無が挙げられる。腫瘍病理組織のバイオマーカー探索同意が得られた 23 例中、抗腫瘍効果の判定ができた 22 例を性別・組織型・Nivolumab 投与の有無の項目で整理した結果を表 1 に示す。

表1 腫瘍病理組織のバイオマーカー探索同意が得られた国内第I/II相臨床試験患者 22例の性別・組織型分類

Phase I/II Male 20 cases

	Nivolumab投与なし	Nivolumab投与あり	Total
Epithelioid	SD 6/PD 4	SD 5/PD 0	15
Biphasic	SD 1/PD 0	SD 1/PD 1	3
Sarcomatoid	SD 1/PD 1	-	2
Total	13	7	20

Phase I/II Female 2 cases

	Nivolumab投与なし	Nivolumab投与あり	Total
Epithelioid	SD 1/PD 0	SD 1/PD 0	2
Biphasic	-	-	-
Sarcomatoid	-	-	-
Total	1	1	2

※赤枠の「男性・上皮型・Nivolumab投与なし」群のSD 3例・PD 4例から腫瘍部分の切り出し、Total RNA抽出、DNAマイクロアレイ解析を実施した。

性別・組織型・Nivolumab 投与の有無が同じ条件で、SD 症例と PD 症例を 3 例以上取れるのは、「男性・上皮型・Nivolumab 投与無し」(SD 6 例/PD 4 例)のみであったため、SD 6 症例中無増悪生存期間 PFS が長い 3 例と PD 4 例から腫瘍部位を切り出し、DNA マイクロアレイ解析を行った。

SD 群 3 例と PD 群 4 例との間で遺伝子発現の群比較を行い、PD 群と比較して SD 群で高発現している遺伝子群と SD 群と比

較して PD 群で高発現している遺伝子群をヒートマップにまとめた(図 1)。

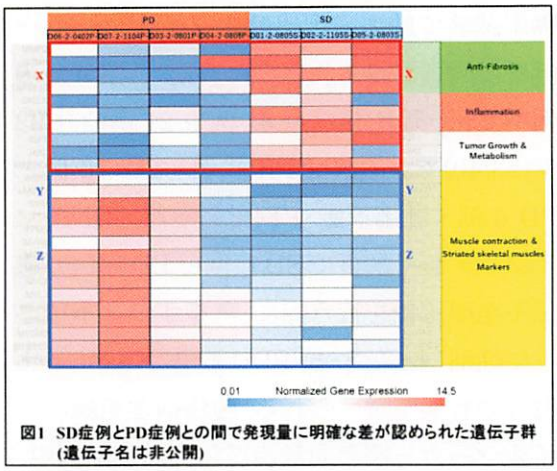

図1 SD症例とPD症例との間で発現量に明確な差が認められた遺伝子群(遺伝子名は非公開)

CD26 抗体の有効性予測バイオマーカーとして特許出願の可能性があるため、具体的な遺伝子名は公開しないが、SD 症例 3 例に共通して高発現しており PD 症例 4 例ではほとんど発現していない遺伝子 X を見出した。また、SD 症例 3 例に共通してほとんど発現しておらず PD 症例では発現が見られる遺伝子 Y と Z の絞り込みを行った。今後、X, Y, Z に関して腫瘍病理組織の免疫染色を行い、PFS の期間が長く CD26 抗体療法が特に有効な症例と有効ではない PD 症例との判別に有用かどうか検討する。

D. 考察

ヒト化 CD26 抗体の予後・治療効果予測バイオマーカーを探索するために、CD26 抗体の国内第 I/II 相臨床試験患者の腫瘍病理組織を用いて、SD 症例 3 例と PD 症例 4 例の DNA マイクロアレイ解析を行った。

CD26 抗体の有効性予測バイオマーカーとして特許出願の可能性があるため、具体的な遺伝子名は公開しないが、SD 群で発現が高かった遺伝子は抗線維化、炎症亢進、増殖・代謝亢進に関わるものが多く見られた。一方で、PD 群で発現が高かった遺伝子は筋細胞、中でも横紋筋に関係する遺伝子群が多数見られ、横紋筋分化が亢進している可能性が考えられた。

今後、腫瘍病理組織の免疫染色により SD 症例と PD 症例とで得られた候補分子の発現を解析する。また、それらの遺伝子を高発現する症例で何故 CD26 抗体が有効なのか無効なのかを解明することで、より CD26 抗体による治療効果が得られる併用療法の開発にも繋がることが期待される。

E. 結論

ヒト化 CD26 抗体の国内第 I/II 相臨床試験患者のホルマリン固定・パラフィン包埋された悪性中皮腫組織から腫瘍部位をマイクロダイセクションで切り出し、得られた微量の Total RNA を用いて SD 症例 3 例と PD 症例 4 例の DNA マイクロアレイ解析を行った。その結果、SD 症例で共通して発現が高い遺伝子 X と共通して発現が低い遺伝子 Y, Z を見出した。

F. 今後の展望

国内第 I/II 相臨床試験患者の腫瘍病理組織を用いて、今回の DNA マイクロアレイ解析により得られた候補分子の免疫染色を行い、これらの分子がヒト化 CD26 抗体の有効性を予測できるバイオマーカーになり得るかを明らかにする。

G. 研究発表

1. 論文発表

1) Ohmachi-Ono A, Yamada S, Uno S, Tamai M, Soga K, Nakamura S, Udagawa N,

Nakamichi Y, Koide M, Morita Y, Takano T, Itoh T, Kakuta S, Morimoto C, Matsuoka S, Iwakura Y, Tomura M, Kiyono H, Hachimura S, Nakajima-Adachi H. Effector memory CD4+ T cells in mesenteric lymph nodes mediate bone loss in food-allergic enteropathy model mice, creating IL-4 dominance. Mucosal Immunol. 2021;14(6):1335-1346

2) Itoh T, Hatano R, Horimoto Y, Yamada T, Song D, Otsuka H, Shirakawa Y, Matsuoka S, Iwao N, Aune TM, Dang NH, Kaneko Y, Okumura K, Morimoto C, Ohnuma K. IL-26 mediates epidermal growth factor receptor-tyrosine kinase inhibitor resistance through endoplasmic reticulum stress signaling pathway in triple-negative breast cancer cells. Cell Death Dis. 2021;12(6): 520

3) Kaneko Y, Hatano R, Hirota N, Isambert N, Trillet-Lenoir V, You B, Alexandre J, Zalcman G, Valleix F, Podoll T, Umezawa Y, Takao S, Iwata S, Hosono O, Taguchi T, Yamada T, Dang NH, Ohnuma K, Angevin E, Morimoto C. Serum soluble CD26 /DPP4 titer variation is a potential prognostic biomarker in cancer therapy with a humanized anti-CD26 antibody. Biomark Res. 2021;9(1):21

4) Komiya E, Tominaga M, Hatano R, kamikubo Y, Toyama S, Sakairi H, Honda K, Itoh T, Kamata Y, Tsurumachi M, Kishi R, Ohnuma K, Sakurai T, Morimoto C, Takamori K. Peripheral endomorphins drive mechanical alloknesis under the enzymatic control of CD26/DPPIV. J Allergy Clin Immunol. in press

5) Pan K, Ohnuma K, Morimoto C, Dang NH. CD26/Dipeptidyl Peptidase IV and Its Multiple Biological Functions. Cureus. 2021; 13(2): e13495

2. 著書

なし

3. 学会発表

1) Komiya E, Tominaga M, Hatano R, Itoh T, Honda K, Toyama S, Kamata Y, Otsuka H, Ohnuma K, Morimoto C, Takamori K. Mu-opioid ligand endomorphin induces alloknesis at the periphery, 日本研究皮膚科学会, 第46回年次学術大会・総会 (オンライン), 2021年12月

2) Komiya E, Tominaga M, Hatano R, Itoh T, Honda K, Toyama S, Kamata Y, Otsuka H, Ohnuma K, Morimoto C, Takamori K. CD26/DPPIV regulates mechanical alloknesis at the periphery, 11th World Congress on Itch (WCI), Online congress, October 2021

3) Hatano R, Otsuka H, Itoh T, Saeki H, Yamamoto A, Shirakawa Y, Iyama S, Iwao N, Sato T, Yamada T, Morimoto C, Ohnuma K. Anti-interleukin-26 therapy for the control of chronic inflammation in GVHD. 第83回日本血液学会 2021年9月

4) 古宮栄利子, 小島豪, 冨永光俊, 森本幾夫, 高森建二. 加齢皮膚におけるアロネーシスの発症機構の解明, 第17回加齢皮膚医学研究会(オンライン), 2021年8月

5) 古宮栄利子, 冨永光俊, 波多野良, 外山扇雅, 伊藤匠, 鎌田弥生, 本田耕太郎, 大沼圭, 森本幾夫, 高森建二. CD26/dipeptidyl-peptidase IV は機械的かゆみ

の調節因子である，第 26 回日本病態プロテアーゼ学会(オンライン)，2021 年 8 月

H. 知的財産権の出願・登録状況（予定を含む）

1. 特許取得

1) 発明者: 森本幾夫、波多野良、大沼圭、金子有太郎. 発明の名称: 抗 CD26 抗体と免疫チェックポイント阻害剤との併用療法. 出願日: 2021 年 5 月 31 日，出願番号: 特願 2021-091761，出願人: ワイズ・エー・シー株式会社、学校法人順天堂

2. 実用新案登録

なし

3. その他

なし

Ⅲ. 研究成果の刊行に関する一覧表

別紙４

研究成果の刊行に関する一覧表

雑誌

発表者氏名	論文タイトル名	発表誌名	巻号	ページ	出版年
Ohmachi-Ono A, Yamada S, Uno S, Tamai M, Soga K, Nakamura S, Udagawa N, Nakamichi Y, Koide M, Morita Y, Takano T, Itoh T, Kakuta S, Morimoto C, Matsuoka S, Iwakura Y, Tomura M, Kiyono H, Hachimura S, Nakajima-Adachi H	Effector memory CD4 + T cells in mesenteric lymph nodes mediate bone loss in food-allergic enteropathy model mice, creating IL-4 dominance.	Mucosal Immunol.	14(6)	1335-1346	2021
Itoh T, Hatano R, Horimoto Y, Yamada T, Song D, Otsuka H, Shirakawa Y, Matsuoka S, Iwao N, Aune TM, Dang NH, Kaneko Y, Okumura K, Morimoto C, Ohnuma K.	IL-26 mediates epidermal growth factor receptor-tyrosine kinase inhibitor resistance through endoplasmic reticulum stress signaling pathway in triple-negative breast cancer cells.	Cell Death Dis.	12(6)	520	2021
Kaneko Y, Hatano R, Hirota N, Isambert N, Trillet-Lenoir V, You B, Alexandre J, Zalcman G, Valleix F, Podoll T, Umezawa Y, Takao S, Iwata S, Hosono O, Taguchi T, Yamada T, Dang NH, Ohnuma K, Angevin E, Morimoto C.	Serum soluble CD26/DPP4 titer variation is a potential prognostic biomarker in cancer therapy with a humanized anti-CD26 antibody.	Biomark Res.	9(1)	21	2021
Komiya E, Tominaga M, Hatano R, kamikubo Y, Toyama S, Sakairi H, Honda K, Itoh T, Kamata Y, Tsurumachi M, Kishi R, Ohnuma K, Sakurai T, Morimoto C, Takamori K.	Peripheral endomorphins drive mechanical allokenesis under the enzymaticcontrol of CD26/DPPIV.	J Allergy Clin Immunol.			(in press)

発表者氏名	論文タイトル名	発表誌名	巻号	ページ	出版年
Pan K, Ohnuma K, Morimoto C, Dang NH.	CD26/Dipeptidyl Peptidase IV and Its Multiple Biological Functions.	Cureus.	13(2)	E13495	2021
Sasaki H, Saisho Y, Inaishi J, Watanabe Y, Tsuchiya T, Makio M, Sato M, Nishikawa M, Kitago M, Yamada T, Itoh H.	Reduced beta cell number rather than size is a major contributor to beta cell loss in type 2 diabetes.	Diabetologia.	64(8)	1816-1821	2021
Kishimoto T, Kojima Y, Fujimoto N.	Significance of secretory leukocyte peptidase inhibitor in pleural fluid for the diagnosis of benign asbestos pleural effusion.	Sci Rep.	11(1)	12965	2021
Hayashi H, Ashizawa K, M, Kato K, Arakawa H, Kishimoto T, Otsuka Y, Noma S, Honda S.	The diagnosis of early pneumoconiosis in dust-exposed workers: comparison of chest radiography and computed tomography.	Acta Radiol.	7	2841851211022501	2021
Mizuhashi K, Okamoto K, Kishimoto T.	A patient with epithelioid pleural mesothelioma (Myxoid variant) who survived for a long period without treatment.	Respir Med Case Rep.	33	101381	2021

Ⅳ. 研究成果の別刷

ARTICLE

Check for updates

Effector memory CD4$^+$T cells in mesenteric lymph nodes mediate bone loss in food-allergic enteropathy model mice, creating IL-4 dominance

Aiko Ono-Ohmachi[1,2], Satoki Yamada[3], Satoru Uno[3], Masato Tamai[3], Kohei Soga[3], Shotaro Nakamura[3], Nobuyuki Udagawa[4], Yuko Nakamichi[5], Masanori Koide[5], Yoshikazu Morita[1], Tomohiro Takano[3], Takumi Itoh[6,7], Shigeru Kakuta[8], Chikao Morimoto[6], Shuji Matsuoka[9], Yoichiro Iwakura[10], Michio Tomura[11], Hiroshi Kiyono[12,13,14], Satoshi Hachimura[3] and Haruyo Nakajima-Adachi[3,12]✉

Intestinal inflammation can be accompanied by osteoporosis, but their relationship, mediated by immune responses, remains unclear. Here, we investigated a non-IgE-mediated food-allergic enteropathy model of ovalbumin (OVA) 23-3 mice expressing OVA-specific T-cell-receptor transgenes. Mesenteric lymph nodes (MLNs) and their pathogenic CD4$^+$T cells were important to enteropathy occurrence and exacerbation when the mice were fed an egg-white (EW) diet. EW-fed OVA23-3 mice also developed bone loss and increased CD44^{hi}CD62L^{lo}CD4$^+$T cells in the MLNs and bone marrow (BM); these changes were attenuated by MLN, but not spleen, resection. We fed an EW diet to F1 cross offspring from OVA23-3 mice and a mouse line expressing the photoconvertible protein KikGR to track MLN CD4$^+$T cells. Photoconverted MLN CD44^{hi}CD62L^{lo}CD4$^+$T cells migrated predominantly to the BM; pit formation assay proved their ability to promote bone damage via osteoclasts. Significantly greater expression of IL-4 mRNA in MLN CD44^{hi}CD62L^{lo}CD4$^+$T cells and bone was observed in EW-fed OVA23-3 mice. Anti-IL-4 monoclonal antibody injection canceled bone loss in the primary inflammation phase in EW-fed mice, but less so in the chronic phase. This novel report shows the specific inflammatory relationship, via Th2-dominant-OVA-specific T cells and IL-4 production, between MLNs and bone, a distant organ, in food-allergic enteropathy.

Mucosal Immunology; https://doi.org/10.1038/s41385-021-00434-2

INTRODUCTION

Intestinal inflammation, such as celiac disease with small intestinal inflammation, as well as inflammatory bowel disease (IBD)[1]—has been reported to have osteoporosis as a comorbidity. Aberrantly activated T cells may play important roles in bone loss after intestinal inflammation[2]. Previously, in a model of non-IgE-mediated gastrointestinal food-allergy model of ovalbumin (OVA) 23-3 mice, which expresses OVA-specific T-cell receptor (TCR) transgenes[3], we demonstrated bone loss development with increased numbers of activated CD4$^+$T cells in the bone marrow (BM)[4]. Enteropathy is induced in these mice simply by feeding an egg-white (EW) diet containing OVA[3]. This model shows typical allergic responses accompanied by weight loss and severe intestinal morphological changes, followed by intestinal infiltration by inflammatory cells (7 to 10 days' EW feeding, primary phase), and serum IgE production (14 days' EW feeding)[3,5]. Prolonged EW feeding (28 days, chronic phase) attenuates OVA-specific CD4$^+$T-cell activation and ameliorates the inflammation via regulatory T-cell (Treg) induction[5,6]. Despite these changes in the enteropathy pathology, bone loss seemed to be maintained during the experimental period[4]. As the enteropathy is triggered by MLNs and their aberrantly activated IL-4-producing MLN CD4$^+$T cells through food-allergen intake alone[5], bone loss in these mice may occur through allergen-specific immune responses activated and promoted in the MLNs. Allergic diseases (e.g., atopic dermatitis) may be associated with osteoporosis[7–9]. One potential mechanism reported from a study of *lck*-IL-4 transgenic mice is that continuous and excessive IL-4 production by activated T cells induces osteoporosis[10]. However, it remains unclear whether food-allergy-associated gastrointestinal inflammatory responses affect bone loss.

[1]Milk Science Research Institute, Megmilk Snow Brand Co., Ltd., Saitama, Japan. [2]Department of Quality Assurance, Bean Stalk Snow Co., Ltd., Tokyo, Japan. [3]Research Center for Food Safety, Graduate School of Agricultural and Life Sciences, The University of Tokyo, Tokyo, Japan. [4]Department of Biochemistry, Matsumoto Dental University, Nagano, Japan. [5]Institute for Oral Science, Matsumoto Dental University, Nagano, Japan. [6]Department of Therapy Development and Innovation for Immune Disorders and Cancers, Juntendo University, Tokyo, Japan. [7]Atopy (Allergy) Research Center, Graduate School of Medicine, Juntendo University, Tokyo, Japan. [8]Laboratory of Biomedical Science, Graduate School of Agricultural and Life Sciences, The University of Tokyo, Tokyo, Japan. [9]Department of Immunological Diagnosis, Graduate School of Medicine, Juntendo University, Tokyo, Japan. [10]Research Institute for Biomedical Sciences, Tokyo University of Science, Chiba, Japan. [11]Laboratory of Immunology, Faculty of Pharmacy, Osaka Ohtani University, Nishikiorikita, Tondabayashi-shi, Osaka, Japan. [12]IMSUT Distinguished Professor Unit, Division of Mucosal Immunology, The Institute of Medical Science, The University of Tokyo, Tokyo, Japan. [13]Mucosal Immunology and Allergy Therapeutics, Future Medicine Education and Research Organization, Institute for Global Prominent Research, Graduate School of Medicine, Chiba University, Chiba, Japan. [14]Division of Gastroenterology, Department of Medicine, School of Medicine, CU-UCSD Center for Mucosal Immunology, Allergy and Vaccines, University of California, San Diego, CA, USA. ✉email: haruyona@g.ecc.u-tokyo.ac.jp

Received: 6 August 2020 Revised: 7 June 2021 Accepted: 6 July 2021
Published online: 29 July 2021

We believed that, to clarify the mechanism by which food-allergic enteropathy induces the loss of bone—an extraintestinal organ—OVA23-3 mice were superior to other mouse models in terms of the technique used to alter their immunological condition, namely by simply feeding EW. We therefore analyzed this mouse model and discovered a specific relationship of the gut–bone axis via Th2-dependent immune responses between inflammatory MLNs and bone loss in food-allergic enteropathy.

RESULTS

EW feeding leads to bone loss in OVA23-3 mice

To minimize the influence of differences in nutrient consumption and body-weight changes on bone metabolism in EW-fed OVA23-3 mice, we conducted pair feeding, in which mice were maintained under the same food-consumption condition (apart from the difference in the protein source) during the experiment. Weight gain (Fig. 1a) and serum biomarker levels (Table S1) did not differ significantly among the four groups, although some EW-fed OVA23-3 mice lost weight and developed enteropathy during the experimental period (Fig. 1a). Serum 1,25-dihydroxyvitamin D_3 levels in EW-fed mice were significantly higher (OVA23-3, Fig. S1 left) than that in casein control diet (CN)-fed mice or the same as in the CN-fed mice (R23-3/BALB, Fig. S1 right) throughout the experimental period, showing the involvement of 1,25-dihydroxyvitamin D_3 in bone loss in our model was not clear. Severe bone loss—a significant decrease in the percentage change in the trabecular bone mineral content (BMC) compared with that in CN- or EW-fed BALB/cA (BALB) mice and CN-fed OVA23-3 mice—began in OVA23-3 mice on day 7 (primary phase; Fig. 1b, left), and significant decreases in cortical BMC started on day 21 of EW feeding (chronic phase; Fig. 1b, right). These bone losses continued to the end of the experiment. Continuing trabecular bone loss was further confirmed by examining other bone-morphologic parameters (bone volume per tissue volume [BV/TV] and BMC/TV, $P < 0.01$, EW-fed OVA23-3 mice vs. CN- or EW-fed BALB mice and CN-fed OVA23-3 mice; Fig. S2A). On day 56 (prolonged feeding of the EW diet), significant decreases in some parameters (BMC, BV/TV, BMC/TV, and trabecular number [Tb.N]) and an increase in trabecular separation (Tb.Sp) in EW-fed OVA23-3 mice were confirmed (Figs. 1c and S2B). These results clearly showed that feeding conditions and absorption alterations via intestinal inflammation were not major factors influencing the severe trabecular bone loss and inhibition of age-dependent increases in cortical bone thickness exhibited by EW-fed OVA23-3 mice.

Like EW-fed OVA23-3 mice, the inbred food-allergic enteropathy BALB mouse model established by EW feeding after sensitization with OVA and alum (BALB/ALUM mice) showed enteropathy, recovery from inflammation[11], and bone loss (Fig. S3). Thus, our model's bone loss did not result from the presence of the TCR transgene but from the food-allergic enteropathy.

Aberrant OVA-specific CD44^{hi}CD62L^{lo}CD4^{+}T-cell activation induced in MLNs and BM by EW feeding triggers bone loss in EW-fed OVA23-3 mice

EW-fed, but not CN-fed, OVA23-3 mice deficient in recombination-activating gene (RAG) 2 mice (R23-3 mice) also showed significant weight loss (Fig. S4A) (a sign of enteropathy induced by IL-4-producing OVA-specific CD4^{+}T cells)[6] and bone loss as a comorbidity. Compared with CN-fed R23-3 mice, the EW-fed mice also had significant decreases in trabecular BMC (Fig. S4B, C), BV/TV, BMC/TV, and Tb.N and a significant increase in Tb.Sp (Fig. S5). In contrast, EW-fed Th1-type RAG-2-deficient D10 mice (RD10 mice)—another strain with OVA-TCR transgenes[6,12]—did not show weight loss or bone loss (Figs. S4 and S5)[6]. Therefore, aberrant activation of Th2-type OVA-specific CD4^{+}T-cells, inducing enteropathy, likely plays an important role in inducing bone loss. In contrast, OVA-specific B cells were not involved, because R23-3 mice developed bone loss despite lacking B cells. We confirmed the above possibility by establishing a model of transfer of OVA-specific MLN CD4^{+}T cells from R23-3 mice into severe combined immunodeficiency mice (SR23-3 mice). Only the EW-fed SR23-3 mice showed significant decreases in BMC and weight (Fig. S6, Results in the Supplementary Information).

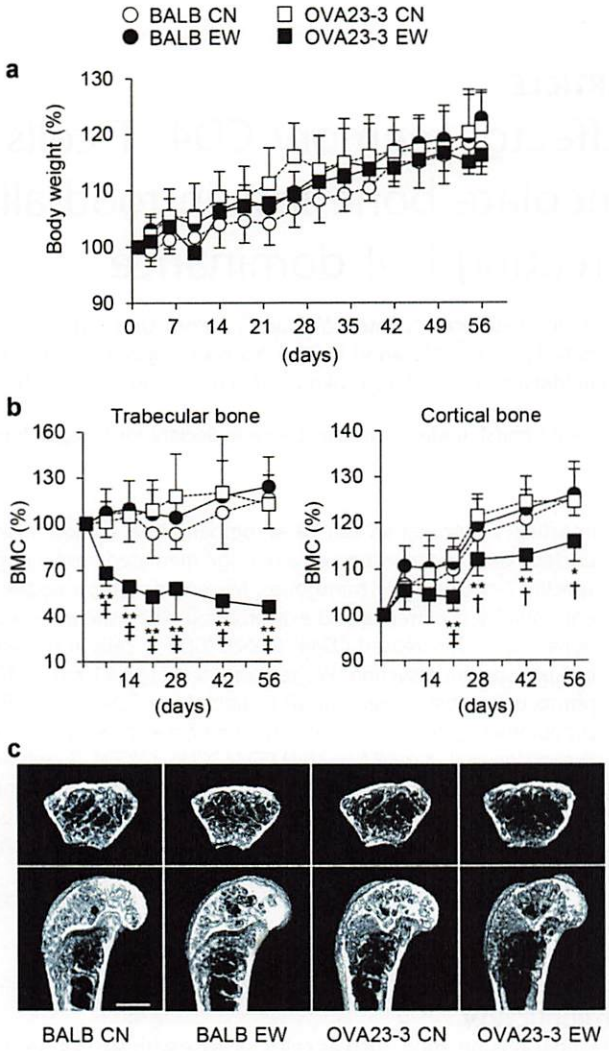

Fig. 1 Egg-white (EW)-fed OVA23-3 mice display bone loss. BALB mice and OVA23-3 mice were fed a control (CN) or EW diet for 56 days. **a** Time course of body-weight relative to initial values (100%). Initial body weights were: for BALB CN, 24 ± 0.99 g; BALB EW, 24.57 ± 0.73 g; OVA23-3 CN, 24.76 ± 1.94 g; OVA23-3 EW 24.99 ± 1.90 g. Body-weight was measured every 2 or 3 days. **b** Time courses of bone mineral content (BMC) in trabecular (left panel) and cortical (right panel) bone relative to initial values (100%). BMC was measured by using micro-computed tomography throughout the 56 days. BALB CN, CN-fed BALB mice (open circle (○)); BALB EW, EW-fed BALB mice (closed circle (●)); OVA23-3 CN, CN-fed OVA23-3 mice (open square (□)); OVA23-3 EW, EW-fed OVA23-3 mice (closed square (■)). **c** Computed tomography images of the distal femur after 56 days of CN or EW diets. Scale bar = 1 mm. $n = 3$ to 5 in each group. Data are representative of two independent experiments. $^{*}P < 0.05$ and $^{**}P < 0.01$ (OVA23-3 EW vs. BALB CN and OVA23-3 CN); $^{\dagger}P < 0.05$ and $^{\ddagger}P < 0.01$ (OVA23-3 EW vs. BALB EW).

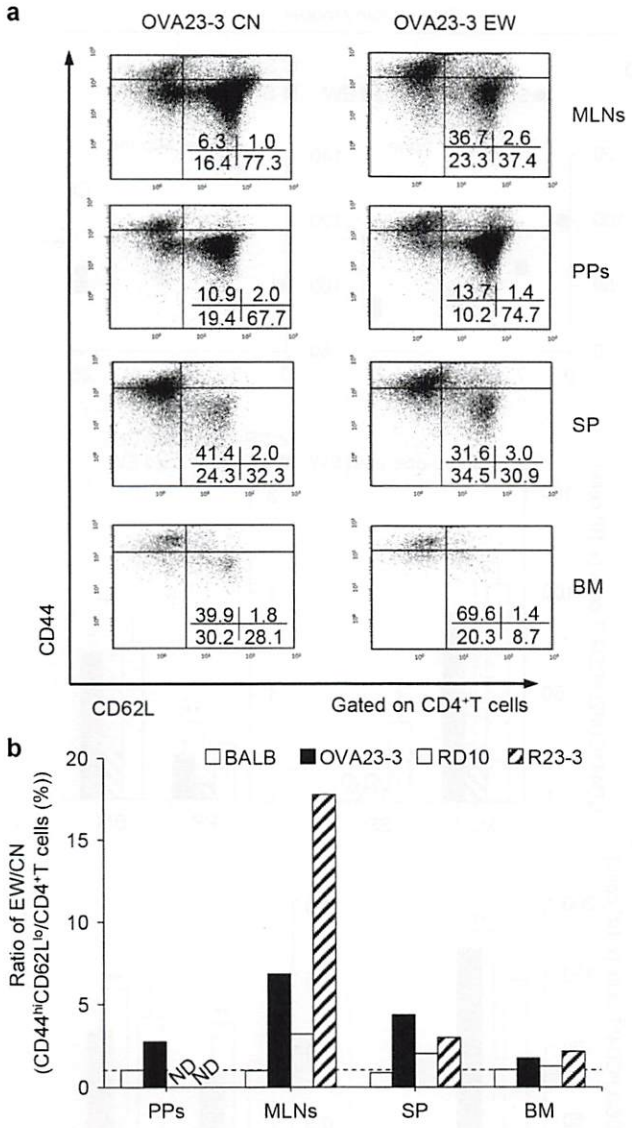

Fig. 2 Egg-white (EW) feeding induces $CD44^{hi}CD62L^{lo}CD4^{+}$T cells in OVA23-3 mice throughout the experimental period. Single-cell suspensions were prepared from mesenteric lymph nodes (MLNs), Peyer's patches (PPs), spleen (SP), and bone marrow (BM) of BALB, OVA23-3, R23-3, and RD10 mice fed a control (CN) or EW diet for 56 days. **a** Dot plots represent CD44 vs. CD62L gated on magnetic-activated-cell-sorting-separated $CD4^{+}$T cells of MLNs, PPs, SP, and BM in OVA23-3 mice fed a CN diet (left) or EW diet (right). Numbers in the plots indicate $CD44^{hi}CD62L^{lo}CD4^{+}$T cells and $CD44^{hi}CD62L^{hi}CD4^{+}$T cells (top row, left and right, respectively) and $CD44^{int}CD62L^{lo}CD4^{+}$T cells and $CD44^{int}CD62L^{hi}CD4^{+}$T cells (bottom row, left and right, respectively) as percentages of the total number of $CD4^{+}$T cells. **b** Each column indicates the ratio in EW-fed mice (BALB, OVA23-3, R23-3, and RD10) to that in CN-fed mice of $CD44^{hi}CD62L^{lo}CD4^{+}$T cells as a percentage of total $CD4^{+}$T cells from different lymphoid tissues (MLNs, PPs, SP, and BM). Dashed lines indicate a ratio of 1. The data were obtained by mixing cells from three mice in the CN or EW group and average of two independent experiments. ND = not detected.

Memory-phenotype $CD4^{+}$T cells maintained in the BM contribute to persistent IBD, with bone loss as a comorbidity[13–15]. To clarify the roles of $CD44^{hi}CD62L^{lo}CD4^{+}$T cells [effector-memory (EM) phenotype], which preferentially reside in BM[16–18], we measured CD44 and CD62L molecule expression on aberrantly activated $CD4^{+}$T cells in MLNs, spleen, Peyer's patches (PPs), and BM of EW- or CN-fed OVA23-3 mice. The proportions of these cells increased after EW feeding in OVA23-3 mice (Fig. 2a)—markedly so in MLNs (to about seven times that in CN-fed OVA23-3 mice) but also in the other tissues (to about two to four times those in CN-fed mice) (Fig. 2b). The proportion and number of $CD44^{hi}CD62L^{lo}$ cells among MLN $CD4^{+}$T cells increased throughout EW feeding (Fig. S7A, B(a)). In MLNs, similar results were obtained in EW-fed R23-3 mice (to 18 times that in CN-fed R23-3 mice), whereas the increase in the proportion in EW-fed RD10 mice was smaller (triple that in CN-fed RD10 mice) (Fig. 2b). Residency of EM T cells in BM[16–18] was supported by our finding them there in CN-fed OVA23-3 mice (Fig. 2a); their proportion was enhanced after EW feeding. (to 1.7 times that in CN-fed OVA23-3 mice, Fig. 2b). EW feeding induced greater RANKL expression on the surfaces of $CD62L^{lo}CD4^{+}$T cells in MLNs and BM than in the spleen or PPs (Fig. S8A). RANKL expression in MLNs was enhanced time dependently (Fig. S7B(b), C); more than 95% of $RANKL^{+}CD4^{+}$T cells were of the $CD44^{hi}CD62L^{lo}$ phenotype in EW-fed OVA23-3 mice (Fig. S8B). As RANKL can stimulate osteoclast differentiation[19], our results suggest that MLNs are a source of $RANKL^{+}CD44^{hi}CD62L^{lo}CD4^{+}$T cells for BM, with associated bone-loss induction, as indicated in different enteropathy models. (For details, see Fig. S9 and Results in the Supplementary Information).

MLNs, but not spleen, are important to bone-loss induction upon EW feeding

MLNs are essential to enteropathy development and as a source of aberrantly activated OVA-specific $CD4^{+}$T cells in EW-fed OVA23-3 mice[5]. To clarify the roles of MLNs in bone loss, we performed mesenteric lymphadenectomy or splenectomy on OVA23-3 mice, followed by EW feeding. On day 28 of EW feeding, in MLN-ectomized mice, the decreases in weight (Fig. S10A) and in trabecular (Fig. 3a, left) and cortical (Fig. 3a, right) BMC seen in MLN-sham-operated mice were mitigated significantly (weight loss, $P < 0.01$; trabecular BMC decrease, $P < 0.05$; cortical BMC decrease, $P < 0.05$; EW-fed MLN-ectomized vs. EW-fed MLN-sham-operated mice). In contrast, with EW feeding, splenectomy alleviated neither the weight loss (Fig. S10B) nor the BMC decrease (Fig. 3b) induced in spleen-sham-operated mice.

BM numbers of $CD44^{hi}CD62L^{lo}CD4^{+}$T cells and $RANKL^{+}CD44^{hi}CD62L^{lo}CD4^{+}$T cells were significantly lower in EW-fed MLN-ectomized mice than in EW-fed MLN-sham-operated mice ($P < 0.01$, Fig. 3c; $P < 0.05$, Fig. 3e, respectively). Spleen numbers of both cell types were significantly greater in EW-fed MLN-ectomized mice than in EW-fed MLN-sham-operated mice ($P < 0.05$, Fig. 3c, e); in PPs, there were no significant differences between these two groups, suggesting that the spleen changes occurring with the intestinal immune response were unrelated to those in the BM. There were no significant differences in BM numbers of either cell type between EW-fed splenectomized and spleen-sham-operated mice (Fig. 3d, f). These results clearly indicate that MLNs, but not the spleen, are important for bone-loss induction in food-allergic enteropathy. Moreover, MLN $CD44^{hi}CD62L^{lo}CD4^{+}$T-cell activation may be associated with BM immune responses in EW-fed OVA23-3 mice.

$CD44^{hi}CD62L^{lo}CD4^{+}$T cells in MLNs promote bone damage via osteoclasts independently of cell-surface RANKL expression

We isolated $RANKL^{+/-}CD44^{hi}CD62L^{lo}CD4^{+}$T cells, $CD44^{int}CD62L^{lo}CD4^{+}$T cells, and $CD44^{int}CD62L^{hi}CD4^{+}$T cells from MLNs of EW-fed or CN-fed OVA23-3 mice (Fig. 4a) and conducted pit-formation assays by adding these cells to preosteoclasts. Pit area, which reflects bone damage (osteoclast differentiation and bone resorption)-promoting ability via osteoclasts, was significantly greater in

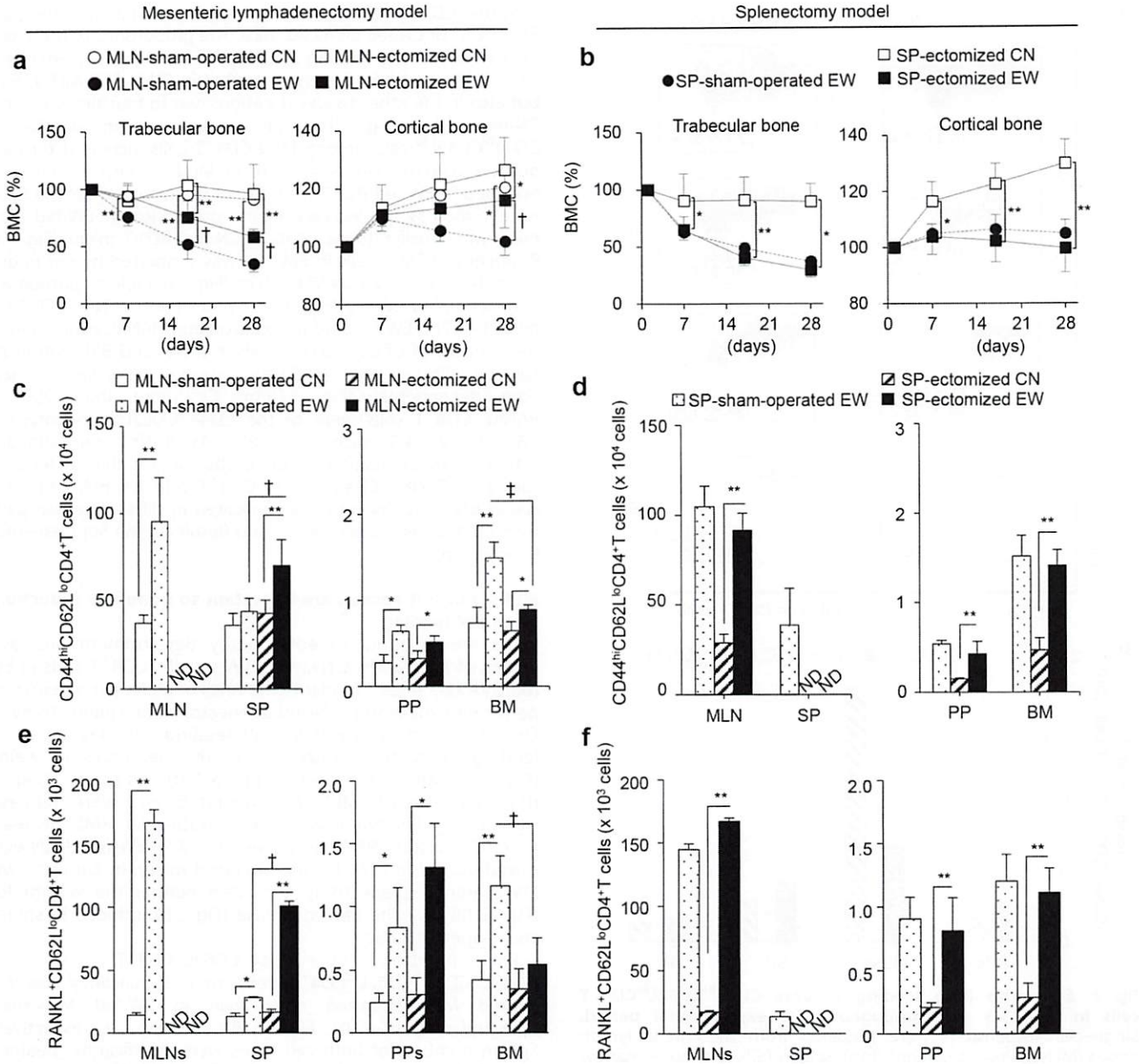

Fig. 3 Mesenteric lymph nodes (MLNs), but not the spleen (SP), play an important role in the bone loss induced by egg-white (EW)-fed OVA23-3 mice. Mesenteric lymphadenectomized (MLN-ectomized), MLN-sham-operated, splenectomized (SP-ectomized), and SP-sham-operated OVA23-3 mice were fed a control (CN) or EW diet for 28 days. Panels show time courses of bone mineral content (BMC) relative to initial values (100%) in trabecular (left) and cortical bone (right) after **a** mesenteric lymphadenectomy or **b** splenectomy. The numbers of $CD44^{hi}CD62L^{lo}CD4^{+}$T cells from different tissues (MLNs, Peyer's patches [PPs], spleen, and bone marrow [BM]) are shown after **c** mesenteric lymphadenectomy or **d** splenectomy. The numbers of $RANKL^{+}CD62L^{lo}CD4^{+}$T cells from different tissues are shown after **e** mesenteric lymphadenectomy or **f** splenectomy. MLN-sham-operated CN, CN-fed MLN-sham-operated OVA23-3 mice; MLN-sham-operated EW or SP-sham-operated EW, EW-fed MLN- or SP-sham-operated OVA23-3 mice; MLN-ectomized CN or SP-ectomized CN, CN-fed MLN- or SP-ectomized OVA23-3 mice; MLN-ectomized EW or SP-ectomized EW, EW-fed MLN- or SP-ectomized OVA23-3 mice; $n = 3$ to 5 in each group. Data are representative of two independent experiments. ND = not detected. $^{*}P < 0.05$ and $^{**}P < 0.01$ (EW vs. CN); $^{\dagger}P < 0.05$ and $^{\ddagger}P < 0.01$ (MLN-ectomized vs. MLN-sham-operated).

the presence of $RANKL^{+}$ or $RANKL^{-}CD44^{hi}CD62L^{lo}CD4^{+}$T cells isolated from EW-fed OVA23-3 mice than in the presence of these cells isolated from CN-fed OVA23-3 mice ($P < 0.01$, Fig. 4b, c). In contrast, $RANKL^{-}CD44^{int}CD62L^{lo}CD4^{+}$T cells from either CN- or EW-fed OVA23-3 mice suppressed bone-damage-promoting ability via osteoclasts (Fig. 4b, c). Notably, in this culture, stimulating preosteoclasts with $CD44^{hi}CD62L^{lo}CD4^{+}$T cells without adding soluble RANKL did not induce the in vitro differentiation of tartrate-resistant acid phosphatase-positive ($TRAP^{+}$) multinucleated cells (i.e., there were no osteoclasts) (Fig. S11). These results indicated that (1) MLN $CD44^{hi}CD62L^{lo}CD4^{+}$T cells activated by EW feeding promoted bone damage, which was independent of T-cell-surface RANKL expression; and (2) $CD44^{hi}CD62L^{lo}CD4^{+}$T cells, but not naive $CD4^{+}$T cells or $CD44^{int}CD62L^{lo}CD4^{+}$T cells (which suppress bone damage), in MLNs induced bone damage in EW-fed OVA23-3 mice.

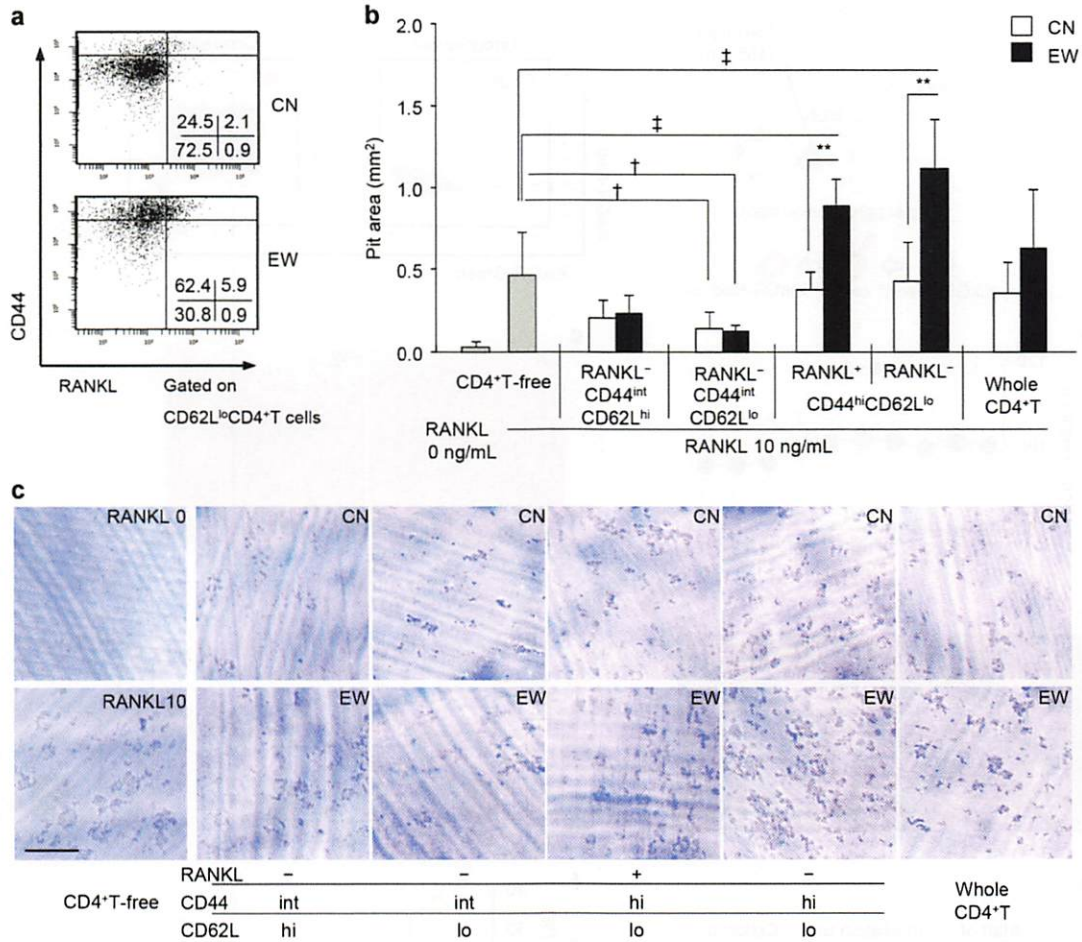

Fig. 4 CD44^{hi}CD62L^{lo}CD4^{+}T cells promote bone damage independently of receptor activator of nuclear factor kappa-B ligand (RANKL) expression. The bone-resorption effects of each CD4^{+}T-cell subset purified from mesenteric lymph nodes (MLNs) of OVA23-3 mice after 28 days' feeding of control (CN) or egg-white (EW) diet were assessed by pit-formation activity. **a** Plots represent CD44 vs. RANKL gated on MLN CD62L^{lo}CD4^{+}T cells separated by using a BD FACS Aria II Cell Sorter. Each number in the panel indicates the number of cells in the corresponding quadrant as a percentage of all CD62L^{lo}CD4^{+}T cells. **b** White columns indicate cells derived from control diet (CN)-fed OVA23-3 mice, black columns represent cells derived from EW-fed OVA23-3 mice, and gray columns indicate CD4^{+}T-cell-free solution; the treatment was soluble RANKL (RANKL, 0 or 10 ng/mL), $n = 3$ to 10 for each column. $^{**}P < 0.01$ (EW vs. CN); $^{\dagger}P < 0.05$ and $^{\ddagger}P < 0.01$ (CD4^{+}T-cell subsets vs. CD4^{+}T cell-free, treated with 10 ng/mL RANKL). **c** Stereo-microscopic images of representative resorption pits. Resorption pits appear as darkly stained areas. + or −, positive or negative expression of RANKL molecule on CD4^{+}T-cell surface. Scale bar = 500 μm.

MLN CD44^{hi}CD62L^{lo}CD4^{+}T cells migrate preferentially to the BM

To examine whether OVA-activated MLN CD4^{+}T cells directly migrated to BM, we generated K23-3 mice from a cross between Kikume Green-Red (KikGR) mice[20] and OVA23-3 mice. Using KikGR mice allowed us to pinpoint the original tissue (i.e., MLN) of cells migrating to BM more precisely than with standard techniques such as adoptive transfer of carboxyfluorescein-succinimidyl-ester-labeled cells. Violet-light exposure of MLNs revealed that over 80% of all MLN cells photoconverted from green to red (Fig. 5a). After 10 days of EW feeding, K23-3 mice, like EW-fed OVA23-3 mice, exhibited enteropathy with weight loss (Fig. 5b, c) and bone loss (Fig. 5d). To analyze the influence of EW feeding on cell migration, MLNs of EW-fed K23-3 mice were exposed to violet light on day 9 (Fig. 5e). We then euthanized the mice and quantified the CD44^{hi}CD62L^{lo} cells as a percentage of the total number of KikGR-red CD4^{+}T cells in each tissue on day 10 (Fig. S12). In CN-fed K23-3 mice, MLN CD4^{+}T cells migrated to BM (3–6% of KikGR-red CD4^{+}T cells); migration was increased significantly by EW feeding (25–33% of KikGR-red CD4^{+}T cells; $P < 0.01$, Figs. 5f and S12). Interestingly, the percentage of KikGR-red-converted CD44^{hi}CD62L^{lo}CD4^{+}T cells in EW-fed K23-3 mice was greater in BM than in MLNs, spleen, and skin-draining lymph nodes (sDLNs) (Fig. 5f). In MLNs, no difference was observed between EW- and CN-fed K23-3 mice in CD44^{hi}CD62L^{lo}CD4^{+}T cells as a percentage of the total number of KikGR-red CD4^{+}T cells (Fig. 5f) or in RANKL^{+}cells as a percentage of the total number of KikGR-red CD44^{hi}CD62L^{lo}CD4^{+}T cells (Fig. S9E), indicating that CD44^{hi}CD62L^{lo}CD4^{+}T cells tended to stay in MLNs during inflammation, probably to respond to invasion by allergens. Therefore, although CD44^{hi}CD62L^{lo}CD4^{+}T cells can migrate easily to BM, even with control feeding, the enteropathy induced by EW feeding promotes migration of these cells from MLNs to BM once they leave the MLNs and enter the circulation.

IL-4 predominates in both intestine and bone of EW-fed OVA23-3 mice

In studies analyzing cytokine mRNA expression, we concluded that IL-4 and IL-1β,—but not IL-6 and TNF-α—were representative cytokines produced by whole cells from each lymphoid organ in our model (Fig. S13). IL-17 was analyzed because exFoxpTh17 cells were reported to induce bone loss[21–24]. On day 9 of severe inflammation from EW feeding, intestinal IL-4 mRNA expression was significantly greater in EW-fed OVA23-3 mice than in CN-fed mice; in the bone, levels of both IL-1β and IL-4 were significantly

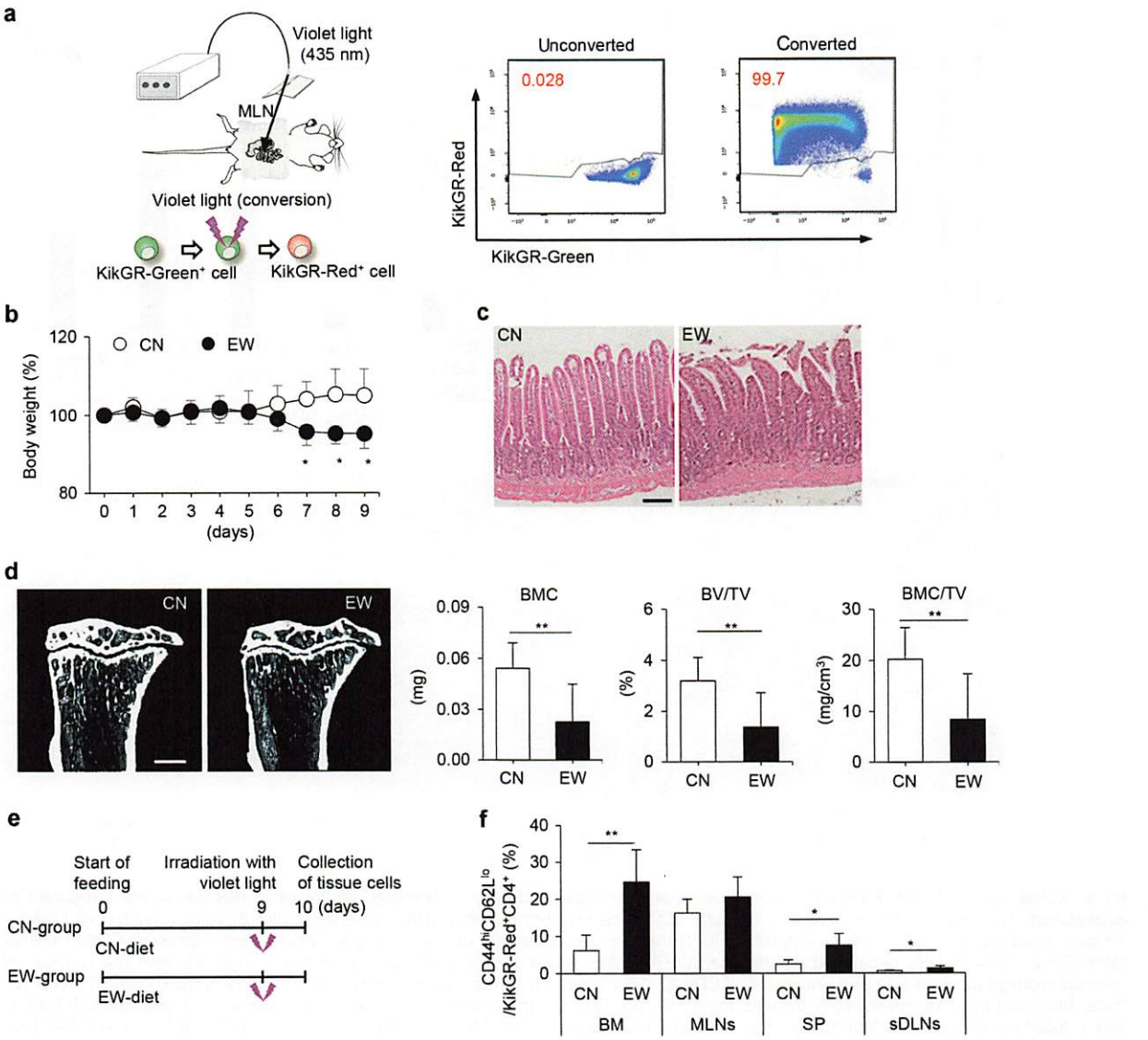

Fig. 5 Egg-white (EW) feeding promotes weight loss, intestinal changes, bone loss, and migration of CD44^{hi}CD62L^{lo}CD4^{+}T cells from mesenteric lymph nodes (MLNs) to bone marrow (BM) in K23-3 mice. a Photoconversion method by irradiation of MLNs with violet light (left). Representative plots (right) of KikGR-green and -red MLN cells of K23-3 mice. The number in each plot indicates KikGR-red cells as a percentage of the total MLN cells. **b** Time course of body-weight relative to initial weight (100%). Initial body-weight of CN-fed K23-3 mice was 28.06 ± 3.42 g and that of EW-fed K23-3 mice was 28.47 ± 1.82 g. **c** Hematoxylin and eosin-stained paraffin-embedded small intestinal tissues (4 μm thick). Scale bar = 100 μm. **d** Right tibia scanned by micro-computed tomography (left). Scale bar = 1 mm. Trabecular bone mineral content (BMC), bone volume per tissue volume (BV/TV), and bone mineral content per tissue volume (BMC/TV) of the tibia (right). **e** Protocol of EW feeding and irradiation of MLNs with violet light. **f** CD44^{hi}CD62L^{lo}CD4^{+}T cells as a percentage of the total KikGR-red-positive CD4^{+}T cells from bone marrow (BM), MLNs, spleen (SP), and skin-draining lymph nodes (sDLNs) of K23-3 mice. Values are expressed as means ± SD. CN-fed K23-3 mice, $n = 4$ to 6; EW-fed K23-3 mice, $n = 6$ to 9. Results are representative of two independent experiments. *$P < 0.05$ and **$P < 0.01$ (EW vs. CN).

greater in EW-fed OVA23-3 mice (Fig. 6a). IL-17 expression was detected in bone even in CN-fed OVA23-3 mice, but it was decreased significantly by EW feeding (Fig. 6a). On day 9 of severe inflammation in EW-fed OVA23-3 mice, the cytokine expression patterns in MLN CD4^{+}T cells and MLNs, spleen, and BM whole cells were similar to those in intestine or bone (Fig. 6b). After EW feeding, expression levels of IL-4—but not IL-5 and IL-13 (other Th2 cytokines of allergic responses)—significantly increased and IL-1β predominated in BM cells, but IL-17 mRNA expression levels were similar to those in the CN groups, with the exception of a significant decrease in expression in MLN CD4^{+}T cells (Fig. 6b). Significantly higher IL-4 mRNA expression levels were observed in KikGR-red cells sorted from BM of K23-3 mice fed EW for 9 days than in those from CN-fed mice. In contrast, levels of CXCR4 mRNA were significantly lower in the EW-fed mice (Fig. S14), suggesting that MLN cells migrated, probably in response to CXCL12 (a ligand for CXCR4) produced in BM, and together with resident BM cells produced IL-4[25,26].

In activated MLN CD44^{hi}CD62L^{lo}CD4^{+}T cells and other MLN CD4^{+}T-cell subsets of OVA23-3 mice on day 28 of EW feeding, when severe bone loss was observed, although there were insufficient RANKL^{+}CD44^{hi}CD62L^{lo}CD4^{+}T cells from CN-fed OVA23-3 mice for analysis [shown as "not detected (ND)" (Fig. 7a)], high IL-4 mRNA expression levels in RANKL^{+}CD44^{hi}CD62L^{lo}CD4^{+}T cells and whole CD4^{+}T cells were detected in EW-fed OVA23-3 mice. However, IL-17 and IL-1β mRNA expression levels were not greater than those in

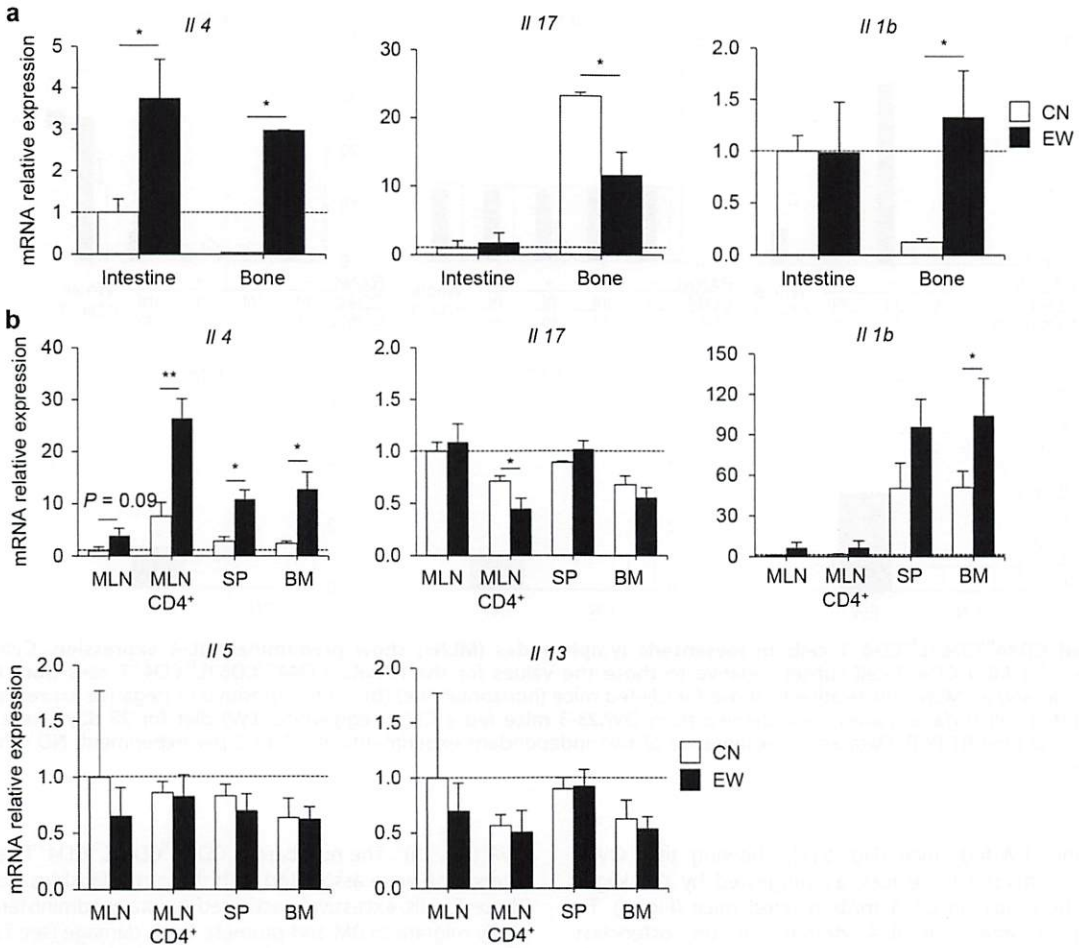

Fig. 6 Analysis of cytokine mRNA expression patterns in egg-white (EW)-fed OVA23-3 mice shows predominant IL-4 and IL-1β production. OVA23-3 mice were fed a control (CN) or EW diet for 9 days. Organs or tissues (intestine or bone) and lymphocytes (from mesenteric lymph nodes [MLNs], spleen [SP], or bone marrow [BM], or MLN $CD4^+$T cells) were examined for cytokine mRNA expression at the end of EW feeding (day 9). Cytokine mRNA expression levels were determined by Quantitative real-time RT-PCR and are shown relative to the values in the intestine or MLN cells of CN-fed mice (horizontal line) for **a** intestine and bone, and **b** MLNs and MLN $CD4^+$T, SP, and BM cells. (open square (□)) CN-fed group, $n = 3$; (closed square (■)) EW-fed group, $n = 3$. Data are representative of two independent experiments. $^*P < 0.05$ and $^{**}P < 0.01$ (EW vs. CN).

CN-fed OVA23-3 mice (Fig. 7a). In MLN cells of OVA23-3 mice on day 28 of EW feeding, the expression level of IL-4—but not IL-1β and IL-17—mRNA was also significantly enhanced (Fig. 7b). Thus, activated IL-4-producing MLN $CD44^{hi}CD62L^{lo}CD4^+$T cells may help create IL-4 dominance, as suggested by the increased numbers of multinucleated inflammatory cells (neutrophils and eosinophils) in BM (Fig. S15).

Primary, but not chronic-phase, IL-4 production is critical for inducing bone loss in food-allergic enteropathy

F1 R23-3/BALB mice were injected intravenously with anti-IL-4 monoclonal antibody (αIL-4 mAb) before diet feeding and on day 7 (Fig. 8a). Weight loss (Fig. 8b), enteropathy (Fig. 8c), and bone loss (Fig. 8d) were relieved by αIL-4 mAb injection. Bone parameters (BMC, BV/TV, and BMC/TV) had recovered significantly in EW-fed αIL-4 mAb-injected mice by 9 days ($P < 0.05$, Fig. 8e). Mice injected with αIL-4 mAb on days 10, 17, and 24 of EW feeding (Fig. 8g) had earlier weight loss recovery and less enteropathy than control Ab-injected EW-fed mice (Fig. 8h, i). However, bone loss was only slightly inhibited by αIL-4 mAb treatment (Fig. 8j), and at 28 days BV/TV, and BMC/TV were still significantly lower than in the controls ($P < 0.01$, CN-fed vs EW-fed control Ab-injected; $P < 0.05$, CN-fed vs EW-fed αIL-4 mAb-injected; Fig. 8k). Serum IL-4 levels did not differ among the three experimental groups (Fig. 8f, l), indicating that the effects of IL-4 occurred not systemically but locally. Thus, the bone loss observed in EW-fed OVA23-3 mice was triggered by activation of, and IL-4 production by, MLN $CD4^+$T cells and occurred IL-4 dependently in the primary phase of inflammation (until day 9 of EW feeding), whereas in the chronic phase the contribution of IL-4 dominance to bone-loss induction was lower.

To examine IL-4 production by $CD4^+$T cells and the effect of IL-4 dominance on bone loss, we first performed intracellular IL-4 staining of BM cells. $CD4^+$T cells of EW-fed R23-3/BALB mice secreted IL-4 in BM at similar levels on days 9 and 28 (Fig. S16). These results suggested that $CD44^{hi}CD62L^{lo}CD4^+$T cells (accounting for more than 60% of BM $CD4^+$T cells) produced IL-4 (Figs. 2a and S12). However, unlike in MLNs, in the BM other lymphoid cells produced more IL-4 than did $CD4^+$T cells (Fig. S16). To confirm the bone-loss-inducing roles of activated T cells, we injected RE2 mAb, which causes the death of activated T cells (resting T cells are insensitive)[27], into EW-fed R23-3 mice on days 0, 3, 6, and 9. Parameters (BV/TV, BMC, BMC/TV) of bone metabolism were significantly higher in RE2-mAb-injected EW-fed mice than in

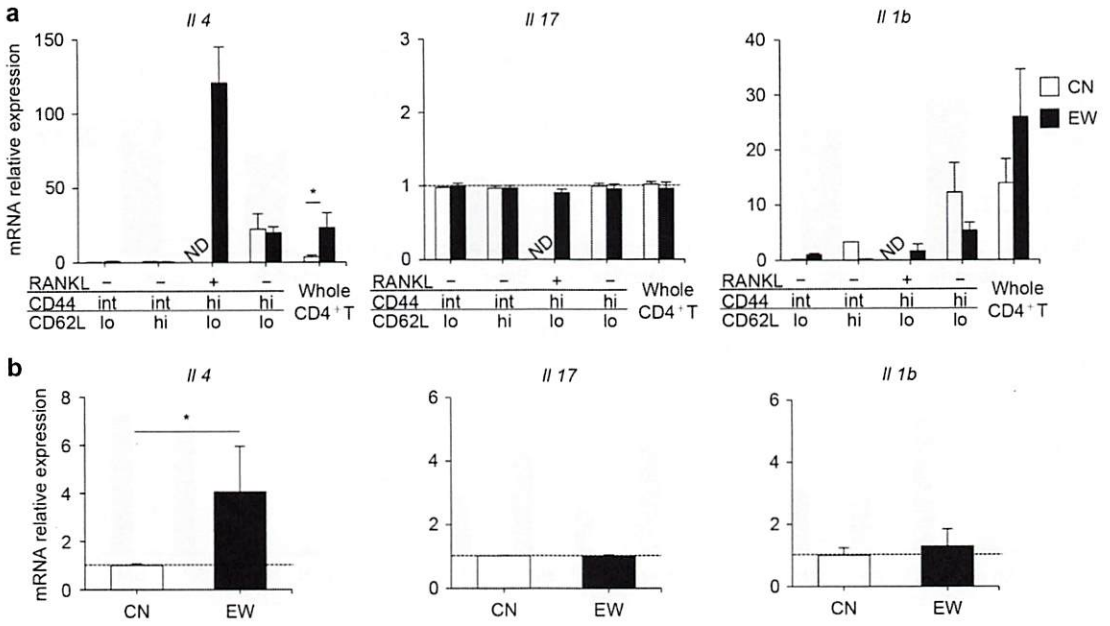

Fig. 7 Activated CD44^{hi}CD62L^{lo}CD4^{+}T cells in mesenteric lymph nodes (MLNs) show predominant IL-4 expression. Cytokine mRNA expression levels for MLN CD4^{+}T-cell subsets relative to those the values for the RANKL^{-}CD44^{int}CD62L^{hi}CD4^{+}T cells from CN-fed mice (horizontal line) (**a**) and all MLN cells relative to those for CN-fed mice (horizontal line) (**b**). + or −, positive or negative expression of RANKL molecule on CD4^{+}T-cell surface. Values were derived from OVA23-3 mice fed a CN or egg-white (EW) diet for 28 days were determined by Quantitative real-time RT-PCR. Data are representative of two independent experiments; $n = 2$ to 5 per experiment. ND = not detected. *$P < 0.05$ (EW vs. CN).

untreated (saline) EW-fed mice (Fig. S17), showing that OVA-activated T cells affected bone loss, as suggested by the slight recovery from bone loss in αIL-4 mAb-injected mice (Fig. 8). To clarify the direct effect of IL-4 dominance on osteoclast differentiation, we confirmed that IL-4 was below the ELISA detection limit in the supernatant of in vitro co-culture of preosteoclasts and CD4^{+}T cells (data not shown). We then found that adding IL-4 in in vitro culture inhibited osteoclast differentiation, although TRAP^{+}cells were observed in the same in vitro conditions upon co-culture of preosteoclasts and IL-1β in addition to IL-4 (Fig. S18). Thus, in this model, IL-4-producing aberrant activated CD4^{+}T cells from MLNs can migrate to BM and trigger osteoclast differentiation, helping to create the IL-4-induced inflammatory milieu[25].

DISCUSSION

We analyzed the immunological mechanism of bone loss after food-allergic enteropathy development in OVA23-3 mice. We found a specific relationship between MLNs and bone via IL-4 dominance created by OVA-specific Th2 cells in this comorbidity triggered by food-allergen intake. We can describe our model's mechanism of bone loss from two perspectives: the role of the immune responses in MLNs and the role of excessive IL-4 production in the lymphoid organs.

Comparison of the results obtained after mesenteric lymphadenectomy and after splenectomy (see Fig. 3), and analysis of cell migration from MLNs to BM (see Figs. 5 and S12), revealed a specific relationship between MLNs and bone. These results showed that MLNs, which orchestrate severe enteropathy as a central inflammatory lesion[5], were directly and IL-4-dependently connected with bone inflammatory responses, at least during the primary phase (until day 9, see Fig. 8). However, the spleen's immune responses differed from those in MLNs and BM, although these lymphoid organs were equally triggered by specific T-cell responses against OVA (Fig. 2a)[5]. The numbers of CD44^{hi}CD62L^{lo}CD4^{+}T cells as an EM phenotype were associated with these relationships (see Fig. 3c, e). These T cells, excessively activated by orally administered OVA, can easily migrate to BM and promote bone damage (see Figs. 4 and 5). However, in the chronic phase, in which there was recovery from severe enteropathy and weight loss in this model (Fig. 8h)[3,6], bone loss continued with only slight regulation by IL-4 (Fig. 8j, k, as shown by the lack of significant difference between αIL-4 mAb-treated and untreated EW-fed R23-3/BALB mice at day 28), contrary to the enteropathy and with the induction of forkhead box p3 (Foxp3)$^{+}$T cells in both the MLNs and spleen[6]. This suggests that the relationship among the lymphoid organs (MLNs, spleen, and BM) may change in the chronic phase (see Fig. S13). The intestinal state termed a "leaky gut,"[28,29] in which gut mucosal permeability increases, leading to the development of certain diseases (i.e., IBD), may promote bone loss continuation via immune responses as a specific gut–bone axis relationship in the chronic phase.

A previous study showed that almost 90% of Foxp3^{+}T cells in MLNs in 28-day EW-fed R23-3 mice express the CD44^{hi}CD62L^{lo} molecule[6]. Recent studies of T-cell roles[30] show that Foxp3^{+}Treg cells are important contributors to osteoclastogenesis inhibition via cytokines or CTLA-4 (cytotoxic T-lymphocyte-associated protein 4)[31], and intestinal bacterial metabolites induce Foxp3^{+}Treg cells and contribute to bone health in the gut–bone axis[32]. However, we found that MLN CD44^{hi}CD62L^{lo}CD4^{+}T cells have an inflammatory EM phenotype and induce osteoclastogenesis, despite long-term EW-feeding-induced dampening of the inflammatory response. Therefore, in our model, MLN EM T cells may change their characteristics (i.e., lose their Foxp3 expression and gain inflammatory ability) after migrating to BM, as suggested by the roles of exFoxpTh17 transdifferentiated into Th17[21,22]. In light of the strong IL-4-production abilities of EM T cells activated in MLNs in enteropathy, we found that these cells were involved in triggering and maintaining bone loss via unknown molecules or mediators (see Fig. S11) by creating IL-4 dominance in BM (Figs. S15 and S16)

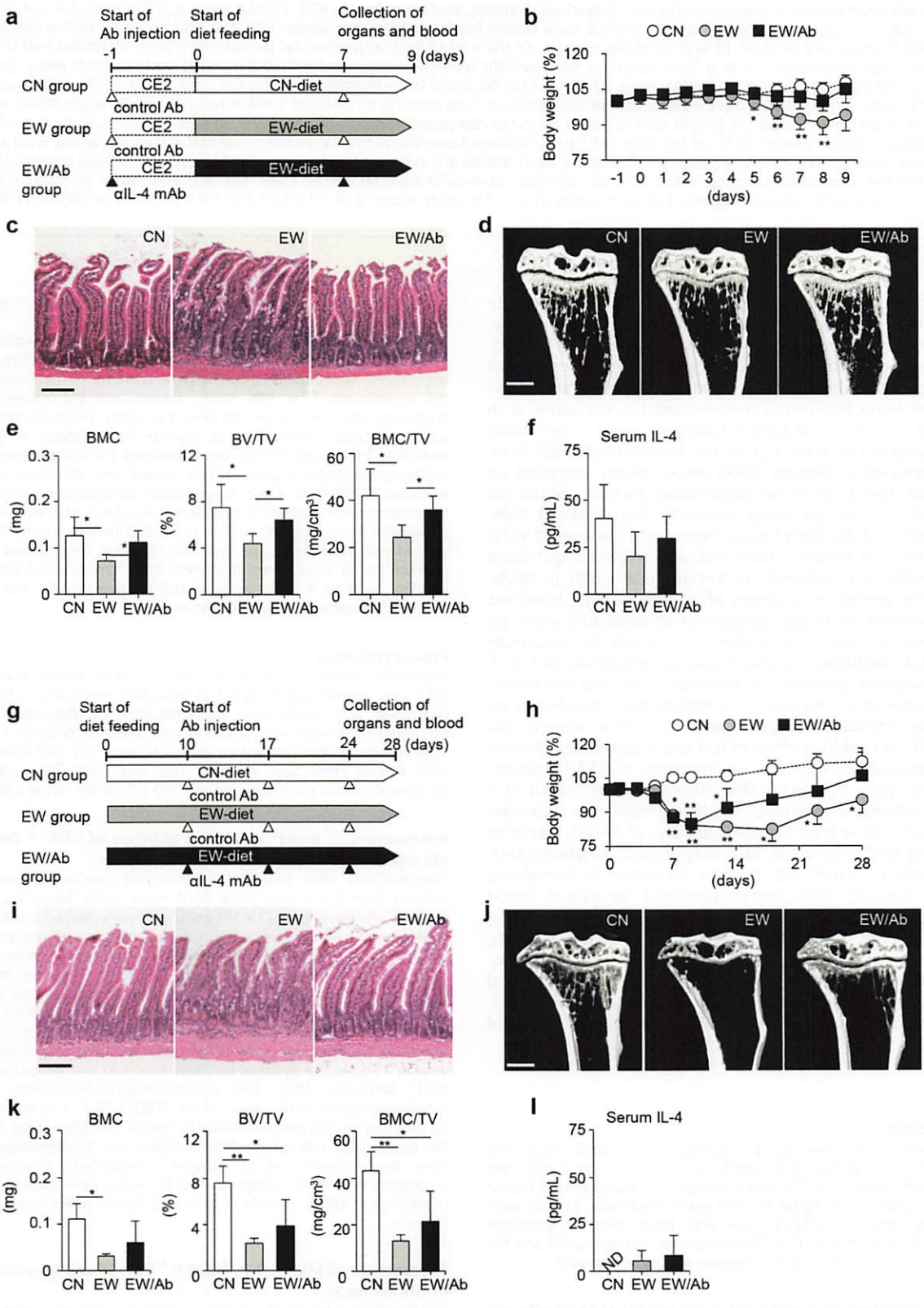

although they may merely migrate into BM as memory cells to enhance protection against continuous invasion by OVA[25].

Our findings suggested that excessive IL-4 production, inducing bone loss, occurred not via changes in serum IL-4 levels (see Fig. 8f, l), but locally and through the migration of IL-4-producing cells from MLNs to bone (Fig. S14) or through IL-4 production by resident BM cells (lymphocytes other than $CD4^+$cells, Figs. 6b and S16). Several reports have demonstrated the roles of IL-4 in bone

Fig. 8 Neutralization of IL-4 prevents weight loss, intestinal changes, and bone loss in R23-3/BALB mice. a, g Protocols for injection of anti-IL-4 monoclonal antibody (αIL-4 mAb) into R23-3/BALB mice before feeding of the egg-white (EW) diet and on day 7 of the diet (**a**) or after 10 days of EW feeding and on days 17 and 24 of the diet (**g**). At the end of each experimental period, mice were dissected and their tissues and serum samples were collected. **b, h** Time course of body-weight relative to initial weight (100%). Initial body weights were: for CN mice, 27.50 ± 1.55 g; EW mice, 27.73 ± 0.71 g; EW/Ab mice, 27.73 ± 1.11 g (**b**). Initial body weights were: for CN mice, 27.23 ± 1.79 g; EW mice, 27.43 ± 1.52 g; EW/Ab mice, 27.48 ± 0.44 g (**h**). **c, i** Hematoxylin-and-eosin-stained paraffin-embedded small intestinal tissues (4 μm thick) at day 9 (**c**) and day 28 (**i**). Scale bar = 100 μm. **d, j** Right tibia scanned by micro-computed tomography at day 9 (**d**) and day 28 (**j**). Scale bar = 1 mm. **e, k** Trabecular bone mineral content (BMC) of the tibia (left), bone volume/bone tissue (BV/TV, center), and BMC/TV (right) at day 9 (**e**) and day 28 (**k**). **f, l** Serum IL-4 levels were measured at day 9 (**f**) and day 28 (**l**). Values are expressed as means ± SD. CN, control-diet-fed control-Ab-injected mice; EW, EW-fed control-Ab-injected mice; EW/Ab, EW-fed αIL-4-mAb-injected mice. Data are representative of two independent experiments; $n = 6$ in each group (**a–e**), $n = 3$ in each group (**f**), $n = 4$ in each group (**g–l**). $^{*}P < 0.05$ and $^{**}P < 0.01$ (CN or EW/Ab vs. EW). ND = not detected.

loss in arthritis mouse models[33–35] or *lck*-IL-4 transgenic mice[10]; IL-4-deficient mice are less prone to the induction of autoantibody-mediated pathogenesis in arthritis, or to continuous IL-4 production in the osteoporosis that develops with decreased osteoblast activity in *lck*-IL-4 transgenic mice. Although the importance of IL-4-dependent bone loss in our mouse model is the same as in other arthritic mice[33–35] or *lck*-IL-4 transgenic mice[10], our model has some unique characteristics. In our system of non-IgE food-allergic enteropathy, allergen (OVA) intake clearly triggered an inflammation chain by internally penetrating the body via the gut mucosa and PPs and activating aberrantly Th2-dominant OVA-specific T cells in MLNs. Therefore, unexpectedly, the roles of MLNs were prominent in inducing bone loss, and a specific gut–bone axis relationship was induced via IL-4-producing cells in MLNs. However, the precise mechanism of IL-4-dependent bone-loss induction remains unclarified because of contradictory views on IL-4 function in bone metabolism[36–38]. IL-4/IL-13 reportedly promotes IL-6 production by osteoblasts synergistically with IL-1, a pro-inflammatory cytokine that promotes osteoclast differentiation[39] and bone loss[38]. However, IL-4 inhibits osteoclast formation by targeting osteoblasts or osteoclasts[30,40,41]. Our analysis also showed both an inhibitory effect of IL-4 and a promoting effect of IL-1β in combination with IL-4 on induction of $TRAP^{+}$multinucleated cells (see Fig. S18). The mechanism by which IL-4 production influences bone loss, including in relation to molecules or components other than specific cytokines or RANKL, needs to be examined further in detail. In non-IgE-mediated gastrointestinal food allergy, which has recently increased in prevalence worldwide, patients' milk-protein-stimulated peripheral blood mononuclear cells show a predominant Th2-skewing phenotype, as in our model[42]. In gastrointestinal food-allergy patients, excessive intestinal T-cell activation may influence bone metabolism. Our study provides new insights into the roles of activated lymphocytes in intestinal lymphoid tissues and other extraintestinal lymphoid organs—notably BM—in response to food allergens.

METHODS

Mice and diets

OVA23-3 mice were generated by isolation of genomic fragments encoding TCR-α and -β from OVA-specific I-A^{d} restricted $CD4^{+}$T cell clone 7-3-7[43]. Offspring with an H-2^{d} genetic background was produced from a mouse carrying transgenes by back-crossing with BALB mice. F1 mice were generated by crossing OVA23-3 mice with BALB mice, to attenuate allergen-specific responses to OVA. The other mice and diets used, and the ethical animal care, are described in Supplementary Information.

OVA administration to a different mice model of food-allergic enteropathy

Six- to 12-week-old mice (OVA23-3, R23-3, RD10, SR23-3, K23-3, R23-3/BALB, and BALB/ALUM) were fed experimental diets (CN or EW). R23-3/BALB mice were used for αIL-4 mAb treatment. R23-3 mice were used to purify OVA-specific $CD4^{+}$T cells and for RE2 mAb (rat anti-mouse pan-MHC class I mAb, provided by S. Matsuoka, Juntendo University)[27] treatment. For details of the establishment of the other experimental systems see Supplementary Information.

At the end of the experimental period, mice were euthanized by cervical dislocation and dissected to collect serum, bone, jejunum, lymphoid organs (PPs, MLNs, spleen, and sDLNs), and BM for further analysis. Single-cell suspensions from PPs, MLNs, spleen, and BM whole cells were prepared, and cells were purified by using magnetic-activated cell sorting[3,4]. Serum biomarkers to indicate health status of mice were analyzed. Tibias and femurs were analyzed by using micro-computed tomography (RmCT, Rigaku, Tokyo, Japan) and 3D bone morphology software (TRI/3D-BON; Ratoc, Tokyo, Japan) as described previously[44]. For bone histological analysis, the left femur was fixed with 70% ethanol and embedded in methylmethacrylate resin, and tissue sections (5 μm) were stained with Villanueva bone stain. For histology, longitudinal sections of jejunum (3 cm) were taken, fixed with 10% formalin, and embedded in paraffin. Sections 4 μm thick were stained hematoxylin and eosin. For details see Supplementary Information.

Flow cytometry

Single-cell suspensions prepared from PPs, MLNs, spleen, and BM whole cells were stained and analyzed as described previously[4–6]. Staining was performed with mAbs (see Supplementary Information). Cell-surface-expressed molecules were analyzed with a BD FACS Canto II and Verse flow cytometer (BD Biosciences, Franklin Lakes, NJ) and then evaluated with FlowJo (Tree Star, Ashland, OR) and FACS Diva software (BD Biosciences). Data were acquired at >100 counts for target cells.

Assessment of bone-damaging abilities of $CD4^{+}$T-cell subsets via osteoclasts

Preosteoclasts were prepared as described previously from BM cells isolated from 8-week-old male BALB mice (CLEA Japan Inc., Shizuoka, Japan)[44]. Preosteoclasts (3×10^{4} cells/well) were placed on dentin slices (Wako Pure Chemical Corporation, Osaka, Japan) in a 96-well plate at 37 °C for 24 h. Purified MLN-$CD4^{+}$T-cell subsets (1×10^{5} cells/well) were added to each well in the presence of 10 ng/mL RANKL (R&D Systems Minneapolis, MN) and 25 ng/mL M-CSF (macrophage colony-stimulating factor, R&D Systems). On day 12 of incubation, the cells were washed away and resorption pits were stained with Meyer's hematoxylin (Wako Pure Chemicals Corporation). Pit area was calculated by using Photoshop CS4 version 11.0 (Adobe Systems Inc., San Jose, CA) and ImageJ version 1.42 (NIH, Bethesda, MD). The osteoclastogenesis-induction ability of membrane-bound RANKL from $CD44^{hi}CD62L^{lo}CD4^{+}$ T cells was assessed by using an in vitro method similar to the pit formation assay but without the dentin slice and soluble RANKL added (see Supplementary Information). Recombinant IL-4 (0, 10 ng/mL, PeproTech, Cranbury, NJ) or recombinant IL-1β (0, 10 ng/mL, R&D Systems), were added at the time of addition of RANKL and M-CSF to induce directly osteoclastogenesis from BM cells.

Assessment of MLN $CD44^{hi}CD62L^{lo}CD4^{+}$T cell migration to BM in KikGR mice

KikGR mice[20] systemically express KikGR fluorescent protein, which is photoconverted from green to red when irradiated with violet light. Seven- to 10-week-old male K23-3 mice were prepared by crossing OVA23-3 and KikGR mice and fed a CN or EW diet for 9 days. Their MLNs were exposed surgically and irradiated with violet light (3 min per each of three sections of each MLN, 435-nm LED; Prizmatix, Holon, Israel) under isoflurane-induced anesthesia (Pfizer, New York, NY). On day 10, the mice were

dissected to collect the right tibia, small intestine, lymphoid organs (PPs, MLNs, spleen, and sDLNs), and BM for further analysis.

Quantitative real-time RT-PCR measurement of cytokine mRNA expression

Measurements of mRNA expression are described in Supplementary Information.

Inhibition of IL-4 or $CD4^+$T cells in EW-fed R23-3/BALB or R23-3 mice

R23-3/BALB mice were given αIL-4 mAb (1 mg per injection; clone 11B11, Bio X Cell, West Lebanon, NH) intravenously every 7 days (the first injection was one day before the start or on day 10). As a control, InVivoMAb Polyclonal Mouse IgG (1 mg/injection, Bio X Cell) was used. Body weights were measured every day. RE2 mAb was injected intraperitoneally into R23-3 mice fed an EW diet. At the end of the experiment, serum and tissues were taken for further analysis. (see Supplementary Information). Jejunal sections (for intestinal histology; hematoxylin and eosin-stained)[3], and bones (for micro-computed tomography analysis and flow cytometry) were taken for further analysis.

Intracellular IL-4 staining

BM cells were prepared from R23-3/BALB mice fed a CN or EW diet for 9 or 28 days. BM cells were resuspended at 2.5×10^6 cells/2 mL in complete RPMI 1640 with 10% fetal calf serum and stimulated with the activation regents ionomycin (2 μg/mL, Sigma-Aldrich, St. Louis, MO), phorbitol myristate acetate (10 ng/mL, Sigma-Aldrich), and brefeldin A (40 μg/mL, Sigma-Aldrich) in 48-well flat-bottomed plates (Falcon, New York, NY) at 37 °C for 4 h. After blocking with anti-CD16/CD32 mAb (BioLegend, San Diego, CA), the cells were stained with APC- or FITC-anti-mouse CD4 mAb (GK1.5, Biolegend) and Fixable Viability Dye eFluor 780 (FVD-eFlour780; eBioscience, Waltham, MA). Intracellular IL-4 was stained with PE- anti-mouse IL-4 mAb (11B11, BioLegend) by using a Flow Cytometry Fixation and Permeabilization Buffer Kit I (R&D Systems) and analyzed with BD FACSVerse (BD Biosciences).

Statistical analysis

For details of the statistical analysis see Supplementary Information.

REFERENCES

1. Amarasekara, D. S., Yu, J. & Rho, J. Bone loss triggered by the cytokine network in inflammatory autoimmune diseases. *J. Immunol. Res.* **2015**, 832127 (2015).
2. Ashcroft, A. J. et al. Colonic dendritic cells, intestinal inflammation, and T cell-mediated bone destruction are modulated by recombinant osteoprotegerin. *Immunity* **19**, 849–861 (2003).
3. Nakajima-Adachi, H. et al. Food antigen causes TH2-dependent enteropathy followed by tissue repair in T-cell receptor transgenic mice. *J. Allergy Clin. Immunol.* **117**, 1125–1132 (2006).
4. Ono-Ohmachi, A., Nakajima-Adachi, H., Morita, Y., Kato, K. & Hachimura, S. Milk basic protein supplementation exerts an anti-inflammatory effect in a food-allergic enteropathy model mouse. *J. Dairy Sci.* **101**, 1852–1863 (2017).
5. Nakajima-Adachi, H. et al. Peyer's patches and mesenteric lymph nodes cooperatively promote enteropathy in a mouse model of food allergy. *PLoS ONE* **9**, 2–11 (2014).
6. Nakajima-Adachi, H. et al. Critical role of intestinal interleukin-4 modulating regulatory T cells for desensitization, tolerance, and inflammation of food allergy. *PLoS ONE* **12**, 1–19 (2017).
7. Gatti, D. et al. Allergy and the bone: unexpected relationships. *Ann. Allergy Asthma Immunol.* **107**, 202–206 (2011).
8. Arima, K. et al. Burden of atopic dermatitis in Japanese adults: analysis of data from the 2013 National Health and Wellness Survey. *J. Dermatol.* **45**, 390–396 (2018).
9. Wu, C. Y. et al. Osteoporosis in adult patients with atopic dermatitis: a nationwide population-based study. *PLoS ONE* **12**, e0171667 (2017).
10. Lewis, D. B. et al. Osteoporosis induced in mice by overproduction of interleukin 4. *Proc. Natl Acad. Sci. USA* **90**, 11618–11622 (1993).
11. Burggraf, M. et al. Oral tolerance induction does not resolve gastrointestinal inflammation in a mouse model offoodallergy. *Mol. Nutr. Food Res.* **55**, 1475–1483 (2011).
12. Nakajima-Adachi, H. et al. Two distinct epitopes on the ovalbumin 323-339 peptide differentiating CD4+T cells into the Th2 or Th1 phenotype. *Biosci. Biotechnol. Biochem.* **76**, 1979–1981 (2012).
13. Kanai, T. et al. Naturally arising CD4+CD25+ regulatory T cells suppress the expansion of colitogenic CD4+CD44highCD62L−effector memory T cells. *Am. J. Physiol. Gastrointest. Liver Physiol.* **290**, G1051–1058 (2006).
14. Nemoto, Y. et al. Bone marrow retaining colitogenic CD4+ T cells may be a pathogenic reservoir for chronic colitis. *Gastroenterology* **132**, 176–189 (2007).
15. Nemoto, Y. et al. Long-lived colitogenic CD4+ memory T cells residing outside the intestine participate in the perpetuation of chronic colitis. *J. Immunol.* **183**, 5059–5068 (2009).
16. Rosa, F. D. & Santoni, A. Memory T-cell competition for bone marrow seeding. *Immunology* **108**, 296–304 (2003).
17. Rosa, F. D. & Pabst, R. The bone marrow: A nest for migratory memory T cells. *Trends Immunol.* **26**, 360–366 (2005).
18. Tokoyoda, K. et al. Professional memory CD4+ T lymphocytes preferentially reside and rest in the bone marrow. *Immunity* **30**, 721–730 (2009).
19. Kikuta, J. et al. Dynamic visualization of RANKL and Th17-mediated osteoclast function. *J. Clin. Invest.* **123**, 866–873 (2013).
20. Nakanishi, Y. et al. Regulatory T cells with superior immunosuppressive capacity emigrate from the inflamed colon to draining lymph nodes. *Mucosal Immunol.* **11**, 437–448 (2018).
21. Tsukasaki, M. et al. Host defense against oral microbiota by bone-damaging T cells. *Nat. Commun.* **9**, 701 (2018).
22. Komatsu, N. et al. Pathogenic conversion of Foxp3+ T cells into TH17 cells in autoimmune arthritis. *Nat. Med.* **20**, 62–68 (2013).
23. Sato, K. et al. Th17 functions as an osteoclastogenic helper T cell subset that links T cell activation and bone destruction. *J. Exp. Med.* **203**, 2673–2682 (2006).
24. Ciucci, T. et al. Bone marrow Th17 TNFα cells induce osteoclast differentiation, and link bone destruction to IBD. *Gut* **64**, 1072–1081 (2015).
25. Collins, N. et al. The bone marrow protects and optimizes immunological memory during dietary restriction. *Cell* **178**, 1088–1101 (2019).
26. Sugiyama, T., Omatsu, Y. & Nagasawa, T. Niches for hematopoietic stem cells and immune cell progenitors. *Int. Immunol.* **31**, 5–11 (2019).
27. Matsuoka, S. et al. A novel type of cell death of lymphocytes induced by a monoclonal antibody without participation of complement. *J. Exp. Med.* **181**, 2007–2015 (1995).
28. Schepper, J. D. et al. Probiotic *Lactobacillus reuteri* prevents postantibiotic bone loss by reducing intestinal dysbiosis and preventing barrier disruption. *J. Bone Miner. Res.* **34**, 681–698 (2019).
29. Mu, Q., Kirby, J., Reilly, C. M. & Luo, X. M. Leaky gut as a danger signal for autoimmune diseases. *Front. Immunol.* **8**, 598 (2017).
30. Srivastava, R. K., Dar, H. Y. & Mishra, P. K. Immunoporosis: Immunology of osteoporosis-role of T cells. *Front. Immunol.* **9**, 657 (2018).
31. Bozec, A. & Zaiss, M. M. T Regulatory cells in bone remodelling. *Curr. Osteoporos. Rep.* **15**, 121–125 (2017).
32. Zaiss, M. M., Jones, R. M., Schett, G. & Pacifici, R. The gut-bone axis: how bacterial metabolites bridge the distance. *J. Clin. Invest.* **129**, 3018–3028 (2019).
33. Svensson, L., Nandakumar, K. S., Johansson, Å., Jansson, L. & Holmdahl, R. IL-4-deficient mice develop less acute but more chronic relapsing collagen-induced arthritis. *Eur. J. Immunol.* **32**, 2944–2953 (2002).
34. Nandakumar, K. S. & Holmdahl, R. Arthritis induced with cartilage-specific antibodies is IL-4-dependent. *Eur. J. Immunol.* **36**, 1608–1618 (2006).
35. Ohmura, K., Nguyen, L. T., Locksley, R. M., Mathis, D. & Benoist, C. Interleukin-4 can be a key positive regulator of inflammatory arthritis. *Arthritis Rheum.* **52**, 1866–1875 (2005).
36. Yang, D. H. & Yang, M. Y. The role of macrophage in the pathogenesis of osteoporosis. *Int. J. Mol. Sci.* **20**, 2093 (2019).
37. Pereira, M. et al. Common signalling pathways in macrophage and osteoclast multinucleation. *J. Cell Sci.* **131**, jcs216267 (2018).
38. Silfverswärd, C. J., Frost, A., Brändström, H., Nilsson, O. & Ljunggren, Ö. Interleukin-4 and interleukin-13 potentiate interleukin-1 induced secretion of interleukin-6 in human osteoblast-like cells. *J. Orthop. Res.* **22**, 1058–1062 (2004).
39. Nakamura, I. & Nakamura, I. Regulation of osteoclast differentiation and function by interleukin-1. *Vitam. Horm.* **74**, 357–370 (2006).
40. Amarasekara, D. S. et al. Regulation of osteoclast differentiation by cytokine networks. *Immune Netw.* **18**, e8 (2018).
41. Yamada, A. et al. Interleukin-4 inhibition of osteoclast differentiation is stronger than that of interleukin-13 and they are equivalent for induction of production from osteoblasts. *Immunology* **120**, 573–579 (2007).
42. Morita, H. et al. Food protein-induced enterocolitis syndromes with and without bloody stool have distinct clinicopathologic features. *J. Allergy Clin. Immunol.* **140**, 1718–21 (2017).
43. Sato, T. et al. Naive T cells can mediate delayed-type hypersensitivity response in T cell receptor transgenic mice. *Eur. J. Immunol.* **24**, 1512–6 (1994).

44. Ono-Ohmachi, A., Ishida, Y., Morita, Y., Kato, K. & Nara, T. Y. Milk basic protein facilitates increased bone mass in growing mice. *J. Nutr. Sci. Vitaminol. (Tokyo)* **63**, 315–322 (2017).

ACKNOWLEDGEMENTS

We thank Erika Hiraide, Mamiko Morinaga, Tomiko Asakura, Takashi Matsuwaki, Yoshikazu Saito, Takuya Miyakawa, and Jun Kunisawa (the University of Tokyo); staff of the Institute of Medical Science and the FACS Core Laboratory at the University of Tokyo; Naoyuki Takahashi (Matsumoto Dental University); Ken Kato, Atsushi Serizawa, and Takayuki Nara (Megmilk Snow Brand Co., Ltd.); Toshimitsu Yoshioka and Takashi Fujita (Bean Stalk Snow Co., Ltd.); and Akemi Ito (Ito Bone Histomorphometry Institute) for their technical advice and support.

AUTHOR CONTRIBUTIONS

H.N.A. and A.O.O. provided substantial contributions to the conception of the work. M.T. provided KikGR mice. S.K. and Y.I. provided recombinant IL-1β and S.M. provided RE2 mAb and performed experiments. N.U., Y.N. and M.K. helped with the analysis of the bone. A.O.O., H.N.A., S.Y., S.U., M.T., K.S., S.N., Y.M., T.T., and T.I. performed the experiments and analyzed the data. H.N.A. and A.O.O. wrote the manuscripts. All authors discussed and interpreted the data.

COMPETING INTERESTS

This work was supported by grants from the Kieikai Research Foundation (H.N.A., 2017S063, 2018T019), a Grant-in-Aid for Scientific Research (C) (H.N.A., 18K05502) from the Japan Society for the promotion of science, a grant from The Food Science Institute Foundation (Ryoushoku-kenkyukai; H.N.A., No. 2019A01), and grants from Megmilk Snow Brand Co., Ltd. (H.N.A., H.K., and S.H.). The authors declare no conflict of interest associated with this manuscript.

ADDITIONAL INFORMATION

Supplementary information The online version contains supplementary material available at https://doi.org/10.1038/s41385-021-00434-2.

Correspondence and requests for materials should be addressed to H.N.-A.

Reprints and permission information is available at http://www.nature.com/reprints

Publisher's note Springer Nature remains neutral with regard to jurisdictional claims in published maps and institutional affiliations.

Itoh et al. *Cell Death and Disease* (2021)12:520
https://doi.org/10.1038/s41419-021-03787-5

Cell Death & Disease

ARTICLE Open Access

IL-26 mediates epidermal growth factor receptor-tyrosine kinase inhibitor resistance through endoplasmic reticulum stress signaling pathway in triple-negative breast cancer cells

Takumi Itoh[1,2], Ryo Hatano[1], Yoshiya Horimoto[3], Taketo Yamada[4,5], Dan Song[1], Haruna Otsuka[1], Yuki Shirakawa[1], Shuji Mastuoka[6], Noriaki Iwao[7], Thomas M. Aune[8], Nam H. Dang[9], Yutaro Kaneko[10], Ko Okumura[2], Chikao Morimoto[1] and Kei Ohnuma[1]

Abstract

Triple-negative breast cancer (TNBC) has a poor prognosis compared to other breast cancer subtypes. Although epidermal growth factor receptor (EGFR) is overexpressed in TNBC, clinical trials with EGFR inhibitors including tyrosine kinase inhibitors (EGFR-TKI) in TNBC have heretofore been unsuccessful. To develop effective EGFR-targeted therapy for TNBC, the precise mechanisms of EGFR-TKI resistance in TNBC need to be elucidated. In this study, to understand the molecular mechanisms involved in the differences in EGFR-TKI efficacy on TNBC between human and mouse, we focused on the effect of IL-26, which is absent in mice. In vitro analysis showed that IL-26 activated AKT and JNK signaling of bypass pathway of EGFR-TKI in both murine and human TNBC cells. We next investigated the mechanisms involved in IL-26-mediated EGFR-TKI resistance in TNBC. We identified EphA3 as a novel functional receptor for IL-26 in TNBC. IL-26 induced dephosphorylation and downmodulation of EphA3 in TNBC, which resulted in increased phosphorylation of AKT and JNK against EGFR-TKI-induced endoplasmic reticulum (ER) stress, leading to tumor growth. Meanwhile, the blockade of IL-26 overcame EGFR-TKI resistance in TNBC. Since the gene encoding IL-26 is absent in mice, we utilized human *IL-26* transgenic (hIL-26Tg) mice as a tumor-bearing murine model to characterize the role of IL-26 in the differential effect of EGFR-TKI in human and mice and to confirm our in vitro findings. Our findings indicate that IL-26 activates the bypass pathway of EGFR-TKI, while blockade of IL-26 overcomes EGFR-TKI resistance in TNBC via enhancement of ER stress signaling. Our work provides novel insights into the mechanisms of EGFR-TKI resistance in TNBC via interaction of IL-26 with its newly identified receptor EphA3, while also suggesting IL-26 as a possible therapeutic target in TNBC.

Introduction

Accounting for 15–20% of breast cancer, triple-negative breast cancer (TNBC) subtype lacks estrogen receptor, progesterone receptor (PgR), and human epidermal growth factor receptor 2 (HER2) expression and has a poor prognosis[1–4]. To date, no effective molecular target has been identified in TNBC[5]. Epidermal growth factor receptor (EGFR) signaling pathway is activated in various neoplasms, and EGFR-tyrosine kinase inhibitors (EGFR-TKIs) are used

Correspondence: Kei Ohnuma (kohnuma@juntendo.ac.jp)
[1]Department of Therapy Development and Innovation for Immune Disorders and Cancers, Graduate School of Medicine, Juntendo University, 2-1-1, Hongo, Bunkyo-ku, Tokyo 113-8421, Japan
[2]Atopy (Allergy) Research Center, Graduate School of Medicine, Juntendo University, 2-1-1, Hongo, Bunkyo-ku, Tokyo 113-8421, Japan
Full list of author information is available at the end of the article
These authors contributed equally: Takumi Itoh, Ryo Hatano
Edited by J.-E. Ricci

as targeted therapy in these cancers[6]. While EGFR is highly expressed in most TNBC and preclinical models showed a significant effect of EGFR-TKIs on TNBC[7,8], results from clinical studies of EGFR-TKIs for TNBC have been disappointing[9,10]. The molecular mechanisms involved in the differences in efficacy of EGFR-TKI on TNBC between human and mouse model should be elucidated to overcome EGFR-TKI resistance in TNBC.

Human IL-26, mainly produced by Th1, Th17, or NK cells, belongs to the IL-10 cytokine family and regulates T cells, monocytes, NK cells, synoviocytes, fibroblasts, and bacterial pathogens in the inflammatory lesions[11–15]. We previously reported that IL-26 secreted by CD4 + T cells activates fibroblasts for collagen production via its functional receptor IL-20RA/IL-10RB, and that IL-26 has an important role in lung fibrosis of chronic graft-versus-host disease[13]. IL-26 also directly acts on endothelial cells to induce angiogenesis, equivalent to the effect of vascular endothelial growth factor (VEGF) at inflammatory sites[14], with a potential role in angiogenesis in the tumor microenvironment (TME) and malignant progression. In addition, IL-26 has a role in the development of other cancers including gastric cancer and hepatocellular carcinoma[16–18], while little is known about its function in breast cancer. Importantly, human IL-26 is conserved in several vertebrate species but not found in rodents including mice and rats[11,19]. The lack of IL-26 in appropriate murine models has impeded research to understand cross-species differences in EGFR-TKI susceptibility or resistance in TNBC. To address this important issue, we now expand on our previous findings and define the molecular mechanisms involved in IL-26-mediated EGFR-TKI resistance in TNBC, and establish that IL-26 is an appropriate therapeutic target in TNBC.

Various factors such as nutrient deprivation, hypoxia, and loss of calcium homeostasis provoke endoplasmic reticulum (ER) stress[20,21]. When unfolded/misfolded proteins accumulate within ER above a critical threshold, the ER stress response is induced to restore homeostasis[20,22]. The ER stress response is mainly initiated via three signal transducers located in the ER known as protein kinase RNA-like ER kinase (PERK), IRE1α, and activating transcription factor (ATF)-6, and is regulated by BCL2 family proteins[23–26]. However, when the ER stress signals are too strong to restore homeostasis, those signals promote apoptosis and cytotoxicity[24–26]. The PERK-mediated pathway increases the expression level of the transcription factors ATF3 and ATF4[27–29], subsequently forming the ATF3/ATF4 complex to induce the transcription of DDIT3 (CHOP), which finally results in apoptosis[30,31]. Although EGFR-TKIs have been reported to induce ER stress response[32], the association between EGFR-TKI resistance and ER stress in cancer cells has not yet been elucidated.

EphA3 belongs to the Eph receptor-tyrosine kinases (RTKs), regulates cell–cell interaction, and has a role in development and tissue organization[33]. Downstream signaling of EphA3 is induced by its preferential binding partner, ephrin-A5, followed by activation of GTPase or ERK and dephosphorylation of AKT, resulting in cytoskeletal re-organization, cell retraction, and differentiation[34]. EphA3 was first identified as a cell surface antigen on a pre-B lymphoblastic leukemia cell line[35], and was then found to be an antigen on melanoma cells recognized by lytic $CD4^+$ T cells[36]. EphA3 is overexpressed in various tumor cells and is implicated in the maintenance of tumor-initiating cells in glioblastoma and leukemia[33,34]. Frequent somatic mutations of EphA3 as an RTK have been shown in various metastatic cancers, suggesting its role as a tumor suppressor[37]. In breast cancer, expression levels of EphA3 vary depending on the disease stage, being highly expressed in lymph node metastases[38]. However, very little is known regarding the potential role of EphA3 in the pathophysiology of breast cancer, including TNBC.

In the present study, we focused on the role of IL-26 in regulating the effect of EGFR-TKI in TNBC. We found that human TNBC is exposed to IL-26 in the TME, and that IL-26 activates the bypass pathway of EGFR-TKI, while blockade of IL-26 overcomes EGFR-TKI resistance in TNBC. Moreover, we determined that the interaction of IL-26 with EphA3 on TNBC cells inhibits the signaling pathway of ER stress via cross-talk with EGFR signaling. Our findings demonstrate the critical role of IL-26 in mediating EGFR-TKI resistance in TNBC, and suggest a potential novel therapeutic strategy for TNBC involving the combination of anti-IL26 and anti-EGFR agents.

Results

Expression of IL-26 in tumor-infiltrating lymphocytes (TILs) in clinical specimens of TNBC

Our evaluation of IL-26 expression in clinical specimens by immunohistochemistry showed that IL-26 was clearly detected in TILs of TNBC (Fig. 1A), as well as HER2 and Luminal tumors (Supplementary Fig. S1). Although IL-26-positive TILs were observed in all subtypes, the mean percentage of IL-26-positive TILs in TNBC and HER2 type was significantly higher than luminal tumors (Fig. 1B). Immunohistochemical analysis revealed that $CD4^+$ T cells, $CD68^+$ M1 macrophages, and $CD163^+$ M2 macrophages in the TME expressed IL-26 (Fig. 1C). These data suggest that TNBC cells are exposed to IL-26 secreted by $CD4^+$ T cells and macrophages infiltrating in the TME.

Exogenous IL-26 activates bypass pathway of EGFR-TKI in mouse and human TNBC

We next evaluated the effects of exogenous IL-26 in combination with EGFR-TKI treatment on murine TNBC

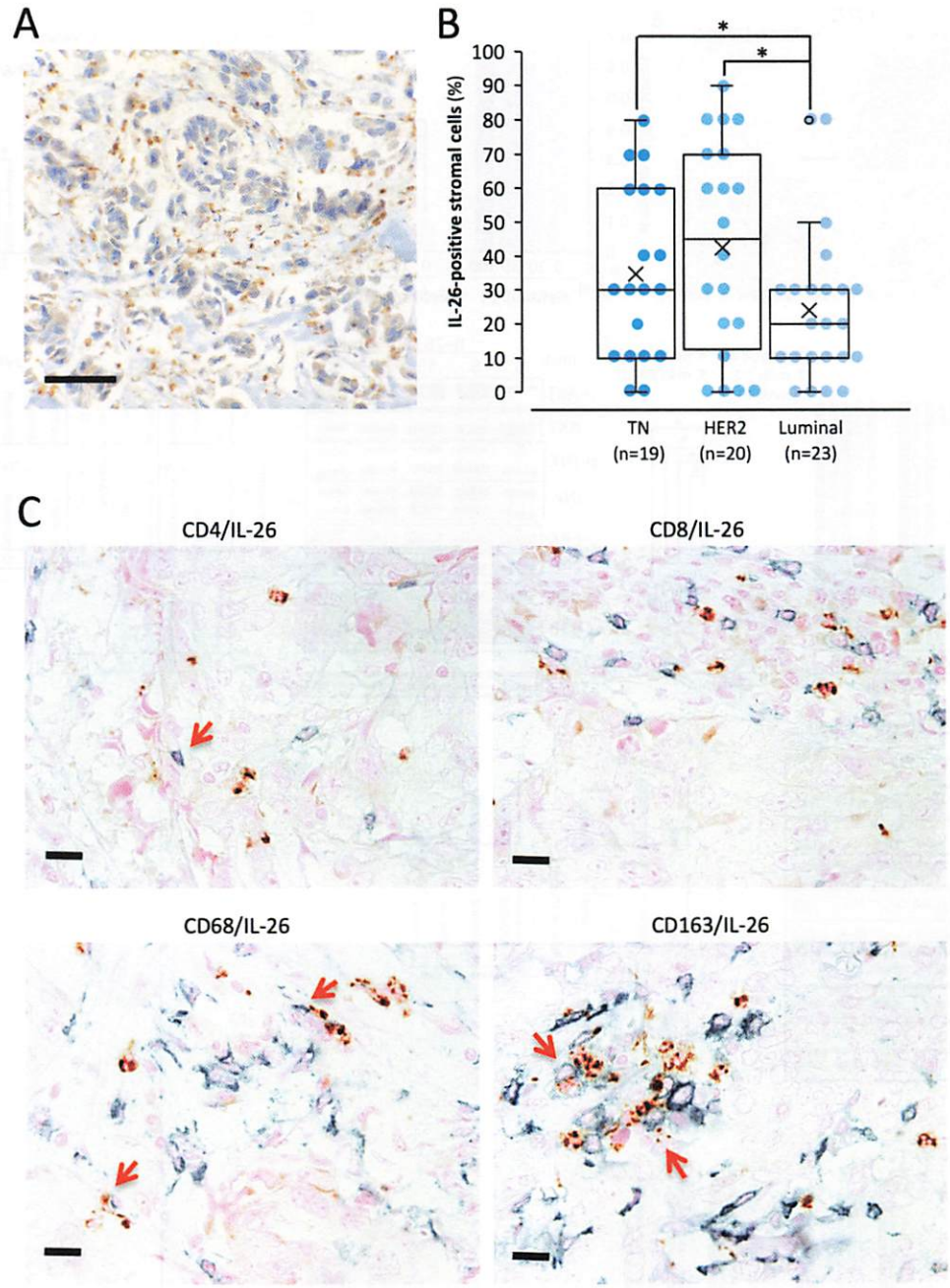

Fig. 1 Immunohistochemistry of breast carcinoma clinical specimens. A TNBC tissue specimens were stained with anti-human IL-26 mAb ($n = 19$). All immunohistochemistry specimens were counterstained with hematoxylin. A representative image of the TNBC case with high IL-26 protein expression was shown. Original magnification, ×100. Scale bar, 50 μm. **B** Each subtype of breast carcinoma tissue specimen was stained with anti-human IL-26 mAb (TNBC ($n = 19$), HER2 ($n = 20$), and Luminal ($n = 23$)). IL-26 in cytoplasm staining of stromal immune cells was determined semi-quantitatively in 10% increments. The percentage of IL-26-positive stromal immune cells in each subtype of breast carcinoma is shown. *$p < 0.05$. **C** TNBC tissue specimens (the same case as shown in **A**) were double-stained with IL-26 (brown) plus CD4, CD8, CD68, or CD163 (blue), respectively. All tissue sections were counterstained with hematoxylin. IL-26 was merged with cell surface CD4, CD68, and CD163 (arrows in each panel). Original magnification, ×40. Scale bar, 25 μm.

cell line E0771 proliferation. Gefitinib treatment suppressed E0771 cell proliferation, while exogenous IL-26 significantly inhibited gefitinib-induced suppression of cell proliferation in a dose-dependent manner of IL-26 (Fig. 2A, B). In addition, exogenous IL-26 significantly inhibited gefitinib-induced suppression of cell proliferation at higher doses of

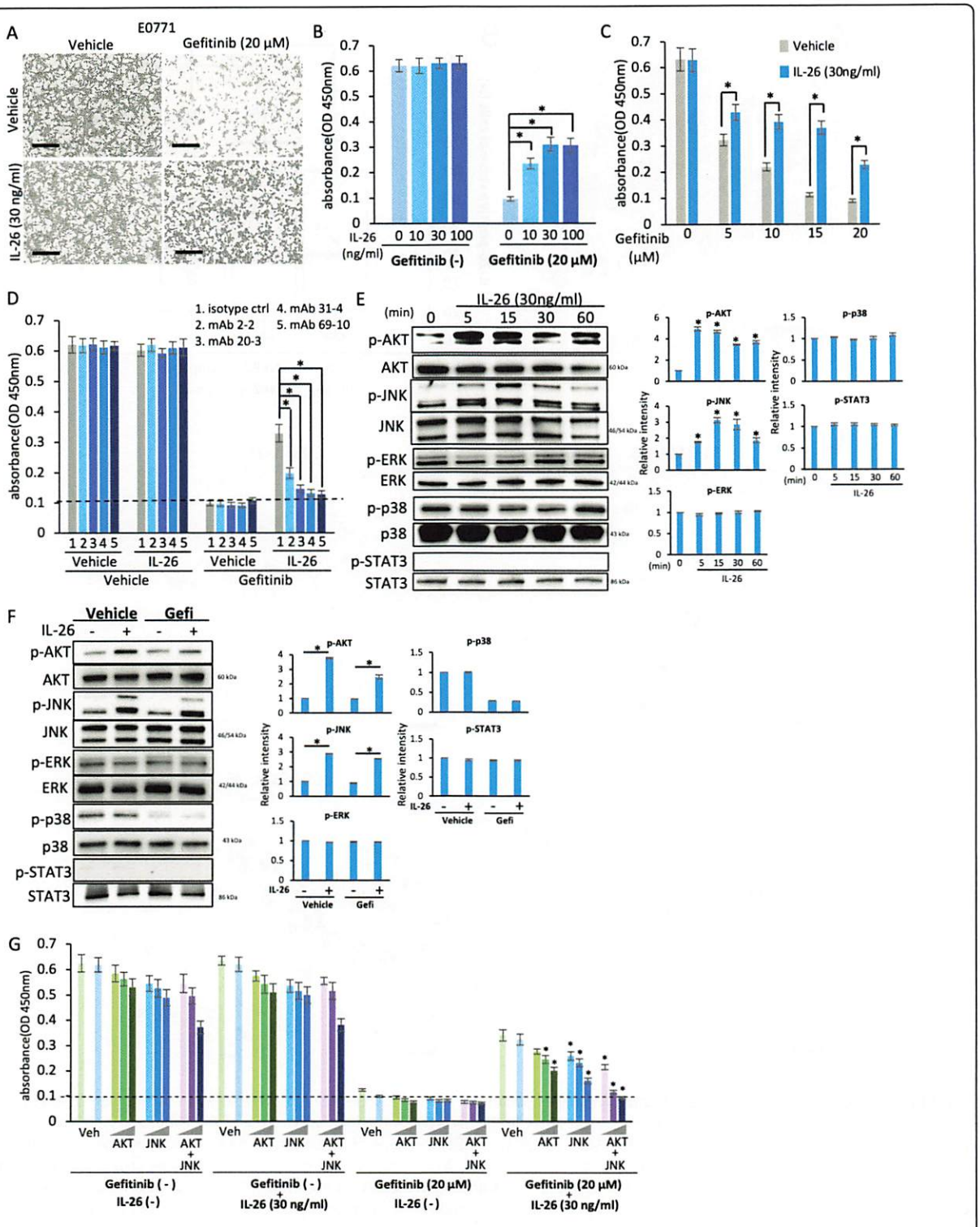

Fig. 2 (See legend on next page.)

(see figure on previous page)

Fig. 2 Exogenous IL-26 activates bypass pathway of EGFR-TKI in mouse TNBC in in vitro assays. A Phase contrast microscopy of E0771 cells (1×10^4) following 48 h incubation with IL-26 or control vehicle in the presence or absence of gefitinib. Original magnification, ×100. Scale bar, 100 μm. Data shown are representative images of five independent experiments with similar results. **B** E0771 cells were treated with the indicated dose of IL-26 in the presence or absence of gefitinib (20 μM) for 48 h. $*p < 0.01$. **C** E0771 cells were treated with IL-26 (30 ng/ml) in the presence of various doses of gefitinib (5, 10, 15, or 20 μM). $*p < 0.01$. **D** E0771 cells were treated with IL-26 (30 ng/ml) and/or gefitinib (20 μM) in the presence of anti-IL-26 neutralizing mAb or isotype control mouse IgG (20 μg/ml, each) for 48 h. The dashed line is the standard value of gefitinib plus vehicle. **E** E0771 cells were stimulated with IL-26 (30 ng/ml) for the indicated periods, and then submitted to Western blot analysis using anti-phosphorylated AKT, JNK, ERK, p38, and STAT3 antibodies, and reblotting with anti-pan AKT, JNK, ERK, p38, and STAT3 antibodies. **F** E0771 cells were stimulated with IL-26 (30 ng/ml) in the presence or absence of gefitinib (20 μM) for 15 min, and then submitted to Western blot analysis as described in **E**. **G** E0771 cells were treated with IL-26 (30 ng/ml) and/or gefitinib (20 μM) in the presence or absence of various concentrations of signal inhibitors (AKT inhibitor, JNK inhibitor or combination of AKT inhibitor and JNK inhibitor) for 48 h. The dashed line is the standard value of gefitinib plus vehicle. $*p < 0.01$. **B**–**D**, **G** Cell proliferation was assessed by MTT assay. Representative data of five (**B**) and three (**C**, **D**, **G**) independent experiments are shown as mean ± S.D. of triplicate samples, and similar results were obtained in each experiment. **E**, **F** Data shown are representative of five independent experiments, and similar results were obtained in each experiment. Band intensity of phospho-proteins was normalized to the appropriate pan proteins, and relative intensity compared with unstimulated cells is shown as mean ± SEM from five independent experiments. $*p < 0.01$.

gefitinib (Fig. 2C). Meanwhile, treatment with IL-26 alone had no effect on cell proliferation of E0771 (Fig. 2A–C). Moreover, four different house-made anti-IL-26 neutralizing mAbs, clones 2-2, 20-3, 31-4, and 69-10, reversed the effect of IL-26 on gefitinib-induced suppression of cell proliferation (Fig. 2D). Investigating specific signaling pathway mediators, we found that exogenous IL-26 activated AKT and JNK phosphorylation but not STAT3 in E0771 cells (Fig. 2E). Moreover, the addition of exogenous IL-26 resulted in activation of AKT and JNK despite treatment with gefitinib (Fig. 2F). Furthermore, inhibition of both AKT and JNK resulted in the marked diminution of IL-26-stimulated proliferation, while inhibition of either AKT or JNK led to partially reduced cell proliferation (Fig. 2G). Similar results were demonstrated with human TNBC cells as obtained with the murine TNBC cells (Supplementary Figs. S2, S3). In addition, exogenous IL-26 significantly inhibited the suppressive effect of erlotinib, another EGFR-TKI, on proliferation of the murine and human TNBC cell lines E0771, HCC70, and MDA-MB468, at similar levels to those seen with gefitinib (Supplementary Fig. S4). These findings indicate that IL-26 induces increased phosphorylation of AKT and JNK, hence activating the EGFR-TKI-associated bypass pathway to result subsequently in tumor growth of both murine and human TNBC.

Interaction of IL-26 and EphA3 in murine TNBC cells

IL-26 stimulation did not induce STAT3 phosphorylation in E0771 cells, suggesting the existence of a novel receptor/signaling pathway other than IL-20RA/IL-10RB-STAT3. To identify the novel interacting proteins of IL-26 in TNBC cells, we performed pathway analysis by DNA microarray of E0771 cells treated with IL-26 (Fig. 3A). The genes related to transmembrane signaling receptor activity and downstream signaling receptor activity were downregulated in E0771 cells treated with IL-26 for both 6 and 24 h. Among them, IL-26 significantly reduced the expression level of EphA3 and altered the downstream signaling of EphA3, indicating the engagement of the EphA3 receptor signaling pathway in IL-26-treated E0771 cells (GEO accession: GSE147804). Of note is the fact that the expression of EphA3 was detected in E0771 (Fig. 3B). On the other hand, while IL-10RB expression was detected, expression of IL-20RA, a major IL-26 binding chain, was not observed in E0771 (Fig. 3B). Blockade of EphA3 by anti-EphA3 pAb resulted in significant inhibition of IL-26-mediated cell proliferation in the setting of EGFR-TKI treatment, in an anti-EphA3 pAb dose-dependent manner (Fig. 3C). Immunocytochemical analysis revealed that exogenous IL-26 was colocalized with cell surface EphA3 (Fig. 3D, E), and that anti-IL-26 mAbs inhibited EphA3/IL-26 interaction (Fig. 3F). Moreover, this colocalization was inhibited by the addition of soluble EphA3-Ig (Supplementary Fig. S5). Taken together, these data suggest that IL-26 interacts with EphA3, but not with the known receptor IL-20RA, on TNBC cells.

Interaction of IL-26 and EphA3 in human TNBC cells

Expression of EphA3 was also detected in both human TNBC cell lines and TNBC cells of human clinical tissue samples (Fig. 4A and Supplementary Figs. S6, S7). On the other hand, while IL-10RB expression was detected, expression of IL-20RA was not observed (Fig. 4A and Supplementary Fig. S6). Immunocytochemical analysis revealed that exogenous IL-26 was colocalized with cell surface EphA3 (Fig. 4B). Meanwhile, anti-IL-26 mAbs inhibited EphA3/IL-26 interaction, and this colocalization was also inhibited by the addition of soluble EphA3-Ig (Fig. 4B). We next performed pull-down assays utilizing recombinant tagged IL-26 and EphA3 proteins, and immunoprecipitation assays with cell lysates. However, direct protein-protein interaction involving IL-26 and EphA3 could not be clearly observed due to the non-specific binding of IL-26 to tag proteins (data not shown). Meanwhile, in situ proximity-ligation assay (PLA) revealed IL-26 and EphA3 existed in close proximity

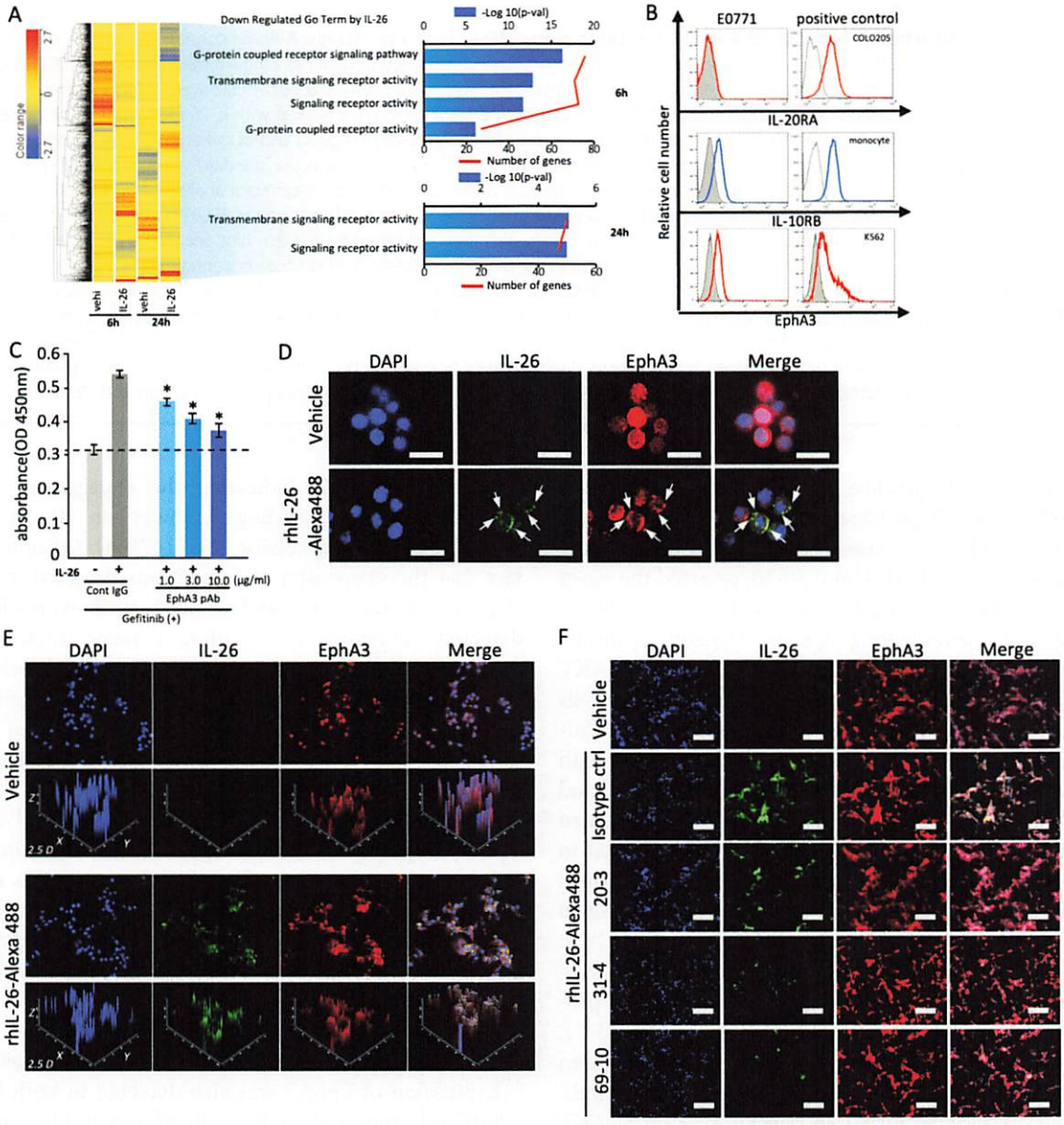

Fig. 3 IL-26 activates bypass pathway of EGFR-TKI via its EphA3 receptor in mouse TNBC cells. A E0771 cells were treated with IL-26 (30 ng/ml) or control vehicle (vehi) for 6 or 24 h, and total RNA was isolated and subjected to DNA microarray analysis as described in the Materials and Methods. Left: A heat map of 960 genes differentially (fold change ≥ 2.0) expressed between vehicle- and IL-26-treated E0771 cells was constructed by hierarchical cluster analysis. Right: significantly downregulated GO terms in IL-26-induced genes. **B** E0771 cells and the indicated positive control cells were stained with each Ab. Data are shown as histogram of IL-20RA, IL-10RB, and EphA3, and the gray area in each histogram shows isotype control data. **C** E0771 cells were treated with IL-26 (30 ng/ml) and gefitinib (20 μM) in the presence of the indicated doses of anti-EphA3 pAb or control IgG for 48 h. Cell proliferation was assessed by MTT assay. The dashed line is the standard value of gefitinib plus vehicle. Data are shown as mean ± S.D. of triplicate samples. *$p < 0.01$. **D** E0771 cells were treated with Alexa Fluor 488-labeled recombinant human IL-26 (rhIL-26-Alexa488 (green)) (30 ng/ml) for 1 h, followed by immunostaining with anti-mouse EphA3 pAb (red) and DAPI (blue). IL-26 was merged with cell surface EphA3 (arrows in lower panel). Original magnification, ×200. Scale bar, 20 μm. **E** Reconstructed 2.5D image shows the intensity of fluorescent peaks of the images from **D**. 2.5D intensity plot of IL-26, EphA3, and DAPI signals represents absolute signal intensities of each pixel. Merged views and individual channels were shown. The 2.5D intensity plots show that IL-26 and EphA3 almost equally distributed and frequently colocalized at the rim. Original magnification, ×200. **F**. E0771 cells were treated with rhIL-26-Alexa488 (green) (30 ng/ml) in the presence of anti-IL-26 mAb (clone 20-3, 31-4 or 69-10) or control IgG (50 μg/ml, each) for 1 h, followed by immunostaining with anti-mouse EphA3 pAb (red) and DAPI (blue). Original magnification ×200. Scale bar, 50 μm. **B–F** Data shown are representative of three independent experiments with similar results.

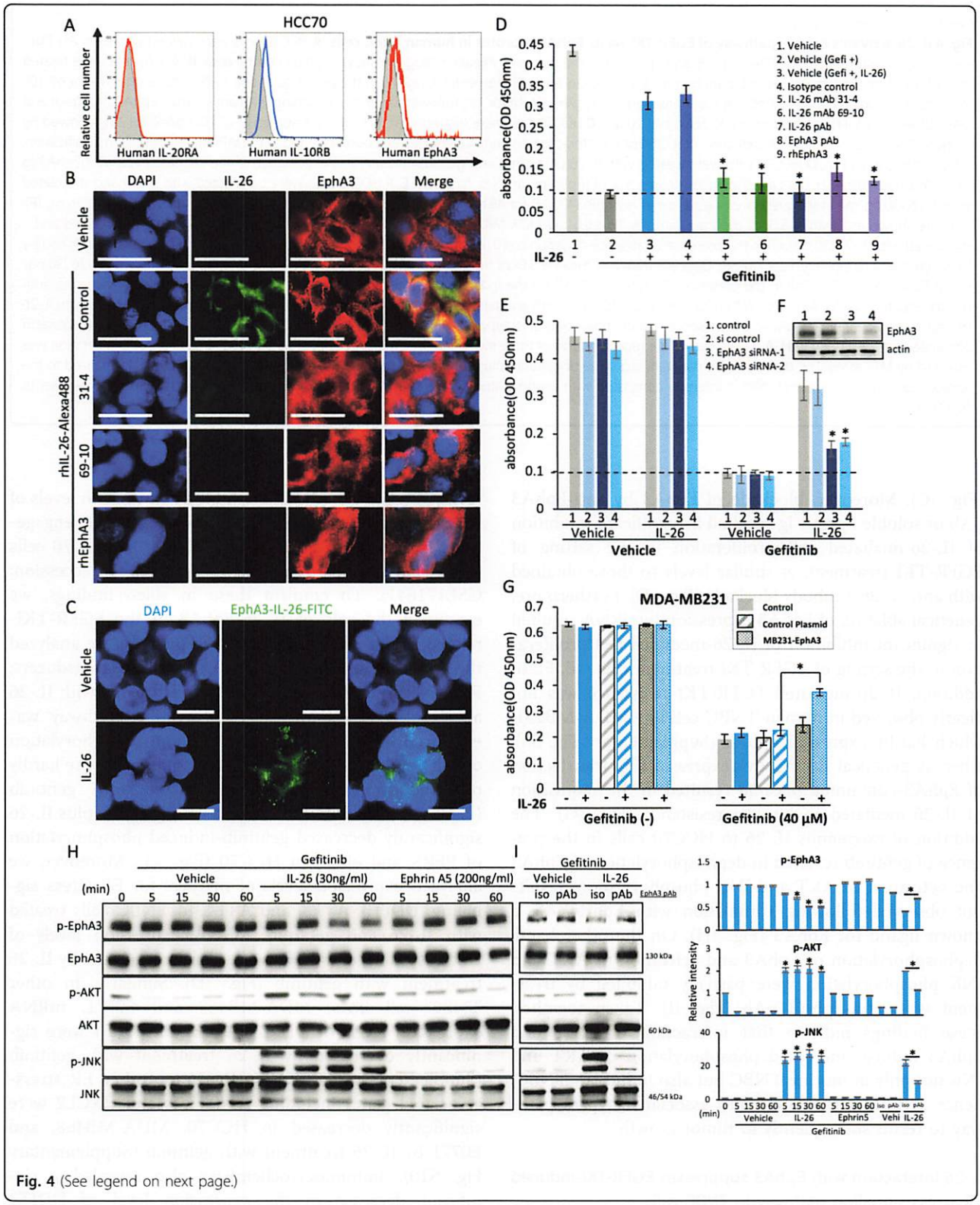

Fig. 4 (See legend on next page.)

(see figure on previous page)

Fig. 4 IL-26 activates bypass pathway of EGFR-TKI via its EphA3 receptor in human TNBC cells. A HCC70 cells were stained with each Ab. Data are shown as histogram of IL-20RA, IL-10RB, and EphA3, and the gray area in each histogram shows isotype control data. **B** HCC70 cells were treated with Alexa Fluor 488-labeled recombinant human IL-26 (rhIL-26-Alexa488 (green)) (30 ng/ml) in the presence of anti-IL-26 mAb (clone 31-4 or 69-10), recombinant human EphA3-Ig (rhEphA3) or control IgG (50 μg/ml, each) for 1 h, followed by immunostaining with anti-human EphA3 pAb (red) and DAPI (blue). Original magnification, ×200. Scale bar, 20 μm. **C** HCC70 cells were treated with recombinant human IL-26 (30 ng/ml) for 1 h, followed by immunostaining and in situ PLA detection of IL-26-EphA3 interaction (green). Cell nuclei are counterstained with DAPI (blue). Original magnification, ×200. Scale bar, 20 μm. **D** HCC70 cells were treated with IL-26 (30 ng/ml) and gefitinib (40 μM) in the presence of the indicated Abs or rhEphA3-Ig (50 μg/ml, each) for 48 h. Data are shown as mean ± S.D. of triplicate samples. $*p < 0.01$. **E, F** HCC70 cells were transfected with siRNA and stimulated with IL-26 (30 ng/ml) in the presence or absence of gefitinib (40 μM) for 48 h. The expression level of EphA3 was confirmed by western blotting (**F**). Data are shown as mean ± S.D. of triplicate samples. $*p < 0.01$. **G** MDA-MB231 cells (EphA3-negative) were transfected with EphA3 plasmid and stimulated with IL-26 (30 ng/ml) in the presence or absence of gefitinib (40 μM) for 48 h. The expression level of cell surface EphA3 was confirmed by Flow cytometry (Supplementary Fig. S8). Data are shown as mean ± S.D. of triplicate samples. $*p < 0.01$. **H** HCC70 cells were treated with IL-26 (30 ng/ml) or Ephrin A5 (200 ng/ml) in the presence of gefitinib (40 μM) for the indicated periods, and then submitted to western blot analysis using anti-phosphorylated EphA3, AKT, and JNK antibodies, and reblotting with anti-pan EphA3, AKT, and JNK antibodies. **I**. HCC70 cells were treated with IL-26 (30 ng/ml) and gefitinib (40 μM) in the presence of anti-EphA3 pAb or isotype control IgG (50 μg/ml, each) for 15 min, and then submitted to Western blot analysis as described in **H**. **A–I** Data shown are representative of three independent experiments with similar results. **D, E, G** Cell proliferation was assessed by MTT assay. The dashed line is the standard value of gefitinib plus vehicle. **H, I** Band intensity of phospho-proteins was normalized to the appropriate pan proteins, and relative intensity compared with unstimulated cells is shown as mean ± SEM from three independent experiments. $*p < 0.01$.

(Fig. 4C). Moreover, blockade of EphA3 by anti-EphA3 pAb or soluble EphA3-Ig resulted in significant inhibition of IL-26-mediated cell proliferation in the setting of EGFR-TKI treatment, at similar levels to those obtained with anti-IL-26 antibody blockade (Fig. 4D). Furthermore, genetical ablation of EphA3 expression by siRNA resulted in significant inhibition of IL-26-mediated cell proliferation in the setting of EGFR-TKI treatment (Fig. 4E, F). In addition, IL-26-mediated EGFR-TKI resistance was not clearly observed in human TNBC cell line MDA-MB231, which hardly expressed EphA3 (Supplementary Fig. S8), whereas genetical EphA3 overexpression by transfection of EphA3-containing plasmid resulted in the acquisition of IL-26-mediated EGFR-TKI resistance (Fig. 4G). The addition of exogenous IL-26 to HCC70 cells in the presence of gefitinib resulted in dephosphorylation of EphA3 and activation of AKT and JNK phosphorylation, results not observed following stimulation with Ephrin A5, a known ligand for EphA3 (Fig. 4H). On the other hand, dephosphorylation of EphA3 and activation of AKT and JNK phosphorylation were partially inhibited by treatment with anti-EphA3 pAb (Fig. 4I). Taken together, these findings indicate that interaction of IL-26 and EphA3 induces increased phosphorylation of AKT and JNK not only in murine TNBC but also in human TNBC, hence activating the EGFR-TKI-associated bypass pathway to result subsequently in tumor growth.

IL-26 interaction with EphA3 suppresses EGFR-TKI-induced ER stress signaling pathway in TNBC cells

To identify a key regulator of tumor growth downstream of IL-26/EphA3 interaction in TNBC, we performed pathway analysis by DNA microarray of HCC70 cells treated with IL-26 and gefitinib (Fig. 5A). This work revealed a significant reduction in the expression levels of ER stress-associated molecules, indicating the engagement of the ER stress signaling pathway in HCC70 cells treated with IL-26 and gefitinib (GEO accession: GSE171641). To confirm these in silico findings, we examined the role of IL-26/EphA3 in the EGFR-TKI-related ER stress pathway. For this purpose, we analyzed the activation of three major ER stress signal transducers, PERK, IRE1, and ATF6, in TNBC cells treated with IL-26 and gefitinib. Although the PERK-eIF2α pathway was enhanced following gefitinib treatment, phosphorylation of IRE1 and upregulation of ATF6 expression were hardly observed in HCC70 cells stimulated with gefitinib (Fig. 5B, C). Of note, stimulation with gefitinib plus IL-26 significantly decreased gefitinib-induced phosphorylation of PERK and eIF2α in HCC70 (Fig. 5B). Moreover, we analyzed expression levels of markers for ER stress signaling, DDIT3, ATF3, and ATF4, in TNBC cells treated with IL-26 and gefitinib. mRNA expression levels of DDIT3, ATF3, and ATF4 were clearly decreased by IL-26 treatment with gefitinib (Fig. 5D). Similarly, in other TNBC cell lines, MDA-MB468 and E0771, mRNA expression levels of DDIT3, ATF3, and ATF4 were significantly decreased by IL-26 treatment with gefitinib (Supplementary Fig. S9). Furthermore, other ER stress-associated genes including IL-6, IL-8, and CXCL2 were significantly decreased in HCC70, MDA-MB468, and E0771 by IL-26 treatment with gefitinib (Supplementary Fig. S10). Immunocytochemistry also revealed a significant decrease in the expression level of DDIT3 (Fig. 5E). In addition, a reduction in mitochondrial activity was significantly inhibited by IL-26 and gefitinib (Fig. 5F). While a decrease in the expression level of DDIT3 mRNA was significantly inhibited by treatment with AKT

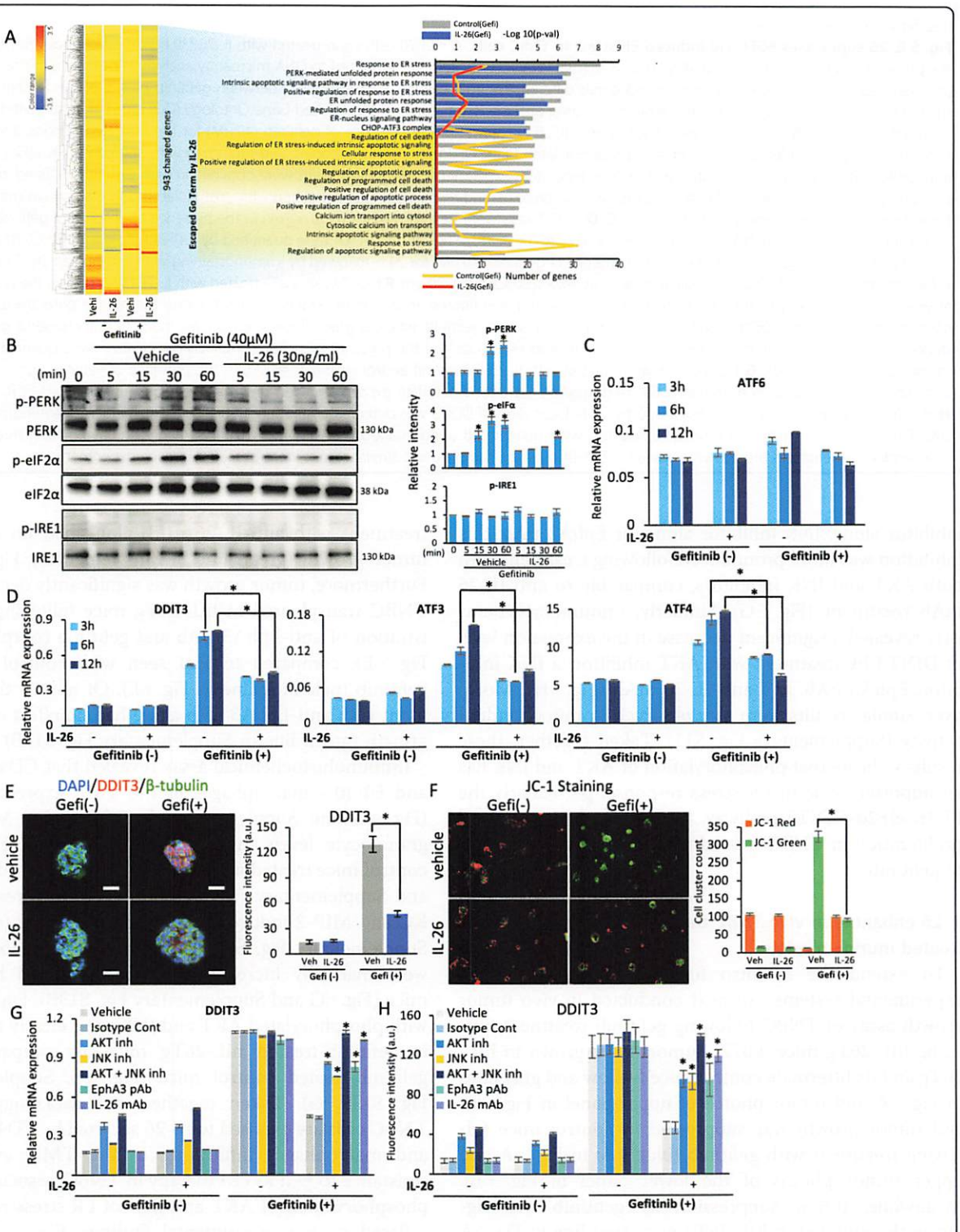

Fig. 5 (See legend on next page.)

(see figure on previous page)

Fig. 5 IL-26 suppresses EGFR-TKI-induced ER stress in TNBC cells. A HCC70 cells were treated with IL-26 (30 ng/ml) or control vehicle (vehi) in the presence or absence of gefitinib (40 μM) for 3 h. Total RNA was isolated and subjected to DNA microarray analysis as described in the "Materials and methods" section. Left: A heat map of 943 genes differentially (fold change ≥ 2.0) expressed between gefitinib plus IL-26- and gefitinib alone-treated HCC70 cells was constructed by hierarchical cluster analysis. Right: significantly enriched Gene Ontology (GO) terms in gefitinib-induced and IL-26-reduced genes. **B** HCC70 cells were treated with IL-26 (30 ng/ml) in the presence of gefitinib (40 μM) for the indicated periods, and then submitted to Western blot analysis using anti-phosphorylated PERK, eIF2α, and IRE1 antibodies, and reblotting with anti-pan PERK, eIF2α, and IRE1 antibodies. Data shown are representative of three independent experiments, and similar results were obtained in each experiment. Band intensity of phospho-proteins was normalized to the appropriate pan proteins, and relative intensity compared with unstimulated cells is shown as mean ± SEM from three independent experiments. * $p < 0.01$. **C**, **D** HCC70 cells were treated with IL-26 (30 ng/ml) in the presence or absence of gefitinib (40 μM) for the indicated periods. mRNA expression levels of ATF6 (**C**) or DDIT3, ATF3, and ATF4 (**D**) were quantified by qRT-PCR. *$p < 0.01$. **E** HCC70 cells were treated with IL-26 (30 ng/ml) in the presence or absence of gefitinib (40 μM) for 24 h, followed by immunostaining with anti-human DDIT3 pAb (red), β-tubulin (green), and DAPI (blue). Original magnification, ×400. Scale bar, 20 μm. **F** HCC70 cells were treated with IL-26 (30 ng/ml) in the presence or absence of gefitinib (40 μM) for 24 h, followed by JC-1 staining. Red fluorescence, sign of preserved mitochondrial membrane potential ($\Delta\Psi_m$), was observed in vehicle- or IL-26-treated HCC70 cells in the absence of gefitinib, whereas green fluorescent signals, index of mitochondrial membrane depolarization were prominently observed in vehicle-treated HCC70 cells in the presence of gefitinib. Stained cell clusters were quantitated using Image-J software. *$p < 0.01$. **G** HCC70 cells were treated with IL-26 (30 ng/ml) and/or gefitinib (40 μM) in the presence of vehicle, signal inhibitors, anti-EphA3 pAb or anti-IL-26 mAb (clone 69-10) (50 μg/ml, each) for 6 h. mRNA expression levels of DDIT3 were quantified by qRT-PCR. *$p < 0.01$. **H** HCC70 cells were treated as described in G for 24 h. Expression of DDIT3 was detected by Immunofluorescence staining with anti-human DDIT3 pAb. Fluorescence intensity and stained cell clusters were quantitated using Image-J software. *$p < 0.01$. **C**–**H** Representative data of three independent experiments are shown as mean ± S.D. of triplicate samples, and similar results were obtained in each experiment.

inhibitor alone, JNK inhibitor alone, or EphA3 pAb, this inhibition was more pronounced following treatment with both AKT and JNK inhibitors, comparable to anti-IL-26 mAb treatment (Fig. 5G). Similarly, immunocytochemistry revealed a significant decrease in the expression level of DDIT3 by treatment with AKT inhibitor, a JNK inhibitor, EphA3 pAb, and anti-IL-26 mAb (Fig. 5H). Moreover, similar results were also observed in mitochondrial activity (Supplementary Fig. S11). Taken together, these results indicate that phosphorylation of AKT and JNK has an important role in ER stress response, particularly the PERK-eIF2α-DDIT3 pathway, to induce cell survival and proliferation in TNBC treated with IL-26 in the presence of gefitinib.

IL-26 enhances in vivo TNBC tumor growth in EGFR-TKI-treated murine models

To extend the in vitro findings above to in vivo experimental systems, we next conducted in vivo tumor growth assay of TNBC following gefitinib treatment, utilizing hIL-26Tg mice. E0771 tumors were grown in hIL-26Tg and its littermate control mice (yellow and gray lines in Fig. 6A and tumor photos of upper panel in Fig. 6B), and tumor growth was suppressed in control mice following treatment with gefitinib (blue line in Fig. 6A and upper tumor photos of the lower panel in Fig. 6B). Meanwhile, tumor suppression by gefitinib was significantly inhibited in hIL-26Tg mice (red line in Fig. 6A and lower tumor photos of the lower panel in Fig. 6B). Moreover, tumor growth was significantly decreased in TNBC transplanted in hIL-26Tg mice following administration of anti-IL-26 mAb and gefitinib (green line in Fig. 6C), compared to that seen with control mAb and gefitinib (pale blue line in Fig. 6C). Of note is that treatment with anti-IL-26 mAb alone had no effect on tumor growth (green line in Supplementary Fig. S12A). Furthermore, tumor growth was significantly decreased in TNBC transplanted in hIL-26Tg mice following administration of anti-EphA3 pAb and gefitinib (purple line in Fig. 6E), compared to that seen with control Ab and gefitinib (pale blue line in Fig. 6E). Of note is that treatment with anti-EphA3 pAb alone had no effect on tumor growth (green line in Supplementary Fig. S12B).

Immunohistochemical assay revealed that $CD4^+$ T cells and F4/80+ macrophages in the TME expressed IL-26 (Fig. 6G and Supplementary Fig. S13C, D). Moreover, granulocyte levels in the TME of both hIL-26Tg and control mice treated with gefitinib were increased (Fig. 6G and Supplementary Fig. S13E), possibly with response to KC and MIP-2 induced by ER stress signaling (shown in Supplementary Fig. S10). PECAM-positive blood vessels were markedly increased in gefitinib-treated hIL-26Tg mice (Fig. 6G and Supplementary Fig. S13B). Finally, cells with phosphorylated AKT and JNK were clearly increased in gefitinib-treated hIL-26Tg mice as compared with gefitinib-treated control mice (Fig. 6G, Supplementary Fig. S13F, G). Taken together, our data suggest that TNBC cells are exposed to IL-26 secreted by $CD4^+$ T cells and macrophages infiltrating in the TME, evoking a resistance to EGFR-TKI therapy in TNBC, associated with phosphorylation of AKT and JNK of ER stress response.

Based on our experimental findings, Fig. 7 depicts a schematic of the inhibitory effect of IL-26 on EGFR-TKI-mediated tumor suppression in TNBC cells.

Discussion

Originally identified in *Herpes saimiri*-infected T cells as AK155 [39], IL-26 has an important role as a mediator of

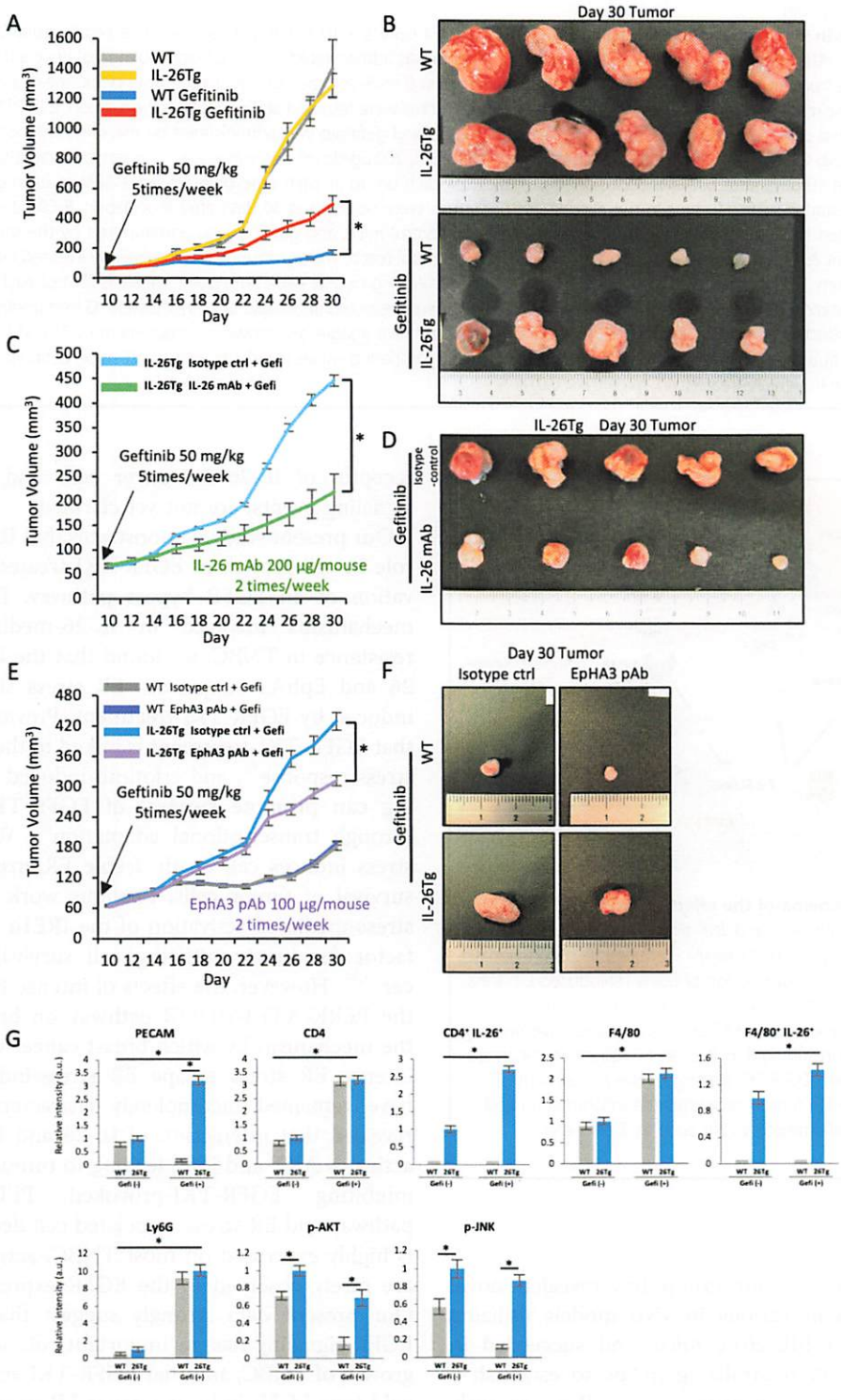

Fig. 6 (See legend on next page.)

(see figure on previous page)

Fig. 6 IL-26 promotes in vivo tumor growth against EGFR-TKI. A E0771 cells (5×10^5) with Matrigel were injected subcutaneously into the flank of hIL-26Tg (IL-26Tg) or littermate control mice (WT) (each, $n = 8$). Gefitinib was administered by oral gavage (50 mg/kg) once a day five times a week for the duration of the study from 10 days after E0771 cell inoculation. $n = 8$ mice for each group at each time point. mean ± SEM of each group. $^*p < 0.01$. **B** Macroscopic manifestation of the tumors in experiment A. Tumors were resected at 30 days after inoculation. **C** E0771 cells (5×10^5) with Matrigel were inoculated subcutaneously into the flank of hIL-26Tg mice, and gefitinib was administered by the same method as described in experiment A. IL-26 mAb (clone 69-10) or mouse IgG isotype control (each, 200 μg/dose) was subsequently injected intraperitoneally once a day twice a week from 10 days after E0771 inoculation. $n = 8$ mice for each group at each time point. mean ± SEM of each group. $^*p < 0.01$. **D** Macroscopic manifestation of the tumors in the experiment C. Tumors were resected at 30 days after inoculation. **E** E0771 cells (5×10^5) with Matrigel were inoculated subcutaneously into the flank of hIL-26Tg or control mice, and gefitinib was administered by the same method as described in experiment A. Anti-mouse EphA3 pAb or goat IgG isotype control (each, 100 μg/dose) was subsequently injected intraperitoneally once a day twice a week from 10 days after E0771 inoculation. $n = 8$ mice for each group at each time point. mean ± SEM of each group. $^*p < 0.01$. **F** Macroscopic manifestation of the tumors in the experiment E. Tumors were resected at 30 days after inoculation. **G** Immunofluorescence staining of tumor specimens resected at 17 days after E0771 inoculation. Representative images are shown in Supplementary Fig. S13. Data are shown as mean ± S.E. of relative fluorescence intensity from 8 mice for each group, comparing values in vehicle-treated WT mice, gefitinib-treated WT mice, or hIL-26Tg mice to those in vehicle-treated WT mice ($^*p < 0.01$).

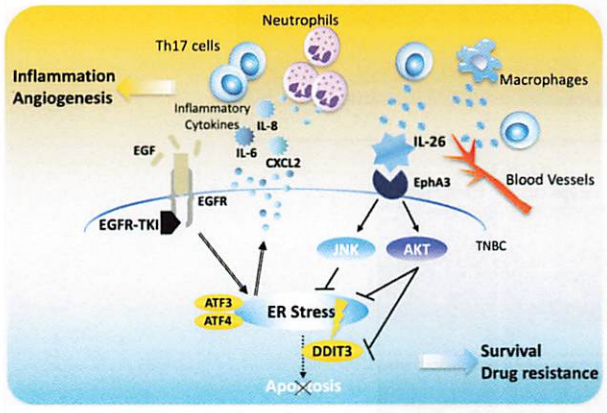

Fig. 7 Hypothetical schema of the effect of IL-26 on EGFR-TKI resistance. IL-26 activates AKT and JNK signaling of bypass pathway of EGFR-TKI via interaction with its newly identified IL-26 functional receptor EphA3, leading to suppression of EGFR-TKI-induced ER stress, which subsequently results in TNBC tumor survival and drug resistance. Moreover, production of ER stress-associated inflammatory cytokines/chemokines including IL-6, IL-8, and CXCL2 was enhanced following treatment with EGFR-TKI, leading to the recruitment of neutrophils in TME, which further promotes the inflammation and recruitment of other inflammatory cells such as T cells and macrophages.

local inflammation[11,12]. Our group has revealed novel functions of IL-26 in various in vivo models utilizing humanized mice or hIL-26Tg mice, and succeeded in developing anti-IL-26 neutralizing mAbs to establish a novel IL-26-targeted therapy[13,40–42]. We recently demonstrated that IL-26 functions as an angiogenic factor equivalent to VEGF, strongly suggesting a role of IL-26 in angiogenesis in the TME and malignant progression. While IL-26 is involved in cancer biology[16,17,43,44], the precise molecular mechanisms associated with this process, including the identification of the functional receptor of IL-26 in cancer cells and its downstream signaling events, are not yet clarified.

Our present study demonstrates that IL-26 has a critical role in cell growth of EGFR-TKI-treated TNBC via activation of an EGFR bypass pathway. By exploring the mechanisms involved in IL-26-mediated EGFR-TKI resistance in TNBC, we found that the interaction of IL-26 and EphA3 suppresses ER stress signaling pathway induced by EGFR-TKI treatment. Previous work showed that EGFR-TKI-treatment is linked to the induction of ER stress response[32], and erlotinib-induced ER stress signaling can promote survival of EGFR-TKI-persister cells through transcriptional adaptation[45]. While intense ER stress induces cell death, feeble ER stress promotes the survival of tumor cells. Previous work showed that ER stress-mediated activation of the IRE1α pathway is a key factor for tumor-initiating cell survival in breast cancer[45,46]. However, the effects of intense ER stress through the PERK-ATF4-DDIT3 pathway on breast cancer, and the mechanism by which breast cancer cells subjected to intense ER stress escape ER stress-induced cell death, have remained incompletely characterized. Our study revealed that interaction of IL-26 and EphA3 in TNBC activates AKT and JNK, leading to tumor proliferation by inhibiting EGFR-TKI-provoked PERK-eIF2α-DDIT3 pathway and ER stress-associated cell death. While EGFR is highly expressed on most TNBC, activating mutations are rarely observed in the EGFR expressed on TNBC[9]. Our present data strongly suggest that EGF-wild-type EGFR signaling has an important role in the survival or growth of TNBC, and that EGFR-TKI acting through this wild-type EGFR induces intense ER stress. Future studies are needed to define the precise role of EGFR in TNBC and the effect of EGFR-TKI on TNBC, in comparison to the role of well-known EGFRs with activating mutations expressed on other neoplasms such as lung or colon cancers. ER stress in cancer cells is associated with the production of various proinflammatory molecules[21,47].

Our data showed that gefitinib-treated TNBC cells exhibited enhanced production of proinflammatory cytokines/chemokines such as IL-6, IL-8, and CXCL2, hence increasing the number of tumor-infiltrating immune cells including IL-26-producing cells in the TME. Recent evidence showed that IL-26 promotes an inflammatory TME of TNBC, at least partially through binding to neutrophil extracellular traps (NET) DNA to stimulate the expression of multiple proinflammatory cytokines in the TME, which collectively contribute to engraftment, tumor growth, and metastasis of TNBC[44]. Since granulocyte levels in the TME of hIL-26Tg mice treated with gefitinib were increased (Fig. 6G and Supplementary Fig. S13E), further studies are needed to clarify whether IL-26 affects the production of inflammatory cytokines from immune cells infiltrating the TME of TNBC treated with gefitinib, and whether these effects of IL-26 influence tumor growth or metastasis of TNBC in our in vivo model.

The previous report showed that IL-26 binds to a cell surface heterodimeric receptor IL-20RA/IL-10RB, inducing downstream signaling cascade events via STAT3 phosphorylation[19]. However, the TNBC cell lines used in the present study did not express IL-20RA. These findings strongly suggest that the downstream signaling events in TNBC following IL-26 stimulation were not mediated by the known receptor complex IL-20RA/IL-10RB. In fact, we identified EphA3 as a novel functionally interacting receptor for IL-26 in TNBC. Human EphA3 is a 110 kDa protein consisting of 983 amino acids and belongs to the ephrin receptor subfamily of the RTK family. EphA3 is well conserved between human and mouse with ~96% homologies and 88% similarities[48], allowing human IL-26 to bind to both human and murine EphA3 on TNBC cells. Mutations of EphA3 were identified as candidate cancer risk genes in breast cancer, colon cancer, lung cancer, glioblastoma, melanoma, and pancreatic carcinoma[33,49–52]. The roles of the EPH family in cancer are controversial. Overexpression of EPH family can promote and inhibit tumor progression, even in the same tumor type[33,53,54]. Previous reports showed that a preferential binding ligand for EphA3 is ephrin-A5[33]. Many cancer cell lines and normal endothelial cells release A-type ephrins from their cell surface[55]. Membrane-bound ephrin-A5 ligand-induced EphA3 clustering and its tyrosine phosphorylation, followed by activation of GTPase or ERK and dephosphorylation of AKT, resulting in cytoskeletal reorganization, cell retraction, and differentiation[56]. A-type ephrins, particularly ephrin A1, A4, and A5, can be released from the cell surface through metalloproteases, phospholipases, or through alternative splicing, which removes the exon encoding the site of GPI anchor attachment[55,57,58]. Binding of unbound, soluble ephrin-A5 to EphA3 resulted in dephosphorylation of EphA3 by recruitment of protein tyrosine phosphatase and autoinhibition of its RTK domain, leading to cell growth and proliferation[56,59,60]. However, our present study showed that the addition of exogenous ephrin-A5 has little impact on the effects of gefitinib in TNBC cells. It is possible that the EphA3 antibody may reduce the effect of IL-26 on gefitinib by preventing access to the IL-26 binding site, not by blocking ephrin-A5 ligand binding. These results suggest that the blockade of IL-26 overcomes EGFR-TKI resistance in TNBC. In the current study, exogenous IL-26 induced dephosphorylation of EphA3 in TNBC, followed by phosphorylation of AKT and JNK leading to suppression of ER stress signaling, resulting in enhanced tumor growth of EGFR-TKI-resistant TNBC. Despite the EphA3-related molecular alterations associated with IL-26 alone, treatment with IL-26 alone did not alter TNBC growth; rather, the effect of IL-26 on TNBC tumor growth was seen in the setting of EGFR-TKI exposure with an increased ER stress response. Our present study did not demonstrate direct IL-26 and EphA3 binding. IL-26 has been reported to be a cationic and amphipathic cytokine, resembling the structure of antimicrobial peptides[61]. Since polycationic proteins are known to bind with various molecules, it is, therefore, possible that IL-26 forms a large complex that includes EphA3 to affect downstream signaling.

In conclusion, we showed that IL-26 activates an EGFR-TKI-associated bypass pathway in TNBC and that EphA3 is a putative novel functional receptor for IL-26 in TNBC, and binding of IL-26 inhibits ER stress signaling via phosphorylation of AKT and JNK downstream of EphA3, leading to cell growth. Blockade of IL-26 overcomes EGFR-TKI resistance in TNBC. These findings reveal the critical importance of IL-26 on EGFR-TKI resistance in TNBC, and serve as the basis for a novel therapeutic strategy in TNBC, as well as potentially other EGFR-TKI resistant cancers such as non-small cell lung cancer or colorectal cancer, with the combination of anti-IL-26 mAb and anti-EGFR agents. In addition, this therapeutic approach may be considered for other medical conditions involving IL-26 and EphA3, such as pulmonary fibrosis[13,14,40,62,63]. By clarifying the mechanisms involved in IL-26-mediated EGFR-TKI resistance in TNBC, our work solves the paradox involving the cross-species difference between murine models and human subjects observed with EGFR-TKI treatment of TNBC.

Materials and methods

Cells, reagents, and antibodies

The mouse breast carcinoma cell line E0771 was purchased from CH3 Biosystems (Amherst, NY). The human breast adenocarcinoma cell lines HCC70, MDA-MB468, and MDA-MB231 were obtained from ATCC. All cell lines had been tested for mycoplasma. For cell

stimulation, a recombinant human IL-26 dimer was purchased from R&D Systems (Minneapolis, MN). Recombinant human IL-26 dimer was labeled with Alexa Fluor 488 utilizing protein labeling kit (ThermoFisher Scientific, Waltham, MA) and used for immunofluorescence staining. Recombinant human and mouse EphA3 Fc Chimera Protein were purchased from R&D Systems. EGFR-TKIs and inhibitors used in this study are shown in Supplementary Table S1. siRNAs against EphA3 were purchased from ThermoFisher Scientific (sequences are shown in Supplementary Table S2), and negative control siRNA (oligonucleotide sequences are not disclosed) was purchased from Qiagen (Hilden, Germany). FuGENE HD Transfection Reagent (Promega, Madison, WI) was used to transfect plasmid pCMV6-ENTRY EPHA3 or pCMV6-ENTRY control (ORIGENE, Rockville, MD) into MDA-MB231 cells. Antibodies used in this study are listed in Supplementary Table S3.

Mice

hIL-26Tg mice were kindly provided by Dr. Thomas Aune and were interbred with C57BL/6 mice in the animal facility in Juntendo University. All mice used in this study were kept under the specific pathogen-free facility in microisolator cages. Female hIL-26Tg mice and littermate control mice at 8–12 weeks of age were used.

MTT assay

Human and mouse breast carcinoma cells (1×10^4) were incubated in RPMI 1640 containing 10% FCS on 96-well flat-bottom plates (Corning, Tewksbury, MA) for 24 h at 37 °C, and then stimulated with IL-26 in the presence or absence of EGFR-TKI (Gefitinib or Erlotinib), signal inhibitors and neutralizing antibodies for 48 h. Tetrazolium monosodium salt (WST-8) was added to each well at a concentration of 1/10 volume for the last 1 h, and the absorbance at 450 nm/595 nm was measured using a Microplate Reader (Bio-Rad, Hercules, CA) and data were analyzed with Microplate Manager 6 software (Bio-Rad).

Western blotting

To analyze phosphorylation of AKT, ERK, p38, JNK, STAT3, EphA3, PERK, eIF2α and IRE1, E0771, and HCC70 cells were stimulated with IL-26 (30 ng/ml) in the presence or absence of Gefitinib and anti-EphA3 pAb (10 μg/ml) in 100-mm dish for the indicated periods. After stimulation, cells were lysed in RIPA buffer supplemented with 2% protease inhibitor mixture (Sigma-Aldrich, Saint. Louis, MO) and 1 × PhosSTOP (Roche Diagnostics, Tokyo, Japan), and lysates were resolved by SDS-PAGE in reducing condition (15 μg/lane) and immunoblotted using anti-phosphorylated AKT, ERK, p38, JNK, STAT3, EphA3, PERK, eIF2α, and IRE1 antibodies recognizing both human and murine antigens. For reprobing, the membranes were submerged in a stripping buffer. After a stripping procedure, the membranes were reprobed with anti-pan AKT, ERK, p38, JNK, STAT3, EphA3, PERK, eIF2α, and IRE1 antibody recognizing both human and murine antigens. The images were taken using C-Digit blot scanner (MS Techno Systems Inc., Osaka, Japan).

Flow cytometry

E0771, HCC70, and MDA-MB468 cells were washed in PBS containing 1% FBS and 0.1% sodium azide, and subsequently stained with fluorochrome-conjugated Abs (anti-IL-20RA and IL-10RB) for 30 min at 4 °C. E0771, HCC70, MDA-MB468, and MDA-MB231 cells were incubated with purified rabbit anti-human/mouse EphA3 pAb for 30 min at 4 °C, and subsequently stained with PE-conjugated donkey anti-rabbit IgG (BioLegend, San Diego, CA) for 25 min at 4 °C. Flow cytometry was performed on two-laser FACSCalibur (BD Biosciences, San Jose, CA), and data were analyzed with FlowJo software (BD Biosciences).

Microarray analysis

E0771 cells were treated with exogenous IL-26 (30 ng/ml) for 6 or 24 h. Total RNA was isolated and subjected to DNA microarray analysis utilizing 3D-Gene mouse mRNA oligo chip (TORAY, Kamakura, Japan). A heat map of 960 genes differentially (fold change ≥ 2.0) expressed between vehicle- and IL-26-treated E0771 cells was constructed by hierarchical cluster analysis using cluster 3.0 software, with results displayed with the TreeView program. HCC70 cells were treated with exogenous IL-26 (30 ng/ml) in the presence or absence of Gefitinib (40 μM) for 3 h. Total RNA was subjected to DNA microarray analysis with 3D-Gene human mRNA oligo chip. A heat map of 943 genes differentially (fold change ≥ 2.0) expressed between vehicle-, IL-26-, gefitinib plus vehicle-, and gefitinib plus IL-26-treated HCC70 cells were constructed and displayed as described above. The fraction of gene categories identified by the microarray Gene Ontology (GO) enrichment analysis is shown as GO terms in descending order of correlation coefficient values. The data discussed in this publication have been deposited in NCBI's Gene Expression Omnibus and are accessible through GEO Series accession number GEO accession: GSE147804 (E0771), GSE171641(HCC70).

In vivo evaluation of IL-26 in a TNBC transplantation model

E0771 cells (5×10^5) with 50% Matrigel were injected subcutaneously into the flank of hIL-26Tg or control mice. Tumor measurements were made using calipers and volumes were calculated using the formula (v = width × width × (length/2)). After 10 days from E0771 cells injection, hIL-26Tg or control mice were randomly selected for treatment with vehicle control, gefitinib or each antibody ($n = 8$; calculated by power analysis based

on our pilot studies). Gefitinib was suspended in H_2O containing 1% Tween 80 for administration by oral gavage (50 mg/kg). Oral gavage was administered once a day 5 times a week for the duration of the study. H_2O containing 1% Tween 80 and no Gefitinib was used as a control. For mAb treatment, anti-IL-26 mAb (clone 69-10) developed in our laboratory[42] or mouse IgG1 isotype control was diluted in sterile PBS at 1 mg/ml and 200 μl (200 μg) was injected intraperitoneally once a day twice a week from 10 days after E0771 cells injection. Anti-EphA3 pAb (R&D Systems) or goat IgG isotype control was diluted in sterile PBS at 500 μg/ml and 200 μl (100 μg) was injected intraperitoneally once a day twice a week from 10 days after E0771 cells injection. Mice were sacrificed when subcutaneous tumor size reached 1600 mm^3. No blinding was involved in animal studies.

Immunofluorescence analysis

E0771 and HCC70 cells (1×10^5) were incubated in RPMI 1640 containing 10% FCS on Lab-Tek chamber slide (ThermoFisher Scientific) for 24 h. After incubation, cells were stimulated with Alexa Fluor 488-labeled IL-26 (30 ng/ml) in the presence or absence of recombinant human and mouse EphA3-Ig for 1 h. HCC70 cells were stimulated with IL-26 (30 ng/ml) in the presence or absence of Gefitinib (40 μM), signal inhibitors, and neutralizing antibodies for 24 h. Subcutaneous tumor samples obtained from mice were fixed in 4% paraformaldehyde (ThermoFisher Scientific), embedded in OCT compound (Tissue-Tek, Sakura Finetek, Tokyo, Japan). Cells and slides were immunostained with each antibody and observed utilizing Zeiss inverted microscope and Apotome.2. program (Carl Zeiss, Oberkochen, Germany). Fluorescence intensity was quantitated using Image-J software (NIH). Images were captured using objectives of ×100–×400.

In situ proximity ligation assay (PLA)

HCC70 cells (1×10^5) were incubated in RPMI 1640 containing 10% FCS on Lab-Tek chamber slide (ThermoFisher Scientific) for 24 h. After incubation, cells were stimulated with recombinant human IL-26 (30 ng/ml) for 1 h. Following stimulation, cells were fixed with 4% paraformaldehyde in PBS for 15 min at RT. The coverslips were incubated with goat anti-human IL-26 pAb (R&D systems) and mouse anti-human EphA3 mAb (Santa Cruz Biotechnology, Santa Cruz, CA), and subjected to in situ PLA using the Duolink Detection kit (ThermoFisher Scientific) according to the manufacturer's instructions. The coverslips were incubated with PLA minus and PLA plus probes (anti-goat PLUS and anti-mouse MINUS diluted in the antibodies diluent provided with the kit) for 1 h at 37 °C in a humidity chamber. The coverslips were washed and processed for probe ligation, signal amplification, fluorescently labeled probe conjugation, and mounting. Cells were observed utilizing Zeiss inverted microscope and Apotome.2. program. Images were captured using objectives of ×400.

JC-1 staining

Mitochondrial stability was assessed using a mitochondrial membrane potential ($\Delta\Psi_m$) assay kit with JC-1 staining (Cayman Chemical, Ann Arbor, MI). HCC70 cells (1×10^4) were stimulated with IL-26 (30 ng/ml) in the presence or absence of Gefitinib (40 μM), signal inhibitors, and neutralizing antibodies on flat-bottom plates 96-well (Corning) for 24 h. After stimulation, cells were stained for JC-1 Staining Solution. The $\Delta\Psi_m$ was assessed using a fluorescence microscope (Nikon, Tokyo, Japan) at wavelengths of 530 and 590 nm, respectively. The $\Delta\Psi_m$ depolarization displayed green fluorescence. Stained cells were quantitated using Image-J software (NIH). Images were captured using objectives of ×40.

Quantitative real-time PCR (qRT-PCR)

E0771, HCC70, and MDA-MB468 cells were incubated in RPMI 1640 containing 10% FCS on 6-well plates (Corning) for 24 h, and then stimulated with IL-26 (30 ng/ml) in the presence or absence of Gefitinib for 3, 6, or 12 h. Cells were collected and total RNA was extracted. cDNA was synthesized using a PrimeScript II first strand cDNA synthesis kit (TaKaRa Bio, Shiga, Japan) with oligo (dT) primers. mRNA levels were measured by 7500 System SDS software (Applied Biosystems, Foster City, CA), being normalized to hypoxanthine phosphoribosyltransferase expression levels. Sequences of primers used in this study are shown in Supplementary Table S4.

Tissue samples and immunohistochemistry

Pathological examinations were carried out by two experienced pathologists. On specimens subjected to IHC, ER status, and PgR status were determined semi-quantitatively and judged as positive when more than 1% of the nuclei of cancer cells showed staining. HER2 was determined as positive when more than 10% of tumor cells showed strong staining of the entire cell membrane. Triple-negative (ER/PgR-HER2-) status was classified when the samples were ER (<1%), PgR (<1%), and HER2 (<10%) by IHC staining. For an immunohistochemical double-staining of IL-26 and CD4, CD8, CD68 or CD163, antigen retrieval was performed by autoclaving in 10 mM citrate buffer (pH 6.0) for 10 min at 120 °C, and the sections were treated with 0.3% H_2O_2 in methanol for 10 min at RT to inactivate endogenous peroxidase. The sections were treated with rabbit anti-human IL-26 mAb, and subsequently treated with HRP-conjugated anti-rabbit Ig antibody (Vector Laboratories, Inc., Burlingame, CA) for 30 min at RT. The reaction was visualized with 3,3′-diaminobenzidine (DAB)

(Dojindo Laboratories, Kumamoto, Japan). After DAB staining, the sections were washed in distilled water, then boiled in 10 mM citrate buffer (pH 6.0) for 5 min at 100 °C to remove antibodies. The sections were subsequently treated with mouse anti-human CD4 mAb, anti-CD8 mAb, anti-CD68 mAb, or anti-CD163 mAb, respectively at 4 °C overnight, and then treated with HRP-conjugated anti-mouse Ig antibody (Vector Laboratories, Inc). The reaction was visualized with Vector SG Reagent (Vector Laboratories, Inc), and the tissue sections were counterstained for the nucleus with hematoxylin. The optical images were taken using Zeiss inverted microscope and Axiovision 2.0 program. Histological studies were conducted in the Department of Breast Oncology of Juntendo University (Tokyo, Japan) after official approval of the Juntendo University School of Medicine Review Board was obtained (No: 17-252).

Statistics

Data were analyzed by two-tailed Student *t*-test for two-group comparison or by one-way ANOVA test with Tukey's for multiple comparison testing. Data are presented as mean ± S.D. of triplicate samples of the representative in vitro experiment, or mean ± S.E. of three independent in vivo experiments. Significance was analyzed using MS Excel (Microsoft) and values of $p < 0.01$ were considered significant and are indicated in the corresponding figures and figure legends.

Acknowledgements
We thank members of Atopy (Allergy) Research Center (Juntendo University Graduate School of Medicine, Japan), members of the Laboratory of Morphology and Image Analysis, Research Support Center (Juntendo University Graduate School of Medicine, Japan), and members of the Laboratory of Cell Biology, Research Support Center (Juntendo University Graduate School of Medicine, Japan) for technical assistance and for the use of the experimental apparatus.

Author details
[1]Department of Therapy Development and Innovation for Immune Disorders and Cancers, Graduate School of Medicine, Juntendo University, 2-1-1, Hongo, Bunkyo-ku, Tokyo 113-8421, Japan. [2]Atopy (Allergy) Research Center, Graduate School of Medicine, Juntendo University, 2-1-1, Hongo, Bunkyo-ku, Tokyo 113-8421, Japan. [3]Department of Breast Oncology, School of Medicine, Juntendo University, 2-1-1, Hongo, Bunkyo-ku, Tokyo 113-8421, Japan. [4]Department of Pathology, Saitama Medical University, 38 Morohongo, Moroyama-machi, Iruma-gun, Saitama 350-0495, Japan. [5]Department of Pathology, Keio University School of Medicine, 35 Shinanomachi, Shinjuku-ku, Tokyo 160-8582, Japan. [6]Department of Immunological Diagnosis, Graduate School of Medicine, Juntendo University, 2-1-1, Hongo, Bunkyo-ku, Tokyo 113-8421, Japan. [7]Department of Hematology, Juntendo University Shizuoka Hospital, 1129 Nagaoka, Izunokuni, Shizuoka 410-2295, Japan. [8]Department of Medicine, Vanderbilt University School of Medicine, Vanderbilt University Medical Center, Nashville, TN 37232, USA. [9]Division of Hematology/Oncology, University of Florida, 1600 SW Archer Road-Box 100278, Room MSB M410A, Gainesville, FL 32610, USA. [10]Y's AC Co., Ltd., 2-6-8 Kudanminami, Chiyoda-ku, Tokyo 102-0074, Japan

Author contributions
Conception and design: C.M. and K.O. Development of methodology: T.I, R.H., and H.O. Acquisition of data (provided animals, acquired and managed patients, provided facilities, etc.): T.I., R.H., D.S., T.Y., H.O., Y.S., and Y.H. Analysis and interpretation of data (e.g., statistical analysis, biostatistics, computational analysis): R.H., Y.H., Y.K., and K.O. Writing, review, and/or revision of the manuscript: T.I., R.H., N.H.D., C.M., and K.O. Review on English language as a native English speaker: N.H.D. Administrative, technical, or material support (i.e., reporting or organizing data, constructing databases): S.M., N.I., Y.H., and T.M.A. Study supervision: K.O. and C.M.

Funding
This study was supported in part by a grant of the Ministry of Health, Labour, and Welfare, Japan (Grant Numbers 180101-01 (C.M.)), JSPS KAKENHI Grant Numbers JP19K21278 (T.I.), JP20K07683 (R.H.), JP20H03471 (C.M.), and JP18H02782 (K.O.).

Data availability
All data generated or analyzed during this study are included in this published article and its Supplementary Information files.

Ethics approval
Animal experiments were conducted following protocols approved by the Animal Care and Use Committees at Juntendo University (300070). For clinical samples, human study protocols were approved by the Ethics Committees at Juntendo University Hospital (no: 17-252) and all specimens were collected after obtaining informed consent from the patients. All experiments were performed in accordance with relevant guidelines and regulations.

Conflict of interest
T.I., R.H, C.M., and K.O. are the patent holders of anti-IL26 mAbs. The remaining authors declare no competing interests.

Supplementary information The online version contains supplementary material available at https://doi.org/10.1038/s41419-021-03787-5.

Received: 9 January 2021 Revised: 1 May 2021 Accepted: 3 May 2021
Published online: 21 May 2021

References

1. Garrido-Castro, A. C., Lin, N. U. & Polyak, K. Insights into molecular classifications of triple-negative breast cancer: improving patient selection for treatment. *Cancer Discov.* **9**, 176–198 (2019).
2. Dent, R. et al. Triple-negative breast cancer: clinical features and patterns of recurrence. *Clin. Cancer Res.* **13**, 4429–4434 (2007).
3. Foulkes, W. D., Smith, I. E. & Reis-Filho, J. S. Triple-negative breast cancer. *N. Engl. J. Med.* **363**, 1938–1948 (2010).
4. Bianchini, G., Balko, J. M., Mayer, I. A., Sanders, M. E. & Gianni, L. Triple-negative breast cancer: challenges and opportunities of a heterogeneous disease. *Nat. Rev. Clin. Oncol.* **13**, 674–690 (2016).
5. Nakhjavani, M., Hardingham, J. E., Palethorpe, H. M., Price, T. J. & Townsend, A. R. Druggable molecular targets for the treatment of triple negative breast cancer. *J. Breast Cancer* **22**, 341–361 (2019).
6. Ciardiello, F. & Tortora, G. EGFR antagonists in cancer treatment. *N. Engl. J. Med.* **358**, 1160–1174 (2008).
7. Liang, Y. J. et al. Interaction of glycosphingolipids GD3 and GD2 with growth factor receptors maintains breast cancer stem cell phenotype. *Oncotarget* **8**, 47454–47473 (2017).
8. McLaughlin, R. P. et al. A kinase inhibitor screen identifies a dual cdc7/CDK9 inhibitor to sensitise triple-negative breast cancer to EGFR-targeted therapy. *Breast Cancer Res.* **21**, 77 (2019).
9. Nakai, K., Hung, M. C. & Yamaguchi, H. A perspective on anti-EGFR therapies targeting triple-negative breast cancer. *Am. J. Cancer Res.* **6**, 1609–1623 (2016).
10. Costa, R. et al. Targeting epidermal growth factor receptor in triple negative breast cancer: new discoveries and practical insights for drug development. *Cancer Treat. Rev.* **53**, 111–119 (2017).

11. Fickenscher, H. & Pirzer, H. Interleukin-26. *Int. Immunopharmacol.* **4**, 609–613 (2004).
12. Stephen-Victor, E., Fickenscher, H. & Bayry, J. IL-26: an emerging proinflammatory member of the IL-10 cytokine family with multifaceted actions in antiviral, antimicrobial, and autoimmune responses. *PLoS Pathog.* **12**, e1005624 (2016).
13. Ohnuma, K. et al. Regulation of pulmonary graft-versus-host disease by IL-26+CD26+CD4 T lymphocytes. *J. Immunol.* **194**, 3697–3712 (2015).
14. Itoh, T. et al. Biological effects of IL-26 on T cell-mediated skin inflammation, including psoriasis. *J. Invest. Dermatol.* **139**, 878–889 (2019).
15. Collins, P. L. et al. Distal regions of the human IFNG locus direct cell type-specific expression. *J. Immunol.* **185**, 1492–1501 (2010).
16. You, W. et al. IL-26 promotes the proliferation and survival of human gastric cancer cells by regulating the balance of STAT1 and STAT3 activation. *PLoS ONE* **8**, e63588 (2013).
17. Xi, Z. F. et al. Expression of IL-26 predicts prognosis of patients with hepatocellular carcinoma after surgical resection. *Hepatobiliary Pancreat. Dis. Int.* **18**, 242–248 (2019).
18. Xue, T., Yang, J., Song, P. & Zhou, G. Investigation on correlations of serum IL-26 with diagnosis and staging of gastric cancer. *J. Buon.* **24**, 215–220 (2019).
19. Donnelly, R. P. et al. Interleukin-26: an IL-10-related cytokine produced by Th17 cells. *Cytokine Growth Factor Rev.* **21**, 393–401 (2010).
20. Zhivotovsky, B. & Orrenius, S. Calcium and cell death mechanisms: a perspective from the cell death community. *Cell Calcium* **50**, 211–221 (2011).
21. Garg, A. D. et al. ER stress-induced inflammation: does it aid or impede disease progression? *Trends Mol. Med.* **18**, 589–598 (2012).
22. Metcalf, M. G., Higuchi-Sanabria, R., Garcia, G., Tsui, C. K. & Dillin, A. Beyond the cell factory: Homeostatic regulation of and by the UPR(ER). *Sci. Adv.* **6**, eabb9614 (2020).
23. Madeo, F. & Kroemer, G. Intricate links between ER stress and apoptosis. *Mol. Cell.* **33**, 669–670 (2009).
24. Pihán, P., Carreras-Sureda, A. & Hetz, C. BCL-2 family: integrating stress responses at the ER to control cell demise. *Cell Death Differ.* **24**, 1478–1487 (2017).
25. Corazzari, M., Gagliardi, M., Fimia, G. M. & Piacentini, M. Endoplasmic reticulum stress, unfolded protein response, and cancer cell fate. *Front. Oncol.* **7**, 78 (2017).
26. Galluzzi, L. et al. Molecular mechanisms of cell death: recommendations of the Nomenclature Committee on Cell Death 2018. *Cell Death Differ.* **25**, 486–541 (2018).
27. Liu, J. et al. Role of ATF3 in synergistic cancer cell killing by a combination of HDAC inhibitors and agonistic anti-DR5 antibody through ER stress in human colon cancer cells. *Biochem. Biophys. Res. Commun.* **445**, 320–326 (2014).
28. Edagawa, M. et al. Role of activating transcription factor 3 (ATF3) in endoplasmic reticulum (ER) stress-induced sensitization of p53-deficient human colon cancer cells to tumor necrosis factor (TNF)-related apoptosis-inducing ligand (TRAIL)-mediated apoptosis through up-regulation of death receptor 5 (DR5) by zerumbone and celecoxib. *J. Biol. Chem.* **289**, 21544–21561 (2014).
29. Luo, J. et al. GRP78 inhibition enhances ATF4-induced cell death by the deubiquitination and stabilization of CHOP in human osteosarcoma. *Cancer Lett.* **410**, 112–123 (2017).
30. Liu, Z. et al. Activating transcription factor 4 (ATF4)-ATF3-C/EBP homologous protein (CHOP) cascade shows an essential role in the ER stress-induced sensitization of tetrachlorobenzoquinone-challenged PC12 cells to ROS-mediated apoptosis via death receptor 5 (DR5) signaling. *Chem. Res Toxicol.* **29**, 1510–1518 (2016).
31. Tang, Q. et al. Withaferin A triggers G2/M arrest and intrinsic apoptosis in glioblastoma cells via ATF4-ATF3-CHOP axis. *Cell Prolif.* **53**, e12706 (2020).
32. Hong, S. et al. EGFR inhibitor-driven endoplasmic reticulum stress-mediated injury on intestinal epithelial cells. *Life Sci.* **119**, 28–33 (2014).
33. Boyd, A. W., Bartlett, P. F. & Lackmann, M. Therapeutic targeting of EPH receptors and their ligands. *Nat. Rev. Drug Discov.* **13**, 39–62 (2014).
34. Janes, P. W. et al. EphA3 biology and cancer. *Growth Factors* **32**, 176–189 (2014).
35. Boyd, A. W. et al. Isolation and characterization of a novel receptor-type protein tyrosine kinase (hek) from a human pre-B cell line. *J. Biol. Chem.* **267**, 3262–3267 (1992).
36. Chiari, R. et al. Identification of a tumor-specific shared antigen derived from an Eph receptor and presented to CD4 T cells on HLA class II molecules. *Cancer Res.* **60**, 4855–4863 (2000).
37. Lisabeth, E. M., Fernandez, C. & Pasquale, E. B. Cancer somatic mutations disrupt functions of the EphA3 receptor tyrosine kinase through multiple mechanisms. *Biochemistry* **51**, 1464–1475 (2012).
38. Vecchi, M. et al. Breast cancer metastases are molecularly distinct from their primary tumors. *Oncogene* **27**, 2148–2158 (2008).
39. Knappe, A., Hor, S., Wittmann, S. & Fickenscher, H. Induction of a novel cellular homolog of interleukin-10, AK155, by transformation of T lymphocytes with herpesvirus saimiri. *J. Virol.* **74**, 3881–3887 (2000).
40. Ohnuma, K. et al. Role of IL-26+CD26+CD4 T cells in pulmonary chronic graft-versus-host disease and treatment with caveolin-1-Ig Fc conjugate. *Crit. Rev. Immunol.* **36**, 239–267 (2016).
41. Corridoni, D. et al. Single-cell atlas of colonic CD8(+) T cells in ulcerative colitis. *Nat. Med.* **26**, 1480–1490 (2020).
42. Hatano, R. et al. Characterization of novel anti-IL-26 neutralizing monoclonal antibodies for the treatment of inflammatory diseases including psoriasis. *MAbs* **11**, 1428–1442 (2019).
43. Sun, H. et al. Natural killer cell-derived exosomal miR-3607-3p inhibits pancreatic cancer progression by targeting IL-26. *Front Immunol.* **10**, 2819 (2019).
44. Trotter, T. N. et al. IL26, a noncanonical mediator of DNA inflammatory stimulation, promotes TNBC engraftment and progression in association with neutrophils. *Cancer Res.* **80**, 3088–3100 (2020).
45. Terai, H. et al. ER stress signaling promotes the survival of cancer "persister cells" tolerant to EGFR tyrosine kinase inhibitors. *Cancer Res.* **78**, 1044–1057 (2018).
46. Chen, X. et al. XBP1 promotes triple-negative breast cancer by controlling the HIF1α pathway. *Nature* **508**, 103–107 (2014).
47. Li, Y. et al. Free cholesterol-loaded macrophages are an abundant source of tumor necrosis factor-alpha and interleukin-6: model of NF-kappaB- and map kinase-dependent inflammation in advanced atherosclerosis. *J. Biol. Chem.* **280**, 21763–21772 (2005).
48. Kou, C. J. & Kandpal, R. P. Differential expression patterns of Eph receptors and ephrin ligands in human cancers. *Biomed. Res. Int.* **2018**, 7390104 (2018).
49. Sjöblom, T. et al. The consensus coding sequences of human breast and colorectal cancers. *Science* **314**, 268–274 (2006).
50. Ding, L. et al. Somatic mutations affect key pathways in lung adenocarcinoma. *Nature* **455**, 1069–1075 (2008).
51. Balakrishnan, A. et al. Novel somatic and germline mutations in cancer candidate genes in glioblastoma, melanoma, and pancreatic carcinoma. *Cancer Res.* **67**, 3545–3550 (2007).
52. Bonifaci, N. et al. Exploring the link between germline and somatic genetic alterations in breast carcinogenesis. *PLoS ONE* **5**, e14078 (2010).
53. Merlos-Suárez, A. & Batlle, E. Eph-ephrin signalling in adult tissues and cancer. *Curr. Opin. Cell Biol.* **20**, 194–200 (2008).
54. Brantley-Sieders, D. M. et al. The receptor tyrosine kinase EphA2 promotes mammary adenocarcinoma tumorigenesis and metastatic progression in mice by amplifying ErbB2 signaling. *J. Clin. Invest.* **118**, 64–78 (2008).
55. Alford, S. C., Bazowski, J., Lorimer, H., Elowe, S. & Howard, P. L. Tissue transglutaminase clusters soluble A-type ephrins into functionally active high molecular weight oligomers. *Exp. Cell Res.* **313**, 4170–4179 (2007).
56. Aoki, M., Yamashita, T. & Tohyama, M. EphA receptors direct the differentiation of mammalian neural precursor cells through a mitogen-activated protein kinase-dependent pathway. *J. Biol. Chem.* **279**, 32643–32650 (2004).
57. Hattori, M., Osterfield, M. & Flanagan, J. G. Regulated cleavage of a contact-mediated axon repellent. *Science* **289**, 1360–1365 (2000).
58. Aasheim, H. C. et al. A splice variant of human ephrin-A4 encodes a soluble molecule that is secreted by activated human B lymphocytes. *Blood* **95**, 221–230 (2000).
59. Clifford, N. et al. The EphA3 receptor is expressed in a subset of rhabdomyosarcoma cell lines and suppresses cell adhesion and migration. *J. Cell Biochem.* **105**, 1250–1259 (2008).
60. Pasquale, E. B. Eph receptors and ephrins in cancer: bidirectional signalling and beyond. *Nat. Rev. Cancer* **10**, 165–180 (2010).
61. Meller, S. et al. T(H)17 cells promote microbial killing and innate immune sensing of DNA via interleukin 26. *Nat. Immunol.* **16**, 970–979 (2015).
62. Kamijo, H. et al. Increased IL-26 expression promotes T helper type 17- and T helper type 2-associated cytokine production by keratinocytes in atopic dermatitis. *J. Invest. Dermatol.* **140**, 636–644.e632 (2020).
63. Peng, J. et al. EPHA3 regulates the multidrug resistance of small cell lung cancer via the PI3K/BMX/STAT3 signaling pathway. *Tumour Biol.* **37**, 11959–11971 (2016).

Kaneko et al. Biomarker Research (2021) 9:21
https://doi.org/10.1186/s40364-021-00273-0

Biomarker Research

RESEARCH Open Access

Serum soluble CD26/DPP4 titer variation is a potential prognostic biomarker in cancer therapy with a humanized anti-CD26 antibody

Yutaro Kaneko[1*], Ryo Hatano[2], Naoto Hirota[3], Nicolas Isambert[4], Véronique Trillet-Lenoir[5], Benoit You[5], Jérôme Alexandre[6], Gérard Zalcman[7], Fanny Valleix[8], Thomas Podoll[9], Yoshimi Umezawa[3], Seiichi Takao[3], Satoshi Iwata[2], Osamu Hosono[10], Tetsuo Taguchi[11], Taketo Yamada[12,13], Nam H. Dang[14], Kei Ohnuma[2], Eric Angevin[15] and Chikao Morimoto[2]

Abstract

Background: The phase I trial of the humanized anti-CD26 monoclonal antibody YS110 for CD26-expressing tumors was conducted recently. The present study identifies a potential prognostic biomarker for CD26-targeted therapy based on the phase I data.

Methods: *Box and Whisker plot* analysis, *Scatter plot* analysis, *Peason product moment correlation/Spearman's rank-difference correlation*, *Bar graph* analysis, and *Receiver Operating Characteristics (ROC)* were used to examine the correlation between sCD26 titer variation with YS110 administration and tumor volume change, RECIST criteria evaluation and progression free survival (PFS). Mechanism for serum sCD26 titer variation was confirmed by in vitro experimentation.

Results: Serum sCD26/DPP4 titer was reduced following YS110 administration and gradually recovered until the next infusion. Serum sCD26/DPP4 titer before the next infusion was sustained at lower levels in Stable Disease (SD) cases compared to Progressive Disease cases. *ROC* analysis defined the cut-off level of serum sCD26/DPP4 titer variation at day 29 pre/post for the clinical outcome of SD as tumor response or PFS. In vitro experimentation confirmed that YS110 addition reduced sCD26 production from CD26-expressing tumor and non-tumor cells.

Conclusions: Our study indicates that serum sCD26/DPP4 titer variation in the early phase of YS110 treatment is a predictive biomarker for evaluating therapeutic efficacy.

Keywords: Serum soluble CD26/dipeptidyl peptidase 4, YS110, Prognostic biomarker, Cancer therapy

* Correspondence: y.kaneko@ys-ac.com
This study was based on further analyses of data obtained in the phase I clinical study which was published in *British Journal of Cancer*. 2017; 116(9): 1126-1134.
[1]Y's AC Co., Ltd., 2-6-8, Kudan-minami, Chiyoda-ku, Tokyo 102-0074, Japan
Full list of author information is available at the end of the article

Background

CD26 is a 110-kDa, type II transmembrane glycoprotein with dipeptidyl peptidase 4 (DPP4) activity in its extracellular domain, capable of cleaving N-terminal dipeptides with L-proline or L-alanine at the penultimate position [1, 2]. CD26 has multiple biological functions and is expressed on various normal cell types and tumors. CD26 is also found as a soluble form with conserved DPP4 activity in the serum and other body fluids. In vitro and in vivo administration of anti-CD26 mAb inhibits tumor growth, migration and invasion via multiple mechanisms of action, leading to enhanced survival of mouse xenograft models inoculated with various cancers including renal cell carcinoma (RCC) and malignant mesothelioma (MM) [3–7].

The first-in-human (FIH) phase I clinical study of YS110 for CD26-expressing solid tumors (23 MM, 9 RCC and 1 urothelial carcinoma (UTC)) was recently conducted [8], demonstrating that YS110 therapy exhibited a favorable safety profile and resulted in encouraging disease control in patients with advanced/refractory tumors.

Biomarkers in cancer management may be used for the prevention, diagnosis, and selection of therapeutic method, as well as for treatment monitoring potentially. Such markers as EGFR or ALK fusion gene (lung cancer), HER2 (breast or gastric cancer), or RAS (colon cancer) are used to select optimal therapy by identifying selected genetic alteration. However, no serum biomarker indicating a predictive outcome during a course of cancer treatment has been heretofore identified.

Serum level of soluble CD26 (sCD26) has been previously evaluated as a potential biomarker. A correlation between baseline serum sCD26 titer and clinical effectiveness of therapy has been described for patients with urothelial, gastric, pancreatic, thyroid, or lung cancer [9–14]. Serum sCD26 titer variation after colon cancer surgery was also reported to be a predictive biomarker for risk of recurrence or metastasis [15–17]. In addition, treatment with the DPP4 inhibitor sitagliptin after surgery for colorectal or lung cancer in patients with diabetes was associated with greater overall survival than treatment with other diabetic medications [18], suggesting that sCD26/DPP4 may have a role in regulating antitumor activity. However, there has been no report of serum sCD26 titer variation during a course of therapy being a prognostic marker of treatment outcome.

In the phase I FIH clinical trial with the humanized antibody YS110 for patients with CD26-expressing tumors, a transient decrease followed by subsequent recovery of serum sCD26/DPP4 titer level was observed during the 4-week period of the first cycle of YS110 administration. In the present study, the correlation between variation in sCD26/DPP4 titer and efficacy metrics as determined by response by RECIST criteria or progression free survival (PFS) was analyzed in a total of 26 evaluable cases or in stratified groups, to identify a potential prognostic biomarker for YS110 therapy.

Materials and methods

Human subjects

In the FIH phase I clinical trial, 33 patients (23 MM, 9 RCC and 1 UTC) who received YS110 were included in the safety analysis, and 26 out of 33 patients (19 MM, 6 RCC and 1 UTC) were evaluable for treatment efficacy, as described previously [8]. To determine the maximum tolerated dose, patients initially received a total of three YS110 infusions on days 1, 15 and 29 (once every 2 weeks, Q2W) at 0.1, 0.4, 1 and 2 mg/kg. On the basis of preliminary pharmacokinetics data, the protocol was then subsequently amended to allow patients to receive a total of five YS110 infusions on days 1, 8, 15, 22 and 29 (once every week, Q1W) at 2, 4 and 6 mg/kg. Among 33 patients, 26 patients (18 and 8 cases in Q2W and Q1W cohorts, respectively) were evaluable for YS110-mediated anti-tumor activity by RECIST criteria or PFS monitoring. Tumor volume variation from baseline was evaluated by a modified RECIST criteria for MM, or by RECIST 1.0 criteria for RCC or UTC on day 43 ± 4.2, two weeks following the completion of the first cycle of YS110 administration on day 29 [8]. Serum sCD26/DPP4 titer was measured immediately prior to and following YS110 administration on days 1, 15 and 29.

Statistical analyses

Box and Whisker plot analysis was employed to observe variation of serum sCD26/DPP4 titer pre/post YS110 infusion on day 1, 15 and 29. *Scatter plot* analysis stratified for Stable Disease (SD) and Progressive Disease (PD) cases was employed to observe a relationship between variation of serum sCD26 titer pre/post YS110 administration on day 1, 15 and 29 and tumor volume variation from baseline on day 43. These two observational analyses then led to the usage of *PPMC* or *SRDC* analysis for the statistical examination of potential correlation between serum sCD26 titer variation from baseline pre/post YS110 administration on days 1, 15 and 29 and tumor volume variation by RECIST criteria on day 43, and PFS. Based on *Pearson product moment correlation/Spearman's rank-difference correlation (PPMC/SRDC)* analyses, *Bar graph* analysis of the variation of serum sCD26/DPP4 titer as stratified by SD and PD cases on day 1pre (baseline, 100%), 15pre and 29pre of YS110 administration was performed to examine for correlation between serum sCD26/DPP4 variation and the incidence of SD or PD cases by RECIST criteria on day 43 with *Wilcoxon's rank sum test*. Based on results from *PPMC/SRDC and Bar graph* analyses, *Receiver Operating*

Characteristics (ROC) analysis was employed to examine the Index (cut-off titer) of serum sCD26 titer variation from baseline for the Outcome of SD by RECIST criteria, PFS ≥ 90, or ≥ 180 days, with *Fisher's exact test*. Difference in background factors between SD and PD cases was examined by *Fisher's exact test* or *Wilcoxon rank sum test* prior to *ROC* analysis.

Cell lines and cultures

Human MM cell lines MSTO-211H (MSTO parent) and NCI-H226 were obtained from the American Type Culture Collection (ATCC, Rockville, MD). MSTO parent cells were stably transfected with a full-length human CD26 (MSTO-CD26) [6]. Human MM cell line JMN cells were transduced with the short hairpin RNA (shRNA)-expressing lentivirus, generating the stable cell lines JMN CD26-shRNA and JMN ctrl-shRNA [19]. For non-tumor human cells, immortalized pleural mesothelial cell line MeT-5A, mammary epithelial cell line MCF10A, fetal lung fibroblast cell line TIG-1, human umbilical vein endothelial cells (HUVEC), and human dermal microvascular endothelial cells (HDMVEC) were used. MeT-5A and MCF10A were obtained from ATCC. TIG-1 was obtained from JCRB Cell Bank (Osaka, Japan). HUVEC, HDMVEC and the culture media for MCF10A, HUVEC, HDMVEC (MEGM, EGM-2, EGM-2MV, respectively) were purchased from LONZA (Walkersville, MD). MSTO parent, MSTO-CD26, JMN ctrl-shRNA, JMN CD26-shRNA, H226 and MeT-5A were grown in RPMI 1640 medium supplemented with 10% FBS. TIG-1 was grown in DMEM medium supplemented with 10% FBS. All the cells were cultured at 37 °C in a humidified 5% CO_2 incubator.

Abs and reagents

Humanized anti-CD26 mAb YS110 was provided by Y's AC Co., Ltd. (Tokyo, Japan) [5]. Human IgG_1 isotype control mAb (clone QA16A12) purchased from BioLegend (San Diego, CA) was used as a control.

Preparation of culture supernatant

Cells were cultured in 500 μl of culture medium in 24-well plates (Corning) in the presence or absence of control human IgG or YS110 for 3 days at 37 °C. For time-course analysis, MSTO-CD26 (1.5×10^5, 4×10^4, or 4×10^3) were cultured in 500 μl of RPMI 1640 medium in 24-well plates in the presence or absence of YS110 (1, 3, 10 μg/ml) at 37 °C for 1, 3, or 7 days, respectively. After incubation, supernatants were collected from confluent cultures.

Quantification of soluble CD26 and DPP4 enzyme activity

Assays for soluble CD26 and DPP4 activity were developed in our laboratory utilizing mouse anti-human CD26 mAbs (clone 5F8 and 9C11) which exhibit no cross-reactivity with the therapeutic humanized anti-CD26 mAb YS110. The relevant experimental methods were detailed previously [20]. Data were analyzed by one-way ANOVA test with Tukey's for multiple comparison testing. Significance was analyzed using GraphPad Prism 6 (GraphPad Software, San Diego, CA). Values of $p < 0.01$ were considered significant and are indicated in the corresponding figures and figure legends.

Results

Changes in levels of serum sCD26/DPP4 titer pre/post YS110 administration, as documented by *Box and Whisker plot*

Several crucial parameters were included in this phase I trial such as 1) tumor histology: 19 MM, 6 RCC and 1 UTC; 2) YS110 dose: 0.1–6 mg/kg; 3) frequency of drug administration: once every 2 weeks (Q2W) for three doses in 18 cases, once every week (Q1W) for five doses in 8 cases. In addition, examination of background factors between SD and PD cases indicated that no bias was found in age, BMI, absolute value of tumor volume or serum sCD26/DPP4 titer before YS110 administration, except for gender (data not shown). In contrast to male patients (4 SD and 7 PD in MM, and 2 SD and 3 PD in RCC), YS110 appeared to be more effective in female patients (6 SD and 2 PD in MM, 1 SD in RCC, and 1PD in UTC), as shown in Additional file 1 (Tables S1) and file 2 (Table S2). Since the number of cases in each antibody dose cohort was not sufficient for statistical analysis, in the present study, a total of 26 cases were further categorized by 1) tumor histology and 2) frequency of drug administration, to examine whether serum sCD26 titer variation can be a prognostic biomarker for YS110 treatment. Detailed information regarding these 26 cases is shown in Additional file 1 (Tables S1).

We first examined serum sCD26 titer variation during a course of YS110 treatment in each group by *Box and Whisker plot* analysis. Serum sCD26 titer was consistently reduced immediately following YS110 administration on day 1, 15, 29, and gradually recovered until the next YS110 infusion, although it never returned to its former pre-dosing level (Fig. 1a). This pattern was similarly observed in the 18 cases treated on the Q2W drug administration schedule (Fig. 1b). In contrast, a clear difference was observed in the 8 cases treated on the Q1W schedule. As shown in Additional file 1 (Tables S1), relatively high antibody dose (2–6 mg/kg) was administered in the Q1W cases as compared with the Q2W cases (0.1–2 mg/kg). These differences in antibody dose and administration frequency strongly affected the serum sCD26 titer on day 15pre and day 29pre (Fig. 1d). Recovery of serum sCD26 titer following YS110 administration

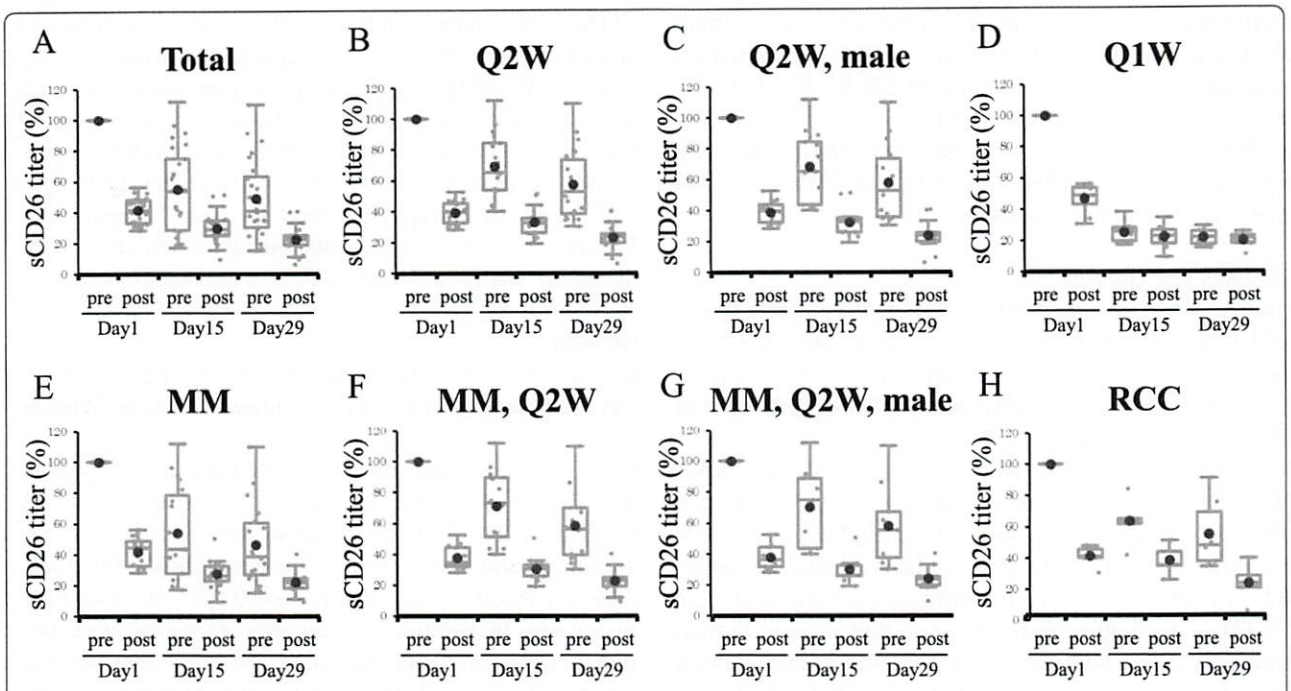

Fig. 1 Changes in serum sCD26 levels following YS110 administration by *Box and Whisker plot* analysis. Each plot indicated the serum sCD26 titer variation from baseline (day 1pre, 100%) to pre/post of YS110 administration on days 1, 15 and 29. Analyzed data were stratified into **a** total 26 cases, **b** 18 cases with Q2W administration, **c** 14 male cases with Q2W administration, **d** 8 cases with Q1W administration, **e** 19 MM cases, **f** 12 MM cases with Q2W administration, **g** 9 MM, male cases with Q2W administration, **h** 6 RCC cases. Data are shown as mean ± S.D. in each group

was not clearly observed with the more frequent drug administration of the Q1W cases. Fourteen male cases and 4 female cases received Q2W administration, while 2 male cases and 6 female cases received Q1W administration (Additional file 2 (Table S2)). The distribution bias between the male cases with Q2W and Q1W administration and the female cases with Q2W and Q1W administration was significant ($p = 0.026$ by Fisher's exact test). In addition, the number of cases in the Q1W cohort (8 cases) was not sufficient for additional statistical analysis. Therefore, we mainly focused on the Q2W cases and the male cases for additional analyses. The initial fall and subsequent recovery of serum sCD26 titer were similarly observed in both the 19 MM cases and 6 RCC cases (Fig. 1e and h), including upon further stratification of the groups into such cohorts as the 14 male cases with Q2W administration, 12 MM cases with Q2W administration, and 9 male MM cases with Q2W administration (Fig. 1c, f and g). As shown in Additional file 3 (Fig. S1), the absolute value or titer variation of serum sCD26 titer was strongly correlated with level of serum DPP4 enzyme activity ($r = 0.908$, $p < 0.001$ or $r = 0.974$, $p < 0.001$, respectively). Since YS110 does not directly inhibit DPP4 enzyme activity [21], reduction of serum DPP4 enzyme activity following YS110 administration is therefore due to decreased serum sCD26 protein level.

Differences in serum sCD26/DPP4 titer variation on day 29pre and tumor volume variation on day 43 for SD and PD cohorts by *Scatter plot* analysis

We next investigated a potential relationship between pre/post serum sCD26 titer variation on days 1, 15 and 29, and tumor volume variation on day 43 by *Scatter plot* analysis after the start of YS110 administration, with a total of 25 cases stratified by SD and PD cohorts. The tumor volume variation of the SD group would be expected to naturally be lower than that of the PD group. Serum sCD26 titers were markedly decreased in both SD and PD cohorts immediately post YS110 infusion on days 1, 15 and 29 (Fig. 2a, c and e). On the other hand, a noticeable difference between the SD and PD groups in the serum sCD26 titer variation was observed on day 29pre. Serum sCD26 titer variation on day 29pre of the SD cohort was at a lower level compared with the PD group (Fig. 2d). Moreover, this phenomenon was clearly observed in each stratified group such as the 17 cases with Q2W administration, 14 male cases with Q2W administration, 18 MM cases, 11 MM cases with Q2W administration, 9 male MM cases with Q2W administration, or 6 RCC cases (Fig. 2f-k, respectively). These *Scatter plot* analyses indicate that the serum sCD26 titer variation of the SD cohort was lower than that of the PD cases when measured prior to YS110 administration,

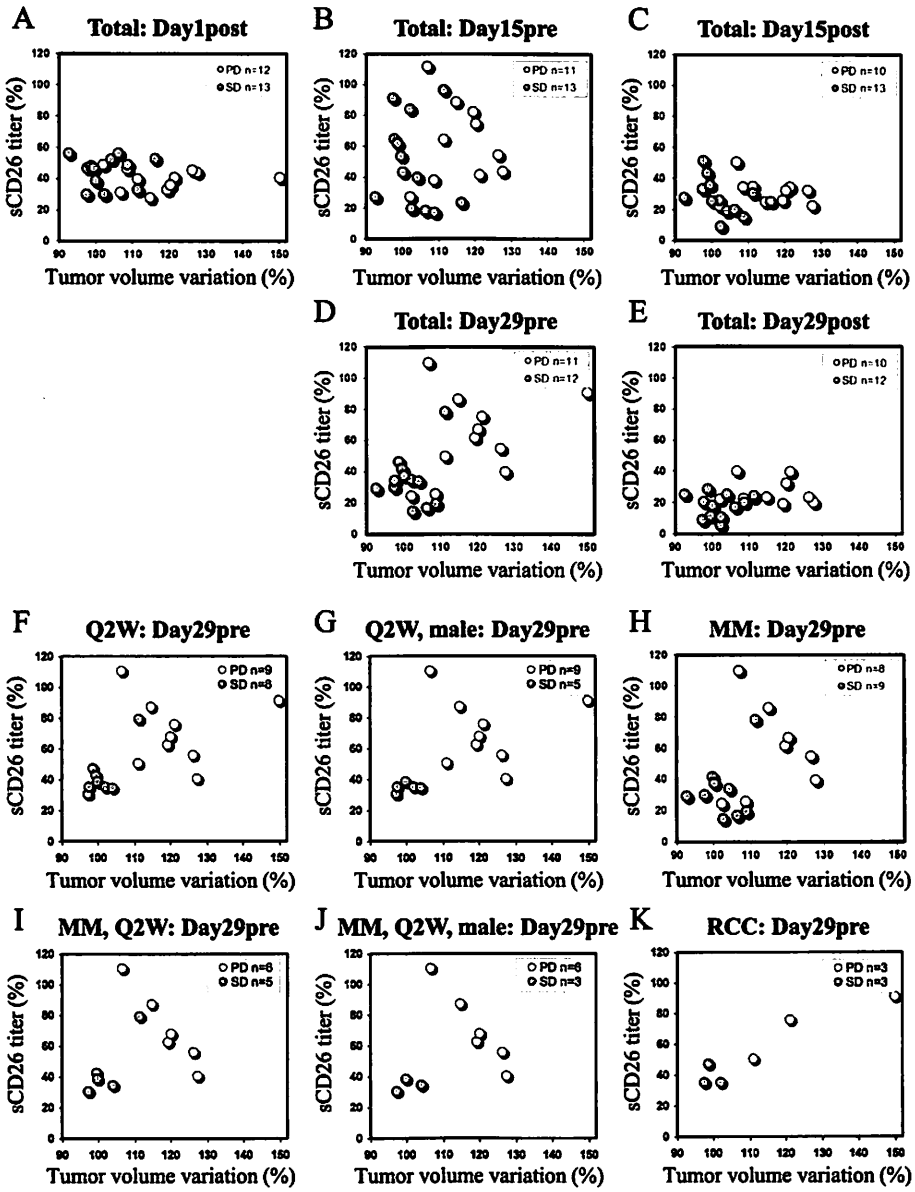

Fig. 2 Relationship between serum sCD26 titer variation and tumor volume variation by *scatter plot* analysis. The serum sCD26 titer variation from baseline (day 1pre, 100%) on **a** day 1post, **b** day 15pre, **c** day 15post, **d** day 29pre, **e** day 29post of YS110 administration, and tumor volume variation by RECIST response criteria on day 43 of a total of 25 cases was plotted. Data were separated into SD (gray circle) and PD (white circle) cohorts. The serum sCD26 titer variation from baseline on day 29pre of YS110 administration, and tumor volume variation by RECIST response criteria on day 43 of **f** 17 cases with Q2W administration, **g** 14 male cases with Q2W administration, **h** 18 MM cases, **i** 11 MM cases with Q2W administration, **j** 9 MM, male cases with Q2W administration, **k** 6 RCC cases with Q2W administration was plotted

and the difference was particularly evident on day 29pre with the Q2W administration.

Correlation of pre/post serum sCD26/DPP4 titer variation on day 29 with tumor volume variation and/or PFS by *PPMC/SRDC* analyses

PPMC and *SRDC* analyses were conducted to examine the correlation between pre/post serum sCD26 titer variation on days 1, 15 and 29, and tumor volume variation as determined by RECIST criteria at day 43 after YS110 administration or PFS. In the FIH phase I clinical trial, 13 cases were assessed as SD and 13 cases were assessed as PD by RECIST, and among the 13 SD cases, YS110 was particularly effective in 7 cases with PFS being longer than 180 days (Additional file 1 (Tables S1)). In a total of 25 cases, statistically significant correlation between day 29pre serum sCD26 titer variation and tumor volume variation on day 43 was observed ($p = 0.006$ or

Table 1 Correlation between serum sCD26/DPP4 titer variation and tumor volume change/PFS by PPMC or SRDC analysis

			Peason' s Product -moment correlation		Spearman' s rank difference correlation	
Var .1	**Var .2**	***n***	**r**	***P* value**	**ρ**	***P* value**
tumor volume %change	PFS	25	- 0. 514	0. 008 **	- 0. 504	0. 014 *
tumor volume %change	sCD26 Day 1 Post	25	- 0. 214	0. 308	- 0. 198	0. 333
〃	sCD26 Day15 Pr e	24	- 0. 085	0. 696	0. 002	0. 993
〃	sCD26 Day15 Post	23	- 0. 115	0. 606	- 0. 169	0. 428
〃	sCD26 Day29 Pr e	23	0. 548	0. 006 *	0. 553	0. 009 **
〃	sCD26 Day29 Post	22	0. 358	0. 102	0. 304	0. 163
〃	DPP4 Day 1 Post	25	- 0. 146	0. 490	- 0. 182	0. 374
〃	DPP4 Day15 Pr e	24	- 0. 068	0. 757	- 0. 023	0. 910
〃	DPP4 Day15 Post	23	- 0. 039	0. 862	- 0. 037	0. 864
〃	DPP4 Day29 Pr e	23	0. 502	0. 014	0. 531	0. 013 *
〃	DPP4 Day29 Post	22	0. 379	0. 082	0. 451	0. 039 *
PFS (days)	sCD26 Day 1 Post	26	0. 047	0. 821	0. 083	0. 678
〃	sCD26 Day15 Pr e	25	- 0. 021	0. 922	- 0. 099	0. 626
〃	sCD26 Day15 Post	24	- 0. 010	0. 964	0. 017	0. 935
〃	sCD26 Day29 Pr e	24	- 0. 351	0. 093	- 0. 205	0. 325
〃	sCD26 Day29 Post	23	- 0. 521	0. 010 **	- 0. 332	0. 119
〃	DPP4 Day 1 Post	26	- 0. 109	0. 600	- 0. 048	0. 809
〃	DPP4 Day15 Pr e	25	- 0. 022	0. 919	- 0. 089	0. 663
〃	DPP4 Day15 Post	24	- 0. 034	0. 877	- 0. 072	0. 732
〃	DPP4 Day29 Pr e	24	- 0. 253	0. 235	- 0. 167	0. 423
〃	DPP4 Day29 Post	23	- 0. 442	0. 034 *	- 0. 381	0. 074

$p = 0.009$ by *PPMC/SRDC*, respectively (Table 1). There was also statistically significant correlation between serum sCD26 titer variation and PFS ($p = 0.011$ by *PPMC* on day 29post for a total 26 cases (Table 1). In addition, there was statistically significant correlation between variation in serum titer of DPP4 enzymatic activity and tumor volume or PFS, similar to the case with serum sCD26 titer (Table 1). Statistically significant correlation was similarly observed in variation between day 29pre serum sCD26/DPP4 titer and tumor volume, and between pre and/or post day 29 serum sCD26/DPP4 titer and PFS in 18 cases with Q2W administration frequency and 14 male cases with Q2W administration frequency (Additional file 4 (Table S3) and file 5 (Table S4)). In 19 MM cases, statistically significant correlation between variation in pre/post day 29 serum DPP4 titer and tumor volume was observed by *SRDC* analysis, while the correlation between day 29pre serum sCD26 titer and tumor volume almost reached statistical significance ($p = 0.065$) by *PPMC* analysis. There was statistically significant correlation between day 29post serum sCD26 titer and PFS by *PPMC* analysis, while the correlation between day 29post serum DPP4 titer and PFS almost reached statistical significance ($p = 0.056$ by *PPMC* or $p = 0.069$ by *SRDC* analysis) (Additional file 6 (Table S5)). In 12 MM cases with Q2W administration frequency, no statistically significant correlation between variation of serum sCD26/DPP4 titer and tumor volume was observed. The correlation between day 29post serum sCD26/DPP4 titer and PFS did reach statistical significance (Additional file 7 (Table S6)). In the 9 male MM cases treated with Q2W administration, no significant difference was observed in variation between serum sCD26/DPP4 titer and tumor volume, although there was a trend for a correlation between pre/post day 29 serum sCD26/DPP4 titer and PFS (Additional file 8 (Table S7)). In the 6 RCC cases and 8 cases treated with Q2W and Q1W administration respectively, the number of cases were not enough for *PPMC/SRDC* statistical analysis. These results indicate that there was a correlation in variation between pre/post day 29 serum sCD26/DPP4 titer (before/after the third YS110 administration) and tumor volume or PFS. Importantly, statistical significance was reached although there was limited number of cases with each stratified cohort, particularly in the 18 cases and 14 male cases treated with Q2W administration.

Day29pre serum sCD26/DPP4 titer of SD cohort was significantly lower than that of PD cohort by *Bar graph* analysis

Based on scatter plot and *PPMC/SRDC* examination, *Bar graph* analysis of day 1pre, 15pre and 29pre serum sCD26 titer variation in SD and PD cases was conducted. Of the total 23 cases (12 SD and 11 PD), serum sCD26 titers of both SD and PD cohorts were reduced from day 1pre to day 29pre samples. Of note, day 29pre serum sCD26 titer variation of SD cases was significantly lower than that of PD cases ($p = 0.016$) (Fig. 3a). Similar results were observed for each stratified group such as the 17 cases treated with Q2W administration ($p = 0.007$), 17 MM cases ($p = 0.068$), 11 MM cases treated with Q2W administration ($p = 0.068$), 9 male MM cases treated with Q2W administration ($p = 0.020$), or 6 RCC cases ($p = 0.049$) (Fig. 3b and e-h). Statistically significant difference between the SD and PD cohorts with the smallest *p*-value was observed in the 14 male cases treated with Q2W administration ($p = 0.003$) (Fig. 3c). In the 8 cases treated with Q1W administration, serum sCD26 titer variation of SD cases was lower than that of PD cases, trending toward statistical significance ($p = 0.053$) on day15pre prior to the third YS110 administration, which represented the same timing for sample collection to evaluate day 29pre serum sCD26 titer in the Q2W treatment schedule (Fig. 3d).

Predictive power of serum sCD26/DPP4 titer variation on outcomes of SD or PFS by *ROC* analysis in the stratified groups

ROC analysis was employed to determine the cut-off titer (the Index) of serum sCD26/DPP4 titer variation on day 29pre/post YS110 administration for the Outcomes of SD and PFS ≥ 90 or ≥ 180 days. Probability was evaluated by *Fisher's exact test* (Table 2). A total of 23 cases was examined to determine the Index (46.4% or 18.2%) for the Outcomes SD, PFS ≥ 90 or ≥ 180 days, with statistically significant results ($p = 0.003$ for SD, and 0.005 or 0.003 for PFS, respectively, and with Area Under the Curve (AUC) 0.795, 0.697 or 0.759, respectively) (Table 2; Column Total). For Column Q2W (17 or 18 cases),

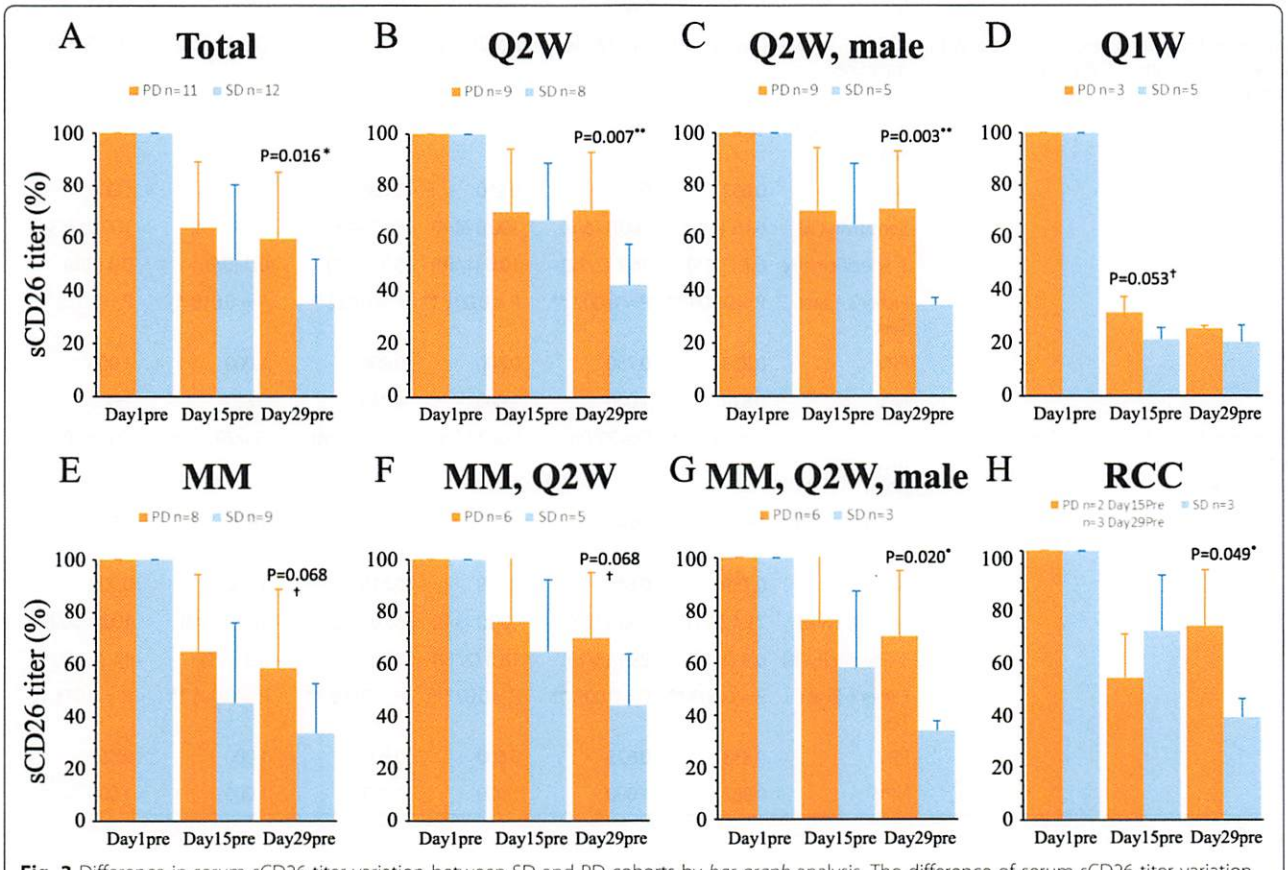

Fig. 3 Difference in serum sCD26 titer variation between SD and PD cohorts by *bar graph* analysis. The difference of serum sCD26 titer variation from baseline (day 1pre, 100%) on day 1pre, day 15pre and day 29pre of YS110 administration between SD and PD cohorts was analyzed. Analyzed data were stratified into **a** total 23 cases, **b** 17 cases with Q2W administration, **c** 14 male cases with Q2W administration, **d** 8 cases with Q1W administration, **e** 17 MM cases, **f** 11 MM cases with Q2W administration, **f** 9 MM, male cases with Q2W administration, **h** 6 RCC cases with Q2W administration. Data are shown as mean ± S.D. in each group

Table 2 ROC analysis

Column No.		Total	Q2W	Q2W, male	MM	MM, Q2W	MM, Q2W, male
Cases of analysis for SD or PFS Outcome		23 cases (SD/PFS)	17 Cases (SD) 18 Cases (PFS)	Male 14 Cases (SD / PFS)	Malignant Mesothelioma 17 Cases (SD) 18Cases (PFS)	Malignant Mesothelioma 11 Cases (SD) 12 Cases (PFS)	Malignant Mesothelioma Male 9 Cases (SD/PFS)
Cases with Administration Frequency	Cases with Q2W	17	17 or 18	14	11 or 12	11 or 12	9
	Cases with Q1W	6	0	0	6	0	0
Outcome: SD Index: Cut-off titer with variation of serum sCD26(%) titer from baseline	sCD26 measured point	Day29 Pre	Day29 Pre	Day29 Pre	Day29 Post	Day29 Post	Day29 Pre
	Index: Cut-off values	46.4	46.4	37.7	18.2	18.2	37.7
	AUC	0.795	0.888	1.000	0.736	0.733	1.000
	Sensitivity(%)	91.7 (11/12)	87.5 (7/8)	100.0 (5/5)	55.6 (5/9)	60.0 (3/5)	100.0 (3/3)
	1-Specificity(%)	27.3 (3/11)	11.1 (1/9)	0.0 (0/9)	0.0 (0/8)	0.0 (0/6)	0.0 (0/6)
	Fisher's Exact Test	P = 0.003 **	P = 0.003 **	P < 0.001 **	*P* = 0.029 *	*P* = 0.061 †	*P* = 0.012 *
	PPV	0.786	0.875	1.000	1.000	1.000	1.000
	NPV	0.889	0.889	1.000	0.667	0.750	1.000
Outcome: PFS > 90 Index: Cut-off titer with variation of serum sCD26(%) titer from baseline	sCD26 measured point	Day29 Post	Day29 Pre	Day29 Pre	Day29 Post	Day29 Post	Day29 Pre
	Index: Cut-off values	18.2	46.4	37.7	18.2	18.2	37.7
	AUC	0.692	0.917	0.950	0.708	0.812	1.000
	Sensitivity(%)	62.5 (5/8)	100.0 (6/6)	100.0 (4/4)	66.7 (4/6)	75.0 (3/4)	100.0 (3/3)
	1-Specificity(%)	6.7 (1/15)	16.7 (2/12)	10.0 (1/10)	8.3 (1/12)	0.0 (0/8)	0.0 (0/6)
	Fisher's Exact Test	P = 0.009 **	*P* = 0.002 **	P < 0.001 **	*P* = 0.022 *	*P* = 0.018 *	P = 0.012 *
	PPV	0.833	0.750	0.800	0.800	1.000	1.000
	NPV	0.824	1.000	1.000	0.846	0.889	1.000
Outcome: PFS > 180 Index: Cut-off titer with variation of serum sCD26(%) titer from baseline	sCD26 measured point	Day29 Post	Day29 Pre	Day29 Pre	Day29 Post	Day29 Post	Day29 Pre
	Index: Cut-off values	18.2	46.4	37.7	18.2	18.2	37.7
	AUC	0.759	0.846	0.879	0.815	1.000	0.929
	Sensitivity(%)	71.4 (5/7)	100.0 (5/5)	100.0 (3/3)	80.0 (4/5)	100.0 (3/3)	100.0 (2/2)
	1-Specificity(%)	6.3 (1/16)	23.1 (3/13)	18.2 (2/11)	7.7 (1/13)	0.0 (0/9)	14.3 (1/7)
	Fisher's Exact Test	P = 0.003 **	P = 0.007 **	P = 0.027 *	*P* = 0.008 **	*P* = 0.005 **	*P* = 0.083 †
	PPV	0.833	0.625	0.600	0.800	1.000	0.667
	NPV	0.882	1.000	1.000	0.923	1.000	1.000

Q2W, males (14 cases), MM (17 or 18 cases), MM, Q2W (11 or 12 cases), and MM, Q2W, males (9 cases), the Indexes of each column for the Outcomes were determined to have statistical significance or tendency toward significance. Particularly for Column Q2W, males (14 cases), the Index 37.7% on day29pre YS110 administration for the Outcome SD was statistically significant ($p < 0.001$ with AUC 1.000). Also, the Index 37.7% for the Outcome PFS ≥ 90 or ≥ 180 days was statistically significant ($p < 0.001$ or $p = 0.027$, and with AUC 0.950 or 0.879, respectively). Taken together, our analyses of serum sCD26/DPP4 titer variation during a course of YS110 treatment demonstrate that serum sCD26/DPP4 titer variation, particularly at the time point immediately prior to/following the third YS110 infusion on Day29 in the Q2W administration schedule, was a potential prognostic biomarker for YS110 anti-tumor therapy.

Addition of humanized anti-CD26 mAb reduced sCD26 levels in culture supernatants of CD26-expressing MM cell lines and non-tumor cells

Since sCD26 serum levels were markedly decreased in patients with CD26-expressing tumors following YS110 treatment in the phase I study (Fig. 1), we investigated the in vitro effect of YS110 on sCD26 production from MM cell lines. For this purpose, we selected various human CD26-positive or negative MM cell lines. MSTO parent was an endogenous human CD26-deficit cell line, while MSTO-CD26 stably expressed a full-length human CD26 [6]. Stable shRNA knockdown of CD26 in JMN, an endogenous human CD26-positive cell line, markedly reduced CD26 expression as compared with JMN ctrl-shRNA cells [19]. Cell surface expression of CD26 on MM cell lines was shown in Additional file 9 (Fig. S2a). We first measured the amount of sCD26 contained in the culture supernatants from a 3-day culture of CD26-positive or negative cells. sCD26 could be quantified in the culture supernatants of CD26-positive MSTO-CD26, JMN ctrl-shRNA and H226 cells, whereas sCD26 could not be detected in the culture supernatants of CD26-negative MSTO parent and JMN CD26-shRNA cells, regardless of YS110 treatment (Fig. 4a). Treatment with YS110 clearly reduced the amount of sCD26 in the culture supernatants of MSTO-CD26, JMN ctrl-shRNA and H226 cells, as compared with those cells incubated with vehicle or control human IgG (Fig. 4a). We next examined the production of sCD26 from non-tumor (normal) cells. CD26 was clearly expressed on the cell surface of HDMVEC and TIG-1, while CD26 was hardly expressed on HUVEC and MCF10A, and partially expressed on MeT-5A (Additional file 9 (Fig. S2b)). sCD26 could be quantified in the culture supernatants of CD26-positive TIG-1 and HDMVEC cells, whereas sCD26 could not be detected in the culture supernatants of CD26-negative or low MCF10A, HUVEC and MeT-5A cells (Fig. 4b). Similar with the results shown in Fig. 4a, YS110 treatment clearly reduced the amount of sCD26 in the culture supernatants of TIG-1 and HDMVEC cells, as compared with those cells incubated with vehicle or control human IgG (Fig. 4b). Treatment with YS110 resulted in decreased production of sCD26 from both MSTO-CD26 and TIG-1 cells in a dose-dependent manner (Fig. 4c). Subsequent time course analysis showed that sCD26 level in the supernatant of a 3-day culture of MSTO-CD26 cells was slightly enhanced compared to 1-day culture of MSTO-CD26 cells, and increased sCD26 level was observed in the supernatant of a 7-day culture of MSTO-CD26 cells (Fig. 4d). Reduction of sCD26 level following YS110 treatment was consistently observed at any culture period. Taken together, these data indicate that sCD26 was produced from both CD26-positive tumor cells and non-tumor cells, and the addition of YS110 reduced sCD26 production from those cells in an antibody dose-dependent manner. It is our hypothesis that these in vitro effects are reflected in the marked reduction of sCD26 level in the serum of patients with CD26-expressing tumors following YS110 administration.

Discussion

In the present study, *scatter plot* analysis of the relationship between serum sCD26/DPP4 titer variation and tumor volume variation by RECIST response criteria suggested that a predictable time period during the course of YS110 treatment can be used to distinguish between SD and PD cases. This predictable time period was found to be day 29pre/post the third dose of YS110 administration in the Q2W treatment schedule, with results being statistically significant by *PPMC/SRDC* and *Bar graph* analyses. The *ROC* analysis defined the cut-off titer of serum sCD26/DPP4 titer variation at day 29pre/post as the Index for the outcome of cases with SD or with PFS longer than 90 or 180 days, resulting in a significantly feasible prediction under the Index obtained. In particular, *ROC* analysis of the 14 male cases treated with the Q2W schedule defined the cut-off titer with $p < 0.001$ (Table 2). Similar results were obtained in the 9 male MM cases treated with the Q2W administration schedule (Table 2). The results were statistically significant despite the small number of cases in the stratified groups, strongly suggesting that serum sCD26/DPP4 titer variation was a definitive prognostic biomarker for cancer patients treated with YS110. In cases treated with the Q1W schedule, the number of cases were not sufficient for analysis, in contrast to the situation with the Q2W schedule. However, serum sCD26 titer variation on Day15pre and not on Day29pre could be used to discriminate SD from PD cases with a trend

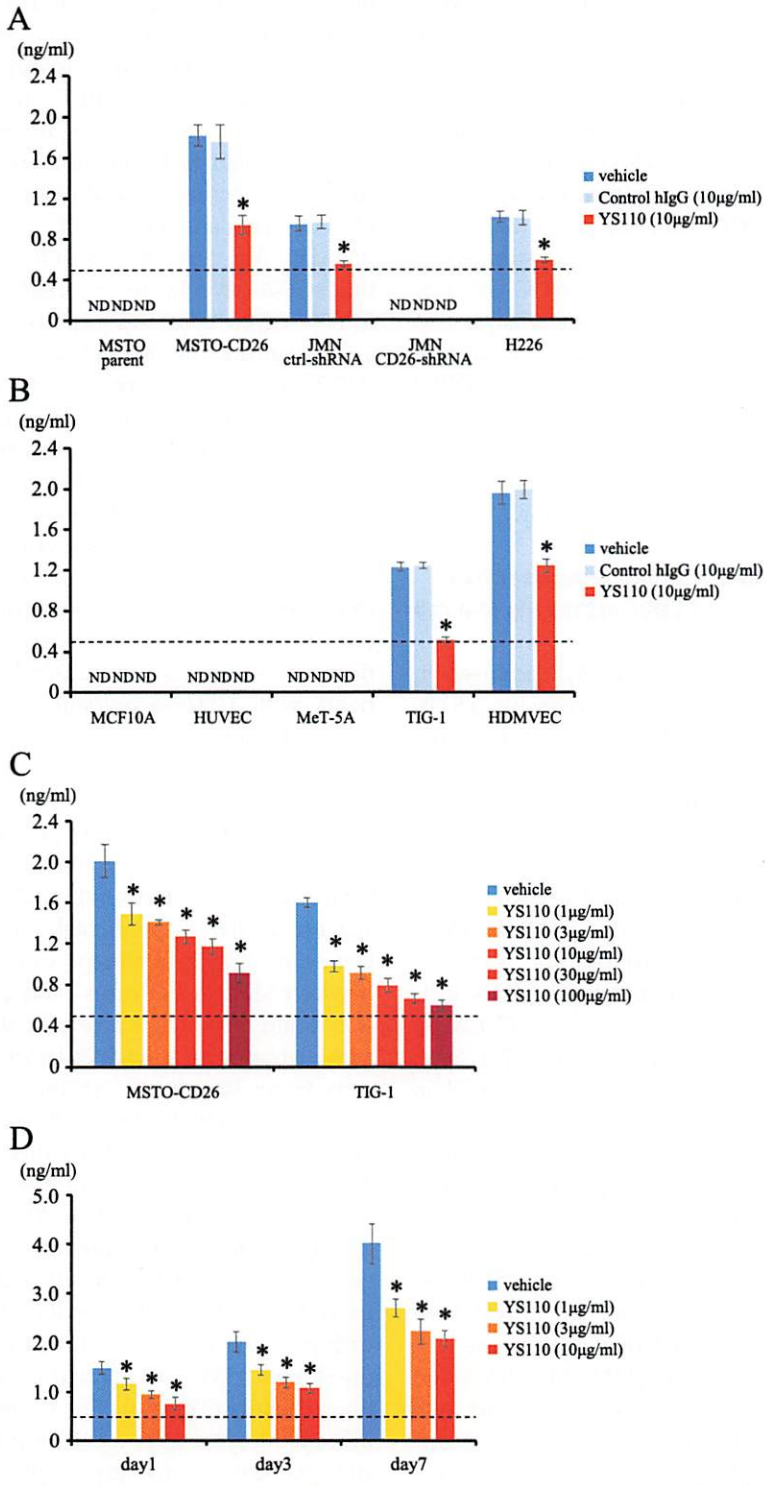

Fig. 4 Addition of YS110 reduced the soluble CD26 production from CD26-positive tumor and non-tumor cells. **a**, **b** MM cell lines (MSTO parent, MSTO-CD26, JMN ctrl-shRNA, JMN CD26-shRNA or H226 cells (3.5×10^4, each)) **a** or non-tumor cells (MCF10A (1.0×10^5), HUVEC (9.0×10^4), MeT-5A (6.0×10^4), TIG-1 (5.0×10^4) or HDMVEC cells (9.0×10^4)) **b** were incubated with control human IgG (hIgG) or the humanized anti-CD26 mAb YS110 (10 μg/ml, each) for 72 h. **c** MSTO-CD26 or TIG-1 cells were incubated with the indicated concentrations of YS110 for 3 days. **d** MSTO-CD26 cells were incubated with the indicated concentrations of YS110 for 1 day, 3 days or 7 days. Concentrations of soluble CD26 in the culture supernatants were examined by ELISA. The dashed line indicates the detection limit (0.488 ng/ml), and ND denotes 'not detected' (under detection limit). Representative data of three independent experiments are shown as mean ± S.D. of quadruplicate samples, comparing values with YS110 to those with vehicle or control human IgG (* $p < 0.01$), and similar results were obtained in each experiment

toward statistical significance ($p = 0.053$) as shown in Fig. 3d. These data would suggest that the increase in drug administration frequency and dosage (Q1W at YS110 dose level 2, 4, 6 mg/kg) could have an effect on the optimal timing of serum sCD26 titer measurement, which can be altered depending on administration frequency and/or dosage of YS110.

Our robust in vitro and in vivo data indicated that YS110 induced cell lysis of MM cells via antibody-dependent cell-mediated cytotoxicity (ADCC) in addition to its direct anti-tumor effect through the induction of cell cycle arrest at S/G1 phase [5, 22]. Another important mechanism of action of YS110 was the nuclear translocation of CD26 molecules by internalization of the CD26-YS110 complexes from the cell surface to inhibit proliferation of MM cells via suppression of POLR2A gene expression, a component of RNA polymerase II. However, in the case of CD26-expressing non-neoplastic cells such as human embryonic kidney HEK293 cells or normal T lymphocytes, the CD26-YS110 complex was not translocated into the nucleus [23, 24]. Moreover, internalization of the CD26-antibody complexes was dependent on the epitope of CD26 recognized by specific mAb. Internalization of CD26 was not observed from the cell surface of MM cells treated with the murine anti-human CD26 mAb 5F8, which recognized a different epitope of CD26 from that recognized by YS110 and did not exert anti-tumor activity [23, 25].

Residues 201 to 211, 730 and 740 of CD26 along with the serine catalytic site at residue 630, which constitute a CD26/DPPIV pocket structure, are essential for DPP4 enzyme activity [26]. In contrast, YS110 recognizes the 248-358th aa region of CD26, which is distinct from its catalytic site [25, 27], and binding of YS110 does not directly affect DPP4 enzyme activity [21]. Our present data showed that YS110 treatment reduced the production of sCD26 from both CD26-expressing MM cell lines and non-tumor cells (Fig. 4). Although the soluble form of CD26 begins at the 39th aa residue and lacks the cytoplasmic and transmembrane regions [28], the precise mechanisms involved in sCD26 production and release from the cell surface are not yet fully elucidated. It is possible that decreased sCD26 production following YS110 treatment was due to antibody-mediated internalization of cell surface CD26 molecules [23]. In the phase I clinical trial involving YS110, serum level of sCD26 immediately following YS110 administration on day 1 (day 1post) was markedly decreased as compared with the level prior to YS110 administration (day 1pre) (Fig. 1). Fc receptor-mediated phagocytosis of sCD26-YS110 complexes by phagocytes may possibly be involved in this rapid reduction of serum sCD26 following YS110 administration. In the present study, we demonstrated that sustained low levels of serum sCD26/DPP4 titer following YS110 administration was commonly observed in SD cases compared with those in PD cases, while there was no significant difference in the serum sCD26/DPP4 levels immediately after YS110 administration (days 1post, 15post and 29post) between SD and PD cases (Figs. 1 and 2). Future research is required to identify the factors involved in the retention or restoration of serum sCD26/DPP4 levels after YS110 administration.

In addition to the mechanisms of action responsible for the anti-tumor activity of YS110 as described above, recent works demonstrated the functional role of DPP4-mediated post-translational modification of chemokines in regulating tumor immunity through its interaction with its substrates. The exact chemokines produced at the tumor microenvironment (TME) are different, depending on tumor histology. In vivo tumor-transplant models showed that the DPP4 inhibitor sitagliptin reduced tumor growth through the preservation of bioactive CXCL10 in the TME of melanoma and colon carcinoma. In the normal physiological state, CXCL10 is rapidly degraded by DPP4, resulting in decreased recruitment and migration of $CXCR3^+$ T cells and NK cells into the TME. In contrast, DPP4 inhibition enhanced tumor rejection by preserving the full-length biologically active form of CXCL10, leading to increased trafficking of $CXCR3^+$ cells into the TME [29, 30]. Similar with CXCL10, administration of sitagliptin resulted in higher concentrations of bioactive CCL11 in the TME of hepatocellular carcinoma and breast cancer, leading to increased migration of eosinophils into solid tumors. In these models, expression of IL-33 in tumors was a key inducer of CCL11 production and eosinophil-mediated anti-tumor responses [31]. In view of these findings, our data showing that serum DPP4 activity was decreased following YS110 treatment would suggest enhancement of tumor immunity via DPP4 inhibition may constitute yet another mechanism of action of YS110.

Conclusions

This is the first finding that the serum sCD26/DPP4 titer variation in the early phase of treatment with the humanized anti-CD26 antibody YS110 may be a predictive biomarker for anti-tumor activity for patients with $CD26^+$ cancers including MM. Future clinical trials involving a larger group of patients would be needed for further validation of the predictive/prognostic value of serum sCD26 in patients treated with YS110.

Abbreviations

AUC: Area under the curve; DPP4: Dipeptidyl peptidase 4; FIH: First-in-human; HDMVEC: Human dermal microvascular endothelial cells; HUVEC: Human umbilical vein endothelial cells; mAb: Monoclonal antibody; MM: Malignant mesothelioma; PD: Progressive disease; PFS: Progression free survival; PPMC: Pearson product moment correlation; Q1W: Once every week; Q2W: Once every 2 weeks; RCC: Renal cell carcinoma; ROC: Receiver

operating characteristics; sCD26: Soluble CD26; SD: Stable disease; shRNA: Short hairpin RNA; SRDC: Spearman's rank-difference correlation; TME: Tumor microenvironment; UTC: Urothelial carcinoma

Supplementary Information

The online version contains supplementary material available at https://doi.org/10.1186/s40364-021-00273-0.

Additional file 1: Table S1. Demographic chart of 26 evaluable cases on administration frequency and dosage, gender, PFS, age, BMI, RECIST evaluation, tumor volume change and serum sCD26/DPP4 titer change

Additional file 2: Table S2. Detailed information about 26 evaluable cases

Additional file 3: Figure S1. Correlation between serum soluble CD26 level and DPP4 enzyme activity

Additional file 4: Table S3. Correlation between serum sCD26/DPP4 titer variation (%) and tumor volume change (%) or PFS (days) in 18 cases with Q2W administration by PPMC or SRDC analysis

Additional file 5: Table S4. Correlation between serum sCD26/DPP4 titer variation (%) and tumor volume change (%) or PFS (days) in 14 male cases with Q2W administration by PPMC or SRDC analysis

Additional file 6: Table S5. Correlation between serum sCD26/DPP4 titer variation (%) and tumor volume change (%) or PFS (days) in 19 MM cases by PPMC or SRDC analysis.

Additional file 7: Table S6. Correlation between serum sCD26/DPP4 titer variation (%) and tumor volume change (%) or PFS (days) in 12 MM cases with Q2W administration by PPMC or SRDC analysis.

Additional file 8: Table S7. Correlation between serum sCD26/DPP4 titer variation (%) and tumor volume change (%) or PFS (days) in 9 MM, male cases with Q2W administration by PPMC or SRDC analysis.

Additional file 9: Figure S2. Cell surface protein expression of CD26 on the human tumor and non-tumor cells.

Acknowledgments

Not applicable.

Authors' contributions

Y.K. established the concept, and designed and coordinated the study, and Y.U., S.T., S.I., O.H., T.T., T.Y., K.O. and C.M. contributed to the conception or design of the study. R.H. conducted the in vitro experiments. N.H. analyzed data and conducted statistical analyses. N.I., V.TL., B.Y., J.A., G.Z., F.V., T.P. and E.A. enrolled patients and conducted the clinical trial. Y.K. and R.H. wrote the manuscript, and N.H.D., K.O. and C.M. participated in editing it. All authors contributed to the interpretations and conclusions presented. The authors read and approved the final manuscript.

Funding

This study was supported by Y's AC Co., Ltd., Tokyo, Japan, Kissei Pharmaceutical Co., Ltd., Tokyo, Japan, and Japan Agency for Medical Research and Development (AMED), Tokyo, Japan. This study was also supported by a grant of the Ministry of Health, Labour, and Welfare, Japan (Grant Number 180101–01 (C.M.)), JSPS KAKENHI Grant Numbers JP20H03471 (C.M.), JP18H02782 (K.O.), JP20K07683 (R.H.).

Availability of data and materials

All data generated or analyzed during this study are included in this article and its supplementary information files.

Declarations

Ethics approval and consent to participate

All patients provided written informed consent. This study was conducted according to the Declaration of Helsinki and was approved by ethics committees and the French National Drug Agency.

Consent for publication

Not applicable.

Competing interests

Yutaro Kaneko is a chief executive officer of Y's AC Co., Ltd., Japan, Thomas Podoll is an employer of Y's Therapeutics Inc., USA, and Chikao Morimoto, Kei Ohnuma, Nam H. Dang and Taketo Yamada are stock holders of Y's AC Co., Ltd. Other authors declare no conflict of interest.

Author details

[1]Y's AC Co., Ltd., 2-6-8, Kudan-minami, Chiyoda-ku, Tokyo 102-0074, Japan. [2]Department of Therapy Development and Innovation for Immune Disorders and Cancers, Graduate School of Medicine, Juntendo University, Tokyo, Japan. [3]Stella Co., Ltd., Tokyo, Japan. [4]Centre Georges-François Leclerc, Unité de Phases Précoces, Dijon, France. [5]Institut de Cancérologie des Hospices Civils de Lyon, CITOHL, Lyon, France. [6]Hôpital Cochin, Paris, France. [7]Centre Hospitalier Universitaire (CHU) de Caen, Centre de Recherche Clinique/Essais de phases précoces, Caen, France. [8]FV Clinical subcontractor for SynteractHCR SAS, Levallois-Perret, France. [9]Y's therapeutics Inc., Redwood City, CA, USA. [10]Department of Rheumatology and Allergy, IMSUT Hospital, The University of Tokyo, Tokyo, Japan. [11]Graduate School of Medicine, Osaka University, Osaka, Japan. [12]Saitama Medical University, Saitama, Japan. [13]Keio University School of Medicine, Tokyo, Japan. [14]Division of Hematology/Oncology, University of Florida, Gainesville, FL, USA. [15]Gustave Roussy, Drug Development Department (DITEP), Université Paris-Saclay, Villejuif, France.

Received: 9 December 2020 Accepted: 10 March 2021
Published online: 23 March 2021

References

1. Ohnuma K, Dang NH, Morimoto C. Revisiting an old acquaintance: CD26 and its molecular mechanisms in T cell function. Trends Immunol. 2008; 29(6):295–301. https://doi.org/10.1016/j.it.2008.02.010.
2. Ohnuma K, Hatano R, Komiya E, Otsuka H, Itoh T, Iwao N, et al. A novel role for CD26/dipeptidyl peptidase IV as a therapeutic target. Front Biosci (Landmark Ed). 2018;23:1754–79.
3. Ho L, Aytac U, Stephens LC, Ohnuma K, Mills GB, McKee KS, Neumann C, LaPushin R, Cabanillas F, Abbruzzese JL, Morimoto C, Dang NH, et al. In vitro and in vivo antitumor effect of the anti-CD26 monoclonal antibody 1F7 on human CD30+ anaplastic large cell T-cell lymphoma Karpas 299. Clin Cancer Res. 2001;7(7):2031–40.
4. Inamoto T, Yamochi T, Ohnuma K, Iwata S, Kina S, Inamoto S, Tachibana M, Katsuoka Y, Dang NH, Morimoto C, et al. Anti-CD26 monoclonal antibody-mediated G1-S arrest of human renal clear cell carcinoma Caki-2 is associated with retinoblastoma substrate dephosphorylation, cyclin-dependent kinase 2 reduction, p27(kip1) enhancement, and disruption of binding to the extracellular matrix. Clin Cancer Res. 2006;12(11 Pt 1):3470–7. https://doi.org/10.1158/1078-0432.CCR-06-0361.
5. Inamoto T, Yamada T, Ohnuma K, Kina S, Takahashi N, Yamochi T, Inamoto S, Katsuoka Y, Hosono O, Tanaka H, Dang NH, Morimoto C, et al. Humanized anti-CD26 monoclonal antibody as a treatment for malignant mesothelioma tumors. Clin Cancer Res. 2007;13(14):4191–200. https://doi.org/10.1158/1078-0432.CCR-07-0110.
6. Yamamoto J, Ohnuma K, Hatano R, Okamoto T, Komiya E, Yamazaki H, Iwata S, Dang NH, Aoe K, Kishimoto T, Yamada T, Morimoto C, et al. Regulation of somatostatin receptor 4-mediated cytostatic effects by CD26 in malignant pleural mesothelioma. Br J Cancer. 2014;110(9):2232–45. https://doi.org/10.1038/bjc.2014.151.
7. Nishida H, Hayashi M, Morimoto C, Sakamoto M, Yamada T. CD26 is a potential therapeutic target by humanized monoclonal antibody for the treatment of multiple myeloma. Blood Cancer J. 2018;8(11):99. https://doi.org/10.1038/s41408-018-0127-y.
8. Angevin E, Isambert N, Trillet-Lenoir V, You B, Alexandre J, Zalcman G, Vielh P, Farace F, Valleix F, Podoll T, Kuramochi Y, Miyashita I, Hosono O, Dang NH, Ohnuma K, Yamada T, Kaneko Y, Morimoto C, et al. First-in-human phase 1 of YS110, a monoclonal antibody directed against CD26 in advanced CD26-expressing cancers. Br J Cancer. 2017;116(9):1126–34. https://doi.org/10.1038/bjc.2017.62.
9. Liang PI, Yeh BW, Li WM, Chan TC, Chang IW, Huang CN, Li CC, Ke HL, Yeh HC, Wu WJ, Li CF, et al. DPP4/CD26 overexpression in urothelial carcinoma confers an independent prognostic impact and correlates with intrinsic biological aggressiveness. Oncotarget. 2017;8(2):2995–3008. https://doi.org/10.18632/oncotarget.13820.

10. Boccardi V, Marano L, Rossetti RR, Rizzo MR, di Martino N, Paolisso G. Serum CD26 levels in patients with gastric cancer: a novel potential diagnostic marker. BMC Cancer. 2015;15(1):703. https://doi.org/10.1186/s12885-015-1757-0.
11. Abooshahab R, Niyazi E, Yaghmaie P, Ghadaksaz HG, Hedayati M. Serum level of dipeptidyl peptidase-4 as a potential biomarker for medullary thyroid cancer. Exp Oncol. 2018;40(4):299–302. https://doi.org/10.31768/2312-8852.2018.40(4):299-302.
12. Sanchez-Otero N, Rodriguez-Berrocal FJ, de la Cadena MP, Botana-Rial MI, Cordero OJ. Evaluation of pleural effusion sCD26 and DPP-IV as diagnostic biomarkers in lung disease. Sci Rep. 2014;4:3999.
13. Ye C, Tian X, Yan L, Guan X, Yin S, Hao C. Elevated serum CD26 level is associated with metastasis and post-operation survival in pancreatic cancer patients. Transl Cancer Res. 2016;5(5):512–9. https://doi.org/10.21037/tcr.2016.08.38.
14. Enz N, Vliegen G, De Meester I, Jungraithmayr W. CD26/DPP4 - a potential biomarker and target for cancer therapy. Pharmacol Ther. 2019;198:135–59. https://doi.org/10.1016/j.pharmthera.2019.02.015.
15. De Chiara L, Rodriguez-Pineiro AM, Cordero OJ, Vazquez-Tunas L, Ayude D, Rodriguez-Berrocal FJ, et al. Postoperative serum levels of sCD26 for surveillance in colorectal cancer patients. PLoS One. 2014;9(9):e107470. https://doi.org/10.1371/journal.pone.0107470.
16. De Chiara L, Paez de la Cadena M, Rodriguez-Berrocal J, Alvarez-Pardinas MC, Pardinas-Anon MC, Varela-Calvino R, et al. CD26-Related Serum Biomarkers: sCD26 Protein, DPP4 Activity, and Anti-CD26 Isotype Levels in a Colorectal Cancer-Screening Context. Dis Markers. 2020:4347936.
17. Larrinaga G, Perez I, Sanz B, Beitia M, Errarte P, Fernandez A, et al. Dipeptidyl-peptidase IV activity is correlated with colorectal cancer prognosis. PLoS One. 2015;10(3):e0119436. https://doi.org/10.1371/journal.pone.0119436.
18. Ali A, Fuentes A, Skelton WI, Wang Y, McGorray S, Shah C, et al. A multi-center retrospective analysis of the effect of DPP4 inhibitors on progression-free survival in advanced airway and colorectal cancers. Mol Clin Oncol. 2019;10(1):118–24. https://doi.org/10.3892/mco.2018.1766.
19. Yamazaki H, Naito M, Ghani FI, Dang NH, Iwata S, Morimoto C. Characterization of cancer stem cell properties of CD24 and CD26-positive human malignant mesothelioma cells. Biochem Biophys Res Commun. 2012;419(3):529–36. https://doi.org/10.1016/j.bbrc.2012.02.054.
20. Ohnuma K, Saito T, Hatano R, Hosono O, Iwata S, Dang NH, Ninomiya H, Morimoto C, et al. Comparison of two commercial ELISAs against an in-house ELISA for measuring soluble CD26 in human serum. J Clin Lab Anal. 2015;29(2):106–11. https://doi.org/10.1002/jcla.21736.
21. Y's Therapeutics Inc. USA IND. 2008;100657:Section 8, 8.2.1.5:289.
22. Hayashi M, Madokoro H, Yamada K, Nishida H, Morimoto C, Sakamoto M, Yamada T et al. A humanized anti-CD26 monoclonal antibody inhibits cell growth of malignant mesothelioma via retarded G2/M cell cycle transition. Cancer Cell Int 2016;16:35, 1, DOI: https://doi.org/10.1186/s12935-016-0310-9.
23. Yamada K, Hayashi M, Madokoro H, Nishida H, Du W, Ohnuma K, et al. Nuclear localization of CD26 induced by a humanized monoclonal antibody inhibits tumor cell growth by modulating of POLR2A transcription. PLoS One. 2013;8(4):e62304. https://doi.org/10.1371/journal.pone.0062304.
24. Hayashi M, Madokoro H, Yamada K, Nishida H, Morimoto C, Sakamoto M, Yanagawa H, Yamada T, et al. Novel antibody-drug conjugate with anti-CD26 humanized monoclonal antibody and transcription factor IIH (TFIIH) inhibitor, Triptolide, inhibits tumor growth via impairing mRNA synthesis. Cancers (Basel). 2019;11(8):1138. https://doi.org/10.3390/cancers11081138.
25. Hatano R, Yamada T, Matsuoka S, Iwata S, Yamazaki H, Komiya E, Okamoto T, Dang NH, Ohnuma K, Morimoto C, et al. Establishment of monoclonal anti-human CD26 antibodies suitable for immunostaining of formalin-fixed tissue. Diagn Pathol. 2014;9(1):30. https://doi.org/10.1186/1746-1596-9-30.
26. Ohnuma K, Yamochi T, Uchiyama M, Nishibashi K, Yoshikawa N, Shimizu N, Iwata S, Tanaka H, Dang NH, Morimoto C, et al. CD26 up-regulates expression of CD86 on antigen-presenting cells by means of caveolin-1. Proc Natl Acad Sci U S A. 2004;101(39):14186–91. https://doi.org/10.1073/pnas.0405266101.
27. Dong RP, Tachibana K, Hegen M, Scharpe S, Cho D, Schlossman SF, et al. Correlation of the epitopes defined by anti-CD26 mAbs and CD26 function. Mol Immunol. 1998;35(1):13–21. https://doi.org/10.1016/S0161-5890(98)80013-8.
28. Iwaki-Egawa S, Watanabe Y, Kikuya Y, Fujimoto Y. Dipeptidyl peptidase IV from human serum: purification, characterization, and N-terminal amino acid sequence. J Biochem. 1998;124(2):428–33. https://doi.org/10.1093/oxfordjournals.jbchem.a022130.
29. Barreira da Silva R, Laird ME, Yatim N, Fiette L, Ingersoll MA, Albert ML. Dipeptidylpeptidase 4 inhibition enhances lymphocyte trafficking, improving both naturally occurring tumor immunity and immunotherapy. Nat Immunol. 2015;16(8):850–8. https://doi.org/10.1038/ni.3201.
30. Ohnuma K, Hatano R, Morimoto C. DPP4 in anti-tumor immunity: going beyond the enzyme. Nat Immunol. 2015;16(8):791–2. https://doi.org/10.1038/ni.3210.
31. Hollande C, Boussier J, Ziai J, Nozawa T, Bondet V, Phung W, Lu B, Duffy D, Paradis V, Mallet V, Eberl G, Sandoval W, Schartner JM, Pol S, Barreira da Silva R, Albert ML, et al. Inhibition of the dipeptidyl peptidase DPP4 (CD26) reveals IL-33-dependent eosinophil-mediated control of tumor growth. Nat Immunol. 2019;20(3):257–64. https://doi.org/10.1038/s41590-019-0321-5.

Publisher's Note

Peripheral endomorphins drive mechanical alloknesis under the enzymatic control of CD26/DPPIV

Eriko Komiya, PhD,[a] Mitsutoshi Tominaga, PhD,[a,b] Ryo Hatano, PhD,[c] Yuji Kamikubo, PhD,[d] Sumika Toyama, PhD,[a] Hakushun Sakairi, MD, PhD,[d] Kotaro Honda, PhD,[a] Takumi Itoh, PhD,[c,e] Yayoi Kamata, PhD,[a,b] Munehiro Tsurumachi, MD,[a,f] Ryoma Kishi, MD,[a,f] Kei Ohnuma, MD, PhD,[c] Takashi Sakurai, MD, PhD,[d] Chikao Morimoto, MD, PhD,[c] and Kenji Takamori, MD, PhD[a,b,f] *Chiba and Tokyo, Japan*

Background: Mechanical alloknesis (or innocuous mechanical stimuli–evoked itch) often occurs in dry skin–based disorders such as atopic dermatitis and psoriasis. However, the molecular and cellular mechanisms underlying mechanical alloknesis remain unclear. We recently reported the involvement of CD26 in the regulation of psoriatic itch. This molecule exhibits dipeptidyl peptidase IV (DPPIV) enzyme activity and exerts its biologic effects by processing various substances, including neuropeptides.

Objective: The aim of the present study was to investigate the peripheral mechanisms of mechanical alloknesis by using CD26/DPPIV knockout (CD26KO) mice.

Methods: We applied innocuous mechanical stimuli to CD26KO or wild-type mice. The total number of scratching responses was counted as the alloknesis score. Immunohistochemical and behavioral pharmacologic analyses were then performed to examine the physiologic activities of CD26/DPPIV or endomorphins (EMs), endogenous agonists of μ-opioid receptors.

Results: Mechanical alloknesis was more frequent in CD26KO mice than in wild-type mice. The alloknesis score in CD26KO mice was significantly reduced by the intradermal administration of recombinant DPPIV or naloxone methiodide, a peripheral μ-opioid receptor antagonist, but not by that of mutant DPPIV without enzyme activity. EMs (EM-1 and EM-2), selective ligands for μ-opioid receptors, are substrates for DPPIV. Immunohistochemically, EMs were located in keratinocytes, fibroblasts, and peripheral sensory nerves. Behavioral analyses revealed that EMs preferentially provoked mechanical alloknesis over chemical itch. DPPIV-digested forms of EMs did not induce mechanical alloknesis.

Conclusion: The present results suggest that EMs induce mechanical alloknesis at the periphery under the enzymatic control of CD26/DPPIV. (J Allergy Clin Immunol 2021;■■■:■■■-■■■.)

Key words: *CD26, dipeptidyl peptidase IV enzyme, endomorphin, mechanical alloknesis, mechanical itch, peripheral μ-opioid receptor, skin*

In many skin disorders with chronic itch, including xerosis, atopic dermatitis (AD), and psoriasis, there often occurs a vicious itch-scratch cycle in which scratching behaviors themselves aggravate the itch sensation by exacerbating skin lesions.[1-3] These skin conditions often concomitantly display itch hypersensitivity, in which the threshold for itch is lower than in healthy controls and sensitivity to pruritogens is increased.[3-5]

The phenomenon of itch hypersensitivity, which is caused by normally innocuous mechanical stimuli, is referred to as mechanical alloknesis and has been reported in various mouse models and patients with dry skin–based skin diseases such as AD.[6-10] Accumulating evidence indicates that innocuous mechanical stimuli–evoked itch (mechanical alloknesis) is mediated by neural pathways distinct from those of chemical itch, which is caused by chemical mediators, including histamine or proteases, released from cutaneous cells or exogenous sources.[9-12]

Chemical itch is transmitted to the spinal cord by various chemical mediators through C-pruriceptors expressing Mas-related GPR A3 (MrgprA3), natriuretic peptide B (Nppb), and gastrin-releasing peptide (GRP) at the peripheral level.[13-15] At the spinal cord level, a subpopulation of excitatory interneurons (INs) expressing the GRP receptor (GRPR) or natriuretic peptide receptor A (Npra) convey chemical itch signals,[14,16,17] whereas inhibitory INs expressing the transcription factor BHLHB5 negatively regulate these signals.[18-20] Regarding the innocuous mechanical stimuli–evoked itch pathway at the spinal cord, a subpopulation of inhibitory neuropeptide Y-expressing (NPY^+) INs was found to negatively modulate this sensation without affecting chemical itch.[12] Moreover, NPY 1 receptor (Y1)-expressing neurons and urocortin 3-expressing ($Ucn3^+$) neurons were identified as

From [a]the Juntendo Itch Research Center, Institute for Environmental and Gender-Specific Medicine, and [b]the Anti-Aging Skin Research Laboratory, Graduate School of Medicine, Juntendo University, Chiba; [c]the Department of Therapy Development and Innovation for Immune Disorders and Cancers and [c]the Atopy (Allergy) Research Center, Graduate School of Medicine, Juntendo University, Tokyo; [d]the Department of Pharmacology, Juntendo University School of Medicine, Tokyo; and [f]the Department of Dermatology, Juntendo University Urayasu Hospital, Chiba.

Supported by a grant-in-aid from the Foundation of Strategic Research Projects in Private Universities from the Ministry of Education, Culture, Sports, Science, and Technology, Japan (grant S1311011 [to K.T.]); Japanese Society for the Promotion of Science Grants-in-Aid for Scientific Research Program (grants 17K16353 [to E.K.], 20K08680 [to E.K.], 18H02783 [to K.O.], 18K07396 [to M.T.], 16H05345 [to C.M.], 16K08997 [to K.T.], and 20H03568 [to K.T.]); the Ministry of Health, Labour, and Welfare, Japan (grants 150401-01 [to C.M.] and 180101-01 [to C.M.]; and a grant from the Lydia O'Leary Memorial Pias Dermatological Foundation (2021 [to M.T.]).

Disclosure of potential conflicts of interest: The authors declare that they have no relevant conflicts of interest.

Received for publication July 22, 2020; revised June 29, 2021; accepted for publication August 2, 2021.

Corresponding author: Kenji Takamori MD, PhD, Juntendo University Graduate School of Medicine, 2-1-1 Tomioka, Urayasu, Chiba 279-0021, Japan. E-mail: ktakamor@juntendo.ac.jp.

0091-6749

https://doi.org/10.1016/j.jaci.2021.08.003

Abbreviations used
AD: Atopic dermatitis
CD26KO: CD26/DPPIV knockout
CGRP: Calcitonin gene–related peptide
DPPIV: Dipeptidyl peptidase IV
EM: Endomorphin
GRP: Gastrin-releasing peptide
GRPR: Gastrin-releasing peptide receptor
IN: Interneuron
MOR: μ-Opioid receptor
Mrgpr: Mas-related gastrin-releasing peptide
NF200: Neurofilament 200
NK1R: Neurokinin 1 receptor
Nppb: Natriuretic peptide B
Npra: Natriuretic peptide receptor A
NPY: Neuropeptide Y
sDPPIV: Soluble intact CD26/DPPIV$^+$
smDPPIV: Soluble mutant CD26/DPPIV$^-$
SP: Substance P
TrkB: Tropomyosin-related tyrosine kinase B
Ucn3: Urocortin 3
WT: Wild-type
Y1: NPY 1 receptor

excitatory neurons gated by NPY$^+$ INs.[21,22] Although evidence obtained from patients with AD suggests involvement of both the central and peripheral nervous systems,[7,8,23,24] the cellular and molecular mechanisms underlying innocuous mechanical stimuli–evoked itch at the periphery remain unknown, except for Merkel cells in the touch dome being important for negative regulation.[25]

CD26 is a 110-kDa multifunctional glycoprotein that is expressed on various cell types, including T cells, epithelial cells, endothelial cells, fibroblasts, and various tumor cells. CD26 exhibits dipeptidyl peptidase IV activity (DPPIV [EC 3.4.14.5]) in its extracellular domain and is capable of cleaving the N-terminus of peptides with L-proline or L-alanine at the penultimate position.[26-28] This enzyme is involved in the activation and inactivation of a number of cytokines, chemokines, and neuropeptides.[29] We recently reported that DPPIV is associated with psoriatic itch by regulating the cleavage of substance P (SP).[30] However, the involvement of the CD26 molecule or DPPIV in mechanical alloknesis remains unclear.

In the present study, we investigated the role of CD26/DPPIV in the regulation of mechanical alloknesis at the periphery by using CD26 knockout (CD26KO) mice. We focused on substrates for DPPIV, namely, the endomorphins (EMs) EM-1 and EM-2, which are selective ligands for μ-opioid receptors (MORs), and we identified them as pruritogens that preferentially provoke mechanical alloknesis over chemical itch. Herein, we have demonstrated that EM-MOR signaling and its degradation pathway by DPPIV play a pivotal role in the peripheral mechanisms of mechanical alloknesis.

METHODS

Animals

C57BL/6 mice were purchased from CLEA Japan (Tokyo, Japan) or Oriental BioService (Kyoto, Japan). CD26KO (*CD26*$^{-/-}$) mice developed from C57BL/6 mice were kindly gifted from the laboratory of Dr Takeshi Watanabe at Kyusyu University (Fukuoka, Japan).[31] These mice were bred in-house and used at 8 to 16 weeks of age. They were kept under controlled temperature (23°C-25°C) and light (exposure to light from 8:00 AM to 8:00 PM) conditions. Food and water were freely available to the mice. All experiments on animals were approved by the animal ethics committee at Juntendo University (authorization nos. 280038, 290132, 300024, 310029, 2020063, and 2021079).

Recombinant proteins, antibodies, and reagents

Recombinant EMs (EM-1 and EM-2) were purchased from the Peptide Institute (Osaka, Japan). Truncated peptides of EMs (YP [common N-terminal side dipeptides], WF-NH_2 [C-terminal side amidated dipeptides of EM-1], and FF-NH_2 [C-terminal side amidated dipeptides of EM-2]) were purchased from BEX Co, Ltd (Tokyo, Japan). All peptides were dissolved in 2.5% dimethyl sulfoxide physiologic saline to make a stock solution. Recombinant soluble CD26/DPPIV (sDPPIV) and sDPPIV lacking DPPIV enzyme activity mutated at catalytic site (Ser630 was replaced by Ala) (soluble mutant DPPIV [smDPPIV]) were produced according to a previously described method.[32] The primary antibodies used in the present study were as follows: goat anti-mouse CD26/DPPIV (1:1000; R&D Systems, Minneapolis, Minn), rabbit anti–EM-1 (1:200; Phoenix Pharmaceuticals, Inc, Burlingame, Calif), rabbit anti–EM-2 (1:200; Phoenix Pharmaceuticals, Inc), guinea pig anti–cytokeratin 10 (anti-CK10, 1:200; Progen Biotechnic GmbH, Heidelberg, Germany), guinea pig anti-CK14 (1:200; Progen Biotechnic GmbH), and chicken anti-vimentin (1:200, Abcam, Cambridge, United Kingdom). A cyanine 3–conjugated rabbit polyclonal anti–β-III tubulin antibody was purchased from Merck Millipore (Temecula, Calif) and used at a dilution of 1:500 to 1:800. A secondary rabbit antibody conjugated with Alexa 488 was obtained from Thermo Fisher Scientific (Rockford, Ill). Other secondary antibodies conjugated with Alexa 488 or Alexa 594 were purchased from Jackson ImmunoResearch Laboratories, Inc (West Grove, Pa). All secondary antibodies were used at a 1:300 dilution. The peripheral MOR antagonist naloxone methiodide was purchased from Merck (Darmstadt, Germany) and dissolved, stocked, and used in saline.

Mechanical alloknesis assay

Mechanical alloknesis assays were performed by using a previously described method with some modifications.[9,22,25] The rostral back of each mouse was shaved at least 2 days before the test. On the day of the test, each mouse was placed in a new cage and habituated for at least 1 hour. Mechanical stimuli were delivered with von Frey filaments (Bioseb, Chaville, France) with bending forces ranging between 0.008 and 1.4 *g*. Unless otherwise noted, von Frey filaments with bending forces of 0.07 and 0.16 *g* were used for the test, and data obtained with a force of 0.16 *g* were shown. Each mouse received 3 innocuous mechanical stimuli on the rostral back by using this filament with longer than 5-second intervals (average 20 seconds). Within a 3-minute interval, this sequence was repeated 10 times (30 stimulations in total). Mechanical alloknesis scores were calculated as the total number of scratching responses. To test the effects of reagents or peptides on mice, CD26KO or control wild-type (WT) mice received a 50-μL intradermal injection of recombinant sDPPIV, smDPPIV, or naloxone methiodide into the center of the shaved area through use of a 29G Myjector syringe (Thermo, Tokyo, Japan). Mechanical alloknesis assays were then immediately conducted. To test EM-evoked mechanical alloknesis, WT mice received an intradermal injection of EM (EM-1, EM-2, or their fragments) with or without naloxone methiodide under the same conditions as used for the CD26KO mouse test, and to prevent scratching behavior caused by spontaneous itch affecting mechanical alloknesis scores, mechanical alloknesis assays were performed 30 minutes after the intradermal injection. Each experiment was performed with 6 or more mice in all groups.

Scratching bout counting assay

The rostral part of the back was shaved at least 2 days before the test. Before behavioral recording, the mice (4 animals per observation) were placed in an acrylic cage (19.5 × 24 × 35 cm) for at least 1 hour for acclimation. The frequency of scratching bouts of the rostral back was analyzed by using the

SCLABA-Real system (NOVERTEC, Kobe, Japan) for the indicated time intervals, with observers being kept out of the experimental room. To test EM-evoked scratching bouts, each mouse received an intradermal injection under the same conditions as used for the EM-evoked mechanical alloknesis assay. After the injection, the mice were immediately placed back in the acrylic cage, and behavioral recording using the SCLABA-Real system was started. "One-time" scratching behavior by mice was defined as scratching occurring from the initiation of scratching with the hind limb to cessation thereof. Each experiment was performed with 6 or more mice in all groups.

Evaluation of skin conditions

Transepidermal water loss and stratum corneum hydration were evaluated in each mouse by using the Tewameter TM300 and Corneometer CM825 (Courage and Khazawa, Cologne, Germany), respectively (at a room temperature of 25.1°C ± 0.6°C and relative humidity of 43.4% ± 1.3%). At the time of both measurements, each measuring device was placed on the surface of murine back skin for approximately 20 to 30 seconds after the achievement of isoflurane anesthesia. Each experiment was performed with 7 WT mice and 8 CD26KO mice.

Immunohistochemistry

Frozen blocks were prepared by embedding the unfixed upper back skin of the mice in optimal cutting temperature (OCT) compound (Sakura Finetechnical Co, Ltd, Tokyo, Japan). Next, 10-μm-thick cryosections were made by cutting the blocks using a CM1850 cryostat (Leica, Wetzlar, Germany). Skin sections were air-dried and fixed with ice-cold acetone for 10 minutes. After rehydration with PBS solution, the sections were blocked with blocking buffer (PBS solution with 5% normal donkey serum, 2% BSA, and 0.2% Triton X-100) at room temperature for 2 hours and then incubated with each primary antibody at 4°C overnight. After washing with wash buffer (PBS solution with 2% BSA and 0.05% Tween 20), secondary antibodies were added to the sections and incubated at room temperature for 2 hours with shading. As negative control experiments, the primary antibodies were either omitted or replaced with normal IgG. After washing with wash buffer with shading, VECTOSHIELD Mounting Medium with 4',6-diamidino-2-phenylindole (Vector Labs, Burlingame, Calif) was added, the sections were covered with coverslips, and images were taken by using a Keyence BZ-X800 microscope (Osaka, Japan). Even in cases without statistical processing, 2 or more mice were examined and 3 to 9 visual fields per sample were photographed.

Semiquantification of β-III tubulin–immunoreactive fibers

There were 8 mice in each group; 3 skin specimens from each mouse were incubated with an anti–β-III tubulin antibody. A BZ-X800 all-in-one fluorescence microscope was used to scan 10-μm-thick sections at a thickness of 1.0 μm in the z-axis of the stained samples, and images were reconstructed in 3 dimensions by using the BZ-X800 viewer (Keyence). The entire fluorescence intensity on the field and its nerve fiber–positive areas (superficial measure) were assessed in 9 fields of view for each mouse by using the BZ-X800 analyzer (Keyence). By dividing the intensity of fluorescence in the whole field by the nerve fiber–positive areas in the field, the fluorescence intensity of each neuronal marker per unit area was calculated. All values are reported as means plus or minus SEMs.

Statistical analysis

Data were expressed as mean values plus or minus SEMs and analyzed by the 2-tailed Student *t*-test for 2 group comparisons or by ANOVA for multiple comparisons followed by the Tukey-Kramer *post hoc* test. *P* values of .05 or less were considered significant. Calculations were performed and graphed by using GraphPad Prism 6 (GraphPad Software Inc, La Jolla, Calif).

RESULTS

CD26KO mice display mechanical alloknesis

We initially conducted mechanical alloknesis assays to clarify susceptibility to innocuous mechanical stimuli in CD26KO mice (Fig 1, *A*). The frequency of hind limb scratching evoked by von Frey filaments (mechanical alloknesis score) with a low bending force (0.04-0.6 *g*) was significantly higher in CD26KO mice than in WT mice (Fig 1, *B*). Only slight differences were observed between these mice at each of the other forces tested (Fig 1, *B*). In contrast, spontaneous scratching with no mechanical stimuli was similar between CD26KO and WT mice (Fig 1, *C*).

Characterization of mechanical alloknesis in CD26KO mice

We examined the skin condition of CD26KO mice, including barrier function and innervation. No significant differences in the degree of transepidermal water loss (Fig 2, *A*) or stratum corneum hydration (Fig 2, *B*) were observed between the WT and CD26KO mice. To assess innervation, the fluorescence intensity of the neuronal marker β-III tubulin per area in the skin was evaluated immunohistochemically. No significant differences were noted in the fluorescence intensity of β-III tubulin between the WT and CD26KO mice (Fig 2, *C* and *D*).

Immunohistochemically, CD26 was expressed in the skin of the WT mice but not in the skin of the CD26KO mice, and it was more strongly expressed in the dermis (Fig 2, *E*) than in nerve fibers (see Fig E1 in this article's Online Repository at www.jacionline.org). The expression of CD26 was markedly weaker in the spinal cord, except for the meninges, than in the skin (see Fig E2 in this article's Online Repository at www.jacionline.org).

We then investigated whether a CD26 deficiency in skin was responsible for the induction of mechanical alloknesis. CD26KO mice were injected intradermally with 0.2 nmol soluble intact CD26/DPPIV$^+$ (sDPPIV), and mechanical alloknesis assays were performed. Mechanical alloknesis scores were significantly lower in sDPPIV-injected CD26KO mice than in vehicle-injected CD26KO mice. In contrast, the smCD26/DPPIV$^-$soluble form (0.2 nmol) did not affect the mechanical alloknesis scores of CD26KO mice (Fig 2, *F*). Moreover, mechanical alloknesis in CD26KO mice was almost completely abrogated by the intradermal injection of 30 μg naloxone methiodide (Fig 2, *G*). These results strongly suggest that DPPIV enzyme activity in the dermal layer of mouse skin negatively regulates MOR-mediated mechanical alloknesis.

EMs are distributed in mouse keratinocytes, nerve fibers, and fibroblasts

EM-1 and EM-2 are selective ligands for MOR and substrates for DPPIV.[33,34] Because these ligands evoke scratching behavior in mice following their intracisternal injection,[35] we focused on whether these EMs are significant pruritogens that are regulated by DPPIV enzyme activity in the skin. Although previous studies reported that these MOR ligands are both expressed in the central nervous system, such as in the brain and spinal cord,[36,37] there is currently no information on whether these ligands are expressed in mouse skin. Therefore, we immunohistochemically examined the expression and distribution patterns of the EM-1 and EM-2 proteins in mouse skin (Fig 3). In murine skin, both EMs were strongly detected in the epidermis, both in the squamous cell layer (Fig 3, *A* and *B*) and basal layer (Fig 3, *C* and *D*) of keratinocytes. In addition to distinct expression in some cutaneous nerve fibers (Fig 3, *E* and *F*), these EMs were also detectable in dermal fibroblasts (Fig 3, *G* and *H*).

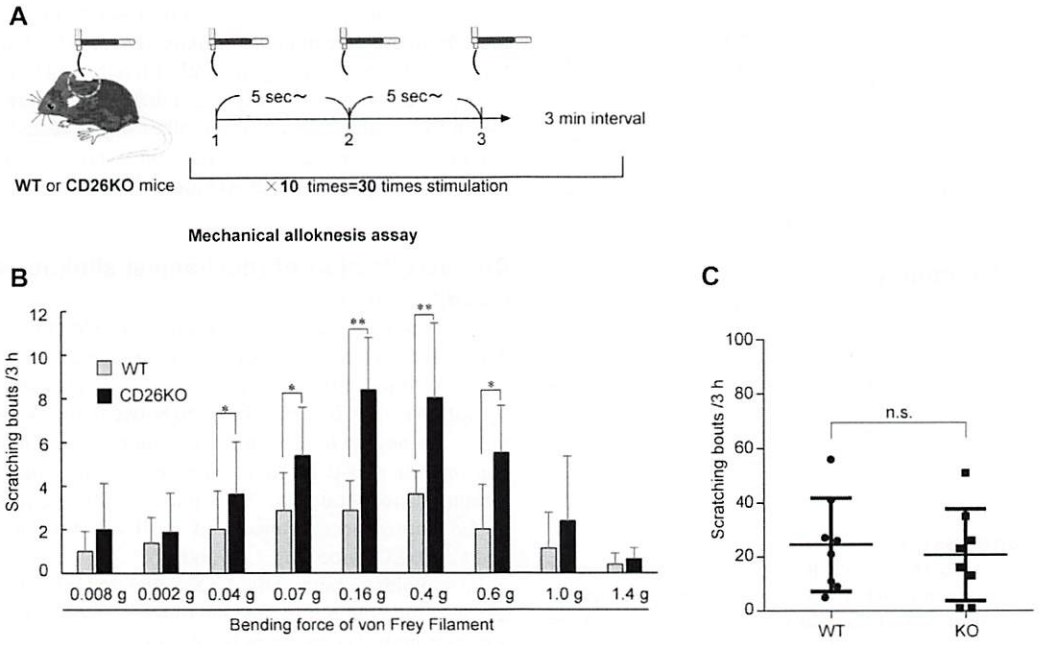

FIG 1. CD26KO mice display mechanical alloknesis. **A,** Schematic showing a mechanical alloknesis assay. **B,** Frequency of scratching bouts induced by von Frey filaments (mechanical alloknesis score) with various bending forces (0.08-1.4 *g*) in WT or CD26KO mice. **C,** Frequency of scratching bouts during 3 hours with no mechanical stimulation in WT or CD26KO mice. $*P < .05$; $**P < .01$. *n.s.*, Not significant.

To further identify subpopulations of EM-containing sensory nerve fibers, costaining and triple staining of mouse skin were conducted by using each EM antibody, C- and A-fiber markers (for costaining and triple staining), and peptidergic neuron and Aβ-fiber markers (for triple staining), respectively.[38,39] The results of costaining revealed EMs in both C- and A-fibers (see Fig E3, *A-D* in this article's Online Repository at www.jacionline.org). Triple staining showed that EM-1 and EM-2 were mainly expressed in peptidergic C- and Aβ-fibers and weakly expressed in Aδ-fibers (see Fig E4, *A-F* in this article's Online Repository at www.jacionline.org).

EM preferentially induce mechanical alloknesis over chemical itch

To clarify whether EM-1 or EM-2 induces innocuous mechanical stimulus–evoked itch, we used WT mice and conducted mechanical alloknesis assays following the intradermal injection of EM-1 or EM-2 at various concentrations (Fig 4, *A*). To exclude the effects of EM-derived spontaneous itch (nonmechanical itch) from mechanical alloknesis scores, we also performed scratching bout counting assays under the same administration conditions (Fig 4, *A*). The results obtained showed that only high concentrations of each EM (eg, 100 or 200 nmol per mouse) evoked scratching bouts compared with when the control vehicle was used under nonmechanical conditions (Fig 4, *B* and *C*); however, the frequency of scratching bouts under these conditions peaked approximately 0 to 20 minutes after administration and then converged to the level of the vehicle within 30 to 40 minutes (see Fig E5, *A* and *B* in this article's Online Repository at www.jacionline.org). Therefore, we performed mechanical alloknesis assays 30 minutes after the subsidence of EM-evoked itch. We found that intradermal injection of EM at a concentration of 25 to 200 nmol caused mechanical alloknesis in a dose-dependent manner (Fig 4, *D* and *E*). Mechanical alloknesis was induced in the presence of mechanical stimuli (Fig 4, *D* and *E*) even at low concentrations at which scratching behaviors hardly occurred in the absence of mechanical stimuli (eg, 25 and 50 nmol) (Fig 4, *B* and *C*).

EM-induced mechanical alloknesis is mediated by MOR and also regulated by DPPIV

To confirm whether EMs evoke mechanical alloknesis via peripheral MORs, mice were coadministered 100 nmol of each EM (EM-1 or EM-2) with 30 μg of naloxone methiodide, after which mechanical alloknesis scores were assessed (Fig 5, *A*). Pharmacologically, naloxone methiodide inhibited EM-evoked mechanical alloknesis to a level similar to that observed with the vehicle (Fig 5, *B* and *C*). We investigated the effects of DPPIV enzyme activity on this alloknesis. Because both EMs comprise 4 amino acids and have a DPPIV cleavage site at the penultimate position, we synthetized 3 types of dipeptides as estimated forms of EM-1 and EM-2 cleaved by the enzyme DPPIV (ie, YP, WF-NH_2, and FF-NH_2 [Fig 6, *A*]). Using a mouse MOR-expressing cell line, we confirmed that the cleaved forms of these peptides did not bind to MOR, whereas full-length EMs did (on the basis of the functional changes that occurred when EM bound to MOR [see Figs E6 and E7 in this article's Online Repository at www.jacionline.org]). We coadministered 100 nmol of these peptides (mixtures of YP and WF-NH_2 or YP and FF-NH_2, as components that make up full-length EM-1 or EM-2, respectively) to WT mice (Fig 6, *B*). None of the combinations of truncated EM peptides induced mechanical alloknesis compared with its intact full-length EM (100 nmol), respectively (Fig 6, *C* and *D*).

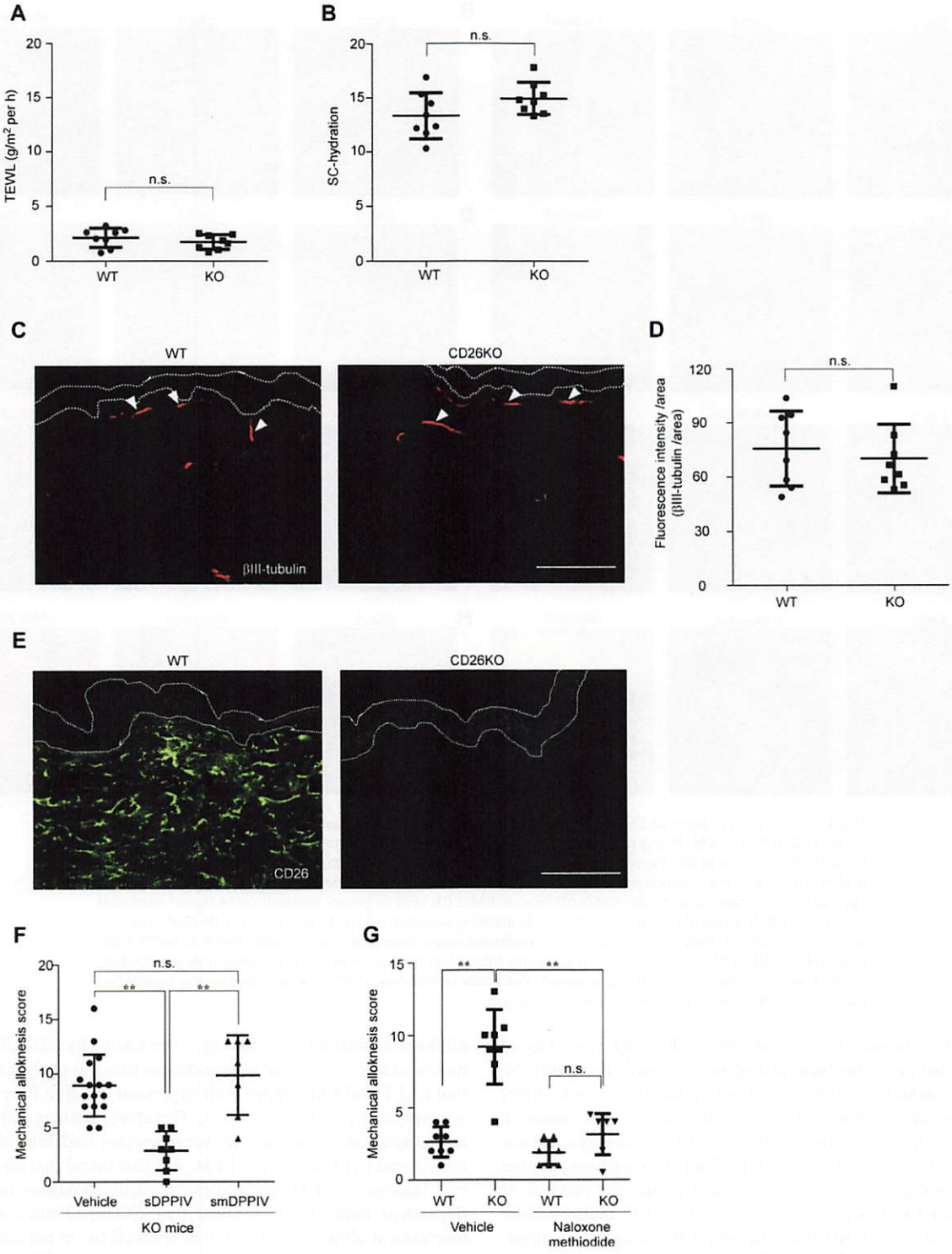

FIG 2. Characterization of mechanical alloknesis in CD26KO mice. **A** and **B,** Transepidermal water loss (TEWL) **(A)** and stratum corneum (SC) hydration **(B)** were evaluated in the skin of WT and CD26KO mice. **C,** Representative immunofluorescence image of the back skin from a WT or CD26KO mouse using a cyanine 3–labeled β-III tubulin antibody (*red indicates a neuronal marker*). Arrowheads indicate β-III tubulin–immunoreactive fibers. Each image between the dotted lines indicates the epidermis. Scale bar = 100 μm. **D,** The fluorescence intensity per unit area of the β-III tubulin antibody was measured for WT or CD26KO mice by using Keyence software (BZ-X800). **E,** Representative immunofluorescence images of the back skin of WT and CD26KO mice obtained by using the anti-CD26 antibody (*green*). Each image between the dotted lines indicates the epidermis. Scale bar = 100 μm. **F,** Effects of sDPPIV and smDPPIV on mechanical alloknesis in CD26KO mice. Mechanical alloknesis in CD26KO mice was inhibited by an intradermal injection of sDPPIV but not smDPPIV. **G,** Naloxone methiodide (a peripheral MOR antagonist) inhibited mechanical alloknesis in CD26KO mice. $^{**}P < .01$. *n.s.*, Not significant.

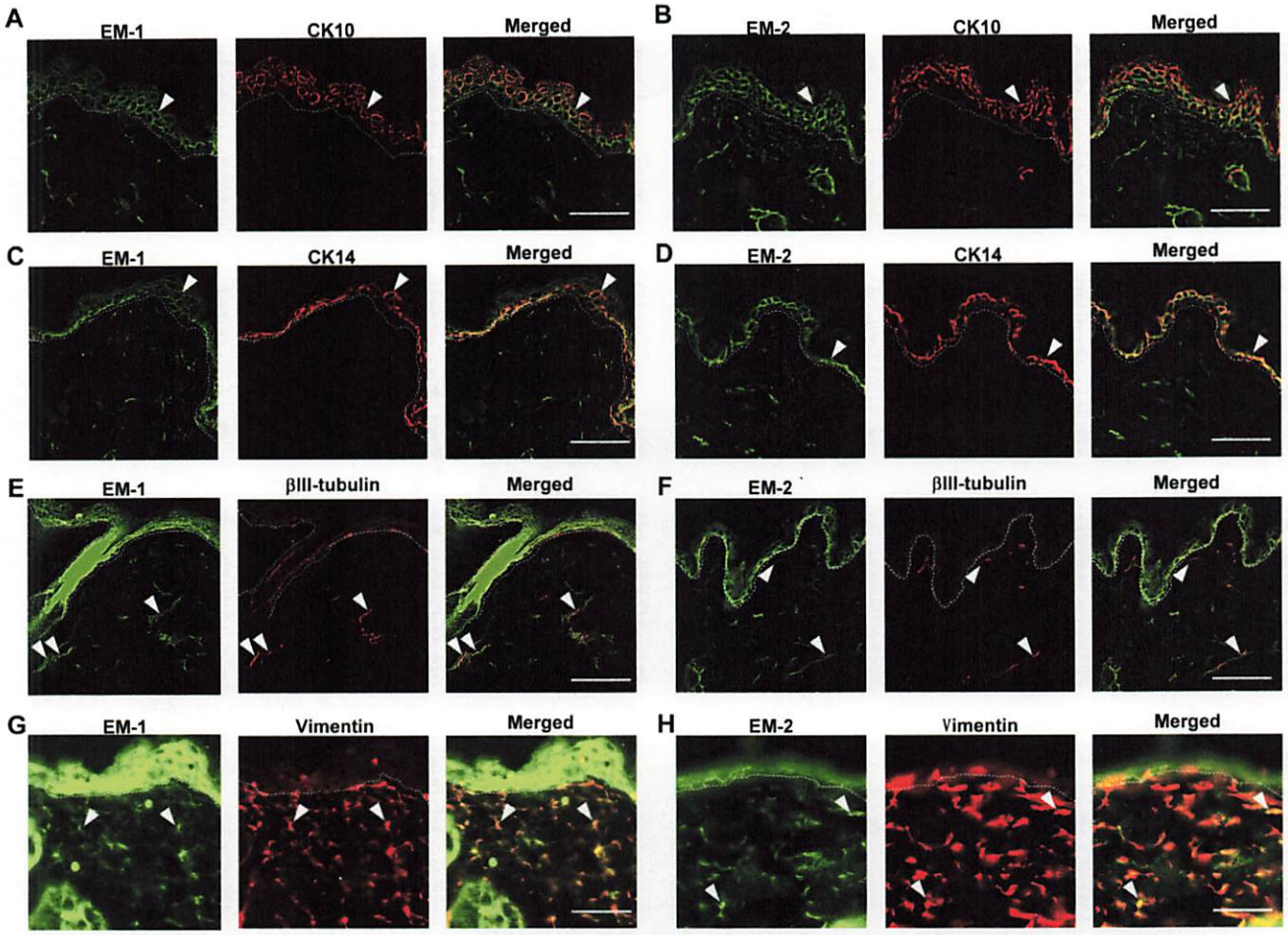

FIG 3. Distribution pattern of EMs in mouse skin. Double immunofluorescence staining with antibodies against EM (EM-1 or EM-2) and marker proteins for epidermal keratinocytes, nerve fibers, or fibroblasts in the skin of WT mice **(A-G)**. Representative images of double staining with anti–EM-1 **(A)** or anti–EM-2 **(B)** (*EM in green*) and anti–cytokeratin 10 (anti-CK10) (*squamous epithelial marker in red*). Representative images of double staining with anti–EM-1 **(C)** or anti–EM-2 **(D)** (*EM in green*) and anti-CK14 (*basal epithelial marker in red*). Representative images of double staining with anti–EM-1 **(E)** or anti–EM-2 **(F)** (*EM in green*) and anti–β-III tubulin (*neuronal marker in red*). Representative images of double staining with anti–EM-1 **(G)** or anti–EM-2 **(H)** (*EM in green*) and anti-vimentin (*fibroblast marker in red*). Arrowheads indicate double-positive signals (*yellow in the merged panel*). The white dotted line in each panel indicates the border between the epidermis and dermis. Scale bar = 50 μm.

To clarify whether the mechanisms underlying EM-induced itch differ between mechanical and nonmechanical conditions, we also conducted scratching bout counting assays under nonmechanical conditions by using the same administration protocol as that used for the mechanical alloknesis assays. Similar to what we observed in the case of mechanical conditions, neither naloxone methiodide (see Fig E5, *C* and *D*) nor the mixture of each truncated EM peptide (see Fig E5, *E* and *F*) induced more frequent scratching bouts than did intact full-length EM alone. Furthermore, when WT or CD26KO mice were intradermally administered 100 nmol of EM-1 or EM-2, the frequency of scratching bouts within 1 hour was significantly higher in CD26KO mice than in WT mice (see Fig E5, *G* and *H*).

DISCUSSION

The present results suggest that a peripheral EM (EM-1 or EM-2)-MOR system mediates mechanical-induced itch (mechanical alloknesis) and that this pathway is modulated by CD26/DPPIV in mouse skin (Fig 7). Our immunohistochemical analyses showed that EM-1 and EM-2 were both expressed in nerve fibers, keratinocytes, and fibroblasts (Fig 3). Therefore, sensory nerve fibers and cutaneous cells, such as keratinocytes and fibroblasts, are considered to be sources of EMs. We also found that an intradermal injection of EM induced mechanical alloknesis in a dose-dependent manner (Fig 4) and that CD26KO mice exhibited mechanical alloknesis, which was rescued by an intradermal injection of the active form of soluble intact CD26/DPPIV$^+$ (sDPPIV) (Fig 2, *F*). Mechanical alloknesis was significantly inhibited by the peripheral MOR antagonist naloxone methiodide (Figs 2, *G* and 5, *B* and *C*). Thus, although further analyses of molecular and cellular mechanisms are needed to obtain a more detailed understanding of mechanical alloknesis, cutaneous EM-MOR may play a pivotal role in its induction under the enzymatic control of DPPIV. This concept may also be supported by the present results showing that cleaved EMs (YP + WF-NH_2

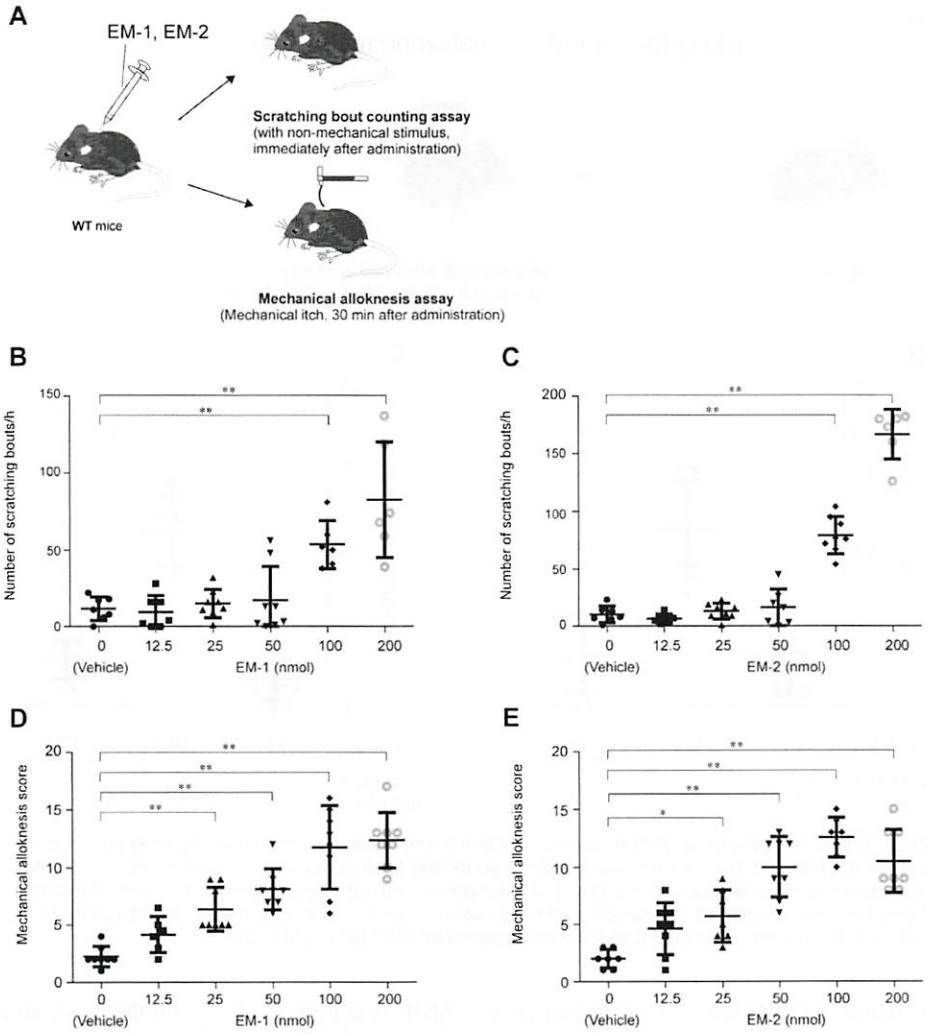

FIG 4. Effects of different concentrations of EMs on scratching bouts and mechanical alloknesis. **A,** Schematic procedure of experiments to assess the sensitivity of EMs (EM-1 and EM-2) at various concentrations in scratching bouts and mechanical alloknesis. A scratching bout counting assay was performed immediately after the intradermal administration of EM, and mechanical alloknesis assays were performed 30 minutes later. **B** and **C,** The frequency of scratching bouts following the intradermal injection of EM-1 **(B)** or EM-2 **(C)** at various concentrations. **D** and **E,** Mechanical alloknesis scores following the intradermal injection of EM-1 **(D)** or EM-2 **(E)** at various concentrations. $*P < .05$; $**P < .01$.

and YP + FF-NH_2) did not induce mechanical alloknesis (Fig 6, *C* and *D*).

CD26 was expressed in the dermal layer of WT mouse skin but not in the dermal layer of CD26KO mouse skin (Fig 2, *E*). Mechanical alloknesis in CD26KO mice was almost completely abrogated by the intradermal injection of sDPPIV but not by the enzymatic mutant (Fig 2, *F*). Thus, although we cannot exclude the possibility of other degradation systems for EM, such as aminopeptidase M[40] or dipeptidyl peptidase III,[41] in CD26KO mice, these results suggest that DPPIV enzyme activity in the dermal layer is at least partially responsible for the negative regulation of mechanical alloknesis in normal mouse skin.

We also found that intradermal injection of EM caused mechanical alloknesis in WT mice in a dose-dependent manner (Fig 4, *D* and *E*). This phenomenon occurred even at low EM concentrations at which scratching behaviors hardly occurred in the absence of mechanical stimuli (Fig 4, *B* and *C*). This may explain why CD26KO mice exhibited only mechanical alloknesis (Fig 1, *B* and *C*).

A previous study also reported that CD26KO mice displayed high susceptibility to nociceptive stimuli, which was restored by a substance P (SP) receptor (NK-1R) antagonist.[42] We recently reported that DPPIV exaggerated itch in psoriasis by cleaving SP.[30] Mechanical alloknesis in CD26KO mice was markedly inhibited (to a level that was not significantly different from that in WT) by the peripheral MOR inhibitor naloxone methiodide (Fig 2, *G*). In contrast, when we examined the effects of SP on mechanical alloknesis induced in CD26KO mice by an intradermal injection of the SP receptor antagonist QWF (Boc-Gln-D-Trp(Formyl)-Phe benzyl ester trifluoroacetate salt, which is an inhibitor of the SP receptors NK1R, the enzyme DPPIV MrgprA1, and MrgprB2),[43] the mechanical alloknesis score was partially

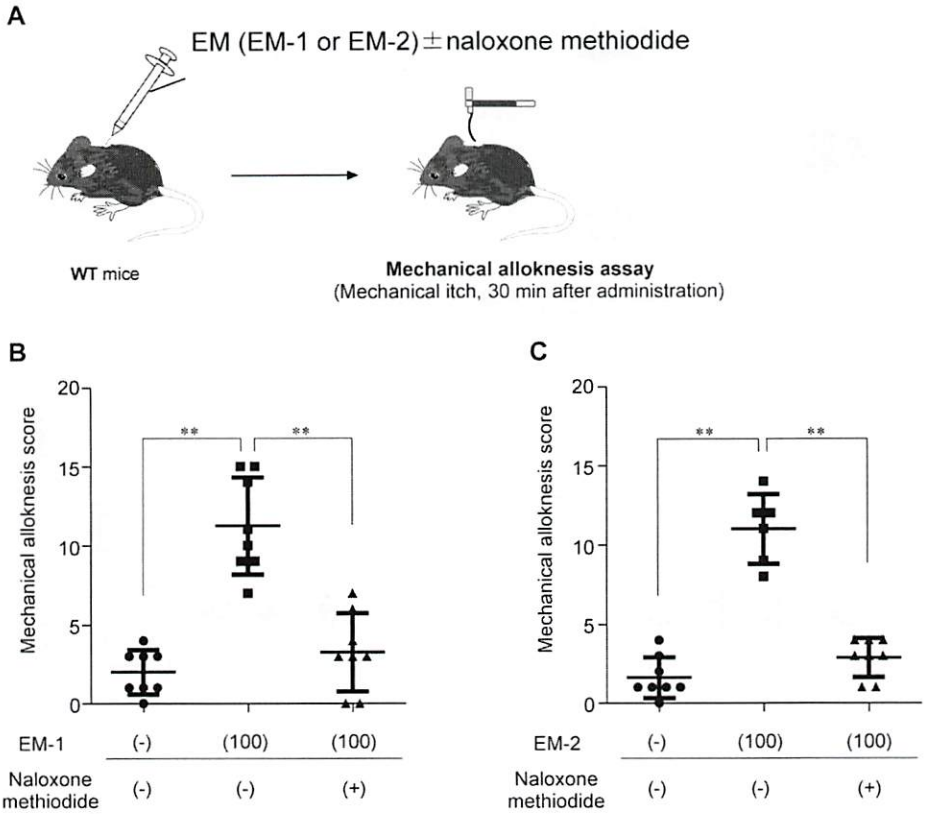

FIG 5. Effects of a peripheral MOR antagonist on EM-induced mechanical alloknesis. **A,** Schematic procedure for the mechanical alloknesis assay under a peripheral MOR antagonist (naloxone methiodide). WT mice were intradermally administered EM-1 or EM-2 with or without naloxone methiodide, and after 30 minutes the measurement of mechanical alloknesis scores in each mouse was started. **B** and **C,** Effects of naloxone methiodide on mechanical alloknesis induced by EM-1 **(B)** or EM-2 **(C)**.

attenuated by the highest dose of QWF (see Fig E8 in this article's Online Repository at www.jacionline.org). Although previous findings showed that SP is an important itch mediator and also a substrate for DPPIV in a psoriasis model,[30] SP and its receptors did not appear to make a significant contribution to the present results. The reason for this may be differences in skin SP levels between previous psoriasis model mice and the CD26KO mice in the present study. In the psoriasis model, SP levels were systemically elevated.[30] Serum SP levels of nontreated CD26KO were significantly lower than those in the WT psoriasis model (unpublished observation, 2017). We speculate that the effects of cutaneous SP were weaker in CD26KO mice than in the WT psoriasis model. Furthermore, SP was shown to play a role in mechanical itch at the spinal level.[2] However, because DPPIV levels in the spinal cord were markedly lower than those in the skin (see Fig E2), the effects of DDPIV on SP in the spinal cord were considered to be limited. Therefore, these results suggest that MOR ligands, rather than SP, play a central role in the regulatory mechanisms of DPPIV-associated mechanical alloknesis at the periphery, and also that the SP-NK1R system may be one of the important signaling pathways for mechanical alloknesis at the spinal level.[10,44]

EM-1 and EM-2 are endogenous opioid peptides that have high affinity and selectivity for MOR.[45] Although EM-1 and EM-2 expression patterns differ in different brain regions, both are strongly expressed in the central nervous system, in which MOR is concentrated.[36,37] Furthermore, an intracisternal injection of both EMs elicited scratching behavior that was inhibited by an MOR antagonist.[35] In the present study, we showed that an intradermal injection of EM elicited mechanical alloknesis, and that this was inhibited by a peripheral MOR antagonist (Fig 5, *B* and *C*). Our histologic analyses revealed that EM-1 and EM-2 were expressed in some sensory nerve fibers (Fig 3, *E* and *F*), which is consistent with previous findings on EM-2 expression in rat skin.[46] We also provided the first evidence for EMs in keratinocytes (Fig 3, *A-D*) and fibroblasts (Fig 3, *G* and *H*). Because general peripheral itch sensations are transmitted and induced through sensory nerve fibers, it appears to be important for EM to act on nerves. EM-1 and/or EM-2 located in nerve fibers may be digested by DPPIV around nerves and involved in the induction of itch and mechanical alloknesis. However, in addition to the nerve fibers themselves potentially secreting these EMs, we were unable to exclude the possibility that EM-1 and/or EM-2 located at nerves are secreted by keratinocytes, which are their most potent expressors in the skin, or fibroblasts localized around nerves in the present study. Similarly, previous findings showing that MORs are located in nerve endings[38,47] and keratinocytes[48,49] imply that EM mediated the induction of mechanical alloknesis via MORs expressed in sensory nerves; however, we cannot completely exclude the possibility of an indirect pathway via MOR-expressing keratinocytes. This concept appears to be supported by the present results showing that

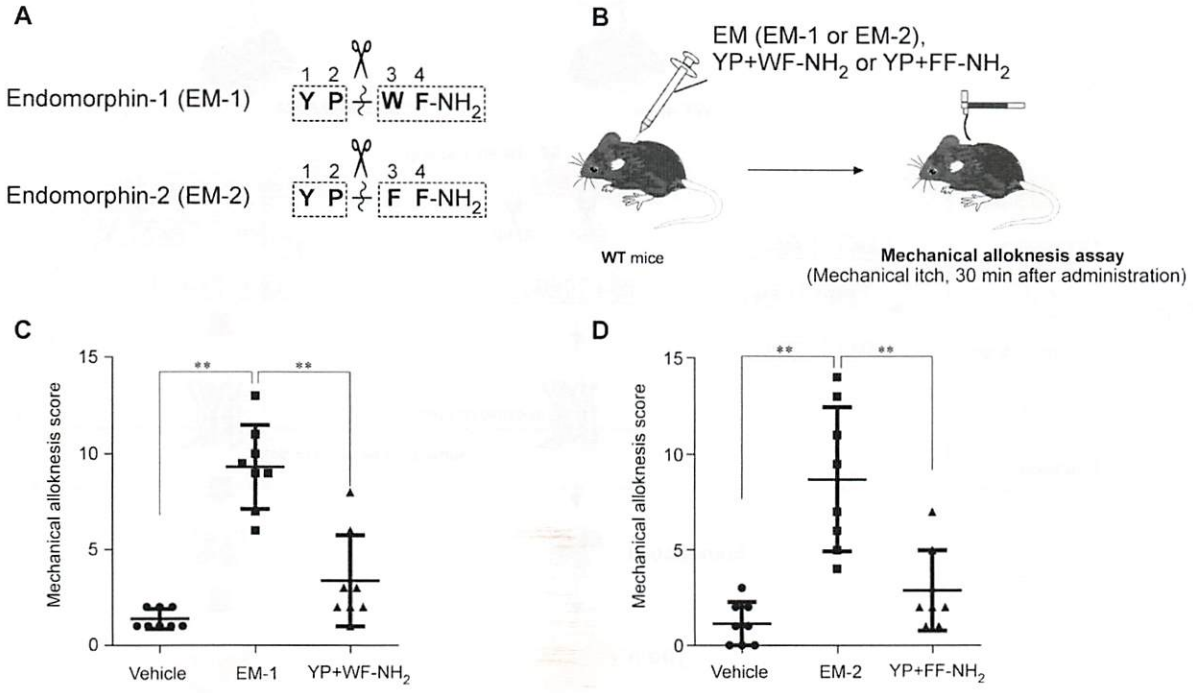

FIG 6. Effect of cleavage by DPPIV on EM-induced mechanical alloknesis. **A,** Schematic diagram of the peptide sequences of EM-1 and EM-2 and their DPPIV cleavage sites. Scissors represent DPPIV, and the short wavy lines represent cleavage sites. **B,** Schematic procedure for the mechanical alloknesis assay for characterization of estimated DPPIV cleaved form mixture of EMs. WT mice were intradermally administered an intact or cleaved form mixture of EM-1 or EM-2. After 30 minutes, measurement of mechanical alloknesis scores in each mouse was started. **C** and **D,** Effects of the DPPIV cleaved form mixture of EM-1 **(C)** or EM-2 **(D)** on mechanical alloknesis. $^{**}P < .01$.

mechanical alloknesis was strongly affected by DPPIV in the dermal layer, which closely surrounds nerve fibers (Fig 2, *E* and *F* and see Fig E1).

In addition to mechanical alloknesis, chemical itch began to appear in normal mice at high concentrations of EMs (>100 nmol) (Fig 4, *B* and *C* and see also Fig E5, *A* and *B*). Our pharmacologic analyses showed that chemical itch was also mediated via MORs and controlled by DPPIV (see Fig E5, *C-H*). Currently, the mechanisms by which MOR agonists induce chemical itch remain unclear. MOR generally suppresses nerve activation by stimulating the heterotrimeric Gi/o protein.[50] Whole-cell patch recordings revealed that EM-1 and EM-2 acted on spinal neurons and attenuated excitatory and inhibitory synaptic currents via MORs.[51] Wang et al recently reported that itch induced by the intrathecal administration of MOR agonists was caused by the suppression of vesicular γ-aminobutyric acid transporter $(Vgat)^+$ inhibitory neurons in the spinal cord.[52] Furthermore, Liu et al demonstrated that one of the isoforms of MOR, MOR-1D, activated nerves by forming a heterodimer with the GRPR.[53]

Accumulating evidence recently showed that similar to the involvement of C-fibers in chemical itch, Aβ-fibers play a pivotal role in mechanical itch.[22,25] Multiple staining of mouse skin with neuronal fiber markers revealed the presence of both EMs in Aβ-fibers (neurofilament 200 $[NF200^+]$/$TrkB^+$) and peptidergic C-fibers ($Peripherin^+$/$CGRP^+$), and to a lesser extent, in Aδ-fibers ($NF200^+$/$CGRP^+$) (see Fig E4); however, their expression profiles in other subpopulations remain unknown. Therefore, we performed a functional silencing experiment on Aβ- and C-fibers[22,54] and found that the functional silencing of Aβ-fibers suppressed EM-evoked alloknesis, whereas silencing of C-fibers did not (unpublished observation, 2020). Moreover, the functional silencing of Aβ-fibers did not attenuate spontaneous scratching behavior (unpublished observation, 2020). Although further studies are needed, these results indicate that EM-1 and EM-2 evoke chemical itch by suppressing the activation of C-fiber neurons innervating inhibitory spinal neurons or activating those innervating excitatory spinal neurons (eg, subpopulation of peptidergic neurons) through a heterodimer of MOR with other G protein–coupled receptors, such as a MOR1D-GRPR heterodimer in the spinal cord,[53,55-57] whereas EM-evoked alloknesis is due to the suppression of Aβ-fiber neurons innervating inhibitory spinal neurons. Because Merkel cells are mechanoreceptors with Aβ-fibers that suppress mechanical itch,[25] they are promising targets for EM-1 and/or EM-2. Although we did not obtain such data in this study, EM-1 and EM-2 may have also been expressed in these cells, because it has been reported that various neuropeptides and opioid receptors are expressed in Merkel cells.[58]

On the basis of the finding showing that many opioids cause mast cell degranulation,[59] in addition to the direct pathway via nerve fibers, a mast cell–mediated pathway is also conceivable as a chemical itch– and/or mechanical itch–inducing pathway. The results of the toluidine blue staining experiment revealed that the mast cell degranulation ratio was significantly higher in CD26KO mice than in WT mice, whereas the number of mast cells in the skin was very low and similar to that in WT

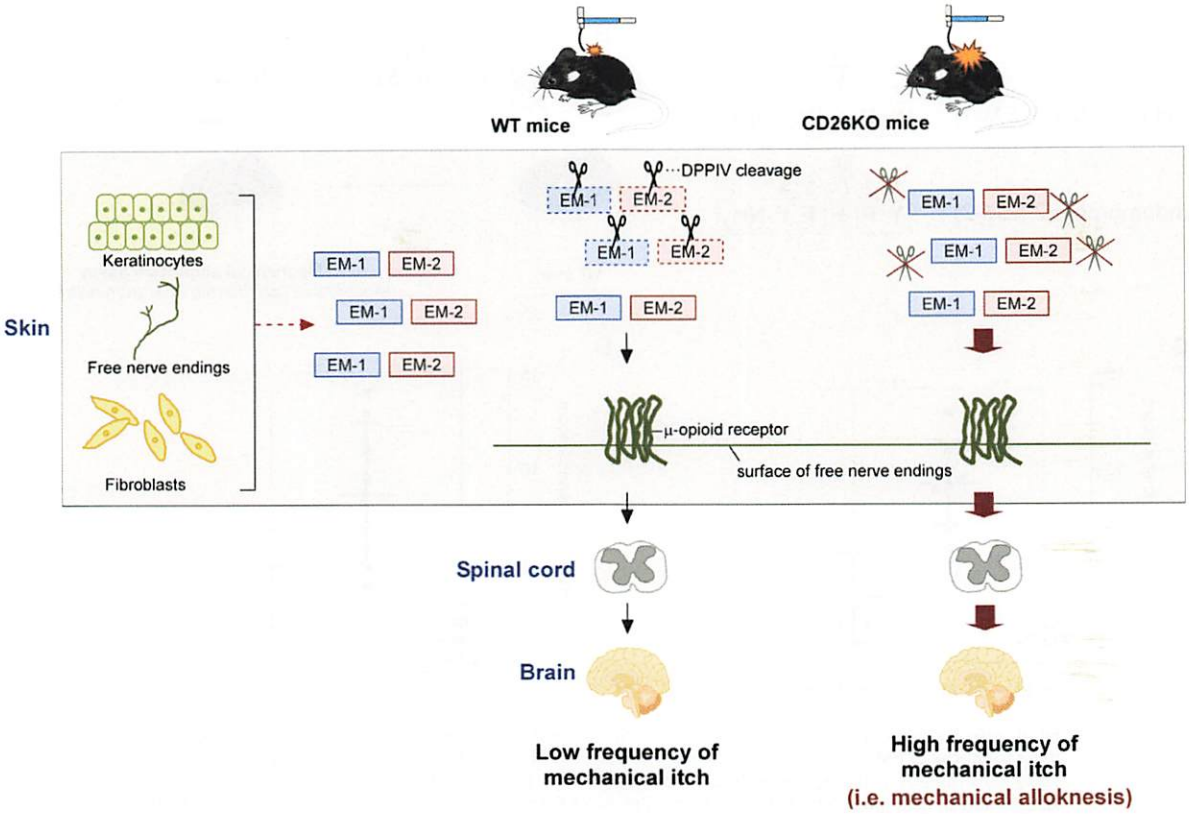

FIG 7. A model for the regulation of EM-induced mechanical alloknesis in mice. Schematic diagram of EM-induced mechanical alloknesis in WT or CD26KO mice. EMs are produced from keratinocytes, parts of nerve endings, and fibroblasts in the skin, and EM may preferentially evoke mechanical alloknesis in a dose-dependent manner over nonmechanical scratching bouts. In WT mice, mechanical alloknesis induced by EM was normally controlled because EM in the skin may have been degraded by DPPIV (one of the functions of CD26). Because EM may not be degraded by DPPIV in CD26KO mice, the sensitivity of innocuous mechanical stimuli–evoked itch (ie, mechanical alloknesis) may be increased via the MOR expressed in skin components, such as sensory nerve fibers.

mice (see Fig E9, *A-D* in this article's Online Repository at www.jacionline.org). Furthermore, our β-hexosaminidase assay on mouse bone marrow–derived mast cells revealed that the highest dose (such as 1 mM) of full-length EM-1 or EM-2, but not the mixture of dipeptides, significantly induced mast cell degranulation (see Fig E10, *B* and *C* in this article's Online Repository at www.jacionline.org). However, in contrast to the results regarding EM-evoked chemical and/or mechanical itch, this degranulation was not inhibited by naloxone (see Fig E10, *D*). Therefore, the contribution of mast cell degranulation to EM-induced chemical and/or mechanical itch is estimated to be small.

We investigated the expression of CD26, EM-1, and EM-2 in the skin of patients with several diseases and in mouse models for which alloknesis has been reported.[6-10,25] Although alloknesis in AD has been reported both in human and mice models, the expression of CD26 was not reduced in human AD skin.[7,8] CD26 expression was also unchanged in human psoriatic skin, mouse dry skin model nor aged mouse skin, which all have been reported to have alloknesis in mouse models[6,9,25] (see Figs E11, *A* and *B* and E12 in this article's Online Repository at www.jacionline.org). According to these data, because the expression of EM-1 and EM-2 was significantly increased in some cases even in the absence of reductions in CD26, DPPIV does not appear to be the sole contributor to the degradation of EM-1 and/or EM-2.[40,41] In addition, no significant differences were observed in skin EM-1 and/or EM-2 levels between WT and CD26KO mice (see Fig E13 in this article's Online Repository at www.jacionline.org). These results may highlight the difficulties associated with using immunohistochemistry to detect alterations in EM-1 and EM-2 levels in skin with alloknesis induced by EM-1 or EM-2. This may also be due to transient or local increases in EM level in skin around the site that received the mechanical stimulus or the low concentration of EM that induced mechanical itch (Fig 4). In contrast to these data, although the number of samples was small, in cutaneous T-cell lymphoma skin, a disease associated with severe itch, the expression of CD26 decreased whereas that of EM-1 and/or EM-2 increased in cancer cells and fibroblasts (see Fig E11, *D*). These data indicate that there are definitely cases of itchy diseases in which there is a significant increase in the expression of EM-1 and EM-2 with the decreased activity of DPPIV. In addition, increased expression of EM-2 was also observed in patients with bullous pemphigoid (a well-known skin disease characterized by itching, in which DPPIV inhibitors, first-line drugs for diabetes,[60] are suspected to be among the causes of its development) who are taking a DPPIV inhibitor (bullous pemphigoid + DPPIV inhibitor [see Fig E11, *C*]).[61] Although as far as we know there are no reports that DPPIV inhibitors directly induce itch or alloknesis, our preliminary results

showing scratching bouts under nonmechanical conditions in WT mice after an intradermal injection of sitagliptin provide support for this concept (Komiya et al, unpublished observations, 2016). These results indicate that in at least some clinical cases, DPPIV enzyme regulates spontaneous itch, and possibly alloknesis, through the degradation of EMs.

In conclusion, the present study showed that EM-1 and EM-2 in the skin preferentially induced mechanical alloknesis over chemical itch and that CD26/DPPIV is the regulatory enzyme for mechanical alloknesis at the periphery. These results at least partly support the role of the peripheral nervous system in the alloknesis-inducing mechanism that has been demonstrated in clinical studies on skin diseases,[7,8] and they also suggest that in addition to being effective in studies of the central nervous system, peripheral approaches are effective for diseases associated with itch hypersensitivity.

We thank Ms H. Otsuka, Dr N. Takahashi, Dr C. S. Moniaga, Dr M. Kurosawa, Mr R. Kosuge, Mrs M. Fujishiro, Mr R. Kosaka, Dr M. Sato, Ms Y. Narita, Ms S. Okamoto, Dr H. Yamazaki, and Dr N. Iwao for their technical support.

Key messages

- **EM-MOR signaling provoked mechanical alloknesis at the periphery under the enzymatic control of CD26/DPPIV.**
- **Topically applied MOR antagonists and CD26/DPPIV are promising treatments for mechanical alloknesis.**

REFERENCES

1. Mack MR, Kim BS. The itch-scratch cycle: a neuroimmune perspective. Trends Immunol 2018;39:980-91.
2. Matsumoto A, Murota H, Terao M, Katayama I. Attenuated activation of homeostatic glucocorticoid in keratinocytes induces alloknesis via aberrant artemin production. J Invest Dermatol 2018;138:1491-500.
3. Moniaga CS, Tominaga M, Takamori K. Mechanisms and management of itch in dry skin. Acta Derm Venereol 2020;100:adv00024.
4. Tominaga M, Takamori K. An update on peripheral mechanisms and treatments of itch. Biol Pharm Bull 2013;36:1241-7.
5. Tominaga M, Takamori K. Itch and nerve fibers with special reference to atopic dermatitis: therapeutic implications. J Dermatol 2014;41:205-12.
6. Sakai K, Sanders KM, Youssef MR, Yanushefski KM, Jensen L, Yosipovitch G, et al. Mouse model of imiquimod-induced psoriatic itch. Pain 2016;157:2536-43.
7. Ikoma A, Fartasch M, Heyer G, Miyachi Y, Handwerker H, Schmelz M. Painful stimuli evoke itch in patients with chronic pruritus: central sensitization for itch. Neurology 2004;62:212-7.
8. Andersen HH, Elberling J, Solvsten H, Yosipovitch G, Arendt-Nielsen L. Nonhistaminergic and mechanical itch sensitization in atopic dermatitis. Pain 2017;158:1780-91.
9. Akiyama T, Carstens MI, Ikoma A, Cevikbas F, Steinhoff M, Carstens E. Mouse model of touch-evoked itch (alloknesis). J Invest Dermatol 2012;132:1886-91.
10. Akiyama T, Nguyen T, Curtis E, Nishida K, Devireddy J, Delahanty J, et al. A central role for spinal dorsal horn neurons that express neurokinin-1 receptors in chronic itch. Pain 2015;156:1240-6.
11. Fukuoka M, Miyachi Y, Ikoma A. Mechanically evoked itch in humans. Pain 2013;154:897-904.
12. Bourane S, Duan B, Koch SC, Dalet A, Britz O, Garcia-Campmany L, et al. NPY Cre Science 2015 Gate control of mechanical itch by a subpopulation of spinal cord interneurons. Science 2015;350:550-4.
13. Han L, Ma C, Liu Q, Weng HJ, Cui Y, Tang Z, et al. A subpopulation of nociceptors specifically linked to itch. Nat Neurosci 2013;16:174-82.
14. Mishra SK, Hoon MA. The cells and circuitry for itch responses in mice. Science 2013;340:968-71.
15. Barry DM, Liu XT, Liu B, Liu XY, Gao F, Zeng X, et al. Exploration of sensory and spinal neurons expressing gastrin-releasing peptide in itch and pain related behaviors. Nat Commun 2020;11:1397.
16. Sun YG, Chen ZF. A gastrin-releasing peptide receptor mediates the itch sensation in the spinal cord. Nature 2007;448:700-3.
17. Sun YG, Zhao ZQ, Meng XL, Yin J, Liu XY, Chen ZF. Cellular basis of itch sensation. Science 2009;325:1531-4.
18. Ross SE, Mardinly AR, McCord AE, Zurawski J, Cohen S, Jung C, et al. Loss of inhibitory interneurons in the dorsal spinal cord and elevated itch in Bhlhb5 mutant mice. Neuron 2010;65:886-98.
19. Kardon AP, Polgár E, Hachisuka J, Snyder LM, Cameron D, Savage S, et al. Dynorphin acts as a neuromodulator to inhibit itch in the dorsal horn of the spinal cord. Neuron 2014;82:573-86.
20. Huang J, Polgár E, Solinski HJ, Mishra SK, Tseng PY, Iwagaki N, et al. Circuit dissection of the role of somatostatin in itch and pain. Nat Neurosci 2018;21:707-16.
21. Acton D, Ren X, Di Costanzo S, Dalet A, Bourane S, Bertocchi I, et al. Spinal neuropeptide Y1 receptor-expressing neurons form an essential excitatory pathway for mechanical itch. Cell Rep 2019;28:625-39.e6.
22. Pan H, Fatima M, Li A, Lee H, Cai W, Horwitz L, et al. Identification of a spinal circuit for mechanical and persistent spontaneous itch. Neuron 2019;103:1135-49.e6.
23. Ikoma A, Handwerker H, Miyachi Y, Schmelz M. Electrically evoked itch in humans. Pain 2005;113:148-54.
24. Andersen HH, Akiyama T, Nattkemper LA, van Laarhoven A, Elberling J, Yosipovitch G, et al. Alloknesis and hyperknesis-mechanisms, assessment methodology, and clinical implications of itch sensitization. Pain 2018;159:1185-97.
25. Feng J, Luo J, Yang P, Du J, Kim BS, Hu H. Piezo2 channel-Merkel cell signaling modulates the conversion of touch to itch. Science 2018;360:530-3.
26. Morimoto C, Schlossman SF. The structure and function of CD26 in the T-cell immune response. Immunol Rev 1998;161:55-70.
27. Ohnuma K, Dang NH, Morimoto C. Revisiting an old acquaintance: CD26 and its molecular mechanisms in T cell function. Trends Immunol 2008;29:295-301.
28. Ohnuma K, Hatano R, Komiya E, Otsuka H, Itoh T, Iwao N, et al. A novel role for CD26/dipeptidyl peptidase IV as a therapeutic target. Front Biosci (Landmark Ed) 2018;23:1754-79.
29. Ohnuma K, Hosono O, Dang NH, Morimoto C. Dipeptidyl peptidase in autoimmune pathophysiology. Adv Clin Chem 2011;53:51-84.
30. Komiya E, Hatano R, Otsuka H, Itoh T, Yamazaki H, Yamada T, et al. A possible role for CD26/DPPIV enzyme activity in the regulation of psoriatic pruritus. J Dermatol Sci 2017;86:212-21.
31. Marguet D, Baggio L, Kobayashi T, Bernard AM, Pierres M, Nielsen PF, et al. Enhanced insulin secretion and improved glucose tolerance in mice lacking CD26. Proc Natl Acad Sci U S A 2000;97:6874-9.
32. Tanaka T, Kameoka J, Yaron A, Schlossman SF, Morimoto C. The costimulatory activity of the CD26 antigen requires dipeptidyl peptidase IV enzymatic activity. Proc Natl Acad Sci U S A 1993;90:4586-90.
33. Shane R, Wilk S, Bodnar RJ. Modulation of endomorphin-2-induced analgesia by dipeptidyl peptidase IV. Brain Res 1999;815:278-86.
34. Sakurada C, Sakurada S, Hayashi T, Katsuyama S, Tan-No K, Sakurada T. Degradation of endomorphin-2 at the supraspinal level in mice is initiated by dipeptidyl peptidase IV: an in vitro and in vivo study. Biochem Pharmacol 2003;66:653-61.
35. Yamaguchi T, Kitagawa K, Kuraishi Y. Itch-associated response and antinociception induced by intracisternal endomorphins in mice. Jpn J Pharmacol 1998;78:337-43.
36. Martin-Schild S, Gerall AA, Kastin AJ, Zadina JE. Differential distribution of endomorphin 1- and endomorphin 2-like immunoreactivities in the CNS of the rodent. J Comp Neurol 1999;405:450-71.
37. Schreff M, Schulz S, Wiborny D, Höllt V. Immunofluorescent identification of endomorphin-2-containing nerve fibers and terminals in the rat brain and spinal cord. Neuroreport 1998;9:1031-4.
38. Bardoni R, Tawfik VL, Wang D, François A, Solorzano C, Shuster SA, et al. Delta opioid receptors presynaptically regulate cutaneous mechanosensory neuron input to the spinal cord dorsal horn. Neuron 2014;81:1312-27.
39. Usoskin D, Furlan A, Islam S, Abdo H, Lönnerberg P, Lou D, et al. Unbiased classification of sensory neuron types by large-scale single-cell RNA sequencing. Nat Neurosci 2015;18:145-53.
40. Tomboly C, Peter A, Toth G. In vitro quantitative study of the degradation of endomorphins. Peptides 2002;23:1573-80.
41. Barsun M, Jajcanin N, Vukelić B, Spoljarić J, Abramić M. Human dipeptidyl peptidase III acts as a post-proline-cleaving enzyme on endomorphins. Biol Chem 2007;388:343-8.

42. Guieu R, Fenouillet E, Devaux C, Fajloun Z, Carrega L, Sabatier JM, et al. CD26 modulates nociception in mice via its dipeptidyl-peptidase IV activity. Behav Brain Res 2006;166:230-5.
43. Azimi E, Reddy VB, Shade KC, Anthony RM, Talbot S, Pereira PJS, et al. Dual action of neurokinin-1 antagonists on Mas-related GPCRs. JCI Insight 2016;1: e89362.
44. Carstens E, Follansbee T, Iodi Carstens M. The challenge of basic itch research. Acta Derm Venereol 2020;100:adv00023.
45. Zadina JE, Hackler L, Ge LJ, Kastin AJ. A potent and selective endogenous agonist for the mu-opiate receptor. Nature 1997;386:499-502.
46. Barr GA, Zadina JE. Maturation of endomorphin-2 in the dorsal horn of the medulla and spinal cord of the rat. Neuroreport 1999;10:3857-60.
47. Ständer S, Gunzer M, Metze D, Luger T, Steinhoff M. Localization of mu-opioid receptor 1A on sensory nerve fibers in human skin. Regul Pept 2002;110:75-83.
48. Bigliardi PL, Bigliardi-Qi M, Buechner S, Rufli T. Expression of mu-opiate receptor in human epidermis and keratinocytes. J Invest Dermatol 1998;111:297-301.
49. Takahashi N, Tominaga M, Kosaka R, Kamata Y, Umehara Y, Matsuda H, et al. Involvement of μ-opioid Receptors and κ-opioid receptors in itch-related scratching behaviour of imiquimod-induced psoriasis-like dermatitis in mice. Acta Derm Venereol 2017;97:928-33.
50. Zhang L, Zhang JT, Hang L, Liu T. Mu opioid receptor heterodimers emerge as novel therapeutic targets: recent progress and future perspective. Front Pharmacol 2020;11:1078.
51. Wu SY, Ohtubo Y, Brailoiu GC, Dun NJ. Effects of endomorphin on substantia gelatinosa neurons in rat spinal cord slices. Br J Pharmacol 2003;140:1088-96.
52. Wang Z, Jiang C, Yao H, Chen O, Rahman S, Gu Y, et al. Central opioid receptors mediate morphine-induced itch and chronic itch via disinhibition. Brain 2021;144: 665-81.
53. Liu XY, Liu ZC, Sun YG, Ross M, Kim S, Tsai FF, et al. Unidirectional cross-activation of GRPR by MOR1D uncouples itch and analgesia induced by opioids. Cell 2011;147:447-58.
54. Binshtok AM, Bean BP, Woolf CJ. Inhibition of nociceptors by TRPV1-mediated entry of impermeant sodium channel blockers. Nature 2007;449:607-10.
55. Borroto-Escuela DO, Romero-Fernandez W, Rivera A, Van Craenenbroeck K, Tarakanov AO, Agnati LF, et al. On the g-protein-coupled receptor heteromers and their allosteric receptor-receptor interactions in the central nervous system: focus on their role in pain modulation. Evid Based Complement Alternat Med 2013: 2013:563716.
56. Akgün E, Javed MI, Lunzer MM, Powers MD, Sham YY, Watanabe Y, et al. Inhibition of inflammatory and neuropathic pain by targeting a mu opioid receptor/chemokine receptor5 heteromer (MOR-CCR5). J Med Chem 2015;58:8647-57.
57. Smeester BA, Lunzer MM, Akgün E, Beitz AJ, Portoghese PS. Targeting putative mu opioid/metabotropic glutamate receptor-5 heteromers produces potent antinociception in a chronic murine bone cancer model. Eur J Pharmacol 2014;743:48-52.
58. Tachibana T, Nawa T. Immunohistochemical reactions of receptors to met-enkephalin, VIP, substance P, and CGRP located on Merkel cells in the rat sinus hair follicle. Arch Histol Cytol 2005;68:383-91.
59. Lansu K, Karpiak J, Liu J, Huang XP, McCorvy JD, Kroeze WK, et al. In silico design of novel probes for the atypical opioid receptor MRGPRX2. Nat Chem Biol 2017;13:529-36.
60. Cahn A, Cernea S, Raz I. An update on DPP-4 inhibitors in the management of type 2 diabetes. Expert Opin Emerg Drugs 2016;21:409-19.
61. Béné J, Moulis G, Bennani I, Auffret M, Coupe P, Babai S, et al. Bullous pemphigoid and dipeptidyl peptidase IV inhibitors: a case-noncase study in the French Pharmacovigilance Database. Br J Dermatol 2016;175:296-301.

Cureus

Open Access Review Article

DOI: 10.7759/cureus.13495

CD26/Dipeptidyl Peptidase IV and Its Multiple Biological Functions

Kelsey Pan [1], Kei Ohnuma [2], Chikao Morimoto [2], Nam H. Dang [3]

1. Internal Medicine, University of Florida, Gainesville, USA 2. Department of Therapy Development and Innovation for Immune Disorders and Cancers, Juntendo University, Tokyo, JPN 3. Oncology, University of Florida, Gainesville, USA

Corresponding author: Kelsey Pan, kelsey.pan@ufl.edu

Abstract

CD26/Dipeptidyl peptidase IV (DPPIV) is a cell surface glycoprotein with numerous roles including glucose metabolism, immunomodulation, and tumorigenesis. CD26/DPPIV is well recognized in diabetes, with DPPIV inhibitors being a class of oral hypoglycemic drugs called gliptins that are commonly used to treat type two diabetes mellitus. Recent work also indicated a potential role for CD26 in infectious diseases, including COVID-19, and immune-mediated disorders such as rheumatoid arthritis, inflammatory bowel disease, and graft-versus-host disease.

In cancer, CD26/DPPIV expression has been characterized in numerous tumors such as hematologic malignancies, malignant pleural mesothelioma (MPM), renal cell carcinoma (RCC), hepatocellular carcinoma (HCC), gastrointestinal stromal tumor (GIST), and prostate, lung, colorectal, and ovarian (PLCO) cancer. Hence, CD26 has been frequently studied as a tumor biomarker and therapeutic target. CD26/DPPIV-targeted therapies have been evaluated in various cancers, including the use of anti-CD26 monoclonal antibodies as anticancer treatment in selected neoplasms.

This review highlights our current understanding of the role of CD26 in cancer, diabetes, immune-mediated diseases, and infectious diseases. Enhanced understanding of CD26 biology and function may lead to novel therapeutic approaches in multiple human diseases.

Categories: Internal Medicine, Infectious Disease, Oncology
Keywords: cd26, dipeptidyl peptidase iv, cancer, diabetes, immunology, infectious disease, covid

Introduction And Background

CD26/Dipeptidyl peptidase IV (DPPIV) is a cell surface glycoprotein that is commonly expressed in many cell types and has numerous biological functions. It cleaves amino-terminal dipeptides with terminal L-proline or L-alanine and is expressed on leukocytes, fibroblasts, mesothelium, endothelial cells, and epithelial cells. It plays a role in multiple biological functions ranging from immunoregulation to glucose homeostasis. Moreover, it is involved in tumorigenesis and may serve as a tumor suppressor or activator, depending on its tumor microenvironment [1-2]. CD26/DPPIV has therefore been extensively studied as a biomarker in various malignancies and as a potential therapeutic target. Interestingly, CD26/DPPIV has recently been implicated to have a role in infectious processes involving Middle East respiratory syndrome coronavirus (MERS-CoV) and also potentially severe acute respiratory syndrome coronavirus 2 (SARS-CoV2) by serving as a cellular receptor to allow for viral entry [2-4]. In this paper, we will review the pertinent literature characterizing the role of CD26/DPPIV, while highlighting some of the major aspects of this molecule in immunology, diabetes, cancer, and infectious diseases.

Review began 02/09/2021
Review ended 02/22/2021
Published 02/22/2021

Review

CD26 in immune system

CD26/DPPIV in T-Cell Activation

A series of studies demonstrated that CD26/DPPIV has a role in the regulation of the human immune system. A marker of activated T cells, CD26 expression, is upregulated during T-cell activation and is preferentially expressed on CD4+ T memory cells [5]. It is a costimulatory molecule capable of enhancing T lymphocyte activation and proliferation induced through the CD3/T-cell receptor complex as well as the CD2 molecule [6-10]. CD26 involvement in T-cell activation is determined in part by its physical and functional association with a number of key molecules involved in T-cell signal transduction processes, leading eventually to intracellular calcium mobilization, tyrosine phosphorylation of downstream signaling proteins, and increased IL-2 production [11-12]. CD26 also plays a role in human thymocyte activation and thymic differentiation through the CD3 pathway [9].

CD26 in Immune-Mediated Disorders

How to cite this article
Pan K, Ohnuma K, Morimoto C, et al. (February 22, 2021) CD26/Dipeptidyl Peptidase IV and Its Multiple Biological Functions. Cureus 13(2): e13495. DOI 10.7759/cureus.13495

Having a key role in the signaling processes of T-cell activation, CD26/DPPIV is involved in immune-mediated disorders such as autoimmune diseases and graft-versus-host disease (GVHD). An accumulation of CD26+ lymphocytes was found in target organs involved in GVHD, rheumatoid arthritis (RA), and inflammatory bowel disease (IBD) [15]. CD26 levels have been shown to correlate with disease severity in chronic inflammatory and autoimmune diseases such as RA, IBD, multiple sclerosis, and Graves' disease, suggesting a role for CD26+ T cells in mediating inflammation and tissue damage. In RA, CD26 levels were inversely correlated with the number of swollen joints. CD26+ T cells are believed to migrate from the peripheral blood into the rheumatoid synovium, thus facilitating inflammation and subsequent tissue destruction in RA. In murine studies, DPPIV inhibitors suppressed RA in a dose-dependent manner [14]. The DPPIV inhibitor sitagliptin was recently found to inhibit fibrosis in systemic sclerosis by inhibiting TGF-B-induced lung fibroblast activation in vitro. It also improved lung injury histologically through the inhibition of proinflammatory cytokines such as IL-1b, TNF-a, and IL-6 [15]. These findings suggest that DPPIV inhibitors may be effective in suppressing immune system in similar inflammatory processes, resulting in clinical improvement of these immune-mediated disorders.

CD26 in Graft-Versus-Host Disease

GVHD is an immune-mediated complication of allogeneic hematopoietic stem-cell transplants (HSCT). Work with a murine model demonstrated that injection of anti-CD26 monoclonal antibodies decreased the severity of GVHD by decreasing IL-26 production, while graft-versus-leukemia effect was still maintained, resulting in prolonged survival [15]. This research suggests that CD26 plays a role in the pathophysiology of GVHD and can be a novel therapeutic target for immune-mediated conditions such as GVHD and chronic inflammatory disorders.

A recent phase II clinical trial showed that treatment with the DPPIV inhibitor sitagliptin in combination with tacrolimus and sirolimus resulted in low incidence of acute GVHD after allogeneic HSCT, compared to 30% in previously published literature. Acute GVHD occurred in two out of 36 patients with an incidence of grade II to IV GVHD of 5%, markedly lower than the observed incidence among patients on sirolimus and tacrolimus alone, which varied from 7% to 47% in prior studies. The one-year cumulative incidence of chronic GVHD was 37% (95% CI: 22% to 53%), compared to observations of 39% to 53% in prior studies [16]. In addition, no toxic effects associated with sitagliptin were observed. This study further supports the role of CD26 in the GVHD, hence the protective properties of DPPIV inhibitors as demonstrated.

CD26 in Diabetes

CD26/DPPIV expression in adipose tissue, pancreatic islet cells, hepatic cells, and microvascular endothelial cells is increased in obesity, diabetes, and other states of inflammation. Incretin hormones such as glucagon-like peptide-1 (GLP-1) and glucose-dependent insulinotropic polypeptide (GIP) regulate post-prandial insulin secretion; however, they are rapidly degraded by CD26/DPPIV. Inhibition of CD26 thus improves post-prandial insulin activity by increasing GLP-1 and GIP levels. Therefore, DPPIV inhibitors, which lower DPPIV activity by 70%-90%, have a significant clinical role in the treatment of type two diabetes [17].

DPPIV-deficient mice have improved glucose tolerance, lower serum glucose levels, and increased insulin secretion after glucose administration [17]. DPPIV inhibition over a longer duration (eight weeks) in mice was associated with increased GLP-1, increased insulin levels, and increased glucose transporter isoform-2 (GLUT-2) expression, even in glucose-intolerant mice. Studies have also suggested the role of DPPIV inhibitors in endothelial growth by inducing endothelial cell proliferation through the activation of TNF-a or IL-1B. These findings suggest a potential role for DPPIV inhibitors in reversing some diabetic vascular complications [17].

In addition, DPPIV levels are elevated in liver diseases, with increased expression in the liver linked to the development of insulin resistance and non-alcoholic fatty liver disease. In mouse models, obesity induces the synthesis of DPPIV by the liver, which subsequently contributes to increased inflammation in adipose tissue, thus exacerbating insulin resistance and metabolic syndrome [18]. Studies with murine models also revealed that DPPIV inhibitors prevented hepatic steatosis and diet-induced inflammation of adipose tissue by inhibiting the infiltration of CD8+ T cells and macrophages [19].

A meta-analysis demonstrated that all DPPIV inhibitors resulted in a moderate reduction of hemoglobin A1c (HbA1c) by 0.5%-0.8%. In a trial of 800 patients with inadequate glycemic control with metformin monotherapy, both saxagliptin and sitagliptin led to reductions in HbA1c by 0.52% and 0.26%, respectively [19]. Amori et al. similarly found that DPPIV inhibitors lowered HbA1c compared to placebo by a weighted mean of 0.74% (95% CI: 0.62%-0.85%). Patients treated with DPPIV inhibitors were found to be more likely to achieve HbA1c less than 7% compared to placebo, without significant differences between sitagliptin and vildagliptin (risk ratio 2.5%; 95% CI: 2.1%-2.8%, $p < 0.005$) [19]. DPPIV inhibitors were shown to be weight neutral with minimal risk of hypoglycemia and gastrointestinal side effects due to the GLP-1-mediated mechanism of action [18-19].

CD26 in cancer

There is extensive literature evaluating the role of CD26/DPPIV in malignant processes. CD26 expression has been characterized on various cancers such as malignant pleural mesothelioma (MPM), colorectal cancer (CRC), hepatocellular carcinoma (HCC), renal cell carcinoma (RCC), lung cancer, prostate cancer, thyroid cancer, gastrointestinal stromal tumor (GIST), thyroid cancer, and selected hematologic malignancies [20]. CD26 presence has been associated with more aggressive variants in certain cancers through its regulation of metastasis and local invasion, while its absence has also been linked to the development of other cancers due to its ability to regulate cancer progression [1,20]. DPPIV inhibitors are believed to have antineoplastic effects partly by regulating CXCL10-mediated activity of CXCR3+ lymphocyte. CXCR3 is a receptor for CXCL10, and its engagement activates antitumor immune response via the recruitment of T cells, monocytes, and macrophages. CD26/DPPIV cleaves CXCL10 to regulate its biological activity, and DPPIV inhibition prevents degradation of CXCL10, thus increasing CXCR3+ T lymphocyte levels and reducing tumor growth [20]. CD26/DPPIV also increases cell sensitivity to apoptosis in response to topoisomerase II inhibitors, such as doxorubicin and etoposide, in in vitro and in vivo studies [21-23]. Following are some of the key findings regarding the role of CD26 in specific malignancies.

Malignant Mesothelioma

Multiple studies have shown CD26 to be an important tumor marker as well as a novel therapeutic target in malignant mesothelioma. CD26 is expressed at high levels in malignant mesothelioma but not in benign mesothelial cells. A study of 79 patients with MPM showed that 73.4% of MPM exhibited CD26 surface expression. In particular, most epithelioid and biphasic MPM variants, but not sarcomatoid MPM, expressed surface CD26 [24]. CD26 surface expression was also correlated with improved survival in MPM patients who received chemotherapy (mean survival time of 18.6 versus 10.7 months, $p = 0.0083$), suggesting an association between CD26 expression and mesothelioma chemosensitivity ($p = 0.053$) [2,24]. Meanwhile, the administration of the humanized anti-CD26 mAb YS110 resulted in growth inhibition of malignant mesothelioma cells in in vitro studies while significantly reducing tumor growth and improving survival in human malignant mesothelioma cell-bearing murine xenograft models. In addition, a first-in-human (FIH) phase I trial involving 33 patients with heavily pretreated CD26-positive malignancies, including 22 patients with malignant mesothelioma, treated with YS110 was recently conducted. Stable disease was observed in half of the patients at 43 days, while prolonged stabilization was seen in seven of 13 patients with stable disease, with a median progression-free survival (PFS) of 33 weeks. This clinical trial demonstrated promising clinical results in CD26-positive MPM patients who previously progressed on multiple chemotherapy agents [25].

In addition, the results of a recently completed phase I trial with Japanese patients with advanced MPM treated with YS110 were reported. Nine Japanese patients were randomized to three different dose cohorts of YS110: two, four, or six mg/kg. While seven of the nine patients developed grade three or four adverse events, most commonly decreased lymphocyte count, and none developed a dose-limiting toxicity. In terms of tumor response, four of seven patients had stable disease, while one achieved a partial response. This phase I trial showed that YS110 administration yielded promising antineoplastic outcome in advanced MPM while remaining relatively well-tolerated, similar to the FIH trial reported previously [26].

Prostate Cancer

Studies of CD26 expression as a biomarker or prognosticator for prostate cancer have demonstrated mixed results. One study showed that malignant prostate tissue expressed twice as high CD26/DPPIV activity compared to benign prostatic hyperplasia (BPH). DPPIV levels were also similarly increased in BPH glands associated with prostatic cancer, suggesting the possible production of local growth factors influencing cancer proliferation. An analysis suggested that high DPPIV expression in prostate cancer tissue samples was associated with poor prognosis ($p < 0.0001$) [27]. Shah et al. identified 15,330 patients with prostate cancer and type two diabetes through the Surveillance, Epidemiology, and End Results (SEER) and Medicare-linked database and found significantly improved overall survival (OS) in patients on DPPIV inhibitors compared to control (HR 0.77, $p = 0.005$). Patients with prostate cancer on metformin also had improved OS compared to controls with HR 0.87 (95% CI: 0.81-0.93, $p < 0.0001$) [28].

On the other hand, an in vitro study by Wesley et al. suggested that DPPIV may have tumor suppressor function by inhibiting the malignant phenotype of prostate cancer via the blocking of basic fibroblast growth factor signaling pathway; therefore, DPPIV inhibition may facilitate tumor growth [29]. Similarly, Sun et al. found that CD26/DPPIV inhibition enhanced invasion and metastasis of prostate cancer cell lines in both in vitro and in vivo assays. CD26/DPPIV cleaves and degrades CXCL12, and in vivo assay found that animals treated with a DPPIV inhibitor had increased prostate cancer cells in all tissues, especially in osseous tissues. These findings suggest that CD26/DPPIV inhibition facilitates prostate cancer invasion into the marrow and metastasis via CXCL12/CXCR4 chemotaxis [30].

Russo et al. found decreased DPPIV mRNA and protein levels in patients with castrate-resistant prostate cancer, and DPPIV inhibition with sitagliptin enhanced prostate cancer xenografts growth after castration. These results suggest that DPPIV may play a role in androgen receptor-regulated tumor suppression, and

DPPIV inhibition facilitates growth factor activity and therefore tumor growth [31]. Nazarian et al. found that DPPIV activity was reduced in patients with metastatic prostate cancer compared to those with localized disease or healthy control subjects, though no difference in DPPIV serum levels was noted. Reduced DPPIV activity was shown to be a significant predictor of cancer status after adjusting for age and PSA level [32].

Colorectal Cancer

Numerous studies have suggested the role of CD26 as a biomarker for early CRC detection [33-34]. Cordero et al. reported reduced serum CD26 level in CRC patients compared to healthy controls, especially in the early stages of disease. Serum CD26 levels had a sensitivity of 81.8% for predicting CRC of Dukes' stages A, B, and C, whereas in stage D, CD26 levels were actually elevated and CEA levels served as a more reliable biomarker [34]. De Chiara et al. measured serum CD26 levels in 299 patients undergoing colonoscopies and found a mean of 641.2 ± 241.2 ng/mL in patients with no colorectal pathology and 403.7 ± 278.2 ng/mL in patients with colorectal cancer. In addition, analysis of polyps revealed a correlation between CD26 levels and grade of dysplasia and the presence of advanced adenomas, with a 58.0% (95% CI: 46.5%-68.9%) sensitivity and 75.5% (95% CI: 68.5%-81.0%) specificity in detecting colorectal cancer and advanced adenomas. Using a 460 ng/mL cut-off, CD26 levels had 81.8% (95% CI: 64.5%-93.0%) sensitivity and 72.3% (95% CI: 65.0%-77.2%) specificity in predicting the absence of or benign colorectal pathology [34].

While prior studies have mostly identified lower serum CD26 levels in CRC, Lam et al. analyzed tumor CD26 expression levels in CRC patients and found significantly higher levels in those with distant metastases compared to non-metastatic disease. In addition, patients with high CD26 expression were found to have worse OS ($p < 0.0001$). Larrinaga et al. similarly measured higher DPPIV activity and mRNA expression in tissue samples of CRC and colon adenomas compared to non-neoplastic tissues while noting significantly lower plasma DPPIV activity in CRC patients [35]. DPPIV inhibition with vidagliptin suppressed the incidence and growth of lung metastases in CRC in mice through increased cell apoptosis by downregulating autophagy and cell cycle modulation. Following treatment with vildagliptin, a decrease in autophagy markers such as LC3, p62, and ATF4; an increase in apoptosis; and inhibition of cell cycle regulator pCDC2 were observed [36].

CD26 has been implicated as a marker of cancer stem cell in CRC by various studies. Injection of isolated CD26+ cells from patients with metastatic CRC into the cecal walls of mice led to the development of distant metastasis, but injection of CD26 negative (CD26-) cells did not. Hence, a subpopulation of CD26+ cancer cells was thought to have stem-like features and were also preferentially found in metastatic liver tissues. In the study, CD26+ cells were found in all primary and metastatic tumors in 20 patients with liver metastasis and in only eight of 27 patients without liver metastasis [37]. Furthermore, Lam et al. demonstrated that higher levels of CD26 expression detected by immunohistochemistry correlated with more advanced tumor stage and worse survival rate [38]. A study by Cheung et al. quantified CD26+ cancer cells in 11 primary CRC tissue samples and showed metastatic tumors to have relatively high CD26+ levels. Specifically, the CD26+ proportion in CRC tumors with metastasis was 7.20% ± 5.20% and 0.43% ± 0.15% in those without metastasis ($p = 0.13$). Tissues with higher CD26+ levels correlated with the presence of metastases ($p = 0.0061$) and even led to the later diagnosis of metastatic disease in two subjects who did not initially have metastases at the time of study enrollment. It was hypothesized that the subpopulation of cancer stem cells arises from CD26- daughter cells via gene manipulation of PIK3CA and TP53 during later stages of carcinogenesis [39].

Lung Cancer

Contrary to certain other cancers, CD26 was actually detected at a reduced or undetectable level in most non-small cell lung cancers (NSCLC) compared to normal bronchial and alveolar epithelial cells. However, CD26 expression was increased only in lung adenocarcinoma, making it a potential tool for distinguishing between lung cancer subtypes [36,40]. Asada et al. examined DPPIV enzyme activity in numerous histological types of lung carcinomas and found that 93.1% of lung adenocarcinoma tissues expressed positive staining for DPPIV activity, while all cases of squamous cell, small cell, carcinoid, and large cell carcinoma were negative. CD26-expressing cells in non-adenocarcinoma lung cancers contained an increased proportion of cells in G0-G1 stages, suggesting a role for CD26 in promoting cell cycle arrest [40]. Wesley et al. similarly found absent or markedly reduced DPPIV expression in all NSCLC cells at both mRNA and protein levels, while normal lung epithelial cells had detectable DPPIV expression. Interestingly, restoring DPPIV expression in NSCLC cells led to inhibition of cell proliferation, anchorage-independent growth, in vitro cell migration, tumorigenicity, increased p21 expression, and therefore apoptosis and cell cycle arrest [29]. Hence, DPPIV is linked to suppression of tumor growth and metastasis of NSCLC, and its loss of function is believed to contribute to the development of NSCLC.

As significantly higher DPPIV expression was found in lung adenocarcinoma, Jang et al. evaluated the effects of DPPIV inhibition by vidagliptin on tumor growth in lung adenocarcinoma. The study showed that vidagliptin reduced growth of lung adenocarcinoma through activation of natural killer cell activity and surfactant-activated macrophages [36]. Bishnoi et al. demonstrated that DPPIV inhibitors resulted in a survival advantage in diabetic patients with lung cancer or colorectal cancer (HR 0.89; 95% CI: 0.82-0.97, p =

0.0007), with a synergistic survival advantage when used in conjunction with metformin (HR 0.83; 95% CI: 0.77-0.90, p < 0.0001) [41].

Hematologic Malignancies

CD26 expression has been associated with aggressive T-large granular lymphocyte (T-LGL) lymphoproliferative disorder, with patients having CD26+ disease being more likely to acquire infections and cytopenias requiring treatment than those with CD26 negative disease [42]. Carbone et al. examined 67 human T-cell Non-Hodgkin's lymphomas and leukemias and found that CD26 expression was exclusive to aggressive pathologies, such as T-cell lymphoblastic lymphoma (LBL)/T-cell acute lymphoblastic leukemia (ALL) and T-cell CD30+ anaplastic large cell (ALC) lymphomas. In addition, CD26 expression has also been associated with higher degree of disease aggressiveness and worse survival outcomes in T-LBL/T-ALL compared to patients with CD26 negative tumors (p < 0.0001). On the other hand, CD26 was undetectable in most tissue samples of mycosis fungoides/Sézary syndrome subtype of T-cell lymphoma. Therefore, CD26 has a potential role as a biomarker for distinguishing among subtypes of T-cell malignancy [43-44].

Reinhold et al. used two CD26/DPPIV inhibitors to suppress DPPIV function of human histiocytic lymphoma cells, which resulted in suppressed DNA synthesis and cytokine production in those with high DPPIV expression. These findings support the hypothesis that CD26/DPPIV contributes to the growth of T-cell lymphoma through cytokine production [45]. Ho et al. demonstrated that administration of anti-CD26 monoclonal antibody resulted in cell cycle arrest and inhibition of tumor proliferation of human CD30+ ALC T-cell lymphoma, suggesting potential clinical benefit of anti-CD26 antibody therapy in CD26+ hematological malignancies as well as potentially CD26+ cancers in general [46].

CD26 in infectious diseases

CD26 in MERS

CD26/DPPIV has been found to play a role in infection mediated by Middle East respiratory syndrome coronavirus (MERS-CoV) and, more recently, potentially by severe acute respiratory syndrome coronavirus 2 (SARS-CoV2) also known as COVID-19. MERS-CoV emerged in 2012 in the Middle East, leading to fatal lower respiratory tract infections with a 35% fatality rate [5]. CD26 is expressed in numerous cell types including bronchial mucosa, alveolar cells (in particular, type two alveolar cells), T lymphocytes, and the systemic circulation. It also functions as a receptor by which the spike protein S1, which is a type I transmembrane glycoprotein, of MERS-CoV is allowed entry into human cells [20]. MERS-CoV activates an inflammatory response by binding to S-protein, which causes a conformational change and interactions with T lymphocytes [4]. Due to the newfound involvement of CD26 in MERS-CoV infectivity, CD26 inhibition raises interest as a potential therapeutic target for the treatment of MERS-CoV.

While CD26/ DPPIV chemical inhibitors did not inhibit binding between DPPIV and MERS-CoV, the use of antibodies directed against CD26 has shown more promising results in MERS-CoV-mediated infection [20]. In a mouse study by Li et al., human DPP4 knockin mice with humanized exons of the mouse DPP4 locus were inoculated with MERS-CoV. Viral replication was observed in the lungs, although these mice did not develop illness [4]. Ohnuma et al. demonstrated that treatment with anti-CD26 mAbs successfully inhibited interaction between CD26 and the spike protein, therefore suppressing MERS-CoV host infection. Various clones of anti-CD26 mAbs and the humanized anti-CD26 mAb YS110 were tested in binding inhibition assays with the fusion protein construct MERS-CoV S1-Fc, with the anti-CD26 mAbs 2F9, 1F7, and YS110 being able to block MERS-CoV infection in vitro [21]. In addition, the humanized anti-CD26 mAb YS110 exhibited tolerable safety profiles in a phase I clinical trial involving patients with CD26-expressing malignancies, as discussed earlier [20,25]. These findings suggest the potential of anti-CD26 mAbs as a novel therapeutic approach in MERS-CoV-mediated infection.

CD26 in COVID-19

The SARS-CoV-2, also known as COVID-19, pandemic has affected over 3.8 million individuals in over 200 countries in 2020. The disease is characterized by severe acute respiratory syndrome with a case fatality rate of 4.58% [47]. Recent work has shown an association between COVID-19 case fatality and hypertension and type two diabetes [47-49]. Coronaviruses have been demonstrated to gain entry into human cells through the spike protein (S-protein) that interacts with certain membrane receptors. In the case of SARS-CoV-2, virus gains cell entry through a type II transmembrane serine protease called TMPRSS2, which activates the viral spike protein and allows binding to angiotensin-converting enzyme two (ACE2). TMPSS2 and ACE2 are co-expressed by type II pneumocytes of human lungs [49]. DPPIV may also function as a co-receptor for viral entry of SARS-CoV-2 by facilitating S-protein binding [47-48]. Computational models have suggested an association between DPPIV dysfunction and COVID-19 disease severity based on the anti-inflammatory effects of DPPIV inhibitors such as vildagliptin and saxagliptin shown in animal studies [48]. Further experimental studies are needed to evaluate the clinical impact of DPPIV inhibition on COVID-19 disease course.

A recent genetic study by Senapati et al. on the interactions among SARS-CoV-2 spike protein, TMPRSS2, and CD26 further characterized the potential role of CD26 in COVID19 infection. CD26 is found to be significantly involved in the expression of key regulatory genes that regulate SARS-CoV-2 internalization. Furthermore, epigenetic modifications that induce CD26 overexpression are hypothesized to have a role in the higher case fatality rate of SARS-CoV-2 among type two diabetics; however, results have not been proven in experimental studies [47]. Due to the known anti-inflammatory effects of DPPIV inhibitors by reducing C-reactive protein and IL-6 levels, it has been hypothesized that DPPIV inhibitors such as sitagliptin may play a role in reducing inflammation in SARS-CoV-2 infection [48]. However, there is currently no published experimental data showing that DPPIV inhibitors decrease binding and viral entry.

Conclusions

The diverse role of CD26/DPPIV in immunology, tumorigenesis, glucose homeostasis, and infectious pathophysiology has been established in numerous studies over the past decades. Beyond the pathophysiological involvement of CD26 in various diseases, recent in vivo studies and clinical trials suggest it to be a promising therapeutic target. For example, DPPIV inhibitor sitagliptin reducing the rate of acute GVHD following allogeneic HSCT suggests an important role in immunosuppression and clinical outcomes of immune-mediated disorders. Furthermore, the administration of the humanized anti-CD26 mAb YS110 yielded promising antineoplastic outcomes in advanced MPM that previously progressed on numerous chemotherapy agents, suggesting a more well-tolerated and possibly more effective treatment potential in certain cancers.

In the arena of infectious disease, studies of mice injected with anti-CD26 mAbs demonstrated successful suppression of MERS-CoV host infection, although this was not tested in human studies prior to the eradication of MERS. More relevant to current times, CD26 is believed to function as a co-receptor for viral entry of COVID-19, while DPPIV inhibitors are hypothesized to reduce the inflammatory response. More experimental and clinical data are needed to demonstrate the role of DPPIV inhibitors in reducing viral entry or downstream inflammation, but CD26/DPPIV remains a promising therapeutic target.

Additional Information

Disclosures

Conflicts of interest: In compliance with the ICMJE uniform disclosure form, all authors declare the following: **Payment/services info:** All authors have declared that no financial support was received from any organization for the submitted work. **Financial relationships:** All authors have declared that they have no financial relationships at present or within the previous three years with any organizations that might have an interest in the submitted work. **Other relationships:** All authors have declared that there are no other relationships or activities that could appear to have influenced the submitted work.

References

1. Thompson MA, Ohnuma K, Abe M, Morimoto C, Dang NH: CD26/dipeptidyl peptidase IV as a novel therapeutic target for cancer and immune disorders. Mini Rev Med Chem. 2007, 7:253-273. 10.2174/138955707780059853
2. Doonan BP, Ohnuma K, Dang LH, Morimoto C, Dang NH: Current and emerging therapy for malignant pleural mesothelioma: focus on CD26/dipeptidyl peptidase IV as a therapeutic target. Curr Cancer Ther Rev. 2017, 13:76-88.
3. Chu H, Chan CM, Zhang X, et al.: Middle east respiratory syndrome coronavirus and bat coronavirus HKU9 both can utilize GRP78 for attachment onto host cells. J Biol Chem. 2018, 293:11709-11726. 10.1074/jbc.RA118.001897
4. Li K, Wohlford-Lenane CL, Channappanavar R, et al.: Mouse-adapted MERS coronavirus causes lethal lung disease in human DPP4 knockin mice. Proc Natl Acad Sci U S A. 2017, 114:3119-3128. 10.1073/pnas.1619109114
5. Morimoto C, Torimoto Y, Levinson G, et al.: 1F7, a novel cell surface molecule, involved in helper function of CD4 cells. J Immunol. 1990, 143:3430-3439.
6. Dang NH, Hafler DA, Schlossman SF, Breitmeyer JB: FcR-mediated crosslinking of Ta1 (CDw26) induces human T lymphocyte activation. Cell Immunol. 1990, 125:42-57. 10.1016/0008-8749(90)90061-u
7. Dang NH, Torimoto Y, Deusch K, Schlossman SF, Morimoto C: Comitogenic effect of solid-phase immobilized anti-1F7 on human CD4 T cell activation via CD3 and CD2 pathways. J Immunol. 1990, 144:4092-4100.
8. Dang NH, Torimoto Y, Schlossman SF, Morimoto C: Human CD4 helper T cell activation: functional involvement of two distinct collagen receptors, 1F7 and VLA integrin family. J Exp Med. 1990, 172:649-652. 10.1084/jem.172.2.649
9. Dang NH, Torimoto Y, Shimamura K, et al.: 1F7 (CD26): a marker of thymic maturation involved in the differential regulation of the CD3 and CD2 pathways of human thymocyte activation. J Immunol. 1991, 147:2825-2832.
10. Torimoto Y, Dang NH, Tanaka T, Prado C, Schlossman SF, Morimoto C: Biochemical characterization of CD26 (dipeptidyl peptidase IV): functional comparison of distinct epitopes recognized by various anti-CD26 monoclonal antibodies. Mol Immunol. 1992, 29:183-192. 10.1016/0161-5890(92)90099-j
11. Torimoto Y, Dang NH, Vivier E, Tanaka T, Schlossman SF, Morimoto C: Coassociation of CD26 (dipeptidyl peptidase IV) with CD45 on the surface of human T lymphocytes. J Immunol. 1991, 147:2514-2517.

12. Dang NH, Torimoto Y, Sugita K, et al.: Cell surface modulation of CD26 by anti-1F7 monoclonal antibody. Analysis of surface expression and human T cell activation. J Immunol. 1990, 145:3963-3971.
13. Hatano R, Ohnuma K, Yamamoto J, Dang NH, Yamada T, Morimoto C: Prevention of acute graft-versus-host disease by humanized anti-CD26 monoclonal antibody. Br J Haematol. 2013, 162:263-277. 10.1111/bjh.12378
14. Ohnuma K, Hatano R, Aune TM, et al.: Regulation of pulmonary graft-versus-host disease by IL-26+CD26+CD4 T lymphocytes. J Immunol. 2015, 194:3697-3712. 10.4049/jimmunol.1402785
15. Liu X, Zhang T, Zhang C: Sitagliptin inhibits extracellular matrix accumulation and proliferation in lung fibroblasts. Med Sci Monit. 2020, 26:e922644.
16. Farag SS, Abu Zaid M, Schwartz JE, et al.: Dipeptidyl peptidase 4 inhibition for prophylaxis of acute graft-versus-host disease. N Engl J Med. 2021, 384:11-19. 10.1056/NEJMoa2027572
17. Takasawa W, Ohnuma K, Hatano R, Endo Y, Dang NH, Morimoto C: Inhibition of dipeptidyl peptidase 4 regulates microvascular endothelial growth induced by inflammatory cytokines. Biochem Biophys Res Commun. 2010, 401:7-12. 10.1016/j.bbrc.2010.08.112
18. Shirakawa J, Fujii H, Ohnuma K, et al.: Diet-induced adipose tissue inflammation and liver steatosis are prevented by DPP-4 inhibition in diabetic mice. Diabetes. 2011, 60:1246-1257. 10.2337/db10-1338
19. Amori RE, Lau J, Pittas AG: Efficacy and safety of incretin therapy in type 2 diabetes: systematic review and meta-analysis. JAMA. 2007, 298:194-206. 10.1001/jama.298.2.194
20. Ohnuma K, Hatano R, Komiya E, et al.: A novel role for CD26/dipeptidyl peptidase IV as a therapeutic target. Front Biosci (Landmark Ed). 2018, 23:1754-1779.
21. Sato K, Aytac U, Yamochi T, et al.: CD26/dipeptidyl peptidase IV enhances expression of topoisomerase II alpha and sensitivity to apoptosis induced by topoisomerase II inhibitors. Br J Cancer. 2003, 89:1366-1374. 10.1038/sj.bjc.6601255
22. Aytac U, Sato K, Yamochi T, et al.: Effect of CD26/dipeptidyl peptidase IV on Jurkat sensitivity to G2/M arrest induced by topoisomerase II inhibitors. Br J Cancer. 2003, 88:455-462. 10.1038/sj.bjc.6600791
23. Yamochi T, Yamochi T, Aytac U, et al.: Regulation of p38 phosphorylation and topoisomerase IIalpha expression in the B-cell lymphoma line Jiyoye by CD26/dipeptidyl peptidase IV is associated with enhanced in vitro and in vivo sensitivity to doxorubicin. Cancer Res. 2005, 65:1973-1983. 10.1158/0008-5472.CAN-04-2611
24. Aoe K, Amatya VJ, Fujimoto N, et al.: CD26 overexpression is associated with prolonged survival and enhanced chemosensitivity in malignant pleural mesothelioma. Clin Cancer Res. 2012, 18:1447-56.
25. Angevin E, Isambert N, Trillet-Lenoir V, et al.: First-in-human phase 1 of YS110, a monoclonal antibody directed against CD26 in advanced CD26-expressing cancers. Br J Cancer. 2017, 116:1126-1134. 10.1038/bjc.2017.62
26. Takeda M, Ohe Y, Horinouchi H, et al.: Phase I study of YS110, a recombinant humanized monoclonal antibody to CD26, in Japanese patients with advanced malignant pleural mesothelioma. Lung Cancer. 2019, 137:64-70. 10.1016/j.lungcan.2019.09.010
27. Lu Z, Qi L, Bo XJ, Liu GD, Wang JM, Li G: Expression of CD26 and CXCR4 in prostate carcinoma and its relationship with clinical parameters. J Res Med Sci. 2013, 18:647-652.
28. Shah C, Hong YR, Bishnoi R, et al.: Impact of DPP4 inhibitors in survival of patients with prostate, pancreas, and breast cancer. Front Oncol. 2020, 10:405-2020. 10.3389/fonc.2020.00405
29. Wesley UV, McGroarty M, Homoyouni A: Dipeptidyl peptidase inhibits malignant phenotype of prostate cancer cells by blocking basic fibroblast growth factor signaling pathway. Cancer Res. 2005, 65:1325-1334. 10.1158/0008-5472.CAN-04-1852
30. Sun YX, Pedersen EA, Shiozawa Y, et al.: CD26/dipeptidyl peptidase IV regulates prostate cancer metastasis by degrading SDF-1/CXCL12. Clin Exp Metastasis. 2008, 25:765-776. 10.1007/s10585-008-9188-9
31. Russo JW, Gao C, Bhasin SS, et al.: Downregulation of dipeptidyl peptidase 4 accelerates progression to castration-resistant prostate cancer. Cancer Res. 2018, 78:6354-6362. 10.1158/0008-5472.CAN-18-0687
32. Nazarian A, Lawlor K, Yi SS, et al.: Inhibition of circulating dipeptidyl peptidase 4 activity in patients with metastatic prostate cancer. Mol Cell Proteomics. 2014, 13:3082-3096. 10.1074/mcp.M114.038836
33. Cordero OJ, Ayude D, Nogueira M, Rodríguez-Berrocal FJ, de la Cadena MP: Preoperative serum CD26 levels: diagnostic efficiency and predictive value for colorectal cancer. Br J Cancer. 2000, 83:1139-1146. 10.1054/bjoc.2000.1410
34. De Chiara L, Rodríguez-Piñeiro AM, Rodríguez-Berrocal FJ, Cordero OJ, Martínez-Ares D, de la Cadena MP: Serum CD26 is related to histopathological polyp traits and behaves as a marker for colorectal cancer and advanced adenomas. BMC Cancer. 2010, 10:333-2010. 10.1186/1471-2407-10-333
35. Larrinaga G, Perez I, Sanz B, et al.: Dipeptidyl-peptidase IV activity is correlated with colorectal cancer prognosis. PLoS One. 2015, 10:0119436-2015. 10.1371/journal.pone.0119436
36. Jang JH, Janker F, De Meester I, et al.: The CD26/DPP4-inhibitor vildagliptin suppresses lung cancer growth via macrophage-mediated NK cell activity. Carcinogenesis. 2019, 40:324-334. 10.1093/carcin/bgz009
37. Pang R, Law WL, Chu AC, et al.: A subpopulation of CD26+ cancer stem cells with metastatic capacity in human colorectal cancer. Cell Stem Cell. 2010, 6:603-615. 10.1016/j.stem.2010.04.001
38. Lam CSC, Cheung AHK, Wong SKM, et al.: Prognostic significance of CD26 in patients with colorectal cancer. PLoS One. 2014, 9:98582-2014. 10.1371/journal.pone.0098582
39. Cheung AH, Iyer DN, Lam CS, et al.: Emergence of CD26+ cancer stem cells with metastatic properties in colorectal carcinogenesis. Int J Mol Sci. 2017, 18:1106-2017. 10.3390/ijms18061106
40. Asada Y, Aratake Y, Kotani T, Marutsuka K, Araki Y, Ohtaki S, Sumiyoshi A: Expression of dipeptidyl aminopeptidase IV activity in human lung carcinoma. Histopathology. 1993, 23:265-270. 10.1111/j.1365-2559.1993.tb01199.x
41. Bishnoi R, Hong YR, Shah C, et al.: Dipeptidyl peptidase 4 inhibitors as novel agents in improving survival in diabetic patients with colorectal cancer and lung cancer: a surveillance epidemiology and endpoint research medicare study. Cancer Med. 2019, 8:3918-3927. 10.1002/cam4.2278
42. Dang NH, Aytac U, Sato K, et al.: T-large granular lymphocyte lymphoproliferative disorder: expression of CD26 as a marker of clinically aggressive disease and characterization of marrow inhibition. Br J Haematol.

2003, 121:857-865. 10.1046/j.1365-2141.2003.04565.x

43. Carbone A, Gloghini A, Zagonel V, et al.: The expression of CD26 and CD40 ligand is mutually exclusive in human T-cell non-Hodgkin's lymphomas/leukemias. Blood. 1995, 86:4617-4626.
44. Jones D, Dang NH, Duvic M, Washington LT, Huh YO: Absence of CD26 expression is a useful marker for diagnosis of T-cell lymphoma in peripheral blood. Am J Clin Pathol. 2001, 115:885-892. 10.1309/UTY6-HAG-5M4M-7AYV
45. Reinhold D, Bank U, Bühling F, et al.: Inhibitors of dipeptidyl peptidase IV (DP IV, CD26) specifically suppress proliferation and modulate cytokine production of strongly CD26 expressing U937 cells. Immunobiology. 1994, 192:121-136. 10.1016/S0171-2985(11)80412-2
46. Ho L, Aytac U, Stephens LC, et al.: In vitro and in vivo antitumor effect of the anti-CD26 monoclonal antibody 1F7 on human CD30+ anaplastic large cell T-cell lymphoma Karpas 299. Clin Cancer Res. 2001, 7:2031-2040.
47. Senapati S, Kumar S, Singh AK, et al.: Assessment of risk conferred by coding and regulatory variations of TMPRSS2 and CD26 in susceptibility to SARS-CoV-2 infection in human. J Genet. 2020, 99:53. 10.1007/s12041-020-01217-7
48. Bassendine MF, Bridge SH, McCaughan GW, Gorrell MD: COVID-19 and comorbidities: a role for dipeptidyl peptidase 4 (DPP4) in disease severity?. J Diabetes. 2020, 12:649-658. 10.1111/1753-0407.13052
49. Huang C, Wang Y, Li X, et al.: Clinical features of patients infected with 2019 novel coronavirus in Wuhan, China. Lancet. 2020, 395:497-506. 10.1016/S0140-6736(20)30183-5

Diabetologia (2021) 64:1816–1821
https://doi.org/10.1007/s00125-021-05467-7

SHORT COMMUNICATION

Reduced beta cell number rather than size is a major contributor to beta cell loss in type 2 diabetes

Hironobu Sasaki[1] · Yoshifumi Saisho[1] · Jun Inaishi[1,2] · Yuusuke Watanabe[1] · Tami Tsuchiya[1] · Masayoshi Makio[1] · Midori Sato[1] · Masaru Nishikawa[1] · Minoru Kitago[3] · Taketo Yamada[4,5] · Hiroshi Itoh[1]

Received: 12 December 2020 / Accepted: 1 March 2021 / Published online: 3 May 2021

Abstract

Aims/hypothesis Type 2 diabetes is characterised by reduced beta cell mass (BCM). However, it remains uncertain whether the reduction in BCM in type 2 diabetes is due to a decrease in size or number of beta cells. Our aim was to examine the impact of beta cell size and number on islet morphology in humans with and without type 2 diabetes.

Methods Pancreas samples were obtained from 64 Japanese adults with ($n = 26$) and without ($n = 38$) type 2 diabetes who underwent pancreatectomy. Using pancreatic tissues stained for insulin, we estimated beta cell size based on beta cell diameter. Beta cell number was estimated from the product of fractional beta cell area and pancreas volume divided by beta cell size. The associations of beta cell size and number with islet morphology and metabolic status were examined.

Results Both beta cell size (548.7 ± 58.5 vs 606.7 ± 65.0 μm^3, $p < 0.01$) and number ($5.10 \times 10^8 \pm 2.35 \times 10^8$ vs $8.16 \times 10^8 \pm 4.27 \times 10^8$, $p < 0.01$) were decreased in participants with type 2 diabetes compared with those without diabetes, with the relative reduction in beta cell number (37%) being greater than for beta cell size (10%). Beta cell number but not size was positively correlated with BCM in participants with and without type 2 diabetes ($r = 0.97$ and $r = 0.98$, both $p < 0.01$) and negatively correlated with HbA_{1c} ($r = -0.45$, $p < 0.01$).

Conclusions/interpretation Both beta cell size and number were reduced in participants with type 2 diabetes, with the relative reduction in beta cell number being greater. Decrease in beta cell number appears to be a major contributor to reduced BCM in type 2 diabetes.

Keywords Beta cell mass · Beta cell number · Beta cell size · Human pancreas · Japanese

Abbreviations

BCA	Beta cell area
BCM	Beta cell mass
DM group	Participants with diabetes
NDM group	Participants without diabetes

✉ Yoshifumi Saisho
ysaisho@keio.jp

1 Department of Internal Medicine, Keio University School of Medicine, Tokyo, Japan

2 Center for Preventative Medicine, Keio University School of Medicine, Tokyo, Japan

3 Department of Surgery, Keio University School of Medicine, Tokyo, Japan

4 Department of Pathology, Keio University School of Medicine, Tokyo, Japan

5 Department of Pathology, Saitama Medical University, Saitama, Japan

Introduction

Type 2 diabetes is characterised by reduced beta cell mass (BCM) [1]. Since type 2 diabetes is a progressive disorder, it is important to develop treatment strategies to preserve BCM in individuals with type 2 diabetes [2].

Although BCM has been shown to decrease by approximately 20–65% in individuals with type 2 diabetes [1, 3, 4], the precise mechanism remains uncertain. Increased beta cell apoptosis in individuals with type 2 diabetes has been reported as one of the underlying mechanisms of reduced BCM [3]; however, recent studies have also suggested beta cell dedifferentiation and/or degranulation

Research in context

What is already known about this subject?

- Beta cell mass (BCM) is decreased by 20–65% in individuals with type 2 diabetes; however, the mechanisms of beta cell loss remain to be established
- Rodent models of type 2 diabetes have demonstrated decreased BCM but increased beta cell size
- In non-diabetic Europids, studies have suggested that the increased BCM in participants with insulin resistance or obesity is due to an increase in beta cell number rather than size

What is the key question?

- Does beta cell size and/or beta cell number contribute to reduced BCM in humans with type 2 diabetes?

What are the new findings?

- Both beta cell size and number were decreased in participants with type 2 diabetes
- There was a greater relative reduction in beta cell number than in beta cell size in type 2 diabetes
- Beta cell number but not size was positively correlated with BCM and negatively correlated with HbA_{1c} in participants with and without type 2 diabetes

How might this impact on clinical practice in the foreseeable future?

- Since reduction in beta cell number rather than size appears to be a major contributor to reduced BCM in humans with type 2 diabetes, efforts should be made towards developing therapeutic strategies to prevent the reduction in beta cell number possibly induced by apoptosis, dedifferentiation and/or degranulation in type 2 diabetes

as possible mechanisms [5, 6]. Rodent models of type 2 diabetes have shown decreased BCM but increased beta cell size [7]. In a previous study on Europids, beta cell number rather than size was increased in non-diabetic individuals with insulin resistance or obesity [8, 9]. However, because the studies did not compare these findings with those in diabetic individuals, it remains unclear how beta cell size and number are altered by diabetes. Therefore, using our previously published data [10], we here aimed to estimate the relative contribution of beta cell size and number to the reduction of BCM in individuals with type 2 diabetes.

Methods

Participants The characteristics of the participants have been reported previously [10] and are shown in ESM Table 1. The Ethics Committee of Keio University School of Medicine approved this study. Further information can be found in ESM Methods. Briefly, 64 Japanese individuals with (n = 26) and without (n = 38) diabetes were included in this study.

Measurements and questionnaire Information about pancreatic disease, surgical procedure, and height and weight at the time of surgery was obtained from the medical records. Preoperative HbA_{1c} was measured by HPLC (HLC723G11; Tosoh, Tokyo, Japan). Participants were asked about their detailed weight trajectory using a questionnaire, as previously reported [10].

Pancreatic tissue processing Surgically removed pancreatic specimens were quickly fixed in formaldehyde and embedded in paraffin for subsequent analysis. Then, 5 μm sections were cut from the tumour-free area and stained for light microscopy as follows: (1) with haematoxylin–eosin; (2) for insulin (peroxidase staining) with haematoxylin; (3) for glucagon with haematoxylin; and (4) for insulin and Ki67 for assessment of beta cell replication, as previously described [10–13].

Morphological analysis To analyse the pancreatic tissues, a single cross-sectional pancreatic section for each participant was used. The entire pancreatic section containing approximately 300 islets (total pancreas area 126 ± 50 mm^2) was imaged at the original magnification of ×200 (×20 objective) using a NanoZoomer-XR slide scanner and viewed with NDP.view2 software (Hamamatsu Photonics, Shizuoka, Japan).

For analysis of islet morphology, the ratio of BCA to total pancreas area was digitally measured using Image Pro Premier software (Media Cybernetics, Silver Spring, MD, USA). All analyses were conducted by a single researcher

(H. Sasaki), and inter- and intra-observer coefficient of variance were approximately 11% and 5%, respectively. Individual pancreatic tissues were analysed twice, with blinding to the metabolic status such as BMI and HbA_{1c}, and the average of the two measurements was used, as previously described [10].

For further morphological analysis, islet density and mean islet size were quantified using NDP.view2 in randomly selected areas of pancreatic tissue containing at least 100 islets in each case (105 ± 5 islets, total 6741 islets) [10, 12, 13]. In addition, we quantified scattered beta cells, insulin-positive duct cells and beta cell replication (i.e. double staining for insulin and Ki67) as surrogate markers for beta cell turnover. The frequency of beta cell apoptosis was not assessed in this study because it was extremely rare, as described in previous reports [11–13].

Scattered beta cells were defined as a cell cluster of no more than three beta cells in acinar tissue, and the density of scattered beta cells was defined as the number of scattered beta cells/pancreas area (no./mm^2). The density of insulin-positive duct cells was also measured and expressed as the number of insulin-positive duct cells/pancreas area (no./mm^2). Beta cell replication frequency was expressed as the percentage of islets with Ki67.

To measure the size of individual beta cells, six islets were randomly selected from each sample using NDP.view2 software, as previously reported [11]. These islets were then examined to identify six representative beta cells within each. We primarily selected cells with a circular shape and that were judged by the observer to have been sectioned through their maximum diameters. To determine the mean beta cell diameter, six distances between two adjacent cell nuclei (including one of the nuclei) were measured in each of the six islets (i.e. a total of 36 diameters in each case).

Estimation of beta cell size and number To estimate beta cell size, mean beta cell diameter was used. As the cells are not entirely circular, we estimated beta cell size as the average of two values calculated as $4\pi r^3/3$ (sphere) and $8r^3$ (cube) (where r = half the mean beta cell diameter).

Beta cell number was calculated, using the reference values of pancreas volume [14], by the following formula:

$$\text{Beta cell number} = \text{Parenchymal pancreas volume}\ (\mu m^3) \times \text{BCA} \div \text{Beta cell size}\ (\mu m^3)$$

The obtained pancreas volume was multiplied by 0.92 in the diabetes group because pancreas parenchymal volume was reduced by 8% in participants with type 2 diabetes [14] and BCM was estimated as the product of BCA (%) and pancreas weight (g), assuming 1 cm^3 pancreas = 1 g.

Statistical analysis Data are presented as mean ± SD unless otherwise specified. Mann–Whitney *U* test was used to analyse the differences between the two groups, and Spearman correlation coefficients were used to examine the correlation between two variables. A p value <0.05 was taken to indicate statistical significance. All analyses were performed using SPSS (version 26; SPSS, IBM, Chicago, IL, USA).

Results

Participant characteristics The characteristics of the 38 non-diabetic participants and 26 diabetic participants have been reported previously [10] and are shown in ESM Table 1. As reported, BCA and estimated BCM were reduced by 34% and 43%, respectively, in the participants with diabetes (DM group) when compared with participants without diabetes (NDM group) (ESM Table 1). Representative photographs of islets from participants in the NDM and DM groups are shown in ESM Fig. 1.

Effects of diabetes and obesity on beta cell size and number Overall, mean beta cell diameter was 9.13 ± 0.36 μm in the total participants. As a result, beta cell size and number were calculated as 583.1 ± 68.3 μm^3 and $6.92 \times 10^8 \pm 3.90 \times 10^8$, respectively, indicating a wider inter-individual variation in beta cell number than in beta cell size (ESM Table 1). There was no significant correlation between beta cell size and number in either the NDM group ($r = -0.23$, $p = 0.16$; Fig. 1a) or the DM group ($r = 0.13$, $p = 0.54$; Fig. 1b).

Both beta cell size (548.7 ± 58.5 vs 606.7 ± 65.0 μm^3, $p < 0.01$; Fig. 1c and ESM Table 1) and number ($5.10 \times 10^8 \pm 2.35 \times 10^8$ vs $8.16 \times 10^8 \pm 4.27 \times 10^8$, $p < 0.01$; Fig. 1d and ESM Table 1) were significantly reduced in the DM group compared with the NDM group. However, in the DM group, the relative reduction was greater for beta cell number (37%) than for beta cell size (10%). In both groups of participants overall, HbA_{1c} was not correlated with beta cell size ($r = -0.19$, $p = 0.14$; Fig. 1e) but was negatively correlated with beta cell number ($r = -0.45$, $p < 0.01$; Fig. 1f) as well as with BCA ($r = -0.38$, $p < 0.01$) and BCM ($r = -0.47$, $p < 0.01$).

In this Japanese cohort, there was no correlation between current BMI (ESM Fig. 2) or maximum BMI (data not shown) and beta cell size or number in either the NDM group or the DM group.

Effects of beta cell size and number on islet morphological characteristics There was no correlation between beta cell size and islet morphology in either the NDM group or the DM group (Fig. 2a,b and ESM Figs. 3, 4). On the other hand, there was a strong correlation between beta cell number and BCM

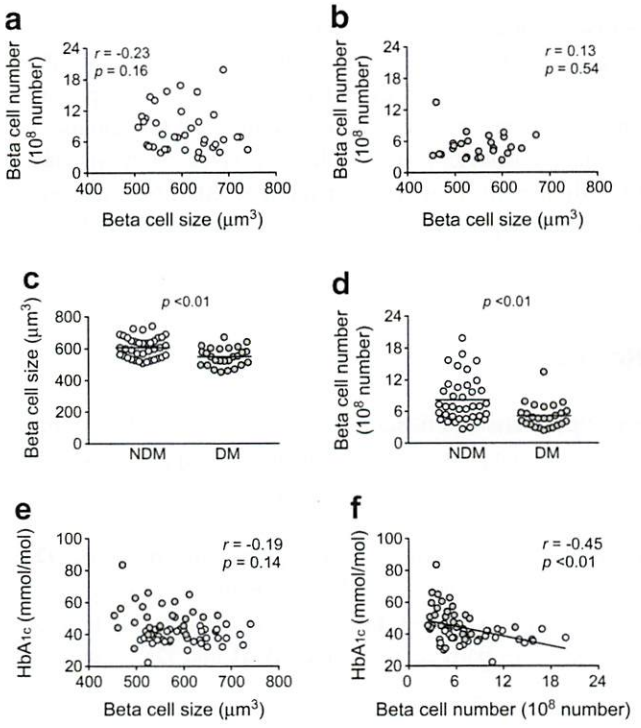

Fig. 1 (**a**, **b**) Correlation between beta cell size and number in the NDM group (**a**) and the DM group (**b**). (**c**, **d**) Effects of diabetes on beta cell size (**c**) and number (**d**). (**e**, **f**) Correlation between HbA_{1c} and beta cell size (**e**) and number (**f**). Grey circles, DM group; white circles, NDM group. Bars indicate mean

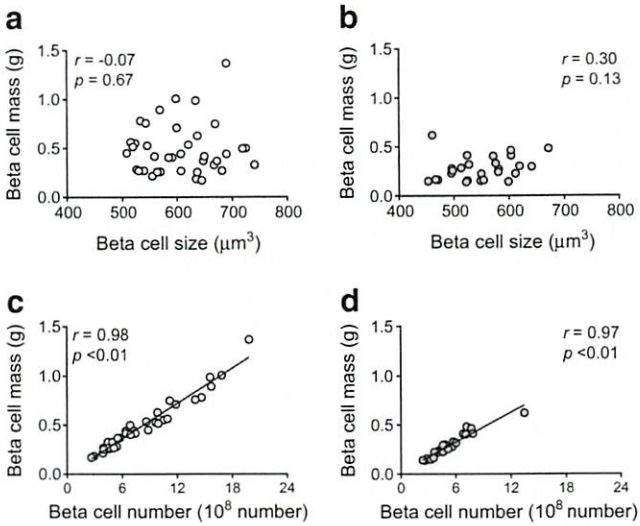

Fig. 2 Correlation between beta cell size and estimated BCM in the NDM group (**a**) and the DM group (**b**) and between beta cell number and estimated BCM in the NDM group (**c**) and the DM group (**d**). Grey circles, DM group; white circles NDM group

in both the NDM and DM groups ($r = 0.98$ and 0.97, respectively, both $p < 0.01$; Fig. 2c,d), indicating that BCM was mostly determined by beta cell number rather than size. There was also a positive correlation between beta cell number and islet density, and number of scattered beta cells in the NDM and DM groups (ESM Figs. 3c,d, 4c,d). Regarding other markers of beta cell turnover, there was no correlation between beta cell number and number of insulin-positive duct cells or beta cell replication in either the NDM group or the DM group (ESM Fig. 4g,h,k,l).

Discussion

In the present study, we found that both beta cell size and beta cell number were decreased in participants with type 2 diabetes. However, because the reduction in beta cell number was greater than the reduction in beta cell size (37% vs 10%), beta cell number is likely to have a major role with respect to the reduced BCM in type 2 diabetes. We also found that beta cell number, as well as BCA and BCM, but not beta cell size was negatively correlated with HbA_{1c}, indicating the importance of beta cell number for glycaemic control. Furthermore, in this study, beta cell number was strongly correlated with BCM and islet density. We reported previously that islet density is strongly correlated with BCA and is a major determinant of BCM [15], consistent with the results of the present study, suggesting that beta cell number is a determinant of BCM through islet number. In this present cohort, we reported a significant positive correlation between birthweight and BCM, with no change in beta cell size, indicating an association between reduced beta cell number and low birthweight [10]. With regard to beta cell turnover, previous studies have suggested that beta cell neogenesis, rather than beta cell replication, is important as the mechanism of regulation of BCM in adults [3, 8, 9]. These results are consistent with the results of the present study, in which the number of scattered beta cells, but not replication of beta cells, was correlated with beta cell number. The close correlations among beta cell number, number of scattered beta cells, islet density and BCM could suggest an important role for newly formed beta cells (through neogenesis) in the regulation and maintenance of BCM in adult humans.

In this study, we found no correlation between beta cell size or number and BMI, in contrast to the previous study in Europids that showed an increase in beta cell number in non-diabetic individuals with insulin resistance [8]. This might be due to the lower BMI of our cohort compared with that in the study in Europids, although we did not evaluate insulin sensitivity. However, it is worth noting that beta cell size was consistent in obese participants regardless of race [9], supporting the concept that BCM is regulated primarily by beta cell number rather than beta cell size in humans.

This study was subject to certain limitations. First, actual BCM, expressed as the product of pancreatic weight and BCA, was not determined because the presence of pancreatic disease made it difficult to measure pancreatic weight or volume.

However, instead we simulated BCM using reference values of pancreas volume taking into account age, BMI and presence of type 2 diabetes [14]. Although estimated beta cell size based on mean beta cell diameter might be inaccurate, the relative difference in beta cell size and number should not be largely affected. Indeed, the results were not changed when we assessed beta cell size and number using only cell diameter and BCA without pancreas volume (data not shown). Second, different sites of pancreatic tissue were analysed in each individual according to the operation; however, the proportion of endocrine cells has been shown to be relatively consistent regardless of pancreatic site, except for the ventral portion of the pancreatic head [4]. Moreover, BCA is widely used as a surrogate marker for BCM; this is supported by the significant correlation between BCA and HbA_{1c} in this and prior studies [12, 13]. Third, the surgical procedures and comorbidities of the participants might have affected islet morphology; however, BCA in this cohort was not different from that in other studies (i.e. BCA 1~2% and BCM 0.6~1.2 g [16]). Fourth, as we used the average value of beta cell diameters, which were assessed in a small population of beta cells (1386 and 936 cells in the NDM group and DM group, respectively), we might overlook the heterogeneity of beta cell size.

In conclusion, both beta cell size and number were decreased in type 2 diabetes. The relative reduction in type 2 diabetes was greater for beta cell number than for beta cell size. Beta cell number but not size was positively correlated with BCM and negatively correlated with HbA_{1c}. These findings indicate that beta cell number rather than size is a major contributor to reduced BCM in humans with type 2 diabetes.

Supplementary Information The online version of this article (https://doi.org/10.1007/s00125-021-05467-7) contains peer-reviewed but unedited supplementary material.

Acknowledgements We thank Y. Madokoro (Department of Pathology, Keio University School of Medicine) for technical assistance, W. Gray (self-employed, London, UK) for editing the manuscript and Y. Tsuda (Davinci Medical Illustration Office, Tokyo, Japan) for editing the graphical abstract.

Data availability The datasets generated during and/or analysed during the current study are available from the corresponding author on reasonable request.

Funding This study was supported by funding from the Japan Diabetes Foundation, Keio Gijuku Academic Development Funds, and a Grant-in-Aid for Scientific Research (18 K08488) from the Ministry of Education, Culture, Sports, Science and Technology (MEXT).

Authors' relationships and activities The authors declare that there are no relationships or activities that might bias, or be perceived to bias, their work.

Contribution statement All authors made substantial contributions to conception and design, acquisition of data or analysis and interpretation of data. They were all responsible for drafting the article and revising it critically for important intellectual content, and approved the version to be published. YS is responsible for the integrity of the work as a whole.

References

1. Saisho Y (2015) Beta-cell dysfunction: its critical role in prevention and management of type 2 diabetes. World J Diabetes 6(1):109–124. https://doi.org/10.4239/wjd.v6.i1.109
2. Saisho Y (2020) An emerging new concept for the management of type 2 diabetes with a paradigm shift from the glucose-centric to beta cell-centric concept of diabetes - an Asian perspective. Expert Opin Pharmacother 21(13):1565–1578. https://doi.org/10.1080/14656566.2020.1776262
3. Butler AE, Janson J, Bonner-Weir S, Ritzel R, Rizza RA, Butler PC (2003) Beta-cell deficit and increased beta-cell apoptosis in humans with type 2 diabetes. Diabetes 52(1):102–110. https://doi.org/10.2337/diabetes.52.1.102
4. Sakuraba H, Mizukami H, Yagihashi N, Wada R, Hanyu C, Yagihashi S (2002) Reduced beta-cell mass and expression of oxidative stress-related DNA damage in the islet of Japanese type II diabetic patients. Diabetologia 45(1):85–96. https://doi.org/10.1007/s125-002-8248-z
5. Hunter CS, Stein RW (2017) Evidence for loss in identity, de-differentiation, and trans-differentiation of islet β-cells in type 2 diabetes. Front Genet 8:35. https://doi.org/10.3389/fgene.2017.00035
6. Marselli L, Suleiman M, Masini M et al (2014) Are we overestimating the loss of beta cells in type 2 diabetes? Diabetologia 57(2):362–365. https://doi.org/10.1007/s00125-013-3098-3
7. Masiello P (2006) Animal models of type 2 diabetes with reduced pancreatic beta-cell mass. Int J Biochem Cell Biol 38(5–6):873–893. https://doi.org/10.1016/j.biocel.2005.09.007
8. Mezza T, Muscogiuri G, Sorice GP et al (2014) Insulin resistance alters islet morphology in nondiabetic humans. Diabetes 63(3):994–1007. https://doi.org/10.2337/db13-1013
9. Saisho Y, Butler AE, Manesso E, Elashoff D, Rizza RA, Butler PC (2013) Beta-cell mass and turnover in humans: effects of obesity and aging. Diabetes Care 36(1):111–117. https://doi.org/10.2337/dc12-0421
10. Sasaki H, Saisho Y, Inaishi J et al (2020) Associations of birthweight and history of childhood obesity with beta cell mass in Japanese adults. Diabetologia 63(6):1199–1210. https://doi.org/10.1007/s00125-020-05127-2
11. Kou K, Saisho Y, Satoh S, Yamada T, Itoh H (2013) Change in beta-cell mass in Japanese nondiabetic obese individuals. J Clin Endocrinol Metab 98(9):3724–3730. https://doi.org/10.1210/jc.2013-1373
12. Inaishi J, Saisho Y, Sato S et al (2016) Effects of obesity and diabetes on alpha- and beta-cell mass in surgically resected human

pancreas. J Clin Endocrinol Metab 101(7):2874–2882. https://doi.org/10.1210/jc.2016-1374

13. Sato S, Saisho Y, Inaishi J et al (2015) Effects of glucocorticoid treatment on beta- and alpha-cell mass in Japanese adults with and without diabetes. Diabetes 64(8):2915–2927. https://doi.org/10.2337/db15-0151
14. Saisho Y, Butler AE, Meier JJ et al (2007) Pancreas volumes in humans from birth to age one hundred taking into account sex, obesity, and presence of type-2 diabetes. Clin Anat 20(8):933–942. https://doi.org/10.1002/ca.20543
15. Kou K, Saisho Y, Sato S, Yamada T, Itoh H (2014) Islet number rather than islet size is a major determinant of β- and α-cell mass in humans. J Clin Endocrinol Metab 99(5):1733–1740. https://doi.org/10.1210/jc.2013-3731
16. Inaishi J, Saisho Y (2020) Beta-cell mass in obesity and type 2 diabetes, and its relation to pancreas fat: a mini-review. Nutrients 12(12):3846. https://doi.org/10.3390/nu12123846

scientific reports

Check for updates

OPEN

Significance of secretory leukocyte peptidase inhibitor in pleural fluid for the diagnosis of benign asbestos pleural effusion

Takumi Kishimoto✉, Yoko Kojima & Nobukazu Fujimoto

Secretory leukocyte peptidase inhibitor (SLPI) is a biomarker present in the respiratory tract that protects against tissue destruction and aids in wound healing. We examined whether SLPI in pleural effusion can be used to distinguish benign asbestos pleural effusion (BAPE) from early-stage malignant pleural mesothelioma (MPM) and other diseases. We measured the levels of SLPI, hyaluronic acid (HA), soluble mesothelin-related peptides (SMRP), CCL2, galectin-3, and CYFRA21-1 in 51 patients with BAPE, 37 patients with early-stage MPM, 77 patients with pleural effusions due to non-small-cell lung cancer (LCa), and 74 patients with other pleural effusions. SLPI levels in the pleural fluid of patients with BAPE were significantly lower than those in patients with MPM, LCa, and other pleural effusions ($p < 0.0001$). The area under the curve (AUC) for SLPI's ability to distinguish BAPE from MPM was 0.902, with a sensitivity of 82.4% and a specificity of 86.5%. This AUC was not only favourable but was better than the AUC for the ability of CYFRA21-1 to distinguish BAPE (0.853). The combination of SLPI and CYFRA21-1 achieved an AUC of 0.965 for the differentiation between BAPE and MPM. Pleural fluid SLPI as well as CYFRA21-1 and HA is useful as a biomarker to diagnose BAPE, which needs to be distinguished from early-stage MPM.

Abbreviations

AUC	Area under the curve
BAPE	Benign asbestos pleural effusion
BRCA1	Breast cancer susceptibility gene I
CCL2	C–C motif chemokine ligand 2
CYFRA21-1	Cytokeratin 19 fragment 21-1
CT	Computed tomography
FISH	Fluorescence in situ hybridization
HA	Hyaluronic acid
HF	Heart failure
IF	Infection
LCa	Lung cancer
MCP1	Monocyte chemotactic factor 1
MPM	Malignant pleural mesothelioma
ROC	Receiver operating characteristic
SLPI	Secretory leukocyte peptidase inhibitor
SMRP	Soluble mesothelin-related peptides

Benign asbestos pleural effusion (BAPE), an inflammatory lesion of the pleura caused by asbestos fibres, was first reported in 1964 by Eisenstadt[1]. The underlying mechanism of BAPE has yet to be elucidated. However, it is a condition that must be differentiated from early-stage malignant pleural mesothelioma (MPM). BAPE is an exudative pleural effusion, and its diagnosis is based on a history of occupational exposure to asbestos, findings of pleural plaque on imaging, and the elimination of other possible causes using pleural fluid markers, cytology, and pleural biopsy.

Department of Medicine, Okayama Rosai Hospital, 1-10-25 Chikko Midorimachi, Minami-ku, Okayama 702-8055, Japan. ✉email: nakisimt@okayamah.johas.go.jp

Early-stage lesions of MPM often present with pleural effusion only; however, as the disease progresses, imaging findings such as pleural rind patterns may suggest a malignant tumour. In early-stage lesions, neoplastic pleural thickening is typically not present, making it difficult to differentiate from other diseases, particularly BAPE. Because the diagnosis of early-stage lesions and surgical treatment can improve prognoses, when patients with a history of asbestos exposure present with pleural effusion, BAPE should be considered for a differential diagnosis from MPM.

In patients who present with pleural effusion, such as macroscopic and neoplastic pleural thickening, with no abnormal findings on computed tomography (CT) of the chest, accurate identification of the lesion site can be challenging, even with thoracoscopic biopsy. When sufficient tumour tissue cannot be obtained from a biopsy site, it can be difficult to make a histopathological diagnosis. In such instances, the detection of p16 gene deletion using fluorescence in situ hybridization (FISH) may be useful[2,3]. In addition, the detection of BRCA1-associated protein 1 deletion in cell nuclei as well as deletion of the p16 gene is reportedly important[4].

In the diagnosis of MPM, elevated levels of hyaluronic acid (HA)[5,6] and soluble mesothelin-related peptides (SMRP)[7,8] in pleural fluid are reportedly useful for its differentiation from other diseases. Secretary leukocyte peptidase inhibitor (SLPI) is a serine protease inhibitor found in the respiratory tract and in the mucous of the cervical canal, nasal discharge, and saliva. Its physiological function is associated with wound healing and the prevention of tissue destruction, and it is considered a promising biomarker of acute renal impairment following heart surgery[9].

In BAPE, which is an inflammatory lesion of the visceral pleura caused by asbestos fibres, the significance of SLPI in pleural fluid has yet to be confirmed. Here, we measured SLPI levels as a biomarker for BAPE, which is difficult to differentiate from early-stage MPM, and obtained results superior to those involving other markers.

Methods

We analysed the pleural fluid of 51 patients with a definitive diagnosis of BAPE, 37 patients with early-stage MPM (diagnosed by histology from pleural biopsy; 31 with epithelial MPM and six with sarcoma-type conditions), 77 patients with malignant pleural effusions due to non-small-cell lung cancer (LCa) (diagnosed by cytological and histological examinations), 27 patients with heart failure (HF), and 47 patients with bacterial pleurisy (IF) diagnosed at Okayama Rosai Hospital between 2015 and 2019. The 74 patients with HF and IF were considered "other" patients.

BAPE can be diagnosed, according to the criteria of Epler et al.[10] in individuals with a history of occupational exposure to asbestos and in whom the presence of pleural effusion can be confirmed. However, a diagnosis of BAPE is based on the presence of an exudate with no cause other than asbestos exposure and deaminase and carcinoembryonic antigen in pleural fluid, as well as cytology, pleural plaque findings and, depending on the patient, pleural biopsy results[11].

In this study, we analysed biomarkers of MPM, such as HA, SMRP, CCL2, galectin-3 and CYFRA21-1, in pleural effusion and compared these markers with SLPI. We measured SLPI using a human SLPI Quantikine enzyme-linked immunosorbent assay (ELISA), HA using latex coagulating nephelometry, SMRP using Lumipulse CLEIA, CCL2 using a human MCP-1 ELISA Kit (PromoKine), galectin-3 using a human galectin-3 ELISA kit (PromoKine), and CYFRA21-1 using a colorimetric fixed quantity assay.

Significant differences between each disease were determined using a nonparametric Kruskal–Wallis test in accordance with Dunn's post hoc test, and a p value < 0.05 was deemed a significant difference. The reliability of each marker was evaluated using a receiver operating characteristic (ROC) curve. The cut-off value was determined based on the curve, and the specificity and sensitivity were calculated. Analyses were performed using R and GraphPad Prism statistical software.

All participants provided written informed consent before inclusion in the study. This study was approved by the 3rd Reserch Ethics Committe of Okayama Rosai Hospital on February 26, 2015 (No.113-1). All study procedures were carried out in accordance with the principles of the Declaration of Helsinki.

Consent for publication. All participants approve this publication.

Results

Biomarkers for BAPE, MPM, LCa and other diseases. As shown in Fig. 1, the SLPI level was 57.8 ± 25.7 ng/mL in patients with BAPE, which was significantly lower than that in patients with MPM (173.0 ± 134.5 ng/mL) ($p < 0.0001$), LCa (103.5 ± 85.7 ng/mL) ($p < 0.01$), and other diseases (124.8 ± 12.9 ng/mL) ($p < 0.05$).

The HA level was 38.7 ± 4.0 μg/mL in patients with BAPE, which was significantly lower than that in patients with MPM (192.4 ± 40.4 μg/mL) ($p < 0.01$). On the other hand, the HA level was 25.1 ± 2.1 μg/mL in patients with LCa and 21.5 ± 2.0 μg/mL in patients with other diseases, indicating a significantly ($p < 0.05$) higher level in patients with BAPE (Fig. 2).

The SMRP level was 7.5 ± 0.5 nmol/L in patients with BAPE, which was significantly lower than that in patients with MPM (28.5 ± 5.5 nmol/L) ($p < 0.01$) and significantly higher than that in patients with other diseases (5.6 ± 0.4 nmol/L) ($p < 0.05$). On the other hand, in LCa patients, the SMRP level was roughly comparable at 11.0 ± 2.5 nmol/L, with no significant difference observed ($p < 0.512$) (Fig. 3).

The CCL2 level was 6.1 ± 0.8 pg/mL in patients with BAPE, which was significantly higher than that in patients with MPM (3.7 ± 0.7 pg/mL), LCa (2.5 ± 0.3 pg/mL), and other diseases (2.0 ± 0.3 pg/mL) (all $p < 0.05$) (Fig. 4). However, the data differed according to the histological type, with a level of 1.5 pg/mL for patients with epithelioid MPM and 9.5 pg/mL for patients with sarcomatoid MPM. This can difference be attributed to the fact that three of six patients with sarcomatoid MPM had relatively high levels (between 12.9 and 18.2 pg/mL).

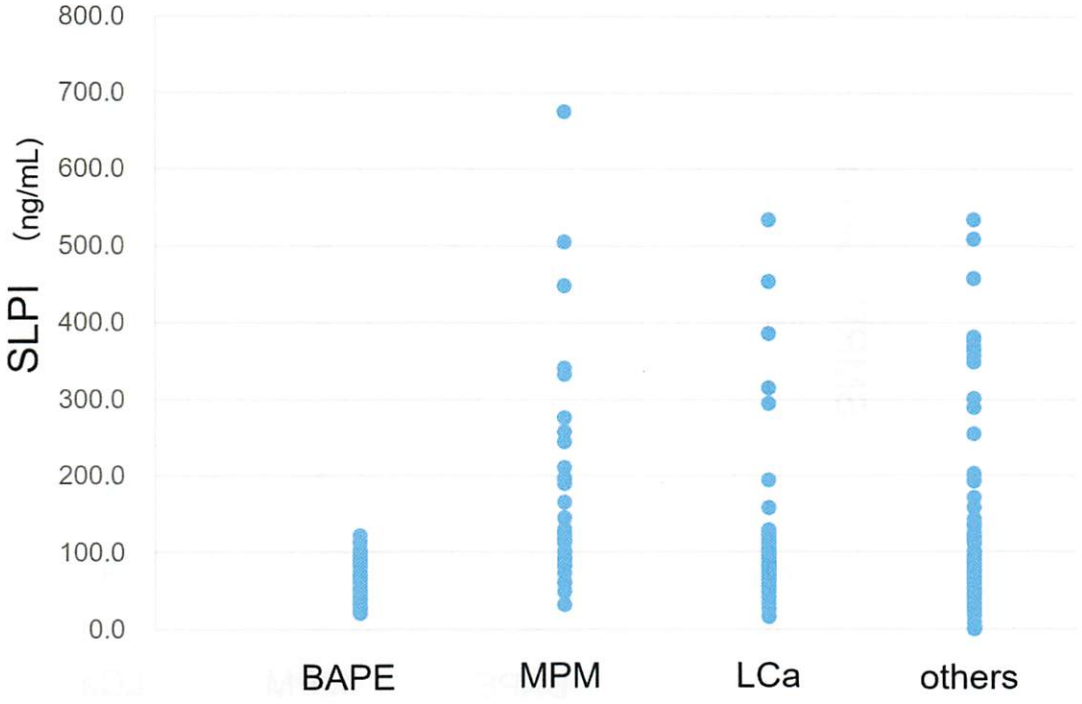

Figure 1. SLPI levels in pleural effusion from patients with BAPE, MPM, LCA, HF and IF. *SLPI* secretory leukocyte peptidase inhibitor, *BAPE* benign asbestos pleural effusion, *MPM* malignant pleural mesothelioma, *LCA* lung cancer, *HF* heart failure, *IF* bacterial pleurisy.

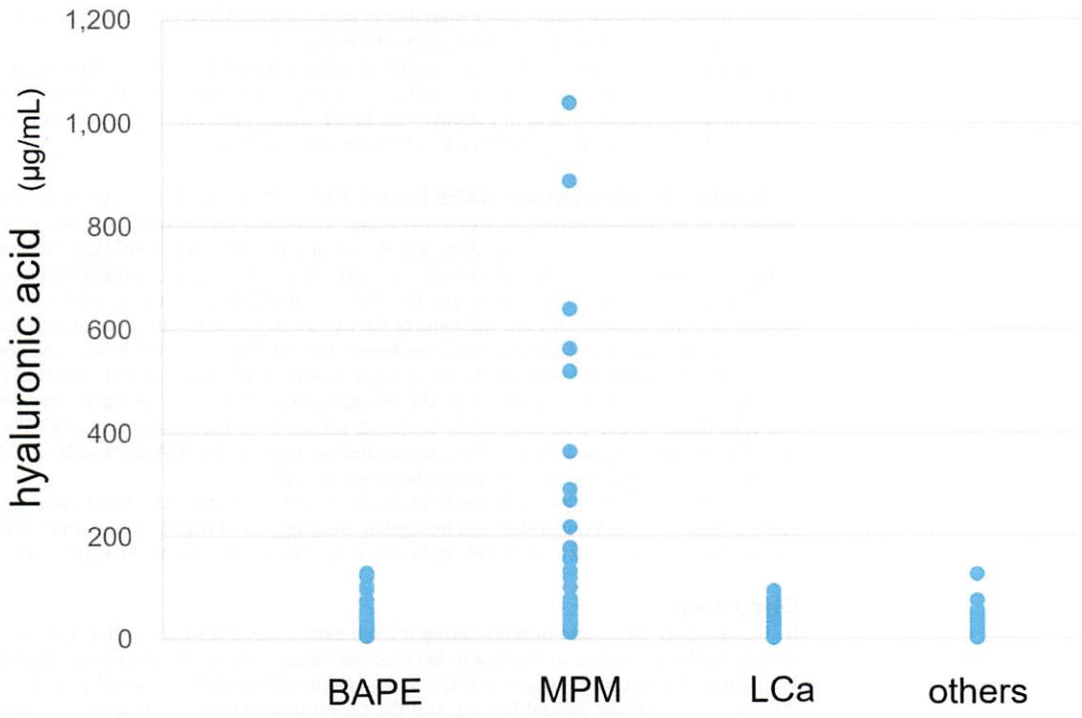

Figure 2. HA levels in pleural effusion from patients with BAPE, MPM, LCA and other diseases. *HA* hyaluronic acid, *BAPE* benign asbestos pleural effusion, *MPM* malignant pleural mesothelioma, *LCA* lung cancer.

Regarding other differential markers, the measured level of galectin-3 was 6.1 ± 0.8 ng/mL in patients with

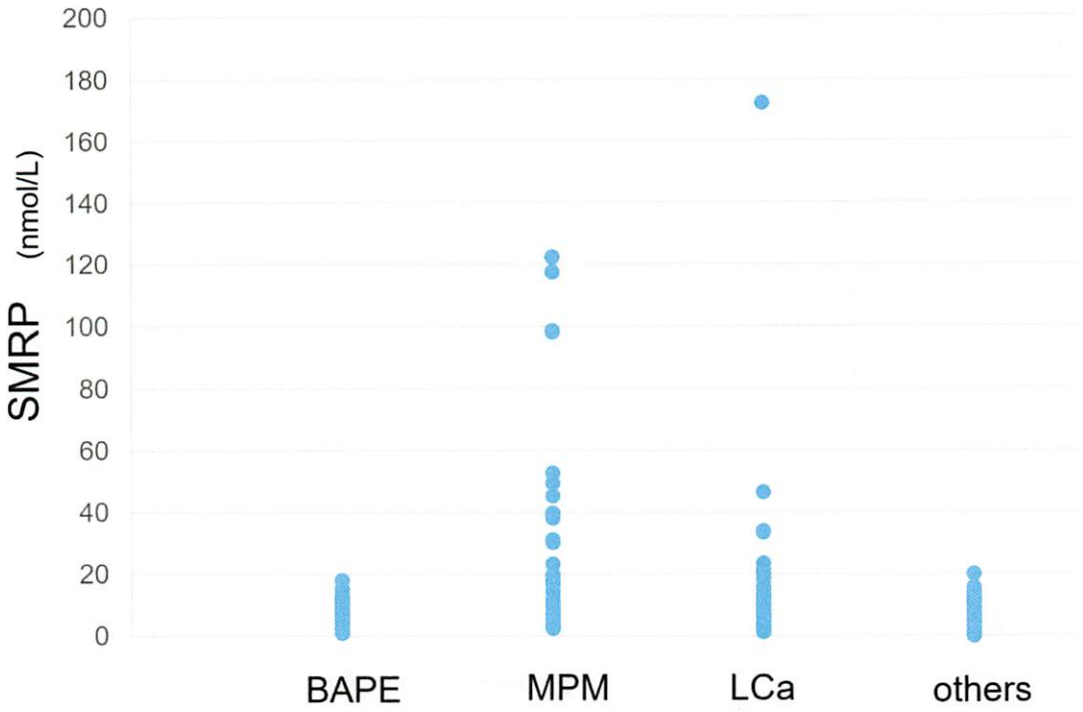

Figure 3. SMRP levels in pleural effusion from patients with BAPE, MPM, LCA, and IF. *SMRP* soluble mesothelin-related peptides, *BAPE* benign asbestos pleural effusion, *MPM* malignant pleural mesothelioma, *LCA* lung cancer, *IF* bacterial pleurisy.

BAPE, which was significantly lower than that in patients with MPM (23.7 ± 4.0 ng/mL), LCa (26.1 ± 3.6 ng/mL), and other diseases (23.4 ± 2.6 ng/mL) (all $p < 0.05$) (Fig. 5).

The CYFRA21-1 level was 20.3 ± 2.3 ng/mL in patients with BAPE, 162.0 ± 35.8 ng/mL in patients with MPM, 164 ± 31.9 ng/mL in patients with LCa, and 21.1 ± 3.9 ng/mL in patients with other diseases. That is, while these levels were significantly lower in patients with BAPE than in patients with MPM and LCa ($p < 0.03$), they were significantly higher than in patients with other diseases ($p < 0.0001$).

Biomarkers to differentiate BAPE from MPM. When the ROC curve was drawn to confirm the reliability of SLPI to differentiate between BAPE and MPM and the cut-off value was 82.9 ng/mL, we found that the sensitivity was 82.4%, the specificity was 86.5%, and the AUC was 0.902, indicating that SLPI is an effective differential marker (Fig. 6). However, with a cut-off value of 47.1 µg/mL in the ROC curve for HA, the sensitivity was 77.0%, the specificity was 75.0%, and the AUC was 0.802 (Fig. 7), which, while useful, were inferior to those of SLPI. Furthermore, with a cut-off value of 9.0 ng/mL in the ROC curve for SMRP, the sensitivity was 72.3%, the specificity was 71.4%, and the AUC was below 8 (0.746; Fig. 8). In the ROC curve for CCL2, the cut-off was 1.8 pg/mL, the sensitivity was 62.7%, the specificity was 44.4%, and the AUC was 0.652. In the ROC curve for galectin-3, the cut-off was 11.4 ng/mL, the sensitivity was 67.9%, the specificity was 59.5%, and the AUC was 0.679. In the ROC curve for CYFRA21-1, the cut-off was 37.3, the sensitivity was 85.3%, and the specificity was 70.3. These results suggest that SLPI is a more effective marker than HA and SMRP, which are differential markers for mesothelioma, for the differential diagnosis of BAPE.

Tests of the ability of each pleural fluid marker to differentiate BAPE from early-stage MPM revealed that, SLPI, CYFRA21-1, HA and SMRP can be used in the diagnosis of BAPE. A combination of SLPI and CYFRA21-1 for the differentiation between BAPE and early-stage MPM achieved an AUC of 0.965.

Discussion

By focusing on BAPE and differentiating it from early-stage MPM and other diseases, we found that SLPI in pleural fluid was a significant indicator because the values were significantly lower than those for other diseases. We believe that the mechanism of BAPE (i.e., asbestos fibres on the visceral pleura) may involve mechanical inflammation without wound healing and the prevention of tissue destruction because of the low SLPI value observed in pleural effusion.

Although HA and SMRP reportedly serve as differential markers for MPM and other diseases, upon drawing the ROC curve, SLPI had an AUC of 0.902, indicating higher reliability than CYFRA21-1, HA and SMRP.

Combining pleural effusion markers with pleural fluid cytology, chest CT, and positron emission tomography–CT images facilitates the differentiation of BAPE from MPM and LCa, which are malignant tumours. However, in the early stages of MPM, many patients do not exhibit significant uptake on chest CT or PET-CT, and

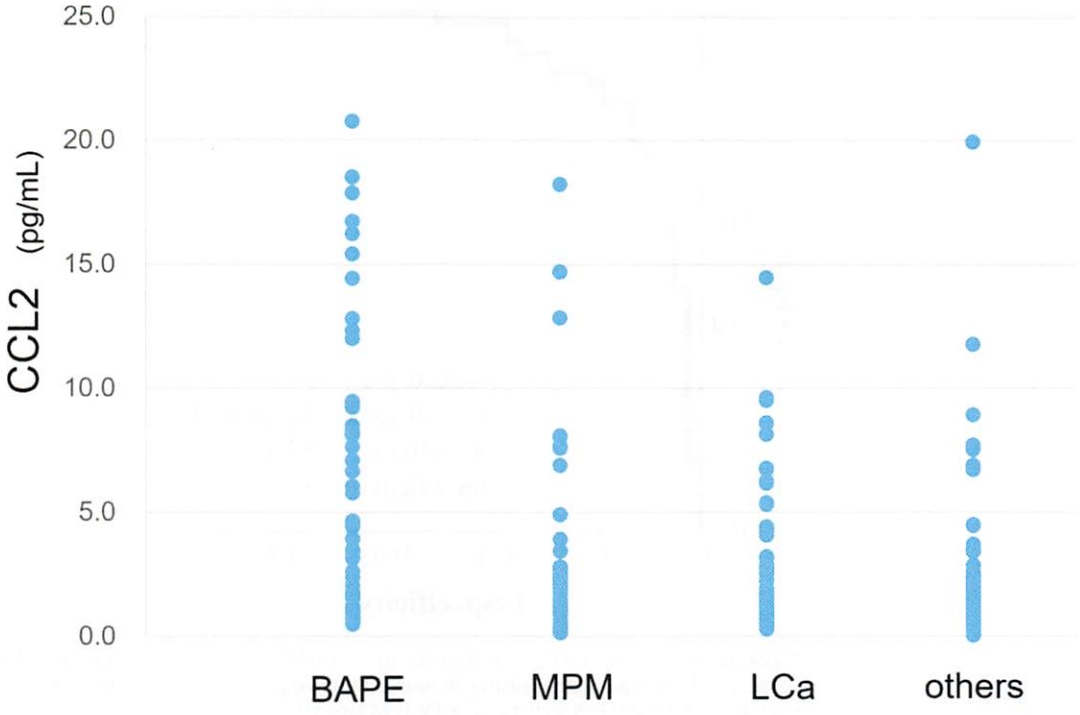

Figure 4. CCL2 levels in pleural effusion from patients with BAPE, MPM, LCA and other diseases. *CCL2* C–C motif chemokine 2, *BAPE* benign asbestos pleural effusion, *MPM* malignant pleural mesothelioma, *LCA* lung cancer.

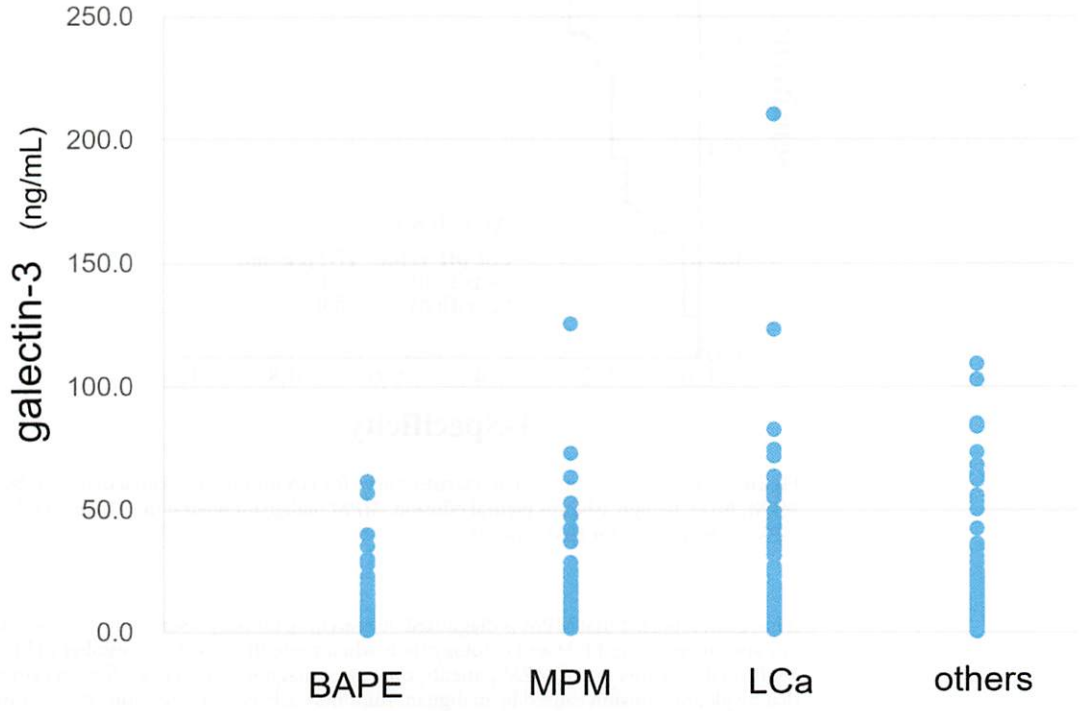

Figure 5. Galectin-3 levels in pleural effusion from patients with BAPE, MPM, LCA and other diseases. *BAPE* benign asbestos pleural effusion, *MPM* malignant pleural mesothelioma, *LCA* lung cancer.

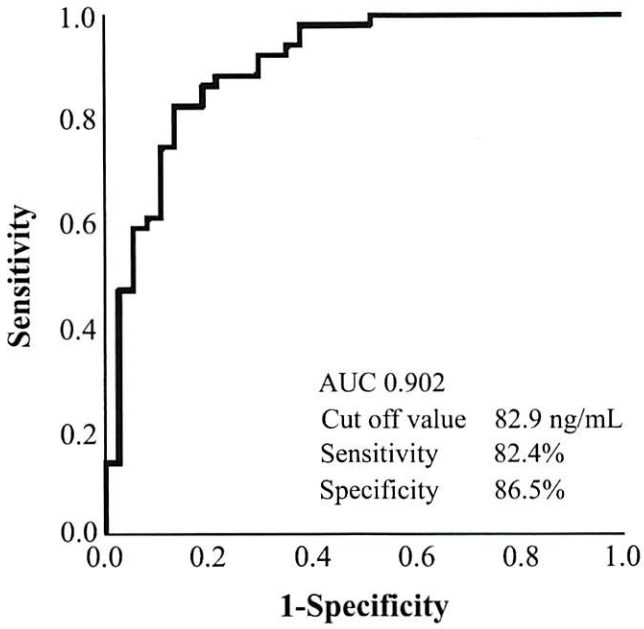

Figure 6. Receiver operating characteristic curve of SLPI for the differential diagnosis between BAPE and MPM. *BAPE* benign asbestos pleural effusion, *MPM* malignant pleural mesothelioma, *SLPI* secretory leukocyte peptidase inhibitor (SPSS Statistics V26 for IBM Japan (https://www.ibm.com/jp-ja/products/spss-statistics)).

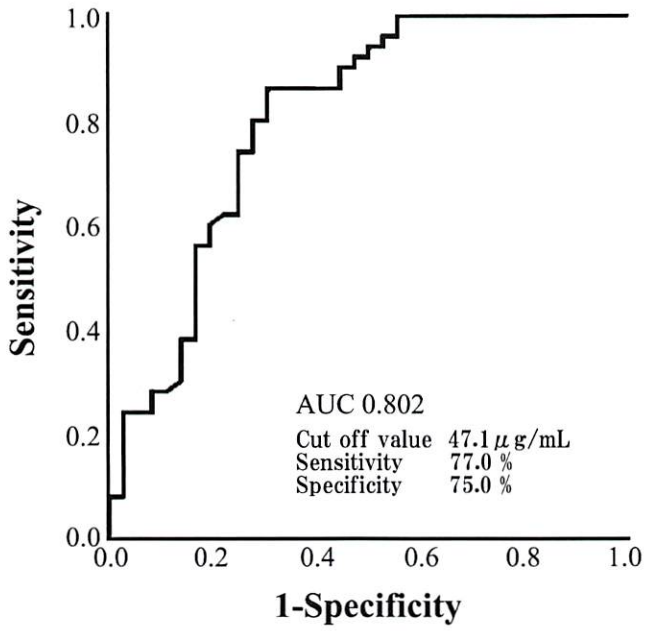

Figure 7. Receiver operating characteristic curve for HA for the differential diagnosis between BAPE and MPM. *BAPE* benign asbestos pleural effusion, *MPM* malignant pleural mesothelioma, *HA* hyaluronic acid (SPSS Statistics V26 for IBM Japan (https://www.ibm.com/jp-ja/products/spss-statistics)).

it has been reported that MPM is diagnosed by searching for the presence of p16 gene mutations in histopathology specimens using FISH and cytology tools when more than a certain number of homozygous deletions are confirmed[2,12]. However, in MPM patients, the rate of diagnosis by pleural effusion cytology is much lower than that by pleural effusion caused by malignant tumours such as LCa. Therefore, even if tumour cells are detected, markers that suggest MPM is present. In the past, such markers included osteopontin[13] and fibulin-3[14,15], but at present, they are rarely evaluated.

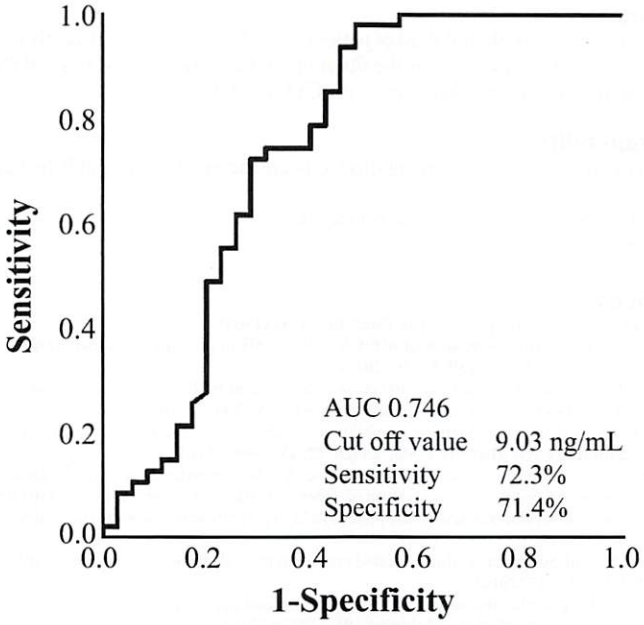

Figure 8. Receiver operating characteristic curve for SMRP for the differential diagnosis between BAPE and MPM. *BAPE* benign asbestos pleural effusion, *MPM* malignant pleural mesothelioma, *SMRP* soluble mesothelin-related peptides (SPSS Statistics V26 for IBM Japan (https://www.ibm.com/jp-ja/products/spss-statistics)).

As a marker for differentiating pleural effusion in MPM, SLPI is described only in a report by Blanquart et al.[16]; however, in their report, three markers (CCL2, galectin-3, and SMRP) were reportedly effective, and if they were used properly, MPM could be differentiated from other diseases that cause pleural effusion, with an AUC of 0.968. However, Blanquart et al. used three markers rather than a single marker. For SLPI alone, the AUC was 0.706, which was the lowest among the markers examined, but its significance was not evaluated. However, our data showed that for the differentiation between BAPE and early-stage MPM, the AUC of a single marker (SLPI) was 0.902, and its combination with CYFRA21-1 achieved an AUC of 0.965, close to the 3 markers described above.

With regard to MPM, CCL2 levels in pleural fluid are high and reportedly increase as the disease progresses[17]. We reported that high levels were found in the serum in patients with advanced-stage MPM[18]. In the present study, we examined CCL2 in pleural fluid and found significantly higher levels in patients with BAPE than in patients with LCa and other diseases. However, with respect to MPM, which should be associated with high levels, we found significantly lower levels compared with BAPE ($p < 0.016$), in contrast to Blanquart et al.[16], who reported that the levels differed according to the histological type, with 2.82 ng/mL in epithelial mesothelioma and 16.73 ng/mL in sarcomatoid mesothelioma. Our patients included 31 with epithelial mesothelioma and six with sarcomatoid mesothelioma (indicating overwhelmingly more patients with epithelial mesothelioma), and the mean level was therefore low, at 2.15 pg/mL. Of the 37 MPM patients included in this study, three had sarcomatoid mesothelioma, and while some patients had a high level, the level in patients with epithelial mesothelioma was 0.4 to 3.0 pg/mL, indicating significant individual variation. We therefore intend to conduct another study with a larger sample size.

Galectin-3 levels were not only high in MPM patients but also in LCa patients, and we therefore suspect that galectin-3 can be used to rule out malignancy because low levels are found in BAPE patients[19]. Similarly, for CYFRA21-1, high levels are common in pleural effusions, even in early-stage MPM, and therefore, even if there is no malignant pleural thickening on imaging, early-stage MPM should be considered because CYFRA21-1 appears to be a marker that can warrant thoracoscopic biopsy[20].

When comparing HA, which is a biomarker of mesothelioma, and SMRP by focusing not on MPM but on BAPE, we found a significantly high AUC of 0.902 for SLPI and significantly lower AUCs for CYFRA21-1 (0.853), HA (0.802) and SMRP (0.746). Even on its own, SLPI was deemed a superior marker for differentiating BAPE from MPM compared with HA and SMRP. We also found that it was more useful than HF or IF for differentiating LCa. A differential diagnosis of LCa can be based on cytology or tumour markers such as carcinoembryonic antigen and CYFRA21-1; for tuberculosis pleurisy among IF, it can be based on adenosine deaminase; and for inflammatory pleurisy, a differential diagnosis can be achieved based on neutrophilia in pleural fluid.

Because SLPI levels were significantly lower in patients with BAPE than in patients with pleurisy caused by other diseases, such as MPM, SLPI may be an effective screening marker for the diagnosis of BAPE and in the differential diagnosis of early-stage MPM.

Conclusions

The levels of SLPI in the pleural fluid of patients with BAPE were significantly lower than those in patients with MPM, LCa, and other diseases. For the differential diagnosis of early-stage MPM, we propose the inclusion of SLPI as a pleural effusion marker along with CYFRA21-1.

Data availability

All data generated or analysed during this study are included in this published article.

Received: 17 February 2021; Accepted: 8 June 2021
Published online: 21 June 2021

References

1. Eisenstadt, H. B. Asbestos pleurisy. *Dis. Chest* **46**, 78–81 (1964).
2. Wu, D. *et al.* Diagnostic usefulness of p16/CDKN2A FISH in distinguishing between sarcomatoid mesothelioma and fibrous pleuritis. *Am. J. Clin. Pathol.* **139**, 39–46 (2013).
3. Hida, T. *et al.* Immunohistochemical detection of MTAP and BAP1 protein loss for mesothelioma diagnosis: Comparison with 9p21 FISH and BAP1 immunohistochemistry. *Lung Cancer* **104**, 98–105 (2017).
4. Bruno, R. *et al.* Differential diagnosis of malignant pleural mesothelioma on cytology: A gene expression panel versus BRCA1-associated protein 1 and p16 tests. *J. Mol. Diagn.* **22**, 457–466 (2020).
5. Martensson, G., Thylen, A., Lindquist, U. & Hjerpe, A. The sensitivity of hyaluronan analysis of pleural fluid from patients with malignant mesothelioma and a comparison of different methods. *Cancer* **73**, 1406–1410 (1994).
6. Fujimoto, N. *et al.* Hyaluronic acid in the pleural fluid of patients with malignant pleural mesothelioma. *Respir. Investig.* **51**, 92–97 (2013).
7. Fujimoto, N. *et al.* Soluble mesothelin-related protein in pleural effusion from patients with malignant pleural mesothelioma. *Exp. Ther. Med.* **1**, 313–317 (2010).
8. Gao, R. *et al.* Diagnostic value of soluble mesothelin-related peptides in pleural effusion for malignant pleural mesothelioma: An updated meta-analysis. *Medicine (Baltimore)* **98**, e14979 (2019).
9. Averdunk, L. *et al.* Secretory leukocyte protease inhibitor (SLPI)-a novel predictive biomarker of acute kidney injury after cardiac surgery: A prospective observational study. *J. Clin. Med.* **8**, 1931 (2019).
10. Epler, G. R., McLoud, T. C. & Gaensler, E. A. Prevalence and incidence of benign asbestos pleural effusion in a working population. *JAMA* **247**, 617–622 (1982).
11. Fujimoto, N. *et al.* Clinical investigation of benign asbestos pleural effusion. *Pulm. Med.* **2015**, 416179 (2015).
12. Nabeshima, K. *et al.* Use of p16 FISH for differential diagnosis of mesothelioma in smear preparations. *Diagn. Cytopathol.* **44**, 774–780 (2016).
13. Lin, H. *et al.* Performance of osteopontin in the diagnosis of malignant pleural mesothelioma: A meta-analysis. *Int. J. Clin. Exp. Med.* **7**, 1289–1296 (2014).
14. Pass, H. I. *et al.* Fibulin-3 as a blood and effusion biomarker for pleural mesothelioma. *N. Engl. J. Med.* **367**, 1417–1427 (2012).
15. Battolla, E. *et al.* Comparison of the diagnostic performance of fibulin-3 and mesothelin in patients with pleural effusions from malignant mesothelioma. *Anticancer Res.* **37**, 1387–1391 (2017).
16. Blanquart, C. *et al.* CCL2, galectin-3, and SMRP combination improves the diagnosis of mesothelioma in pleural effusions. *J. Thorac. Oncol.* **7**, 883–889 (2012).
17. Thomas, R., Cheah, H. M., Creaney, J., Turlach, B. A. & Lee, Y. C. Longitudinal measurement of pleural fluid biochemistry and cytokines in malignant pleural effusions. *Chest* **149**, 1494–1500 (2016).
18. Kishimoto, T. *et al.* Serum levels of the chemokine CCL2 are elevated in malignant pleural mesothelioma patients. *BMC Cancer* **19**, 1204 (2019).
19. Mlika, M. *et al.* Is galectin-3 antibody a useful marker in the diagnosis of malignant pleural mesothelioma? *J. Immunoassay Immunochem.* **34**, 111–125 (2013).
20. Otoshi, T. *et al.* Pleural effusion biomarkers and computed tomography findings in diagnosing malignant pleural mesothelioma: A retrospective study in a single center. *PLoS ONE* **12**, e0185850 (2017).

Acknowledgements

We would like to thank S. Sato and K. Yonemori for writing this manuscript.

Author contributions

T.K. and N.F.: Contributed for evaluation of these data. Y.K.: Contributed for the measurement of biomarker.

Funding

This study was funded by the Industrial Disease Clinical Research Grants.

Competing interests

The authors declare no competing interests.

Additional information

Correspondence and requests for materials should be addressed to T.K.

Reprints and permissions information is available at www.nature.com/reprints.

Publisher's note Springer Nature remains neutral with regard to jurisdictional claims in published maps and institutional affiliations.

Original Article

Acta Radiologica
0(0) 1–5

DOI: 10.1177/02841851211022501
journals.sagepub.com/home/acr
SAGE

The diagnosis of early pneumoconiosis in dust-exposed workers: comparison of chest radiography and computed tomography

Hideyuki Hayashi[1], Kazuto Ashizawa[2], Masashi Takahashi[3], Katsuya Kato[4], Hiroaki Arakawa[5], Takumi Kishimoto[6], Yoshinori Otsuka[7], Satoshi Noma[8] and Sumihisa Honda[9]

Abstract

Background: Chest radiography (CR) is employed as the evaluation of pneumoconiosis; however, we sometimes encounter cases in which computed tomography (CT) is more effective in detecting subtle pathological changes or cases in which CR yields false-positive results.

Purpose: To compare CR to CT in the diagnosis of early-stage pneumoconiosis.

Material and Methods: CR and CT were performed for 132 workers with an occupational history of mining. We excluded 23 cases of arc-welder's lung. Five readers who were experienced chest radiologists or pulmonologists independently graded the pulmonary small opacities on CR of the remaining 109 cases. We then excluded 37 cases in which the CT data were not sufficient for grading. CT images of the remaining 72 cases were graded by the five readers. We also assessed the degree of pulmonary emphysema in those cases.

Results: The grade of profusion on CR (CR score) of all five readers was identical in only 5 of 109 cases (4.6%). The CR score coincided with that on CT in 40 of 72 cases (56%). The CT score was higher than that on CR in 13 cases (18%). On the other hand, the CT score was lower than that on CR in 19 cases (26%). The incidence of pulmonary emphysema was significantly higher in patients whose CR score was higher than their CT score.

Conclusion: CT is more sensitive than CR in the evaluation of early-stage pneumoconiosis. In cases with emphysema, the CR score tends to be higher in comparison to that on CT.

Keywords
Pneumoconiosis, chest radiography, computed tomography, chest, pulmonary emphysema

Date received: 3 April 2020; accepted: 10 May 2021

Introduction

Pneumoconiosis, an occupational lung disease caused by the inhalation of silica, coal particles, or asbestos, still has a serious effect on occupational health worldwide (1). Silicosis, a pneumoconiosis, is an incurable lung disease caused by the inhalation of dust containing free crystalline silica. Early recognition is important

[1]Department of Radiology, Isahaya General Hospital, Nagasaki, Japan
[2]Department of Clinical Oncology, Nagasaki University Graduate School of Biomedical Sciences, Nagasaki, Japan
[3]Department of Radiology, Yujin-Yamazaki Hospital, Shiga, Japan
[4]Department of Radiology, Kawasaki Medical School Hospital, Okayama, Japan
[5]Department of Radiology, Dokkyo Medical University, Tochigi, Japan
[6]Asbestos Research Center, Okayama Rosai Hospital, Okayama, Japan
[7]Department of Internal Medicine, Hokkaido Chuo Rosai Hospital, Hokkaido, Japan
[8]Department of Radiology, Tenri Hospital, Tenri, Japan
[9]Department of Public Health & Nursing, Nagasaki University Graduate School of Biomedical Sciences, Nagasaki, Japan

Corresponding author:
Kazuto Ashizawa, Department of Clinical Oncology, Unit of Translational Medicine, Nagasaki University Graduate School of Biomedical Sciences, 1-7-1 Sakamoto, Nagasaki 852-8501, Japan.
Email: ashi@nagasaki.u.ac.jp

in the management of this disease. Early-stage pneumoconiosis is defined as profusion 0/1 to 1/1 cases on chest radiography (CR) based on the international classification of radiographs of pneumoconiosis published by International Labour Office (ILO) (2,3). Because they do not have pulmonary dysfunction, a radiological examination is essential for the diagnosis of pneumoconiosis for both clinical and epidemiological purposes (1). Although workers with possible exposure to occupational dust are screened using CR, there are some limitations in the assessment of pneumoconiosis on CR.

Computed tomography (CT) is more sensitive than CR in detecting lung parenchymal abnormalities. CR as well as CT findings in patients with silicosis have been documented, and it has been reported that discordance between the two was high, especially for CR-negative and early-stage pneumoconiosis cases (2). In addition, we sometimes encounter cases in which nodules, which are suspected on CR, are not evident on CT, especially in patients with pulmonary emphysema. The aim of the present study was to compare the CR and CT findings in the diagnosis of early-stage pneumoconiosis. Moreover, we also would like to evaluate whether the presence or degree of pulmonary emphysema is associated with the CR and CT scores.

Material and Methods

The present retrospective study was approved by the institutional review board of our hospitals, and the requirement for informed written consent was waived from all participants.

Patients

CR and CT examinations were performed for 132 workers with an occupational history of mining, who were recruited from two laborers' hospitals. Because the imaging findings of arc-welder's pneumoconiosis are different from those of silicosis (4), we excluded 23 cases of arc-welder's lung (Fig. 1). Thus, 109 individuals (109 men; age range = 48–89 years; mean age = 74.8 years) with silicosis or coal workers' pneumoconiosis were included. They included 25 smokers, 72 ex-smokers, and 12 never-smokers. None of the workers in the study had a history of pulmonary disease, such as tuberculosis, pneumonia, or lung cancer.

Interpretation of chest radiography

Posteroanterior CR was taken at full inspiration. CR images were displayed in 3-megapixel LCD medical-grade gray-scale monitor (Radiforce GS 320; Eizo, Ishikawa, Japan). Five readers, who were experienced chest radiologists (MT, KK, and SN, with 21–35 years of experience) or pulmonologists (TK and YO, with 27 and 15 years of experience, respectively) independently graded the profusion of lung abnormalities on CR of 109 cases in comparison to a set of standard radiographs provided by Ministry of Health, Labour and Welfare Labour Standards Bureau. In this set, CR findings are classified into one of seven PR (profusion) categories (PR 0, 1, 2, 3, 4A, 4B, and 4C). No radiographic signs of pneumoconiosis are graded as PR0 and those with pneumoconiotic small opacities as PR1–PR3, depending on increasing number

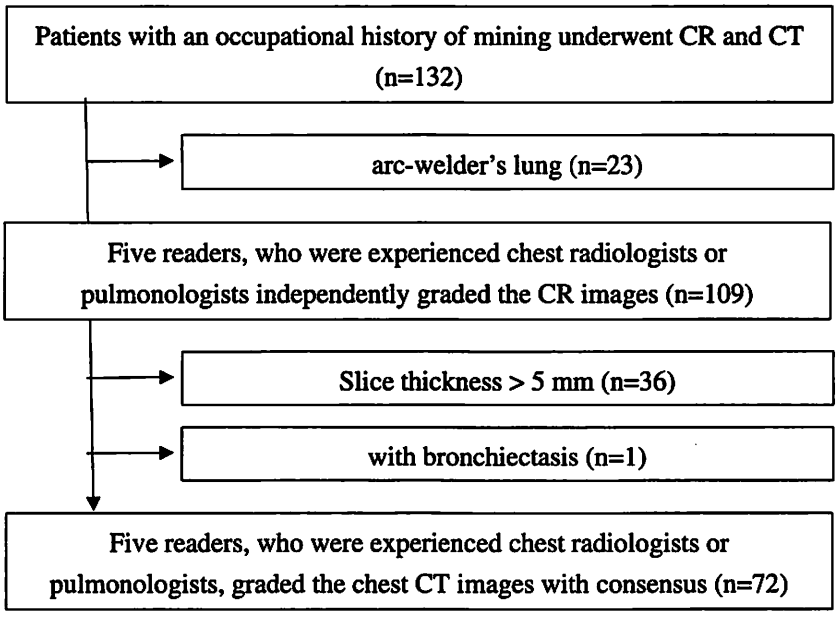

Fig. 1. Study selection process.

Table 1. Observer performance of the experienced chest radiologists or pulmonologists in the interpretation of CR images (n = 109).

CR score	5/5 agreement	4/5 agreement	3/5 agreement
0/1	4	14	11
1/0	1	7	28
1/1	0	3	14
>1/1	0	2	4
Total	5 (4.6%)	26 (24%)	57 (52%)

CR, chest radiography.

(profusion), and large opacities as PR4. Small opacities profusion is recorded on a 12-point scale from 0/– to 3/+, in which 0/– indicates no abnormality and 3/+ signifies the highest concentration of small opacities. We analyzed the observer performance of the five readers in the interpretation of CR. After the analysis of their scores (Table 1), the images from cases for which there was disagreement among the reviewers were reviewed to reach a consensus.

Interpretation of CT

All individuals were scanned in two CT scanners (TSX-302A/1A Aquilion PRIME (Toshiba Medical Systems, Tochigi, Japan) and Light Speed VCT (GE Healthcare, Chicago, IL, USA). Because of the retrospective design of this study, various CT scan protocols were used, and CT images were obtained with slice thicknesses in the range of 3–8 mm and slice intervals in the range of 5–8 mm at full inspiration. We excluded 36 cases with a slice thickness of >5 mm, and one case with marked bronchiectasis in the interpretation of CT images (Fig. 1). CT images were also displayed in 3-megapixel LCD medical-grade gray-scale monitor (Radiforce GS 320; Eizo, Ishikawa, Japan). All CT images were viewed on lung window setting (level = –700 HU; width = 1500 HU). Five readers also graded the profusion of lung abnormalities on CT images of 72 cases with consensus.

We compared the scores in both the CR and CT images. Two other experienced chest radiologists (HH and KA, with 22 and 30 years of experience, respectively) evaluated each CT image and classified the degree of emphysema into three levels: none; mild; and severe. These three levels correspond to the classification in the Fleischner Society guidelines as follows: none = none or trace; mild = mild or moderate; and severe = confluent or advanced destructive (5). The relationship between the degree of emphysema and the CR/CT scores was examined.

Table 2. Comparison of both CR and CT scores (n = 72).

	CT score			
CR score	0/1	1/0	1/1	1/<1
0/1 (n = 27)	21	5	0	1
1/0 (n = 27)	13	9	4	1
1/1 (n = 15)	3	2	8	2
1/<1 (n = 3)	0	1	0	2

CR, chest radiography; CT, computed tomography.

Table 3. Correlation between the degree of pulmonary emphysema and CR/CT scores (n = 72).

Pulmonary emphysema	CR > CT	CR = CT	CR < CT
None (n = 43)	5	26	12
Mild (n = 21)	7	13	1
Severe (n = 8)	7	1	0

CR, chest radiography; CT, computed tomography.

Data analysis

The weighted value of kappa was calculated for the comparison of CR and CT scores (Table 2). Spearman's rank correlation coefficient was calculated to assess the correlation between the degree of pulmonary emphysema and the CR/CT scores (Table 3).

Results

The observer performance in the interpretation of CR images is shown in Table 1. The scores of all five observers were identical in only 5 of 109 cases (4.6%). There were 26 cases (24%) in which the scores of four of the five observers matched. There were 57 cases (52%) in which the scores of three of the five observers matched.

A comparison of CR and chest CT according to the categories is shown in Table 2. The weighted value of the kappa coefficient between the CR and CT scores was 0.456 ($P < 0.01$). 21 out of 27 cases with a CR score of 0/1 matched the score of the CT images. Six cases with a CR score of 0/1 were scored as 1/0 (n = 5) or 1/<1 (n = 1) on CT images. Five cases with a CR score of 1/0 were scored as 1/1 (n = 4) or 1/<1 (n = 1) on CT images. Two cases with a CR score of 1/1 were scored as 1/<1 (n = 2) on CT images. Therefore, there were 13 cases in which the CT score was higher than the CR score (Fig. 2). On the other hand, there were 19 cases in which CR score was higher than the CT score (Fig. 3).

The correlation between the degree of pulmonary emphysema and the CR/CT scores is shown in Table 3. The incidence of pulmonary emphysema was significantly higher (r = 0.503; $P < 0.001$) in cases in which the CR score was higher than the CT score.

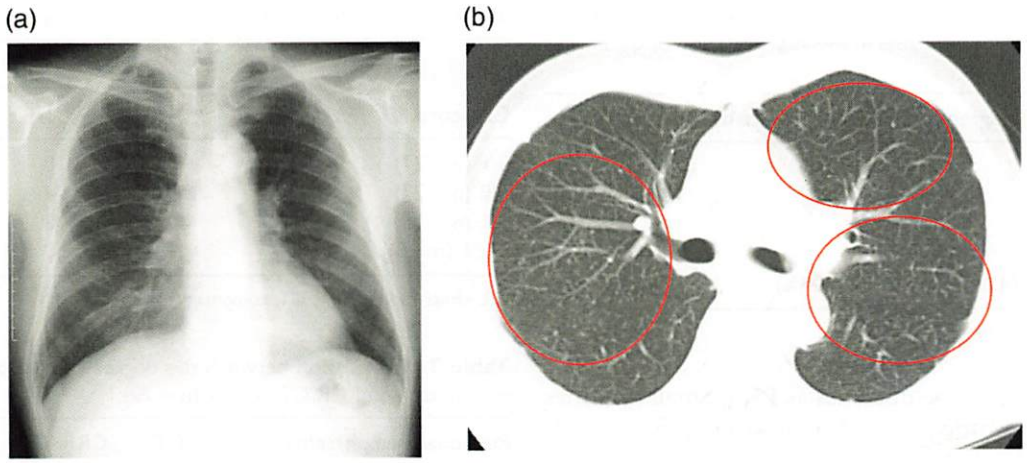

Fig. 2. (a) A 72-year-old man with an exposure duration of 30 years. Chest radiography was judged as profusion 0/1. (b) Computed tomography images revealed many small opacities in the lung parenchyma (circles).

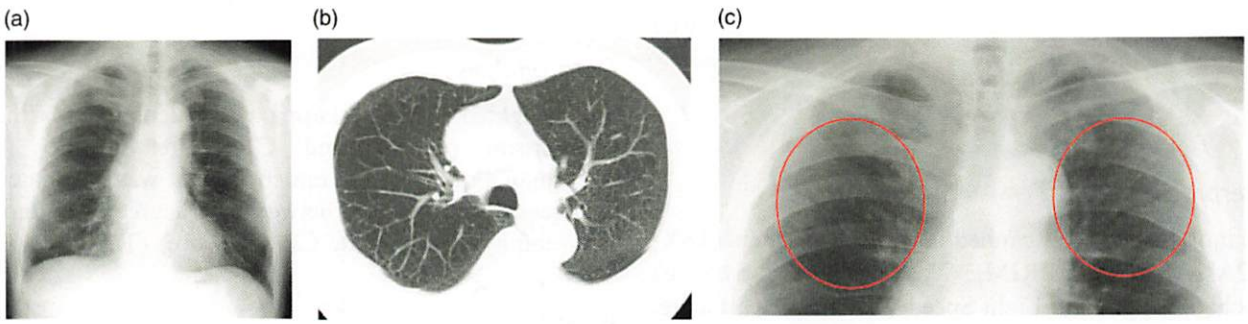

Fig. 3. (a) An 81-year-old man with an exposure duration of 34 years. CR was judged as profusion 1/1. (b) Computed tomography images revealed pulmonary emphysema with a few small opacities in the lung parenchyma. (c) Magnified image of the upper lung fields of CR (a). There appear to be small nodules in the upper lung fields (circles). CR, chest radiography.

Discussion

In the present study, CT is more sensitive than CR in the evaluation of pneumoconiosis. Pneumoconiosis is usually diagnosed based on CR. Currently the diagnosis is based on the international classification of radiographs of pneumoconiosis, published by the ILO in 1980 (3); however, CR is of limited value in cases of low-grade diffuse infiltrative lung disease (6,7). In this study, 18% (13/72) of cases had small nodular lesions that could only be detected on CT, or in which more nodules could be detected by CT. There are some cases in which tiny nodules can only be depicted on CT. Suganuma et al. (8) reported that the CR categorical classification was similar to high-resolution CT (HRCT), with the exception of category 0, in which HRCT was more sensitive.

In patients with pulmonary emphysema, the CR score tended to be higher than the CT score. Although Savranlar et al. (2) also reported that the CR categorical score was higher than the CT score in 15 of 67 patients, the reason was not shown. Patients with silicosis often have pulmonary emphysema. Bergin et al. (9) reported that pulmonary emphysema associated with silicosis was easily detected on CT. To the best of our knowledge, there are no reports on the overestimation of silicotic nodules by correlated with pulmonary emphysema.

It is difficult to diagnose pulmonary emphysema based on CR alone. Thurlbeck and Simon (10) described two different roentgenologic patterns of altered pulmonary vascularity in patients with pulmonary emphysema, namely, "arterial deficiency" and "increased marking". "Increased marking" refer to prominent vascular markings which tend to be irregular in contour. This pattern is thought to occur in patients with mild or moderate emphysema due to redistribution of blood flow, pulmonary arterial hypertension and lung overinflation. We hypothesize that the presence of "increased marking" is one of the factors associated with overestimation of tiny nodules on CR.

Although image interpretation was performed by experienced radiologists or pulmonologists in this study, there were only 5 cases (4.6%) in which all five scores of pneumoconiosis on CR matched. The diagnosis is based on the international classification of radiographs; however, the criterion is ambiguous due to the number of nodules. Since this ambiguity cannot be completely eliminated, even by CT, we are of the opinion that objective evaluation by a system such as computer-assisted diagnosis will be necessary in the future.

The present study has some limitations. First, this was a retrospective study. Second, the study population was relatively small. Third, the slice thickness of CT was relatively thick, not thin-section CT, because CT scans with thick slice thickness have been performed in the past for screening purposes at many institutions, and they are performed in some institutions in our country, even at the present time. Therefore, this limitation might influence the CT profusion score.

In conclusion, CT is more useful than CR in the evaluation of pneumoconiosis. In addition to depicting tiny nodules, we could reduce overestimation, especially in cases with pulmonary emphysema. We suggest using CT as a standard screening method to distinguish between normal and early-stage pneumoconiosis.

Acknowledgments

The authors thank Yuko Nishimoto and Tetsuhisa Nita for their helpful comments.

Declaration of conflicting interests

The authors declared no potential conflicts of interest with respect to the research, authorship, and/or publication of this article.

Funding

The authors received the following financial support for the research, authorship, and/or publication of this article: This study was supported by the Ministry of Health, Labour and Welfare Scientific Research Grant of Japan.

ORCID iD

Kazuto Ashizawa https://orcid.org/0000-0001-6726-1297

References

1. Akira M. High-resolution CT in the evaluation of occupational and environmental disease. High-resolution CT of the lung II. Radiol Clin North Am 2002;40:43–59.
2. Savranlar A, Altin R, Mahmutyazicioğlu K, et al. Comparison of chest radiography and high-resolution computed tomography findings in early and low-grade coal worker's pneumoconiosis. Eur J Radiol 2004;51:175–180.
3. International Labour Office. Guideline for the use of ILO international classification of radiographs of pneumoconiosis, revised ed. 31. Occupational Safety and Health Series No.2. Geneva: International Labour Office, 1980.
4. Yoshii C, Matsuyama T, Takazawa A, et al. Welder's pneumoconiosis: diagnostic usefulness of high-resolution computed tomography and ferritin determinations in bronchoalveolar lavage fluid. Intern Med 2002;12:1111–1117.
5. Lynch DA, Austin JHM, Hogg JC, et al. CT-definable subtypes of chronic obstructive pulmonary disease: a statement of the Fleischner Society. Radiology 2015;277:192–205.
6. Gevenois PA, Pichot E, Dargent F, et al. Low-grade coal worker's pneumoconiosis. Comparison of CT and chest radiography. Acta Radiol 1994;35:351–356.
7. Epler GR, McLoud TC, Gaensler EA, et al. Normal chest roentgenograms in chronic diffuse infiltrative lung disease. N Engl J Med 1978;298:934–939.
8. Suganuma N, Kusaka Y, Hosoda Y, et al. The Japanese Classification of Computed Tomography for pneumoconiosis with the ILO international classification of radiographs for pneumoconiosis. J Occup Health 2001;43:24–31.
9. Bergin CJ, Muller NL, Vedal S, et al. CT in silicosis: correlation with Plain Films and Pulmonary Function Tests. AJR Am J Roentgenol 1986;146:477–483.
10. Thurlbeck WM, Simon G. Radiographic appearance of the chest in emphysema. AJR Am J Roentgenol 1978;130:429–440.

Respiratory Medicine Case Reports 33 (2021) 101381

Contents lists available at ScienceDirect

Respiratory Medicine Case Reports

journal homepage: http://www.elsevier.com/locate/rmcr

Case report

A patient with epithelioid pleural mesothelioma (Myxoid variant) who survived for a long period without treatment

Keiichi Mizuhashi [a,*], Kenzo Okamoto [b], Takumi Kishimoto [c]

[a] Center for Asbestos-Related Diseases, Toyama Rosai Hospital, Uozu-shi, Toyama, Japan
[b] Department of Pathology, Hokkaidoutyuuou Rosai Hospital, Iwamizawa-shi, Hokkaidou, Japan
[c] Research and Training Center for Asbestos-Related Diseases, Okayama-shi, Okayama, Japan

ARTICLE INFO

Keywords:
Epithelioid mesothelioma
Myxoid variant
Long-term survival
No history of asbestos exposure
Female

ABSTRACT

Pleural mesothelioma is a disease with a very poor prognosis. Here, we report a mesothelioma patient who survived for 5 years and a half. As a result of the autopsy, the tumor was diagnosed as a myxoid variant, which is internationally proposed as a histological subtype of epithelioid mesothelioma with a relatively favorable prognosis. Since patients with this disease are expected to survive for a long period even without treatment, careful determination of the therapeutic approach is considered necessary. This report is considered to be the first of a myxoid variant epithelioid pleural mesothelioma in Japan.

1. Introduction

According to mortality statistics by the Ministry of Health, Labour and Welfare of Japan, the number of deaths due to mesothelioma throughout Japan in 2018 was 1,512, consisting of 1275 males and 237 females (male/female ratio = 5.38:1) [1]. Asbestos exposure is considered to have been the cause of the disease in about 80% of the patients, and pleural mesothelioma accounted for about 80% of all cases. Patients with pleural mesothelioma have a chance of cure only if diagnosed at a very early stage and undergo extrapleural pneumonectomy. In other patients, the survival period is about 1–2 years, even with a combination of cisplatin + pemetrexed, which is presently the standard chemotherapy for mesothelioma. According to the survey of the Japanese Association of Clinical Cancer Centers (compiled in February 2018) cited in the Guidelines for Malignant Mesothelioma in the Guidelines for Diagnosis and Treatment of Lung Cancer 2018, the 5-year survival rate by stage is 14.6% for stage I, 4.5% for stage II, 8.0% for stage III, and 0.0% for stage IV. The prognosis is extremely poor in all stages [2]. However, since the immune checkpoint inhibitor nivolumab began to be covered by health insurance in the summer of 2018 in Japan, some improvement in the therapeutic outcome is expected for the future. We encountered a female patient with pleural mesothelioma without a clear history of asbestos exposure who was diagnosed during a health checkup and survived for five years and six months even without treatment. Since autopsy could be performed, we report this case with details of the histopathological findings.

1.1. Case presentation

The patient was an 82-year-old female with dyspnea as the primary complaint. She had no particular past or familial history. She used to be a nurse (until the age of 72 years) and had no history of occupational asbestos exposure. There was also no history of residence in an asbestos-contaminated environment.

Regarding the history of the present illness, she presented with abnormal chest radiographs (Fig. 1a) during a community health screening in July 2006. Still, she left the findings unattended because of the absence of symptoms. On a retrospective review of the plain chest radiographs taken one year before, in July 2005, the right costophrenic angle was already blunted. The plain chest radiographs taken during the community health screening in July 2007 indicated abnormalities again (Fig. 1b). At this time, as the chest radiographs showed a mass in the right thoracic wall in addition to right pleural effusion, the patient was referred to a hospital for close examination. In the chest CT scans taken in July 2007 (Fig. 2), a small amount of pleural effusion was noted on the right side, and pleural masses were found in the right anterior mediastinum and anterior and lateral thoracic regions. A percutaneous pleural needle biopsy was performed for the mass of the right lateral chest wall, and a diagnosis of pleural mesothelioma was made. The pathologist in charge of the needle biopsy described the pathological findings as

* Corresponding author.
E-mail address: kmizuhashi-ind@umin.ac.jp (K. Mizuhashi).

https://doi.org/10.1016/j.rmcr.2021.101381
Received 17 November 2020; Received in revised form 22 February 2021; Accepted 3 March 2021
Available online 8 March 2021

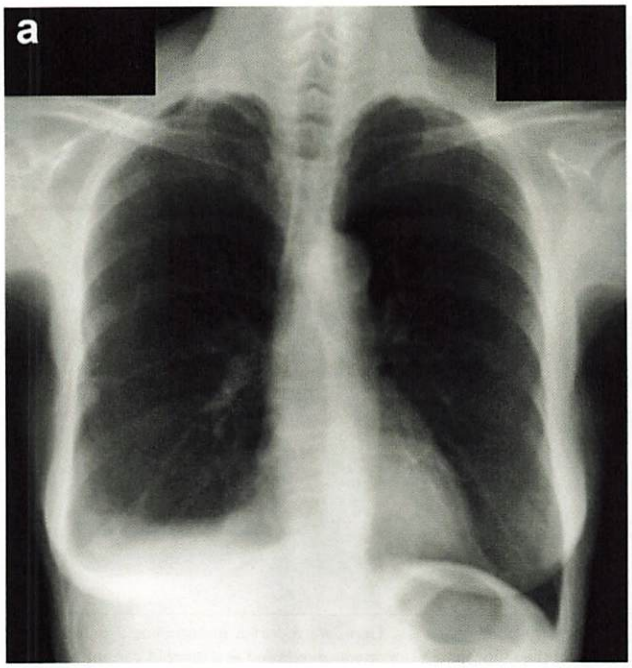

Fig. 1a. Chest radiographs July 2006
The right costophrenic angle is blunted, but no other abnormalities were noted at this point.

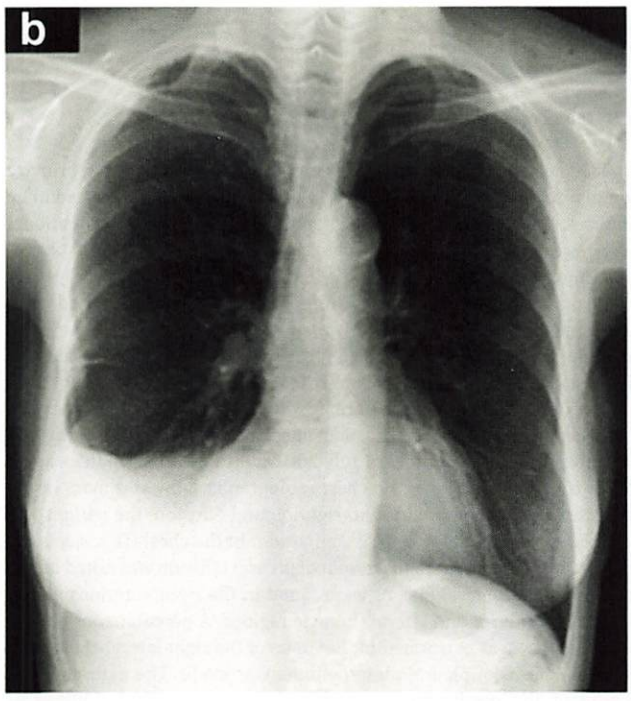

Fig. 1b. Chest radiographs
Blunting of the right costophrenic angle has progressed, and a mass is observed in the thoracic wall.

epithelioid mesothelioma with edematous stroma, and intracytoplasmic mucinous vacuoles are outstanding. However, when we re-evaluated the specimen, it was an epithelioid mesothelioma with abundant myxoid stroma and was completely homogeneous with the histological image at autopsy as described below.

Therefore, the clinician recommended anticancer drug treatment. However, as the patient did not wish for aggressive treatment, she was followed-up without treatment.

Fig. 3 shows a plain chest radiograph taken in April 2008. Masses were observed in the area corresponding to the right lower lung field's peripheries and the right lateral chest wall. Dyspnea appeared in the middle of May 2010, and the patient was admitted to Toyama Rosai Hospital in late May.

1.2. Physical findings on admission

The patient had clear consciousness, a blood pressure of 110/42 mmHg, a regular heart rate of 102 bpm, a body temperature of 36.8 °C, and a respiratory rate of 32/min. Hypoxemia with an arterial blood oxygen tension of 67.1 Torr under inhalation of room air was noted, and the alveolar-arterial oxygen gradient was widened to 36.0 Torr. Mild anemia was noted in the palpebral conjunctiva. Breath sounds were weakened in the right lung region on chest auscultation.

1.3. Laboratory findings on admission

As shown in Table 1, blood tests on admission indicated anemia with a hemoglobin level of 9.9 g/dL, but the platelet count was increased at $53.0 \times 10^4/\mu L$. CRP (8.1 mg/dL) and fibrinogen (600 mg/dL) were high, and the ESR was increased. The concentrations of tumor markers CA125 (147 μ/mL) and TPA (96 μ/mL) were elevated. The CEA, SCC antigen, and ProGRP levels were normal. The serum ERC/mesothelin level [3] was elevated at 35.5 ng/mL (cut-off value: 5–10 ng/mL) [3].

1.4. Clinical course after admission

Fig. 4 shows plain chest radiographs, and Fig. 5 shows contrast-enhanced CT scans of the chest, taken in May 2010, when the patient was first admitted. In addition to many giant tumor-like shadows in the right lower thoracic cavity, shadows of multiple masses extending along the pleura were noted in the right upper thoracic region. Part of the interior of some masses was hypodense. A giant mass was also pointed out in the mediastinum, and the heart was markedly displaced to the left. No clear abnormal shadows suggesting metastasis or infiltration were observed in the lungs. ^{18}F-FDG-PET/CT images were obtained in the same period. No apparent FDG accumulation was noted in areas other than the chest. While contrast-enhanced MRI of the head was also performed, there were no abnormal findings. Thus no extrathoracic distant metastasis was detected.

Therefore, we judged that no aggressive intervention or treatment was necessary at this point and temporarily discharged the patient in June 2010 after introducing opioid administration and home oxygen therapy.

However, the patient was re-admitted in October 2010 due to worsening of dyspnea. After that, the masses in the right thoracic cavity further enlarged.

The patient died at the end of January 2011 due to respiratory insufficiency. We, fortunately, had an opportunity to perform an autopsy. The patient was asymptomatic from 2005. This time is considered to be the time of onset from the radiographs. The diagnosis was made by needle biopsy in August 2007. The patient was observed without treatment until about April 2008. The disease is considered to have progressed slowly during this period but rapidly after that.

1.5. Pathological findings by autopsy

The lesion located in the lower right thoracic cavity was a large lobulated mass that extended widely around the right lung and squeezed it. Necrosis/degeneration was notable in some areas, but translucent collagenous grayish-white areas were predominant. These areas

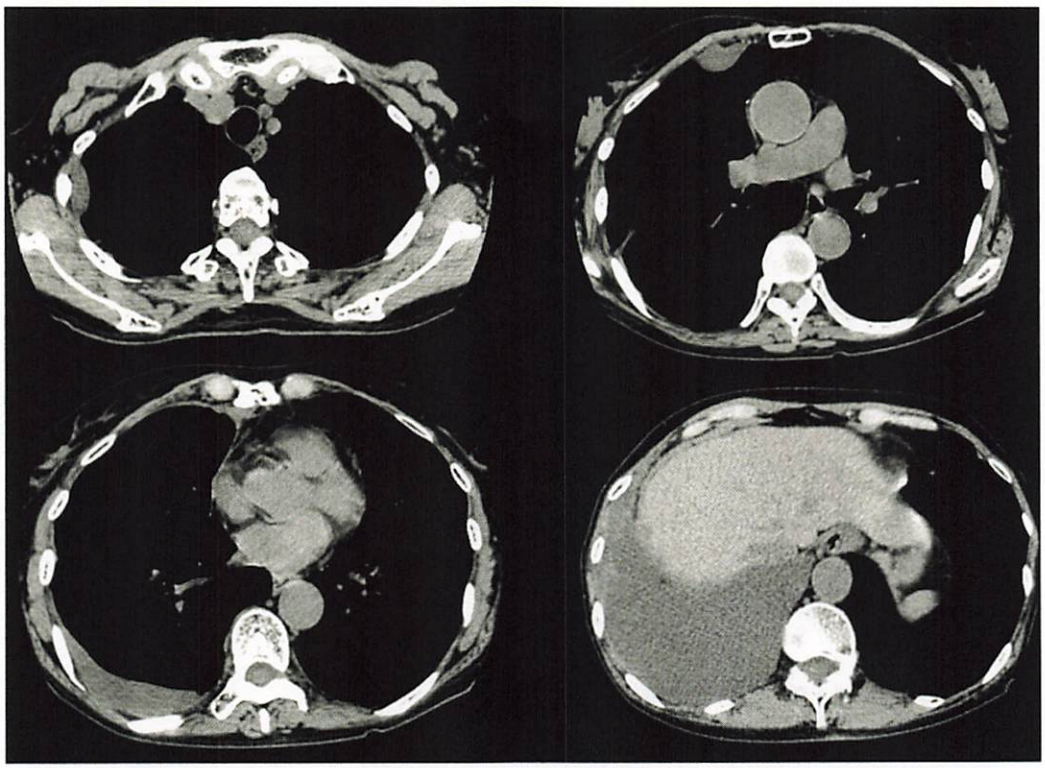

Fig. 2. Chest plain CT scans at the first examination by the previous hospital (July 2007)
A small amount of pleural effusion is present on the right side. Pleural masses are noted in the right anterior mediastinum and anterior and lateral thoracic regions, and irregular pleural thickening extends from the right mediastinum to the anterior thoracic wall.

corresponded to the non-enhancing and highly radiolucent nodules in the mass. Thease nodules are among the multiple mass-like shadows observed in contrast-enhanced chest CT scans(Fig. 5). They were identified with the part of the tumor rich in hyaluronic acid myxoid stroma (Fig. 6).

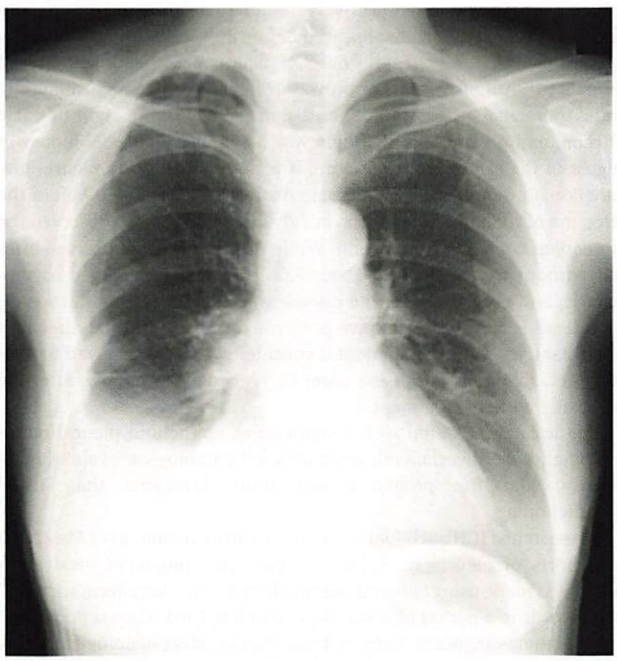

Fig. 3. Chest radiographs taken at in April 2008. Masses were observed in the area corresponding to the peripheries of the right lower lung field and the right lateral chest wall.

On histological examination, the lesion showed a lobulated structure segmented by fiber bundles, and while some parts were solid, rich in cellular components, and necrosed/degenerated, many features exhibited mildly atypical epithelioid tumor cell proliferation consisting of eosinophilic cells rich in the myxoid stroma, low in density, and with a binding tendency (Fig. 7). These features differed from those of a well-differentiated papillary tumor. Infiltrative proliferation into the lungs and mediastinum was observed in some areas, but displacive proliferation was predominant. No lymph node metastasis or distant metastasis was noted.

Myxoid stroma and tumor cells were stained with Alcian Blue and consisted of hyaluronic acid mucus digested by hyaluronidase (Fig. 8). Immunohistochemically, the lesion was positive for Calretinin, D2-40, WT1. Immunohistochemical staining was positive for HEG1(focal) in a small number of tumor cells and EMA (membrane, focal), while was negative for CEA, TTF-1 and desmin.

The loss of BAP1 in tumor cells could not be assessed because the lymphocytes, which should be the internal positive controls, were not stained with BAP1.We guess that the reason for the poor staining of lymphocytes is that it has been more than eight years since the autopsy. (Fig. 9) (Table 2). The Ki-67 index, which was examined simultaneously, varied, being 12.2% in stroma-rich areas but 17.2% in stroma-deficient regions, and was higher than 3.3% determined by needle biopsy in 2007 at the previous hospital. From these findings, a diagnosis of epithelioid pleural mesothelioma (myxoid variant) was made. The number of asbestos bodies detected in the autopsied lungs was 627/g (dry lung), which did not differ from the population average.

Table 1
Laboratory findings on admission

WBC	7300 /μL	TP	7.7 g/dL	Alb %	41.6 %
Neut	72.5 %	Na	139 mEq/L	α1-glb %	5.3 %
Eo	0.3 %	K	4.1 mEq/L	α2-glb %	15.2 %
Baso	0.1 %	Cl	100 mEq/L	β-glb %	9.6 %
Lym	20.3 %	Ca	4.2 mEq/L	γ-glb %	28.3 %
Mo	6.8 %	UA	2.9 mg/dL	ERC/mesothelin	35.5 ng/mL
RBC	443 ×10⁴/μL	UN	14 mg/dL		
Hb	9.9 g/dL	Cr	0.4 mg/dL		
Ht	33.9 %	TB	0.25 mg/dL	BGA	
MCV	82.9 fL	AST	15 IU/L	pH	7.45
MCH	24.2 pg	ALT	14 IU/L	$PaCO_2$	39.7 Torr
MCHC	29.2 g/dL	γ-GTP	29 IU/L	PaO_2	67.1 Torr
PLT	53.0 ×10⁴/μL	ALP	383 IU/L	HCO_3	27.1 mEq/L
CRP	8.1 mg/dL	LD	143 IU/L	A-aDO_2	36.0 Torr
ESR	127 mm/hr	TC	129 mg/dL	BE	3.2
	137 mm/2hrs	TG	69 mg/dL		
Fbg	600 mg/dL	CPK	45 IU/L	Urine	
				S.G	1.011
PT	81.2 %	CA125	147 U/mL	pH	6
APTT	28.7 Sec	TPA	96 U/mL	Prot	(−) mg/dL
FDP	8.0 μg/mL	SLX	27.2 U/mL	sugar	(−) g/dL
AT-III	99.4 fL	NSE	13.7 mg/L	keton	0 mg/dL
D-Dimer	1.6 μg/mL	hyaluronic acid		OB	(−)
			236 ng/dL	Urob.	0.1 EU/dL

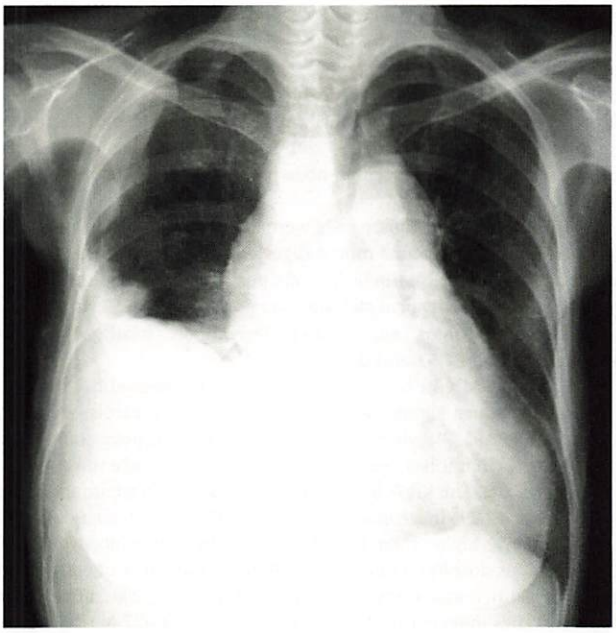

Fig. 4. Chest radiographs taken on admission to Toyama Rosai Hospital (May 2010)
The inside of the right thorax was mostly occupied by multiple masses, and the mediastinum is displaced to the left.

2. Discussion

While the findings in the chest radiographs taken on community health screening in July 2005 were considered normal, the right costophrenic angle was retrospectively found to be blunted, so pleural effusion is believed to have appeared before July 2005. Pleural effusion is reported to be observed at the onset of pleural mesothelioma in 91% of patients [4]. After two years, in July 2007, masses appeared ipsilaterally in the thoracic region with an increase in the amount of right thoracic effusion, and pleural mesothelioma was diagnosed by needle biopsy in August of the same year. Therefore, it is highly likely that pleural mesothelioma accompanied by pleural effusion had developed before the detection of right pleural effusion in July 2005 and that we observed the subsequent course of progression. While the patient was observed after that without treatment until about April 2008, she remained asymptomatic, and progression of the disease was slow. After that, however, the disease is considered to have progressed rapidly, resulting in death in late January 2011. The patient is considered to have survived for five years and six months after the onset (3 years and six months after the diagnosis) without treatment.

The lesion was definitively diagnosed as epithelioid pleural mesothelioma (myxoid variant) through detailed pathological evaluation by autopsy, and the prognosis was more favorable than usual mesothelioma.

We searched ICHUSHI (Japan centra revuo medicina) as of May 2020 for reports of pleural mesothelioma patients' long-term survival. A search was made using "pleural mesothelioma" and "long-term survival" as keywords in a period of about 30 years after 1981. Case reports with mesothelioma diagnoses made by tissue biopsy, clear histological types, non-surgical treatments, and survival for five years or longer were selected. As shown in Table 3, 7 case reports met the above conditions,

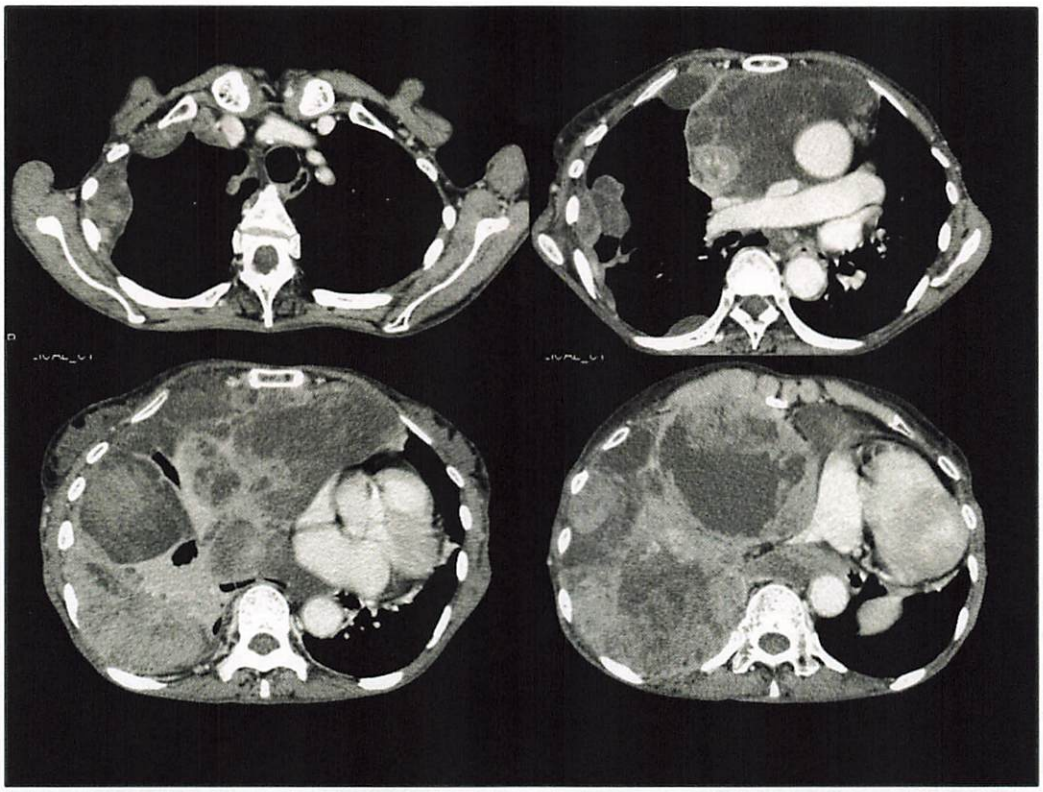

Fig. 5. Contrast-enhanced CT scans of the chest (May 2010)
The right thoracic cavity is filled with multiple masses of various sizes, and part of the masses spread to, and compressed, the left mediastinum. The interior of more than half these masses was extremely hypodense.

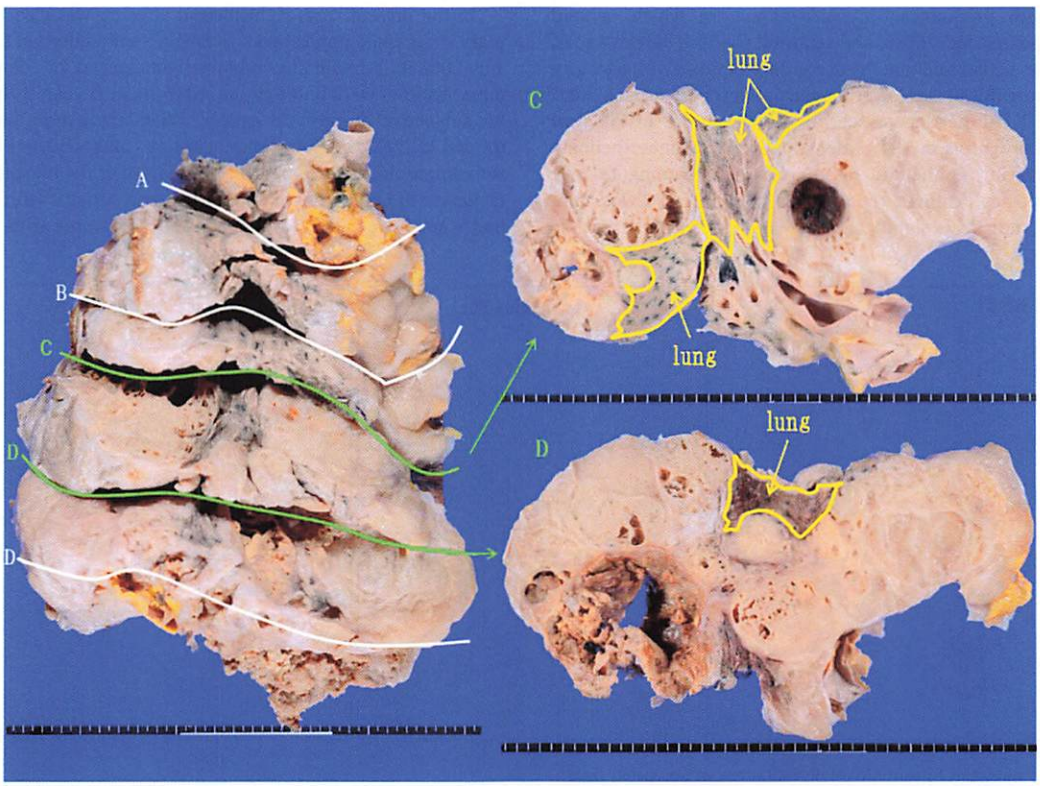

Fig. 6. Macroscopic views of an autopsy sample
A whole picture of a giant mass occupying the right lower thoracic cavity. It was a gelatinous, lobulated, and grayish white tumor showing displacive proliferation and enveloping the lung.

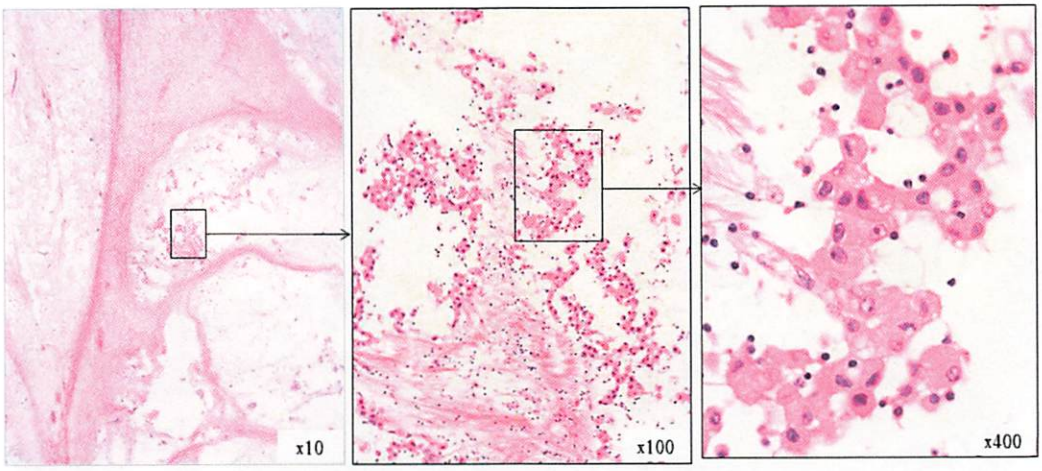

Fig. 7. HE-stained autopsy sample.
A multinodular lesion rich in myxoid stroma segmented into lobules by fiber bundles. Epithelioid tumor cells floating in myxoid stroma are observed.

and they were all-conference proceedings.

The histological type was sarcomatoid and biphasic in 1 case each and epithelioid in the remaining 5. Case 2 was 80 years old at the time of diagnosis and reportedly survived for ten years by repeated drainage of pleural effusion alone. Case 6 received palliative treatment alone, and Case 5 with sarcomatoid mesothelioma was still alive with combination chemotherapy of cisplatin + irinotecan. The histological type was mostly epithelioid, and some of the 5 cases were reported as epithelioid mesotheliomas, which may have been myxoid variants.

It has recently been proposed that epithelioid mesothelioma rich myxoid stroma is a histological characteristic associated with a favorable prognosis. Such lesions can be identified as a subtype of epithelioid mesothelioma. Shia et al. studied 19 patients with epithelioid pleural mesothelioma with pronounced myxoid stroma, in which myxoid components accounted for ≥50%, and reported that the percentage of females (47%) was higher and that the percentage of those with a history of asbestos exposure (53%) was lower than in patients with usual pleural mesothelioma [5]. Also, Alchami et al. evaluated the histological morphology and prognosis in 191 patients with pleural mesothelioma and, by subclassifying epithelioid mesotheliomas according to pronounced morphological features, reported that the prognosis was more favorable with statistical significance in the myxoid/microcystic subtype, with a median survival time of 24 months and a 2-year survival rate of 50% than the tubulopapillary, solid, micropapillary, and pleomorphic subtypes [6]. Based on the report by Shia et al., 2016 WHO classification of tumors of the pleura described the prognosis of epithelioid mesothelioma with abundant myxoid change as favorable [6]. It is necessary to recognize this subtype of epithelioid mesothelioma rich in myxoid components as a myxoid variant, and the present case supports this view. This is considered to be the first detailed case report of a myxoid variant of epithelioid pleural mesothelioma from Japan.

Shia et al. reported that the Ki-67 index was <5% in 7 and 10–30% in 5 of 19 patients [6]. In our present case, also, it was 3.3% by biopsy at the previous hospital and 17.2% even in the stroma-deficient part by autopsy, indicating that the tumor was not highly malignant.

In the present case, right pleural effusion was clearly observed on plain chest radiographs taken during a community health screening in July 2005, but the findings remained unchanged for one year. Although mass shadows were noted in the chest the next year, it took three years for subjective dyspnea to appear. When the needle biopsy was performed in 2007, neither pathologists nor clinicians knew that the mesothelioma shows the characteristic feature of the myxoid stroma. Also, clinicians did not know that mesothelioma patients with this pathology had a good prognosis. Although chest radiograms after the transfer to

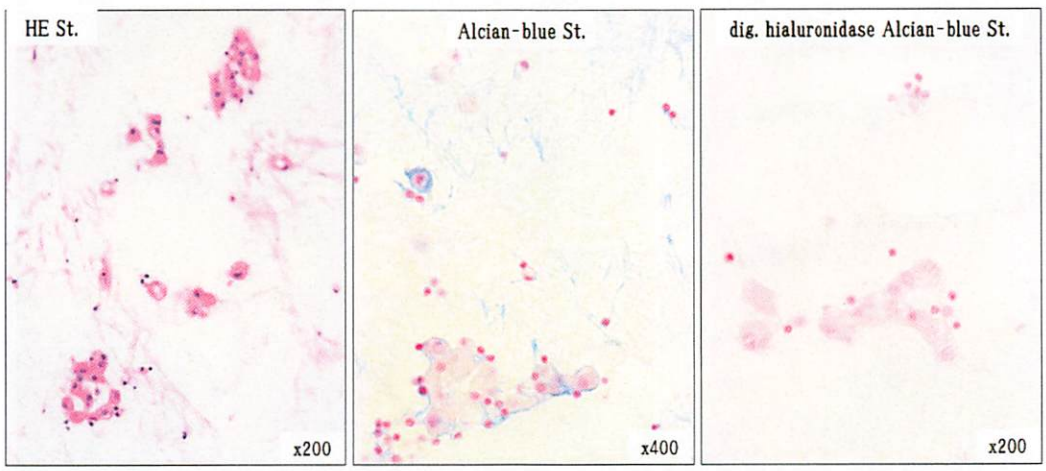

Fig. 8. Alcian blue stain and hyaluronidase digestion test of autopsied tissue.
Myxoid stroma was shown to consist of hyaluronic acid, because it is stained with Alcian blue and digested by hyaluronidase. . (For interpretation of the references to colour in this figure legend, the reader is referred to the Web version of this article.)

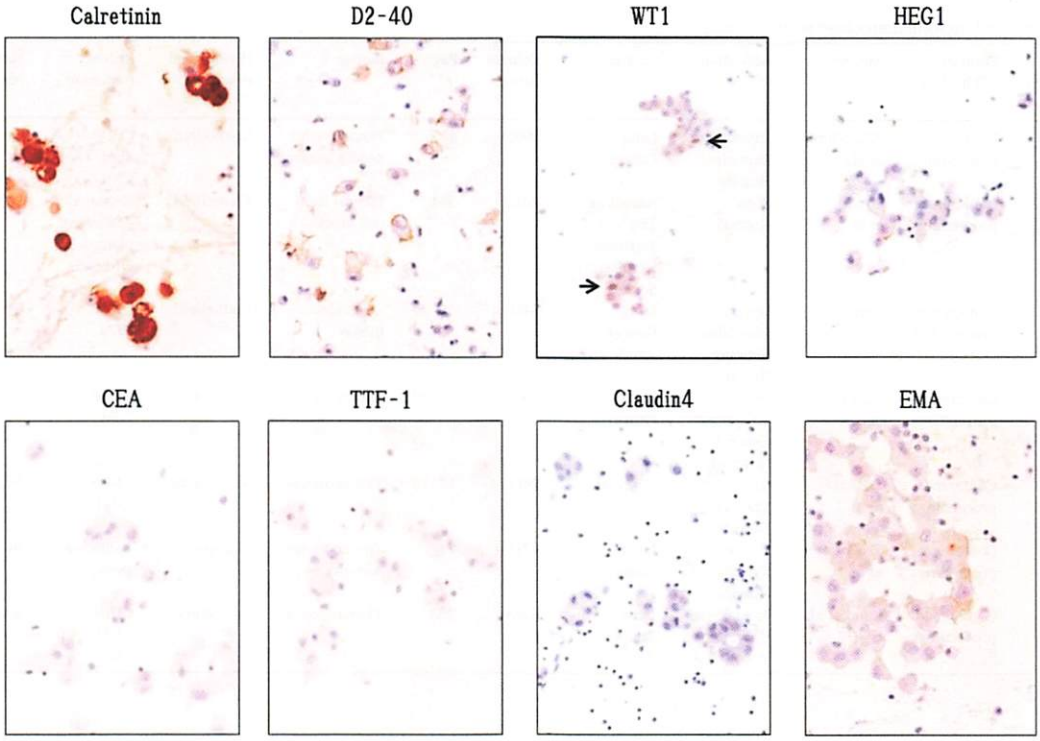

Fig. 9. Immunohistochemical staining.
Tumor cells were positive for calretinin, D2-40, WT1, and HEG1 (focal)
and negative for CEA and TTF-1. EMA
(focal) was positive in the membrane part of the cell.

Toyama Rosai Hospital in 2010 confirmed the accelerated progression of the disease.

Although mass shadows were noted in the chest the next year, It took 3 years for the subjective complaint of dyspnea. When the needle biopsy was performed in 2007, neither pathologists nor clinicians knew that the mesothelioma shows the characteristic feature of the myxoid stroma. Also, clinicians did not know that mesothelioma patients with this pathology had a good prognosis. Although chest radiograms after transfer to Toyama Rosai Hospital in 2010 confirmed the accelerated progression of this disease. Neither pathologists nor clinicians knew that mesothelioma patients with this pathology had a good prognosis.

The tumor is considered to have grown slowly in the early stages but enlarged rapidly and displaced the surrounding tissues after a certain point.

When a myxoid variant of epithelioid mesothelioma has been diagnosed, it may be necessary to develop a therapeutic strategy different from the one for usual pleural mesothelioma, because the disease may progress slowly, at least in the early stages.

Table 2
List of immunohistochemical staining results

Antibody	Reaction	Antibody	Reaction
CK (AE1/AE3)	Positive, diffuse	CEA	Negative
Calretinin	Positive, diffuse	TTF-1	Negative
D2-40	Positive, focal	Naspin A	Negative
WT1	Positive, a few	Ber-EP4	Negative
CK5/6	Positive, diffuse	MOC-31	Negative
Mesothelin	Positive, diffuse	Claudin4	Negative
HEG1	positive, focal	Desmin	Negative
EMA	Positive.(membrane, focal)	MTAP	No defect
Ki-67 index	Stroma-rich area: 12.2% Stroma-deficient area: 17.2% (Ki-67 index of biopsy sample obtained in 2007: 3.3%)		

3. Conclusions

1 We reported a patient with pleural mesothelioma who survived for five years and six months without treatment.
2 Pathologically, the lesion was a myxoid variant of epithelioid mesothelioma rich in a myxoid stroma.
3 The myxoid variant of epithelioid mesothelioma is characterized as a good-prognosis subtype of epithelial mesothelioma, and the present case supports this view.
4 Patients with such pleural mesothelioma may live relatively long even without treatment, and the selection of treatment appropriate for the histological type based on an accurate diagnosis is considered necessary.

An abstract of this paper was presented at the 60th Annual Meeting of the Japanese Society of Occupational Medicine and Traumatology (November 5th-6th, 2010; Chiba City).

Table 3
Long-term survival pleural mesothelioma case search results

Case No.	Year of publication	Form of publication	Authors	Affiliation	Journal	Volume (issue)	Page	Biopsy	Histological type	Primary treatment	Survival period	Dead or alive
1	2019	Conference proceedings	Fukushima et al.	Ichinomiya Municipal Hospital	Lung Cancer	59(6)	402	Percutaneous needle biopsy	Epithelioid	CDDP + PEM, PEM, VNR	≥6 years	Alive
2	2019	Conference proceedings	Oyama et al.	Koto Hosptal	Annals of The Japanese Respiratory Society	Vol.8	361	Pleural fluid cell block	Epithelioid	Repeated drainageof pleural effusion	10 years	Dead
3	2014	Conference proceedings	Suzuki et al.	Seirei Mikatahara General Hospital	Lung Cancer	54(1)	38–39	CT-guided biopsy	Epithelioid	CDDP + GEM	5y.9m.	Dead
4	2014	Conference proceedings	Suzuki et al.	Seirei Mikatahara General Hospital	Lung Cancer	54(1)	38–39	Thoracoscopy	Epithelioid	CDDP + PEM	8y.3m.	Dead
5	2008	Conference proceedings	Yoshida et al.	Gunma University Hospital	Thermal Medicine	24(1)	17–18	Thoracoscopy	Sarcomatoid	CDDP + CPT11	5y.2m.	Alive
6	2007	Conference proceedings	Tsukada et al.	Yokosuka Kyosai Hospital	Lung Cancer	47(1)	71	Thoracoscopy Autopsy	Biphasic	Palliative therapy	9y.3m.	Dead
7	2002	Conference proceedings	Kano et al.	Kanazawa University Hospital	Lung Cancer	42(3)	233	Thoracoscopy	Epithelioid	CDDP + ADM + VP-16(a)	8 years	Alive

[a] Intrathoracic.

Declaration of competing interest

The authors declare no conflicts of interest associated with this manuscript.

Acknowledgments

The author would like to thank the Medical English Service (https://www.med-english.com) for the English language review (for editing the draft of this manuscript).

References

[1] Trends in the number of deaths from mesothelioma by prefecture based on Vital Statistics of Japan (Final data): Ministry of Health, Labor and Welfare https://www.mhlw.go.jp/toukei/saikin/hw/jinkou/tokusyu/chuuhisyu18/dl/chuuhisyu.pdf. (accessed 2020-06-30).

[2] Guidelines for the diagnosis and treatment of lung cancer 2018 Part 2: overview of the Guidelines for diagnosis and treatment of malignant pleural mesothelioma, 2018 accessed 2020-06-30, https://www.haigan.gr.jp/guideline/2019/2/0/190200000100.html.

[3] M. Shuji, H. Okio, Biochemical markers of pleural/peritoneal effusion–recent discoveries, Pathology and Clinical Medicine 28 (2010) 1125–1128.

[4] Y. U M, et al., Computed tomographic findings of environmental asbestos-related malignant pleural mesothelioma, Respiology 3 (1) (1998) 33–38.

[5] J. Shia, et al., Malignant mesothelioma with pronounced myxoid stroma : a clinical and pathological evaluation of 19 cases, Virchows Arch. 447 (2005) 828–834.

[6] F.S. Alchami, et al., Myxoid variant epithelioid pleural mesothelioma defines a favourable prognosis group: an analysis of 191 patients with pleural malignant mesothelioma, J. Clin. Pathol. 70 (2017) 179–182.

労災疾病臨床研究事業費補助金

悪性胸膜中皮腫に対するヒト化抗CD26抗体と免疫チェックポイント阻害薬との革新的併用療法の開発

令和3年度　総括・分担研究報告書

令和4年3月31日発行

発行：研究代表者　森本　幾夫
〒113-8421　東京都文京区本郷2-1-1
順天堂大学大学院医学研究科　免疫病・がん先端治療学講座
TEL：03-3868-2310